Modelling Angiogenesis: A Discrete to Continuum Approach

Samara Pillay

Balliol College

University of Oxford

A thesis submitted for the degree of

Doctor of Philosophy

Trinity 2017

Acknowledgments

I would like to thank my supervisors, especially Helen Byrne and Philip Maini, for their support and guidance over the years; it has been an invaluable experience to learn from you both. I would also like to thank Michael Ward at the University of British Columbia for helpful discussions leading to a piece of work included in Appendix F of this thesis.

I would like to acknowledge the funding bodies that supported my studies, including the Natural Sciences and Engineering Research Council of Canada (NSERC), the Schlumberger Foundation and the Oppenheimer Memorial Trust. Conference travel and research visits were made possible by travel awards and assistance from the following bodies: Society for Industrial and Applied Mathematics, American Physical Society, Society for Mathematical Biology, Santander and the Mathematical Institute.

Finally, thanks to my parents, sister, aunt, partner and Taylor for their love and support.

Declaration

The work in this thesis has been conducted by myself under the guidance of my supervisors, Helen Byrne and Philip Maini, unless otherwise stated.

A version of Chapter 2 has been published in Physical Review E, 95, 012410, 2017, entitled 'Modelling Angiogenesis: A Discrete to Continuum Description' by S. Pillay, H. M. Byrne and P. K. Maini.

A version of Chapter 4, entitled 'The Impact of Exclusion Processes on Angiogenesis Models' by S. Pillay, H. M. Byrne and P. K. Maini, is under review for publication in the Journal of Mathematical Biology, Karl Hadeler Special Issue.

The work contained within Appendix F has been completed in collaboration with Michael Ward at the University of British Columbia.

Abstract

Angiogenesis is the process by which new blood vessels develop from existing vessels. Angiogenesis is important in a number of conditions such as embryogenesis, wound healing and cancer. It has been modelled phenomenologically at the macroscale, using the well-known '*snail-trail*' approach in which trailing endothelial cells follow the paths of other, leading endothelial cells. In this thesis, we systematically determine the collective behaviour of endothelial cells from their behaviour at the cell-level during corneal angiogenesis. We formulate an agent-based model, based on the snail-trail process, to describe the behaviour of individual cells. We incorporate cell motility through biased random walks, and include processes which produce (branching) and annihilate (anastomosis) cells to represent sprout and loop formation. We use the transition probabilities associated with the discrete model and a mean-field approximation to systematically derive a system of non-linear partial differential equations (PDEs) of population behaviour that impose physically realistic density restrictions, and are structurally different from existing snail-trail models. We use this framework to evaluate the validity of a classical snail-trail model and elucidate implicit assumptions. We then extend our framework to explicitly account for cell volume. This generates non-linear PDE models which vary in complexity depending on the extent of volume exclusion incorporated on the microscale. By comparing discrete and continuum models, we assess the extent to which continuum models, including the classical snail-trail model, account for single and multi-species exclusion processes. We also distinguish macroscale exclusion effects introduced by each cell species. Finally, we compare the predictive power of different continuum models. In summary, we develop a microscale to macroscale framework for angiogenesis based on the snail-trail process, which provides a systematic way of deriving population behaviour from individual cell behaviour and can be extended to account for more realistic and/or detailed cell interactions.

Contents

Abbreviations and Parameters

TC	Tip cell
EC	Endothelial cell (also known as a stalk cell)
VE	Volume exclusion
TAF	Tumour angiogenic factor
tip-to-tip anastomosis	Tip cell connects with another tip cell
tip-to-sprout anastomosis	Tip cell connects with another endothelial cell
CA	Cellular automaton
PDE	Partial Differential Equation
ODE	Ordinary Differential Equation
DCE	Discrete Conservation Equation
CA Model 0	No volume exclusion
CA Model 1	TC VE with probability $1 - a_n$ and tip-to-tip anastomosis with probability a_n
CA Model 2	TC VE with probability $1 - a_n$ and tip-to-tip anastomosis with probability a_n, and EC VE with probability $1 - a_e$ and tip-to-sprout anastomosis with probability a_e
Model 0 PDEs	PDEs derived from CA Model 0
Model 1 PDEs	PDEs derived from CA Model 1
Model 2 PDEs	PDEs derived from CA Model 2
BC model	Byrne and Chaplain (1995a) model
P_m	Motility probability in CA
P_p	Branching probability in CA
a_n	Probability of tip-to-tip anastomosis
a_e	Probability of tip-to-sprout anastomosis
h	Lattice spacing in CA
$\bar{K}$	Time step in CA
τ	Relates discrete and continuum timescales
D	Diffusion coefficient
χ	Chemotactic coefficient
λ	Branching rate
μ	Motility rate
β_n	Tip-to-tip anastomosis rate in BC model
β_e	Tip-to-sprout anastomosis rate in BC model

Chapter 1

Introduction

Angiogenesis is the process by which blood vessels develop from existing vasculature. Blood vessel networks are prevalent throughout the body and provide tissue with oxygen and nutrients, and therefore angiogenesis is important in a number of pathological and non-pathological processes. During embryogenesis, sprouting angiogenesis creates the network of arteries and veins (Potente et al., 2011). In adulthood, generally, vessels are quiescent unless stimulated by pro-angiogenic signals. For example, angiogenesis is stimulated in wound healing to regenerate tissue. Deviations from normal vessel growth are implicated in a number of pathological conditions, including blinding eye diseases (e.g. age-related macular degeneration), stroke, and cancer (Potente et al., 2011; Carmeliet, 2005). Given the importance of angiogenesis in pathological conditions, there has been much interest in recent years in developing therapeutic strategies to promote or inhibit angiogenesis (Carmeliet and Jain, 2011).

Cancer is a devastating disease that affects many people worldwide. In 2014, there were approximately 357,000 new cancer cases diagnosed in the UK (Cancer Research UK, 2017). The controls that regulate healthy cell function are disrupted in cancer cells, which results in their rapid and excessive growth, and may eventually lead to the formation of solid tumours. A tumour requires a supply of nutrients, via

a vascular network, to grow in size. Solid tumours initiate vascular development via angiogenesis, a hallmark of cancer (Hanahan and Weinberg, 2000, 2011), to increase nutrient and oxygen supply, and remove metabolic waste (Hanahan and Weinberg, 2011).

Since angiogenesis is important for tumour growth and spread, the treatment of cancer via anti-angiogenic therapies is an active area of research (Samant and Shevde, 2011; Carmeliet and Jain, 2011; Jain, 2001; Carmeliet, 2005; Folkman, 1971; Jain, 2014). Anti-angiogenic therapies inhibit vessel growth by targeting components involved in the angiogenic process. For example, they may inhibit proteins that stimulate the formation of new vessels (Samant and Shevde, 2011). Paradoxically, however, it is thought that certain anti-angiogenic treatments transiently "normalise" tumour vasculature, resulting in improved nutrient supply (Jain, 2001). Combination therapies, in which a cytotoxic drug is administered once the blood flow has been improved by an anti-angiogenic drug, is a promising methodology for treatment (Jain, 2001; Samant and Shevde, 2011; Carmeliet, 2005). However, for these treatments to be successful, a suitable dosing schedule must be identified. This requires an understanding of how cell-level (microscale) properties, such as vessel structure (formed via angiogenesis), affect tissue-level (macroscale) dynamics, including nutrient and drug transport. Mathematical modelling can provide this insight, and therefore, is a powerful tool for increasing our understanding of angiogenesis, thereby facilitating the development of new drugs and combination treatment protocols for cancer.

This thesis focuses on connecting discrete and continuum models of angiogenesis, thereby providing a concrete methodology to move from a cell to tissue scale description. In light of this objective, we now review the biology of tumour angiogenesis and the relevant mathematical literature.

1.1 Tumour Angiogenesis

A number of *in vitro* and *in vivo* assays (e.g. chick chorioallantoic membrane (CAM) assay) are used to study angiogenesis. However, given its avascular nature, the corneal assay (see Fig. 1.1) is widely used to study angiogenesis *in vivo* (Auerbach et al., 2003). A tumour fragment or a pellet containing angiogenic factors (AFs) implanted into the cornea of a small animal, usually a mouse (Auerbach et al., 2003), stimulates new vessels to emerge from the limbus, which forms the border between the cornea and sclera (the white of the eye), typically situated 1 to 2 mm from the TAF source (Muthukkaruppan et al., 1982; Gimbrone et al., 1974). We now describe how blood vessel formation may be stimulated during tumour angiogenesis.

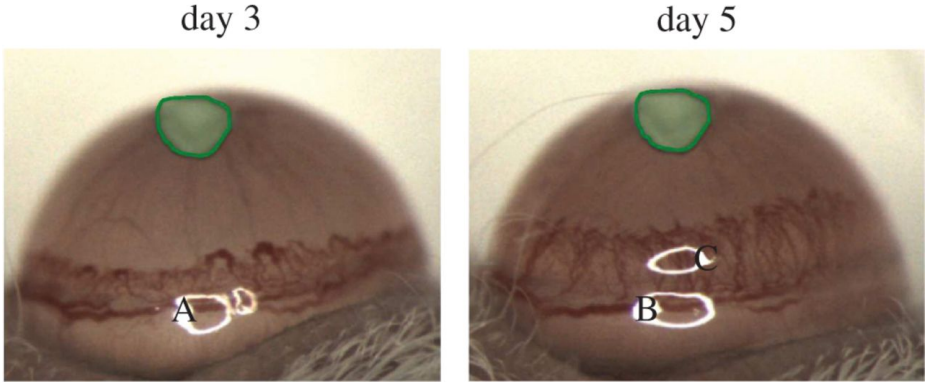

Figure 1.1: Corneal assay. A pellet (encircled in green) containing angiogenesis-inducing factors has induced the growth of vessels from the limbus. A, B and C indicate artefacts introduced through camera lighting. Figure reproduced from Connor et al. (2015), Anthony J. Connor, Radosław P. Nowak, Erica Lorenzon, Markus Thomas, Frank Herting, Stefan Hoert, Tom Quaiser, Eliezer Shochat, Joe Pitt-Francis, Jonathan Cooper, Philip K. Maini, Helen M. Byrne, An integrated approach to quantitative modelling in angiogenesis research, Journal of the Royal Society Interface, 2015, Volume 12, Issue 110, 20150546, by permission of the Royal Society.

Avascular tumours, composed of a core of cancer cells unconnected to a blood supply, undergo diffusion-limited growth: they rely on the diffusive transport of nutrients, including oxygen, from nearby capillaries for their growth. Without additional nutrient supply, the tumour eventually reaches an equilibrium size at which the net rate of

cell proliferation in the tumour periphery balances the net rate of cell death towards its centre (Folkman and Hochberg, 1973). Therefore, avascular tumours cannot grow beyond a few millimetres in diameter (Folkman and Hochberg, 1973).

Hypoxic tumour cells (i.e. cells that are starved of oxygen) secrete diffusable tumour angiogenic factors (TAFs), such as vascular endothelial growth factor (VEGF), that stimulate the growth of new blood vessels from the existing vasculature (Klagsbrun and Moses, 1999; Folkman and Klagsbrun, 1987; Carmeliet and Jain, 2011). The VEGF signalling pathway usually plays a key role in regulating angiogenesis in pathological and non-pathological angiogenesis (Carmeliet and Jain, 2011; Blanco and Gerhardt, 2013). Other angiogenic factors include the fibroblast growth factor (FGF) family, which can stimulate angiogenesis indirectly by "inducing the release of angiogenic factors from other cell types" (Carmeliet and Jain, 2011).

TAFs diffuse towards the nearby vasculature, establishing a spatial gradient between the tumour and the vasculature. Once the TAFs reach the blood vessels, endothelial cells (ECs) lining the vessels are induced to degrade the vessel's basal membrane and the extracellular matrix (Klagsbrun and Moses, 1999; Carmeliet and Jain, 2011; Potente et al., 2011), and migrate, via chemotaxis (the directed movement of cells in response to a chemical spatial gradient), up spatial gradients of the TAFs and towards the tumour (Ausprunk and Folkman, 1977), using filopodia to sense environmental guidance cues (Carmeliet and Jain, 2011; Potente et al., 2011; Benitez and Heilshorn, 2013) (see Fig. 1.2).

Recruitment of ECs from the vessels results in the formation of finger-like capillary sprouts: ECs (also known as stalk cells) follow the paths of leading ECs (Carmeliet and Jain, 2011; Potente et al., 2011), known as tip cells (TCs), producing a 'snail-trail' of vessels (Klagsbrun and Moses, 1999) (see Fig. 1.2). Sprouts increase in length through continued migration up the TAF gradient, and proliferation of ECs (stalk cells) behind the leading TC (Klagsbrun and Moses, 1999; Potente et al., 2011;

Carmeliet and Jain, 2011). The snail-trail process is a description of the vessel-branching model (Carmeliet and Jain, 2011; Potente et al., 2011). In this thesis, we will refer to stalk cells as ECs.

As the sprouts approach the tumour, they fuse and form interconnected loops through anastomosis (see Fig. 1.2). Capillary loop formation and perfusion are essential for blood circulation and nutrient supply. As the sprouts approach the tumour, new TCs emerge. This process, stimulated by TAFs (Carmeliet and Jain, 2011) and mediated by Delta-Notch signalling (Carmeliet and Jain, 2011; Potente et al., 2011), is known as branching (see Fig. 1.2). Experimental results (Ausprunk and Folkman, 1977; Muthukkaruppan et al., 1982) in the corneal assay indicate that the density of the vascular network, specifically the density of the TCs, increases as the tumour is approached, producing the so-called brush-border effect. Delta-Notch signalling and VEGF cross-talk dynamically select TCs and ECs, and regulate TC migration and EC proliferation (Blanco and Gerhardt, 2013).

Other processes, such as haptotaxis (the migration of cells up an adhesive gradient) aid TC migration (Klagsbrun and Moses, 1999). Lumen formation, vessel maturation and stabilisation also occur during angiogenesis (Blanco and Gerhardt, 2013). Once the sprouts reach the tumour, vascularisation occurs, followed by network reorganisation and remodelling.

We note that there are other ways in which cancerous tissue can become vascularised, such as vessel intussusception, in which vessels split into daughter vessels, or vessel co-option, in which tumours co-opt existing vessels (Carmeliet and Jain, 2011), however, we will not consider these processes in this thesis.

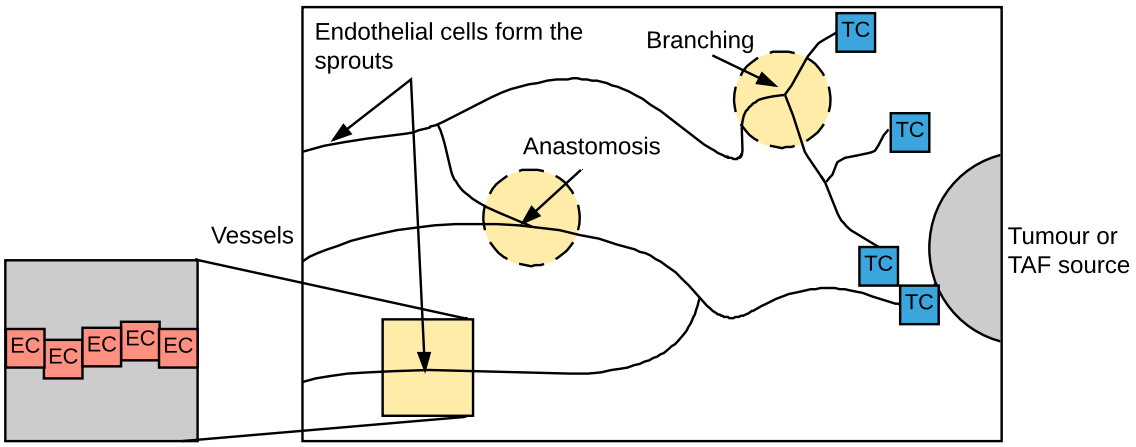

Figure 1.2: Schematic of angiogenesis based on the snail-trail process. TCs move via diffusion and chemotaxis towards a TAF source, forming a trail of vessels (ECs, also known as stalk cells) via the snail-trail. New TCs emerge through branching while sprouts fuse through anastomosis.

1.2 Mathematical Models of Angiogenesis

Understanding of the complex biological processes associated with tumour angiogenesis has been aided by the development and analysis of mathematical models (see the reviews Byrne et al. (2006); Byrne (2010); Mantzaris et al. (2004); Scianna et al. (2013); Alarcón et al. (2006)). Mathematical models of angiogenesis can, broadly speaking, be split into two distinct types: discrete and continuum models. Some of the earliest continuum models, known as snail-trail models, were developed phenomenologically to describe angiogenesis in the corneal assay (Balding and McElwain, 1985; Byrne and Chaplain, 1995a) (Balding and McElwain (1985) based on Edelstein's model of fungal growth, Edelstein (1982)). Given the negligible thickness of the cornea (approximately 100 μm in mice (Schulz et al., 2003; Zhang et al., 2013)), angiogenesis has been approximated as a two-dimensional process in the corneal assay.

Byrne and Chaplain (1995a) (BC) extended Balding and McElwain (1985) to include secondary TC proliferation and random motion of TCs. The one-dimensional model of angiogenesis presented in Byrne and Chaplain (1995a) describes the spatio-

temporal evolution of the TC density, $N(x,t)$, in units of number of TCs per unit area, vessel density, $\rho(x,t)$, in units of length per unit area and TAF concentration per unit area, $c(x,t)$. The dimensionless model is defined on $(x,t) \in [0,1] \times [0,\infty)$ where the TAF source (the tumour) is located at $x = 0$ and the limbus at $x = 1$. This corresponds to a dimensional distance of 3 mm. The timescale of interest is assumed to be 14 days, this being the time taken for the vasculature to migrate from the limbus to the pellet (see Folkman's experimental results Folkman (1976)).

As we will evaluate the BC model in this thesis, we provide a detailed description here. The dimensionless model equations, incorporating positive, constant parameter values, are (Byrne and Chaplain, 1995a,b)

$$\frac{\partial \rho}{\partial t} = D\frac{\partial N}{\partial x} - \chi N\frac{\partial c}{\partial x} - \gamma\rho, \tag{1.1}$$

$$\frac{\partial N}{\partial t} = D\frac{\partial^2 N}{\partial x^2} - \chi\frac{\partial}{\partial x}\left(N\frac{\partial c}{\partial x}\right) + \lambda N c H(c-\hat{c}) + \alpha\rho c - \beta_e N\rho - \beta_n N^2, \tag{1.2}$$

$$\frac{\partial c}{\partial t} = \frac{\partial^2 c}{\partial x^2} - \eta c, \tag{1.3}$$

where $J = -D\frac{\partial N}{\partial x} + \chi N\frac{\partial c}{\partial x}$ is the TC flux, D is the diffusion coefficient, χ is the chemotactic coefficient, γ is the rate of natural decay of vessel density, $\alpha\rho c$ and $\lambda N c H(c-\hat{c})$ model the appearance of new TCs (branching) from vessels and TCs ($\hat{c}$ is a threshold TAF concentration for branching), respectively. The sink term, $-\beta_e N\rho$ represents TC loss through tip-to-sprout anastomosis, and η is the rate of decay of TAFs. The BC model predicts 'an increasingly developed' (Byrne and Chaplain, 1995a) network evolving behind the TC front. We incorporate tip-to-tip anastomosis by including a term of the form $-\beta_n N^2$ in equation (1.2).

Equations (1.1)-(1.3) are closed using the following boundary and initial condi-

tions:

$$N(x,0) = 0 \quad \text{for} \quad 0 \leq x < 1, \quad N(0,t) = 0, \quad N(1,t) = \exp(-kt), t \geq 0 \tag{1.4}$$

$$\rho(x,0) = 0 \quad \text{for} \quad 0 \leq x < 1, \quad \rho(1,0) = 1, \tag{1.5}$$

$$c(0,t) = 1, \quad c(1,t) = 0, \quad c(x,0) = 0 \quad \text{for} \quad 0 \leq x < 1. \tag{1.6}$$

These incorporate the model assumptions that TCs emanate from the limbus (at $x = 1$) at a rate that decays exponentially with time. Further, TAFs are produced at constant rate at $x = 0$ (e.g. tumour site) and are removed by a sink at the limbus ($x = 1$).

The diffusion and chemotactic coefficients in the BC model (estimated from experiments conducted by other authors (see Byrne and Chaplain (1995a)) are

$$D = 10^{-3}, \quad \chi = 0.4. \tag{1.7}$$

The dimensional TAF diffusion coefficient is approximately three orders of magnitude larger than the TC diffusion coefficient (Balding and McElwain, 1985; Byrne and Chaplain, 1995b). As a result, the timescale for TAF diffusion is much faster than the timescale for TC migration, proliferation and vessel formation. Thus, in the BC model, a quasi-steady-state approximation is made for the TAF. With $\frac{\partial}{\partial t} = 0$ in equation (1.3), we have

$$c(x) = \frac{\sinh\left(\sqrt{\eta}(1-x)\right)}{\sinh\sqrt{\eta}} \to 1 - x \quad \text{as} \quad \eta \to 0. \tag{1.8}$$

Byrne and Chaplain's numerical solutions to (1.1)-(1.6) (as well as our own; results not shown), indicate that the TAF concentration does not vary markedly over the timescale considered and that (1.8) is a good approximation to $c(x)$ for $\eta \ll 1$. (The

reader is directed to Appendix A, Fig. A.1 for a typical solution to the BC model.)

Other continuum models based on snail-trail models (Byrne and Chaplain, 1995a; Balding and McElwain, 1985) include Chaplain and Stuart (1993); Chaplain (1995, 1996); Connor et al. (2015). In Connor et al. (2015), a modified (two angiogenic factors were incorporated instead of a generic TAF source) continuum snail-trail model was compared to experimental images to validate and parametrize it. Orme and Chaplain (1997) formulated a two-dimensional snail-trail model for the TC densities in two dimensions, and explored the effect of different anti-angiogenesis strategies. Other continuum angiogenesis models may include cell signalling. For example, Zheng et al. (2013) formulate a continuum model of angiogenesis, modelling the initiation, extension and maturation of new blood vessels, incorporating molecular and cellular interactions.

The snail-trail models, whilst a good first approximation of the corneal assay, have some limitations. As these models are formulated in terms of densities, network morphology is not represented. As a result, snail-trail models cannot distinguish between a tissue region perfused by one large vessel and another perfused by many smaller vessels with the same vessel density. This is important as nutrient supply in these cases is markedly different. Furthermore, structural information about the network may be needed to compare model output to real vascular networks. To address these shortcomings, discrete models that account for details of the network structure and morphology have been developed.

Agent-based models, which account for the behaviour of individual cells (Stokes and Lauffenburger, 1991; Anderson and Chaplain, 1998; Chaplain, 2000; Stéphanou et al., 2005; Plank and Sleeman, 2004), cell-cell interactions and sub-cellular processes such as signalling (Bentley et al., 2008, 2009; Jakobsson et al., 2010), have been developed to reveal emergent behaviour at the macroscale. Stokes and Lauffenburger (1991) used stochastic ordinary differential equations (ODEs) to model

the migration of individual TCs, through random motion and chemotaxis, in response to a chemoattractant source such as a wound or tumour, in two dimensions in an off-lattice framework. The authors also incorporated branching, proliferation and remodelling. Anderson and Chaplain (1998) developed a two-dimensional continuum model describing the evolution of TC density in response to the TAF and fibronectin, a component of the extracellular matrix. They then discretised the continuum model to produce a two-dimensional lattice-based cellular automaton (CA) model of angiogenesis using a probabilistic framework incorporating branching, tip-to-sprout anastomosis, and EC proliferation. Chaplain extended the discrete model to three dimensions (Chaplain, 2000). Plank and Sleeman (2004) developed a circular random walk model to simulate angiogenesis. The cellular Potts model, developed by Glazier and Granier (Graner and Glazier, 1992; Glazier and Graner, 1993), has also been used to simulate network structures (e.g. Bauer et al. (2007); Shirinifard et al. (2009)).

Hybrid models (Harrington et al., 2007; Tong and Yuan, 2001, 2008; Vilanova et al., 2014) couple discrete and continuum models; they model microscale cell behaviour in response to macroscale fields, such as TAFs, which are described by PDEs. Hybrid models can also couple cell dynamics to models of blood flow (Stéphanou et al., 2005; Owen et al., 2009; Perfahl et al., 2011; Macklin et al., 2009) and drug delivery in the vascular network (Stéphanou et al., 2005) as well as tumour growth (Perfahl et al., 2011; Macklin et al., 2009). These frameworks have been used to test the impact of different therapeutic strategies (Stéphanou et al., 2005; Harrington et al., 2007). For example, Stéphanou et al. (2005) utilised the discrete model in Anderson and Chaplain (1998) and simulated flow through the networks to determine drug delivery. Alarcón et al. (2005) and Owen et al. (2009) have developed multiscale models of vascular tumour growth including blood flow, remodelling of the vasculature, and sub-cellular and tissue scale dynamics. Perfahl et al. (2011) have integrated

images of mouse vascular networks into their multiscale model in order to simulate tumour growth. Bauer et al. (2010) developed a stochastic, Boolean signal transduction network model of receptor cross-talk in angiogenesis to map environmental cues to cell phenotype.

An important use of continuum (and discrete) models is their ability to predict population and microscale behaviour (e.g. Benzekry et al. (2014)) that might be challenging to determine from experiment. Recently, there has been much interest in comparing models which represent the same biological phenomena to determine which model best describes and which best predicts the behaviour of the biological system (Benzekry et al., 2014; Toni et al., 2009; Toni and Stumpf, 2010; Turner and Van Zandt, 2012; Baker et al., 2005a,b; Oden et al., 2010a,b; Oden and Prudencio, 2013) (as compared to experimental data). As yet, to our knowledge, there have been no attempts to compare different snail-trail models of angiogenesis in terms of descriptive and predictive power.

1.3 Connecting Discrete and Continuum Descriptions

Discrete models typically describe the local behaviour of cells whereas continuum models describe dynamics at the macroscale. Both approaches have their advantages. Whilst discrete models can produce detailed vascular structures, continuum models provide a tractable framework for efficient analysis such as sensitivity analyses or parameter sweeps; these may prove time-consuming with a discrete model. Continuum models yield insight into the effective behaviour of a large number of cells; an insight which may be difficult to discern using a discrete model. Taken together, discrete and continuum models provide complementary perspectives of the same biological system, and, as such, provide a broader understanding of the pro-

cesses involved. Furthermore, experimental data may represent both individual and population-level behaviour (e.g. Tong and Yuan (2008) (hybrid model) and Connor et al. (2015) (continuum model) have analyzed images of corneal angiogenesis to validate and parametrize their models). Thus, having both model types at hand can allow for model validation at both scales. Increasing recognition of these benefits has stimulated efforts to connect discrete and continuum models in a variety of biological contexts (see, for example, the review by Codling et al. (2008)).

In light of the aims of this thesis, we now review briefly the relevant mathematical literature bridging discrete and continuum descriptions. Whilst the application areas differ, the methodologies are relevant to the approach that we will use to relate discrete snail-trail models of angiogenesis with their continuum counterparts.

The so-called "Keller-Segel" type models have been used extensively to describe the chemotactic response of biological systems on the macroscale (Keller and Segel, 1970, 1971; Hillen and Painter, 2009). Much work has been devoted to revealing the microscopic behaviour that leads to these continuum models.

A common method used to elucidate the microscopic behaviour is to consider cell movement as a biased random walk on a lattice. In Hillen and Painter (2009); Othmer and Stevens (1997); Painter and Hillen (2002), cell movement takes place on a one-dimensional lattice with lattice spacing h. Transition probabilities determine a cell's (the random walker's) ability to move from position x to neighbouring lattice sites at $x \pm h$. The authors consider various forms of the transition probabilities, which allows them to consider various types of cell movement. The authors formulate a continuous-time, discrete-space master equation for the probability of a walker being at a lattice site using the transition rates. By equating the probability distribution with the cell density, the authors are able to formulate an equation that effectively describes how particle numbers at a site change over time by considering the movement of cells into and out of that site. To derive the macroscopic model, Hillen and Painter (2009),

following Othmer and Stevens (1997), expand the relevant terms in a Taylor series in space and take a limit as the lattice spacing tends to zero. In Othmer and Stevens (1997), the authors consider strictly local models and non-local gradient models, based on different transition probabilities. In Painter and Hillen (2002), the authors account for volume exclusion (VE) effects and quorum sensing models, which take cell density into account. In Painter and Hillen (2002), the PDE for cell density, u, excluding VE effects takes the form

$$\frac{\partial u}{\partial t} = D\frac{\partial^2 u}{\partial x^2} - \frac{\partial}{\partial x}\left(u\chi(v)\frac{\partial v}{\partial x}\right), \tag{1.9}$$

where D is the constant diffusion coefficient, χ is the chemotactic sensitivity (dependent on v) and v is the underlying chemoattractant field. With VE, u satisfies

$$\frac{\partial u}{\partial t} = \frac{\partial}{\partial x}\left(D(q(u) - q'(u)u)\frac{\partial u}{\partial x}\right) - \frac{\partial}{\partial x}\left(q(u)u\chi(v)\frac{\partial v}{\partial x}\right), \tag{1.10}$$

where the function $q(u)$ describes the probability of a cell finding space at its neighbouring location. Generally, therefore, VE introduces non-linearity into the diffusion (and chemotactic) term. However, for the simple choice of $q(u) = 1 - u/U_{max}$, where U_{max} is the maximum number of cells allowed at a site, the diffusion term is linear in u. We will comment further on simple exclusion processes in what follows.

Simpson et al. (2010a, 2009a, 2010b, 2011) model a variety of biological processes using a two-dimensional CA model on a regular square lattice. The transition probabilities in these models are then used to write down a discrete time and space conservation equation for the cell density or cell occupancy over many realizations of the discrete model. To derive the PDE models, the relevant terms are first expanded in a Taylor series in space. Then a limit is taken in which τ, the discrete time step, and h, the lattice spacing, tend to zero, while h^2/τ is held constant. Solutions of the resulting continuum models are then compared to discrete model simulations. In

Simpson et al. (2010a), proliferation and random motion are considered and a modified version of Fisher's equation (Fisher, 1937) generated, while in Simpson et al. (2009a), VE from multiple species is considered in a model describing unbiased and biased random walks. In Simpson et al. (2010b), the authors consider mesoscale patterns in motile populations, and in Simpson et al. (2011), the authors consider cells with a variable aspect ratio (length and width of cells differ) and found that the non-linear diffusivity depends on the aspect ratio.

The framework outlined by Othmer and Stevens (1997) can be extended to treat more complex scenarios, such as cell migration on growing domains (Baker et al., 2010) and angiogenesis (Jain and Jackson, 2013; Plank and Sleeman, 2004). Penington et al. (2011) derive non-linear diffusion coefficients for a variety of interactions described by different transition probabilities. The master equation framework can also be used to derive macroscale dynamics and properties from the Potts model (Alber et al., 2007; Lushnikov et al., 2008), and off-lattice models (Dyson et al., 2012; Plank and Simpson, 2012). Plank and Simpson (2012) compared lattice-based and lattice-free agent-based models and mean-field continuum models of diffusive motion and proliferation incorporating cell crowding effects. They found that the population growth rate in the lattice-free model is slower at high cell densities than in the lattice-based case (as space is not occupied as 'fully' as in the lattice-based case, i.e. there is empty space in the lattice-free model that cannot accommodate more cells).

In many of the models mentioned above, the occupancy of lattice sites is assumed to be independent (mean-field approximation). This is a valid assumption provided that spatial correlations are low. However, mechanisms such as proliferation, enhance spatial correlations. In such cases, the mean-field approximation can be corrected for by using distribution and correlation functions (see Baker and Simpson (2010) and discussion that follows).

Recently, several authors have derived continuum models of angiogenesis from

stochastic microscale models (Jain and Jackson, 2013) or mesoscale models (Spill et al., 2015; Bonilla et al., 2014; Terragni et al., 2016) using a mean-field approach. For example, Bonilla et al. (2014) used a stochastic, mesoscale framework to derive a deterministic integro-differential PDE for the TC population. Spill et al. (2015) used a mesoscale, lattice-based, mean-field approach to reproduce the BC snail-trail model (Byrne and Chaplain, 1995a), introducing a norm to ensure the positivity of the TC flux. Jain and Jackson (2013) developed a hybrid model of angiogenesis incorporating chemotaxis and sprout formation, including molecular interactions between VEGF and cell-surface receptors. In Spill et al. (2015); Bonilla et al. (2014); Jain and Jackson (2013), the discrete/mesoscale model is coupled to a continuum TAF field.

In some cases, it is not possible to take a limit as the lattice spacing tends to zero, as this may eliminate important terms in the PDEs. For example, in Hywood et al. (2013), the diffusion term would have been eliminated in the limit as $h \to 0$. Instead, these terms were retained, as diffusive motion was incorporated in their individual-based simulations and thus should be present in the PDE model. A similar approach was used in Ross et al. (2015) to retain a growth term. In both Hywood et al. (2013) and Ross et al. (2015), the authors argue that retaining higher-order terms in h is reasonable, as small non-zero values of h are used in the PDE models when compared to agent-based simulation results. In Davies et al. (2014), a discussion of ratios of time and spatial scales, and the corresponding equations and limitations, is presented.

A variety of algorithms have been used to update the positions of cells or agents in discrete stochastic models. For example, the Gillespie algorithm (Gillespie, 1977), a type of Monte Carlo method, has been used to simulate reaction-diffusion processes (Markham, 2014; Spill et al., 2015; Erban et al., 2007). Many authors use a random sequential update (asynchronus update) (Simpson et al., 2010a, 2009a; Ross et al., 2015). It is well-known that this update method produces simulation results consistent with a continuous time master equation (Rajewsky et al., 1998; Hywood et al.,

2013). There are a variety of other update methods, such as synchronous (Wolfram, 1983) or order-sequential updates (Rajewsky et al., 1998).

Other methods by which macroscale descriptions could be derived from microscale or mesoscale frameworks include homogenization or volume averaging. For example, continuum models can be derived from periodic network structures using asymptotic homogenization methods (Chapman et al., 2008; Shipley and Chapman, 2010; Davit et al., 2013).

1.3.1 Volume Exclusion

Simple exclusion processes, which account for VE, are used frequently to model motile cell populations (see Penington et al. (2011); Simpson et al. (2010a, 2009a,b, 2007); Painter and Hillen (2002) and references therein) as they allow at most one motile agent to occupy a lattice site, and therefore describe biologically realistic interactions (Simpson et al., 2009b) (since cells cannot occupy the same space).

Symmetric exclusion processes, such as lattice-based unbiased random walks, can be described at the macroscale by a linear diffusion equation (Liggett, 1999; Simpson et al., 2010a, 2009a,b). Whilst agents interact via VE (moves to occupied sites are aborted), the interactions are symmetric and, thus, do not appear in the macroscale description (Simpson et al., 2009a; Penington et al., 2011; Liggett, 1999). Indeed, computer simulations of unbiased random walks have confirmed that the solution of a linear diffusion equation captures the population-level behaviour well (Simpson et al., 2009a,b). This is more readily explained if one formulates discrete conservation equations (DCEs) for expected cell occupancy using a mean-field approximation (see Simpson et al. (2009a), Liggett (1999)). For an unbiased random walk, the non-linear interaction terms (representing moves to vacant sites only) in the DCE cancel, resulting in a linear diffusion equation. However, this is not the case for off-lattice unbiased random walks, where the size of a cell, in addition to how far it moves,

results in a deviation from linear diffusion (Dyson et al., 2012).

Asymmetric on-lattice exclusion processes (see Penington et al. (2011) and references therein, Simpson et al. (2009a)), such as biased random walks, or multi-species exclusion processes (Simpson et al., 2009a), give rise to non-linear advection-diffusion equations. Simpson et al. (2009a) derived a system of non-linear advection-diffusion equations describing a biased random walk for multiple species, which can be interpreted in terms of fluxes for interacting subpopulations. In this case, the diffusive and chemotactic fluxes of a subpopulation are reduced by exclusion from all other species/subpopulations. Additionally, there is a first order flux term of the subpopulation down the gradient of the total cell density. Dyson and Baker (2015) considered two interacting subpopulations in an off-lattice framework and, using a mean-field approximation, derived non-linear advective-diffusive equations for each population. They found that the first population is excluded by the second population only through spatial inhomogeneity of the second population and *vice versa*. In other words, if the second population is homogeneously distributed, than the dispersal of the first population is not affected. Any direct exclusion of the first population by the second population occurs at higher-orders and is negligible in their derivation.

Corrections to mean-field descriptions of exclusion-process-based models have been investigated (Simpson and Baker, 2011; Baker and Simpson, 2010; Markham, 2014). Simpson and Baker (2011), within an agent-based framework utilising spatially inhomogeneous initial conditions, proposed methods using correlation functions and a moment closure approximation (Kirkwood superposition approximation) to derive corrected mean-field macroscale descriptions of exclusion processes incorporating unbiased motility, biased motility and unbiased motility with birth and death processes. In particular, the exclusion process is described in terms of ODEs for the evolution of k-point distribution functions (multivariate probability distribution functions representing the occupancy of k-tuplets of sites; it is these distribution functions that

provide information about the correlations between the occupancies of different sites). These models are known as moment dynamics models. It is natural that 2-point distribution functions depend on 3-point distribution functions and so on. Thus, this moment dynamics framework leads to an infinite system of coupled non-linear ODEs, unless a moment closure approximation is used to truncate the system. In Simpson and Baker (2011); Baker and Simpson (2010), the Kirkwood superposition approximation, which expresses the behaviour of triplets in terms of singlets and doublets, is used to truncate the system of equations.

In Simpson and Baker (2011), the authors found that in the unbiased motility case (simple exclusion process), correlation effects cancel and the population behaviour is described by a linear diffusion equation. This explains why the result obtained using a mean-field approximation is in good agreement with numerical simulations of discrete models. However, for biased motility and unbiased motility with birth and death processes, correlation effects do not cancel and Simpson and Baker (2011) found that the corrected models outperform mean-field models in all cases.

In Baker and Simpson (2010), it was found that, in the context of an agent-based framework for an initially uniformly seeded lattice, an exclusion process with unbiased motility and birth and death processes gives rise to correlations between the occupancy of lattice sites as birth and death rates increase relative to the motility rate. In these cases the corrected models derived using distribution functions are in better agreement with simulation results than the models based on the mean-field approximation.

Moment dynamics models can become intractable even when pairwise distribution functions (doublets) are considered (Markham, 2014). For spatially inhomogeneous initial conditions, the closure approximation leads to unbounded correlation functions when the occupancy probability of lattice sites is either 0 (vacant) or 1 (occupied). Moment dynamics models are also limited by the closure approximation used to

truncate the system. Thus, many authors have continued to use the mean-field approximation to derive macroscale descriptions of microscale models that incorporate exclusion processes. In most cases, these continuum models (PDEs) provide adequate descriptions of the population behaviour in a variety of biological contexts (see, for example, Simpson et al. (2010a, 2009a,b); Dyson et al. (2012); Dyson and Baker (2015); Liggett (1999); Penington et al. (2011); Ross et al. (2015)).

In the context of angiogenesis, VE is typically neglected in many continuum models (Balding and McElwain, 1985; Byrne and Chaplain, 1995a; Connor et al., 2015; Chaplain and Stuart, 1993; Chaplain, 1995, 1996; Anderson and Chaplain, 1998; Chaplain, 2000; Stéphanou et al., 2005). In Balding and McElwain (1985); Byrne and Chaplain (1995a); Connor et al. (2015), VE from both the TC and EC population is neglected. Only the TC population is modelled in the continuum models in Anderson and Chaplain (1998); Chaplain (2000); Chaplain and Stuart (1993); Chaplain (1995, 1996), consequently interactions between TCs and ECs are neglected, leaving no scope to account for EC VE. VE is also neglected in the TC motility mechanisms. Spill et al. (2015) incorporate TC crowding effects in the diffusion mechanism only, and the mesoscale formulation gives rise to linear diffusion (as expected) and chemotactic terms in their PDE formulation. Thus TC crowding effects are neglected during chemotaxis, and EC crowding effects are neglected altogether. In general, none of the existing continuum models explicitly account for VE in a systematic manner.

By contrast, several discrete models of angiogenesis (Stokes and Lauffenburger, 1991; Tong and Yuan, 2001; Harrington et al., 2007) incorporate VE naturally when they describe anastomosis. These models assume that when a TC encounters a part of the vessel network, an anastomosis event occurs, thus implying that no two cells can occupy the same space. Tong and Yuan (2001) explicitly forbid the overlap of vessels, and thus once anastomosis occurs, the TC ceases to migrate. Likewise, in Stokes and Lauffenburger (1991), once a TC encounters a sprout, anastomosis occurs and the TC

is no longer permitted to move. Anderson and Chaplain (1998) incorporate VE into the branching process (though the manner in which anastomosis and movement are implemented could lead to TC overlap with other sprouts). Recent discrete/hybrid models of angiogenesis (Perfahl et al., 2011; Bentley et al., 2009, 2008) account for the finite volume of cells.

In other applications, continuum models neglecting VE have been used to model migratory cells (see Hillen and Painter (2009); Othmer and Stevens (1997) and references therein). Continuum models that neglect VE are generally linear, and therefore more analytically tractable. Dyson and Baker (2015) found that VE effects are most important in biased movement, such as chemotactic migration. In these cases, continuum models that account for exclusion effects more accurately capture individual-based simulations than those that do not (Dyson and Baker, 2015).

1.4 Discussion and Thesis Outline

In this chapter, we have reviewed a variety of angiogenesis models. Continuum models provide tractable frameworks for analysis and describe the population behaviour. For example, the continuum snail-trail models of Balding and McElwain (1985) and Byrne and Chaplain (1995a) qualitatively capture angiogenesis in the corneal assay in terms of cell densities. On the other hand, discrete and hybrid angiogenesis models are able to produce detailed network structures. Thus, discrete and continuum models provide us with complementary perspectives of angiogenesis. Further, since experimental data may represent both population and cell-level dynamics, having both a discrete and continuum description of angiogenesis (or any biological system) is advantageous. Increasing recognition of these benefits has stimulated efforts to link discrete and continuum models in a variety of biological contexts, including angiogenesis. Additionally, such a framework should help to elucidate the microscale

assumptions that underpin phenomenological continuum models.

VE and crowding effects are important in biological systems as cells have finite size. We reviewed a variety of models incorporating VE, and noted that many discrete and continuum angiogenesis models neglect VE due to computational and analytic tractability. For example, the phenomenological snail-trail models of Byrne and Chaplain (1995a) and Balding and McElwain (1985) implicitly assume that cells are point particles. In snail-trail models of angiogenesis, a systematic study of the effects of TC and EC VE on microscale and macroscale behaviour, and vessel formation, has not yet been conducted.

The primary aim of this thesis is to systematically determine the population behaviour of TCs and ECs in terms of PDEs from their microscale behaviour during corneal angiogenesis, based on the snail-trail approach. We will use this framework to determine the conditions and assumptions at the microscale under which the BC model is recovered. We will then extend our framework to incorporate cell volume and determine how this affects microscale and population behaviours as well as the structure of the PDEs derived. We will evaluate whether the BC model can capture macroscale VE effects. Finally, we will assess the predictive power of the continuum models that we develop, and attempt to link underlying network structure with predictive power at the macroscale.

The remainder of this thesis is structured as follows (with the main content chapters summarised in Fig. 1.3). In Chapter 2, we use a mean-field approximation to systematically derive a continuum model from a two-dimensional lattice-based CA model of corneal angiogenesis, based on the snail-trail process. We use this framework to elucidate, at a more fundamental level, the assumptions underpinning the phenomenological BC model. We compare solutions of both PDE models to agent-based simulations to assess agreement, and determine how microscale cell behaviour manifests at the macroscale. In Chapter 3, we determine how VE affects our dis-

crete and continuum models of angiogenesis. We use a mean-field approximation to derive continuum models of angiogenesis from two CA models that account for TC VE (Model 1) as well as TC and EC VE (Model 2). In so doing, we will determine how VE incorporated on the microscale affects cell behaviour at the population level and, further, how it affects the structure of the PDE models by introducing non-linearities. We also highlight the pitfalls of the mean-field approximation when applied to multi-species exclusion processes. In Chapter 4, we relax mean-field restrictions and develop a methodology to account for multi-species exclusion effects through parameter estimation in our continuum model instead of deriving more detailed continuum models from the CA model. We also use this approach to determine whether the linear BC model can account for macroscale VE effects through suitable parameter choices. In Chapter 5, we compare the predictive power of the continuum models discussed in this thesis. In Chapter 6, we outline how it may be possible to relate the predictive and descriptive powers of continuum models discussed in this thesis to underlying network morphology extracted from the CA. In Chapter 7, we discuss our conclusions and outline avenues for future work.

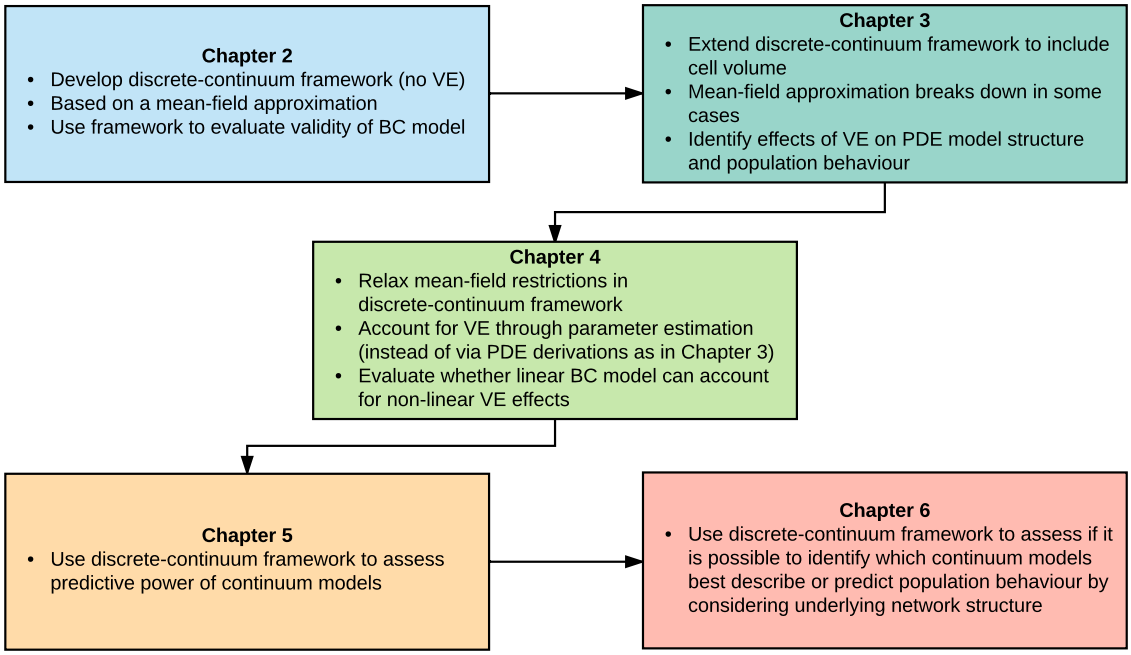

Figure 1.3: Summary of main content chapters in this thesis.

Chapter 2

A Discrete to Continuum Approach to Modelling Angiogenesis

In this chapter, we develop a two-dimensional lattice-based CA model of angiogenesis in the corneal assay (CA Model 0), based on the snail-trail process. We then use transition probabilities associated with the discrete model along with a mean-field approximation and DCEs for expected cell occupancy to systematically derive a continuum model in the form of PDEs (Model 0 PDEs). From the two-dimensional continuum model, we derive a one-dimensional model which represents angiogenesis in two dimensions. By comparing the discrete and one-dimensional continuum models, we determine how individual cell behaviour manifests at the macroscale and generate new insights. We also compare the phenomenological BC model to our discrete and continuum models. This enables us to determine the conditions/assumptions under which the BC model is recovered.

Note: A version of this chapter has been published in Physical Review E, 95, 012410, 2017; entitled 'Modelling Angiogenesis: A Discrete to Continuum Description' by

2.1 Introduction

As discussed in Chapter 1, numerous discrete and continuum models of angiogenesis have been developed (see the reviews Byrne et al. (2006); Byrne (2010); Mantzaris et al. (2004); Scianna et al. (2013); Alarcón et al. (2006)).

The BC model and the model of Balding and McElwain (1985) are one-dimensional PDE models representing TC and EC densities averaged in the direction perpendicular to propagation of the vascular front. They were developed phenomenologically to establish qualitative agreement with angiogenesis in the corneal assay, and are still widely used, though they have some limitations. As these models have been developed phenomenologically, it is unclear what the underlying microscale assumptions are. Spill et al. (2015) used a stochastic one-dimensional mesoscale compartment approach to recover the BC model (with the introduction of a norm in the equation for the EC density to preserve positivity). Within this mesoscale framework, the lattice spacing is much larger than the size of a cell, and thus does not account for the movement of individual cells, but rather the changes in cell numbers or densities within each lattice box. Further, the lattice spacing in the mesoscale framework does not have a direct biological interpretation, but must adhere to certain restrictions (i.e. must not be too small or large, see Spill et al. (2015)). To our knowledge, the BC model has not been derived from first principles i.e. recovered from a rule-based model at the cell level.

In this chapter, we determine the macroscopic behaviour of TCs and ECs from their microscale behaviour during corneal angiogenesis, based on the snail-trail process. Specifically, we develop a two-dimensional lattice-based CA model of angiogen-

esis in the corneal assay. Then, using a mean-field approximation, we systematically derive a new continuum snail-tail model describing the spatio-temporal evolution of the TC and EC densities. In particular, our framework enables us to elucidate, at a more fundamental level, the assumptions underlying phenomenological snail-trail models (Byrne and Chaplain, 1995a; Balding and McElwain, 1985). By comparing solutions to our PDE model and the BC model to averaged CA simulation results, we determine how individual cell behaviour manifests itself at the macroscale.

2.2 Cellular Automaton

We represent the cornea as a two-dimensional, regular lattice, $(x, y) \in [0, 1] \times [0, 1]$, with lattice spacing h. Each lattice site is indexed by (i, j) where $i, j, \in \mathbb{Z}^+$ $(0 \leq i, j \leq R,\ Rh = 1)$, so that the position of a site is given by $(x_i, y_i) = (ih, jh)$. The lattice spacing h represents the diameter of a cell. The limbus and TAF source are located at $x = 0$ and $x = 1$, respectively[1].

Our CA model is presented in dimensionless units; we rescale distance with the limbus to TAF source separation L and time with a characteristic timescale for vascularisation. Generally, the TAF concentration (non-dimensional), $c(x, y, t)$, satisfies a reaction-diffusion equation (Byrne and Chaplain, 1995a; Anderson and Chaplain, 1998; Connor et al., 2015; Orme and Chaplain, 1997). Since the timescale for diffusion of TAFs is typically much faster than the timescale for changes in the vessel network (see Byrne and Chaplain (1995a) and Chapter 1), we apply a quasi-steady-state approximation, (setting $\partial c/\partial t = 0$) and, for simplicity, assume that the TAF field is

[1]The limbus and source location in the BC model introduced in Chapter 1 have been switched.

diffusion-dominated. Thus, the TAF field satisfies

$$\nabla^2 c = 0, \text{ for } 0 \leq x, y, \leq 1, \tag{2.1}$$

$$c(0, y) = 0, \; c(1, y) = 1, \text{ for } 0 \leq y \leq 1 \tag{2.2}$$

$$\frac{\partial c}{\partial y}(x, 0) = 0, \; \frac{\partial c}{\partial y}(x, 1) = 0, \text{ for } 0 \leq x \leq 1. \tag{2.3}$$

We have also assumed that TAFs are maintained at constant levels at $x = 1$ and $x = 0$. The solution to equations (2.1)-(2.3) is

$$c(x, y) = x. \tag{2.4}$$

This simplified TAF profile[2] enables us to focus on the ways in which TC movement and sprout creation influence angiogenesis.

Based on the biological assumptions of angiogenesis (ECs follow migrating TCs), we distinguish two agent types in our CA model: active TCs and passive ECs. The following processes are assumed to regulate TC dynamics: movement via random motion and chemotaxis towards the TAF source (at $x = 1$), new TC formation through branching, and TC annihilation through tip-to-tip and tip-to-sprout anastomosis. ECs are assumed to be created as a result of TC movement (snail-trail process) and tip-to-tip anastomosis.

Our algorithm for updating TCs on the lattice is both random and sequential. If there are $\bar{N}$ TCs on the lattice at the beginning of a discrete time step $\bar{K}$, then $\bar{N}$ TCs are selected independently at random, with replacement. Once chosen, a TC is given the opportunity to move with probability, P_m. A further set of probabilities $P^{x\pm}$ and $P^{y\pm}$ dictate the site to which a TC moves (described later). Once $\bar{N}$ motility attempts have been made, another $\bar{N}$ TCs are selected (at random, with replacement) during

[2]We are aware that a steady linear TAF profile is not biologically realistic. However, this profile enables us to focus on cell movement and evaluate the BC model.

the same discrete time step, and are given the opportunity to branch with probability P_b. ECs are not actively updated in the CA model, rather, they are created as a consequence of TC movement. We now discuss the specific rules governing TC motility and branching.

2.2.1 Movement and Anastomosis

Consider a TC at lattice site (i, j). The probabilities $P_{i,j}^{x\pm}$ and $P_{i,j}^{y\pm}$, defined as

$$P_{i,j}^{x\pm} = \frac{1 \pm g_{i,j}^{x}}{4},\ 0 < i, j, < R, \tag{2.5}$$

$$P_{i,j}^{y\pm} = \frac{1 \pm g_{i,j}^{y}}{4},\ 0 < i, j, < R, \tag{2.6}$$

govern its ability to move from site (i, j) to a site within its von Neumann neighbourhood $(i \pm 1, j \pm 1)$. The functions $g_{i,j}^{x}$ and $g_{i,j}^{y}$, which bias the TC random walk, are central difference approximations to the TAF gradient in the x- and y-directions, respectively, at site (i, j). They represent the TC's ability to migrate up the TAF gradient via chemotaxis. We define $g_{i,j}^{x}$ and $g_{i,j}^{y}$ as follows

$$g_{i,j}^{x} = k\left(c_{i+1,j} - c_{i-1,j}\right),\ 0 < i, j < R, \tag{2.7}$$

$$g_{i,j}^{y} = k\left(c_{i,j+1} - c_{i,j-1}\right),\ 0 < i, j < R, \tag{2.8}$$

where $c_{i,j}$ is the TAF concentration and the constant parameter k (independent of time and space) scales the TAF gradient and therefore the chemotactic response, and is also chosen so that $g^x, g^y \in [-1, 1]$ to ensure that $P_{i,j}^{x\pm}, P_{i,j}^{y\pm} \in [0, 1]$. For a linear TAF (equation (2.4)), $c_{i,j} = c_i$, $g_{i,j}^{y} = 0$ and therefore $P_{i,j}^{y\pm} = \frac{1}{4}$. Our CA model is valid until TCs reach the TAF source at $i = R\,(0 \leq j \leq R)$. We do not allow TCs to cross lattice boundaries (no flux), and neglect interactions between the TAF source and TCs. A schematic of the CA model is shown in Figure 2.1.

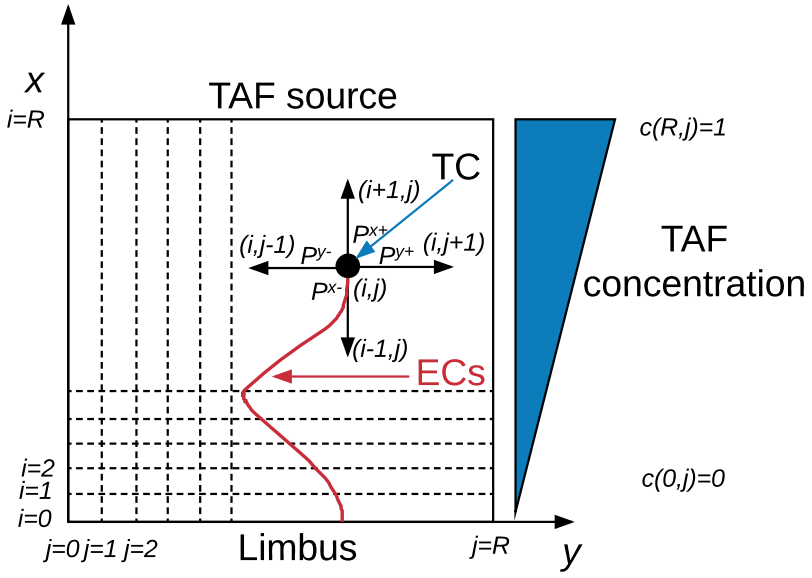

Figure 2.1: Schematic of CA model set-up. A TC at site (i, j) can move to a site within its von Neumann neighbourhood based on the movement probabilities $P_{i,j}^{x\pm}, P_{i,j}^{y\pm}$. TCs may also branch, with probability P_b and anastomose with other sprouts.

When a TC moves to a site within its neighbourhood, an EC is left behind, creating the trail of vessels associated with the snail-trail.

If a TC moves to a site that is occupied, an anastomosis event occurs. We assume that anastomosis annihilates TCs (as ECs are responsible for lumen formation once connections form (Potente et al., 2011; Carmeliet and Jain, 2011; Blanco and Gerhardt, 2013)). We distinguish two types of anastomosis events. If the target site is occupied by a TC, a tip-to-tip anastomosis event occurs, and an EC is deposited at the site of annihilation (i.e. TC + TC $\rightarrow$ EC; see Fig. 2.2a). If the target site is occupied by an EC, a tip-to-sprout anastomosis event occurs, the TC is annihilated and the EC remains (i.e. TC + EC $\rightarrow$ EC; see Fig. 2.2b).

We introduce two binary variables, a_n and a_e, to act as switches for tip-to-tip and tip-to-sprout anastomosis, respectively. If these variables are set to 1, then the corresponding anastomosis process is active. In more detail, we have the following:

- $a_n = a_e = 0 \Leftrightarrow$ no anastomosis,

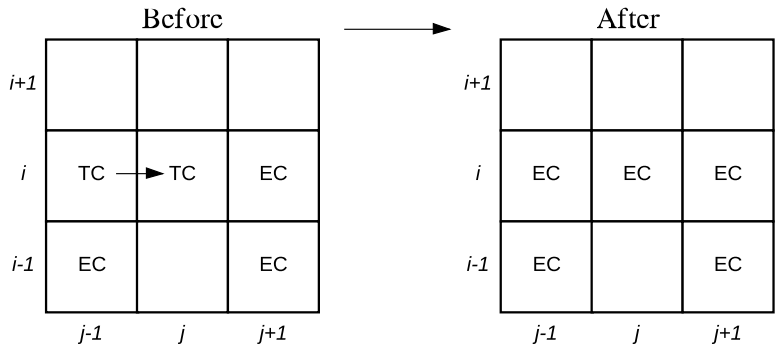

(a) tip-to-tip anastomosis

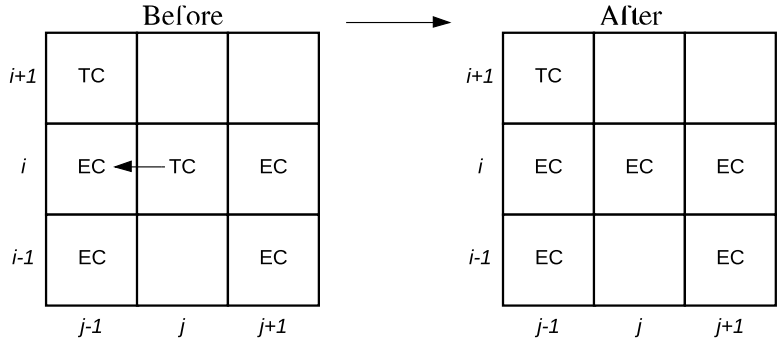

(b) tip-to-sprout anastomosis

Figure 2.2: If a TC at site $(i, j-1)$ moves to site (i, j), occupied by a TC, then a tip-to-tip anastomosis event occurs. Both TCs are removed from the simulation and ECs are placed at sites (i, j) and $(i, j-1)$. (b) If a TC at site (i, j) moves to site $(i, j-1)$, occupied by an EC, then a tip-to-sprout anastomosis event occurs. The TC is removed from the simulation, the EC at site $(i, j-1)$ remains and an EC is placed at site (i, j).

- $a_n = 1, a_e = 0 \Leftrightarrow$ tip-to-tip anastomosis active,
- $a_n = 0, a_e = 1 \Leftrightarrow$ tip-to-sprout anastomosis active,
- $a_n = 1, a_e = 1 \Leftrightarrow$ tip-to-tip and tip-to-sprout anastomoses active.

2.2.2 Branching

Given that TCs propagate towards the TAF source in the positive x-direction, as a result of the linear TAF profile, we assume that branching occurs in the direction perpendicular to the direction of propagation of the TCs (i.e. in the y-direction). Branching is stimulated by TAFs (Carmeliet and Jain, 2011), and further the TC

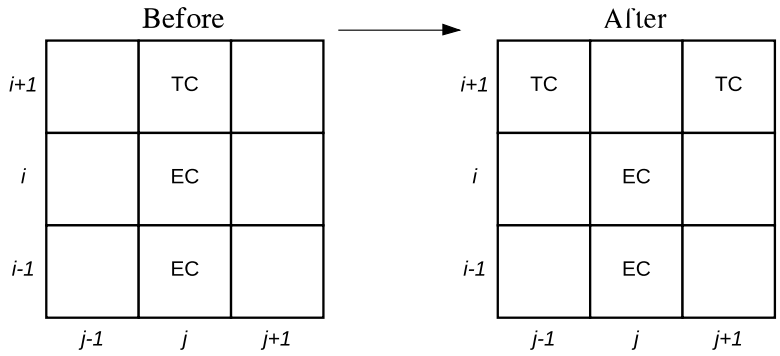

Figure 2.3: A TC at site $(i+1, j)$ branches by placing daughter TCs at $(i+1, j \pm 1)$.

density increases as the vascular front approaches the TAF source (the so-called "brush-border" effect (Muthukkaruppan et al., 1982)). Therefore, we assume that the probability, P_b, with which a TC at site (i, j) branches, increases linearly with the TAF concentration, c, such that

$$P_b(i, j) = P_p c_{i,j} \in [0, 1], \tag{2.9}$$

where P_p is a constant (independent of time and space) that scales the TAF concentration. Branching from a TC located at (i, j) places daughter TCs at $(i, j \pm 1)$ and the TC at site (i, j) is removed (see Fig. 2.3). Thus, we assume no ECs are created via branching. The resulting Y-pattern (see Fig. 2.3) simulates the branching pattern and TC selection that is in practice mediated by complex signalling involving the DLL4/Notch pathway (Potente et al., 2011; Carmeliet and Jain, 2011). Given that new TCs predominantly emanate from the front of the propagating vascular front (brush-border), we assume branching occurs from the TCs only. We acknowledge that our implementation of branching is not unique; in the next chapter we consider alternative approaches, including branching from ECs.

2.2.3 Initial Conditions and CA Algorithm

TCs are placed at alternating lattice sites along $i = 0$ so that

$$\text{TCs placed at } (i = 0, j = 1, 3, \cdots, R - 1), \tag{2.10}$$

representing sprouting from the corneal limbal vessels, following the initiation of angiogenesis. ECs are created once TCs begin to move, and thus, initially, there are no ECs on the lattice. In practice, as with branching, TC selection at the limbus is mediated by TAF (VEGF) and Notch signaling (Potente et al., 2011; Carmeliet and Jain, 2011; Blanco and Gerhardt, 2013).

The CA algorithm for updating TCs after initialisation is outlined in Algorithm 1.

2.2.4 Cell Occupancy

Branching and movement (incorporating anastomosis) are viewed as distinct processes in our CA model: each process affects lattice-site occupancies differently. Movement does not incorporate VE explicitly, i.e. a TC move is not aborted if the target site is occupied. However, anastomosis imposes occupancy restrictions. In particular, tip-to-tip anastomosis ($a_n = 1, a_e = 0$) implies that only one TC can occupy a site (though a TC and an EC can occupy the same site), tip-to-sprout anastomosis ($a_n = 0, a_e = 1$) implies that a TC and EC cannot occupy the same site (though multiple TCs can occupy the same site). Taken together, tip-to-tip and tip-to-sprout anastomosis ($a_n = 1, a_e = 1$) imply that no two cells of any kind can occupy the same site.

Branching does not incorporate VE i.e. branching may deposit daughter TCs at sites already occupied by other TCs or ECs. Therefore, branching does not adhere to the occupancy restrictions imposed by anastomosis. We discuss this issue further

Algorithm 1 CA Model 0 algorithm for updating TCs after initialisation

While $\bar{K} \leq \bar{K}_{\text{final}}$ and TCs have not reached $i = R$

1. Choose $\bar{N}$ TCs at random with replacement

   Loop 1: For 1 to $\bar{N}$

   (a) Choose a random number, $\bar{T} \in [0, 1]$

   (b) If $\bar{T} \leq P_m$, then the TC attempts to move as follows:

   - A random number $\bar{S} \in [0, 1]$ is chosen
   - The TC moves according to probabilities $P^{x\pm}, P^{y\pm}$ (see equations (2.6) and (2.5)) and an EC is left behind
   - If $a_n = 1$ and the target site is occupied by TCs, tip-to-tip anastomosis occurs
   - Otherwise if $a_e = 1$, and the target site is occupied by ECs, tip-to-sprout anastomosis occurs
   - Otherwise the TC remains at the target site

   End Loop 1

2. Choose $\bar{N}$ TCs at random with replacement

   Loop 2: For 1 to $\bar{N}$

   (a) Choose a random number, $\bar{R} \in [0, 1]$

   (b) If $\bar{R} \leq P_b = P_p c$, then branching occurs

   End Loop 2

3. Increment time step: $\bar{K} = \bar{K} + 1$

End While Loop

below (see Section 2.3.2).

These rules lead to cases where multiple TCs and/or ECs can occupy a site. In our CA algorithm, only one anastomosis event can occur during a TC move (see Figs. 2.2a and 2.2b), and we have imposed the hierarchy that a tip-to-tip anastomosis event occurs first (if a TC occupies the target site).

2.2.5 Ensemble Averages

To relate the discrete model to a continuum, macroscopic description, we average the occupancy of site (i, j) over M realizations of the discrete model at discrete times $1, 2, \cdots, \bar{K}$. In particular, we define $n_{i,j}(\bar{K})$ and $e_{i,j}(\bar{K})$ as follows:

$$n_{i,j}(\bar{K}) = \frac{1}{M}\sum_{m=1}^{M} n_{i,j}^{m}(\bar{K}), \quad e_{i,j}(\bar{K}) = \frac{1}{M}\sum_{m=1}^{M} e_{i,j}^{m}(\bar{K}), \tag{2.11}$$

where $n_{i,j}^{m}(\bar{K})$ and $e_{i,j}^{m}(\bar{K})$ are the TC and EC occupancies of site (i, j) after $\bar{K}$ discrete time steps at the m-th realization, respectively. We also define the column averages as follows:

$$N_i(\bar{K}) = \frac{1}{M(R+1)}\sum_{m=1}^{M}\sum_{j=0}^{R} n_{i,j}^{m}(\bar{K}), \tag{2.12}$$

$$E_i(\bar{K}) = \frac{1}{M(R+1)}\sum_{m=1}^{M}\sum_{j=0}^{R} e_{i,j}^{m}(\bar{K}), \tag{2.13}$$

where R is the number of columns on the lattice.

2.3 Discrete-to-Continuum Derivation in Two Dimensions

We derive our continuum PDE model by formulating DCEs that relate $n_{i,j}(\bar{K}+1)$ and $e_{i,j}(\bar{K}+1)$ (defined in equation (2.11)), the average TC and EC occupancies at site (i,j) at time $\bar{K}+1$, to the average occupancies at site (i,j) at time $\bar{K}$ and the change in occupancy during a discrete time step. In formulating these conservation equations, we must include TC movement due to diffusion and chemotaxis, anastomosis and branching, as well as EC creation due to TC movement and tip-to-tip anastomosis. Defining $\delta n_{i,j}$ and $\delta e_{i,j}$ by

$$\delta n_{i,j} = n_{i,j}(\bar{K}+1) - n_{i,j}(\bar{K}), \tag{2.14}$$

$$\delta e_{i,j} = e_{i,j}(\bar{K}+1) - e_{i,j}(\bar{K}), \tag{2.15}$$

the DCEs for the TC and EC population within the lattice ($0 < i,j < R$) are, respectively,

$$\begin{aligned}
\delta n_{i,j} = P_m \Bigg(& \underbrace{P^{x+}_{i-1,j} n_{i-1,j} + P^{x-}_{i+1,j} n_{i+1,j} + P^{y+}_{i,j-1} n_{i,j-1} + P^{y-}_{i,j+1} n_{i,j+1}}_{\text{1. movement into } (i,j)} \\
& - \underbrace{\left(P^{x+}_{i,j} + P^{x-}_{i,j} + P^{y+}_{i,j} + P^{y-}_{i,j}\right) n_{i,j}}_{\text{2. movement out of } (i,j)} \\
& - \underbrace{a_n n_{i,j} \left(P^{x+}_{i-1,j} n_{i-1,j} + P^{x-}_{i+1,j} n_{i+1,j} + P^{y+}_{i,j-1} n_{i,j-1} + P^{y-}_{i,j+1} n_{i,j+1}\right)}_{\text{3. tip-to-tip anastomosis}} \\
& - \underbrace{a_e e_{i,j} \left(P^{x+}_{i-1,j} n_{i-1,j} + P^{x-}_{i+1,j} n_{i+1,j} + P^{y+}_{i,j-1} n_{i,j-1} + P^{y-}_{i,j+1} n_{i,j+1}\right)}_{\text{4. tip-to-sprout anastomosis}} \Bigg) \\
& + \underbrace{P_p c_{i,j} \left(n_{i,j-1} + n_{i,j+1} - n_{i,j}\right)}_{\text{5. branching}},
\end{aligned} \tag{2.16}$$

and

$$\delta e_{i,j} = P_m \Bigg(\underbrace{P^{x+}_{i,j} + P^{x-}_{i,j} + P^{y+}_{i,j} + P^{y-}_{i,j}}_{1'.\,\text{movement of TCs out of } (i,j)} + \underbrace{a_n \left(P^{x+}_{i-1,j} n_{i-1,j} + P^{x-}_{i+1,j} n_{i+1,j} + P^{y+}_{i,j-1} n_{i,j-1} + P^{y-}_{i,j+1} n_{i,j+1} \right)}_{3'.,\text{tip-to-tip anastomosis}} \Bigg) n_{i,j}. \tag{2.17}$$

Equations (2.16) and (2.17) describe how TC and EC occupancy, respectively, change during a time step assuming that the occupancy of lattice sites is independent (mean-field approximation). We remark that equations (2.16) and (2.17) hold for a general TAF field, and that for the linear TAF field in our model, $P^{y\pm} = \frac{1}{4}$.

In equation (2.16), term 1 represents TC movement from sites $(i\pm1, j)$ and $(i, j\pm1)$ into site (i, j). TC movement from site (i, j) into a neighbouring site is represented by term 2. Terms 3 and 4 model tip-to-tip and tip-to-sprout anastomosis, respectively. If a TC from a neighbouring site moves into site (i, j) and it is already occupied by a TC or EC, then the TCs are lost, and a new EC is deposited at (i, j) for tip-to-tip anastomosis, whilst for tip-to-sprout anastomosis, the EC at site (i, j) remains. Term 5 represents branching into the site (i, j) from a TC located at $(i, j-1)$ or $(i, j+1)$ (source terms), and the loss of a TC from site (i, j) if it branches into neighbouring sites (sink term).

We can combine terms 1 to 4 of equation (2.16) as follows:

$$P_m \left(\left(P^{x+}_{i-1,j} n_{i-1,j} + P^{x-}_{i+1,j} n_{i+1,j} + P^{y+}_{i,j-1} n_{i,j-1} + P^{y-}_{i,j+1} n_{i,j+1} \right) (1 - a_n n_{i,j} - a_e e_{i,j}) - \left(P^{x+}_{i,j} + P^{x-}_{i,j} + P^{y+}_{i,j} + P^{y-}_{i,j} \right) n_{i,j} \right). \tag{2.18}$$

Written in this form, we conclude that when anastomosis is active (i.e. $a_n \neq 0$ or $a_e \neq 0$) a TC can always move out of site (i, j), with the outcome depending on the

occupancy of the target site. A TC only remains a TC if the target site is vacant.

In equation (2.17), ECs are created when a TC moves out of a site and via tip-to-tip anastomosis. These source terms are the counterparts of terms 1 and 3 in equation (2.16).

We now relate the DCEs to a continuum description. We expand the dependent variables n, e and c, in equations (2.16) and (2.17) in a Taylor series about the site (i, j). Recall that $P^{x\pm}$ and $P^{y\pm}$ are defined in equations (2.5) and (2.6), respectively. By setting $x_i \to x, y_j \to y$, $n_{i,j}(\bar{K}) \to n(x, y, t), e_{i,j}(\bar{K}) \to e(x, y, t)$ and dividing the resulting expressions by τ ($t = \tau\bar{k}$, τ relates the discrete and continuum timescales), we eventually arrive at the following expressions:

$$\begin{aligned}
&\frac{1}{\tau}\left(n(x, y, t+\tau) - n(x, y, t)\right) = \\
&(1 - a_n n - a_e e)\frac{P_m}{\tau}\left(\frac{h^2}{4}\nabla^2 n - h^2 k\nabla\cdot(n\nabla c) + O\left(h^4\right)\right) - \frac{P_m}{\tau}\left(a_n n^2 + a_e n e\right) \\
&+\frac{P_p c}{\tau}\left(n + h^2\frac{\partial^2 n}{\partial y^2} + O\left(h^4\right)\right),
\end{aligned} \tag{2.19}$$

and

$$\begin{aligned}
&\frac{1}{\tau}\left(e(x, y, t+\tau) - e(x, y, t)\right) = \\
&\frac{P_m n}{\tau}\left(1 + a_n n\right) + \frac{a_n P_m n}{\tau}\left(\frac{h^2}{4}\nabla^2 n - h^2 k\nabla\cdot(n\nabla c) + O\left(h^4\right)\right),
\end{aligned} \tag{2.20}$$

for the TC and EC populations, respectively.

By taking the limit as $\tau \to 0$, and neglecting terms of $O(h^4)$ and higher, we obtain

the following PDEs:

$$\begin{aligned}\frac{\partial n}{\partial t} &= (1 - a_n n - a_e e)\left(D\nabla^2 n - \chi\nabla\cdot(n\nabla c)\right) \\ &\quad -\mu(a_n n^2 + a_e n e) + c\left(\lambda n + D_b\frac{\partial^2 n}{\partial y^2}\right),\end{aligned} \tag{2.21}$$

and

$$\frac{\partial e}{\partial t} = \mu n + a_n n\left(\mu n + D\nabla^2 n - \chi\nabla\cdot(n\nabla c)\right), \tag{2.22}$$

where

$$\mu = \lim_{\tau\to 0}\frac{P_m}{\tau}, \quad \lambda = \lim_{\tau\to 0}\frac{P_p}{\tau}, \tag{2.23}$$

and the diffusion coefficient, D, chemotactic coefficient, χ, and diffusion coefficient due to branching, D_b, are defined as

$$D = \frac{\mu h^2}{4} = \lim_{\tau\to 0}\frac{P_m h^2}{4\tau}, \quad \chi = \mu k h^2 = \lim_{\tau\to 0}\frac{P_m k h^2}{\tau}, \tag{2.24}$$

$$D_b = \lambda h^2 = \lim_{\tau\to 0}\frac{P_p h^2}{\tau}. \tag{2.25}$$

Our expressions for D, χ and λ are consistent with the literature (Simpson et al., 2010a, 2009a; Codling et al., 2008), although we have not taken the limit $\tau, h \to 0$ with h^2/τ constant. If we took the limit as $h \to 0$ with μ defined by equation (2.23), the diffusive and chemotactic terms, as well as the diffusive term due to branching, would vanish and our PDE for n would involve only source terms. This is at odds with our CA model, where TCs move by diffusion and chemotaxis. By defining $\bar{D} = \mu/4$, $\bar{\chi} = \mu k$ and $\bar{D}_b = \lambda$, and rewriting D, χ and D_b as $D = h^2\bar{D}$, $\chi = h^2\bar{\chi}$ and $D_b = h^2\bar{D}_b$, respectively, it is clear that in the limit as $h \to 0$, we have a singular perturbation problem. Since we use small, non-zero values for h and τ in the discrete simulations, and to define the continuum model parameters, we retain the $O(h^2)$ terms in (2.21) and (2.22) in order to capture the boundary layer in which

the TC density changes rapidly. As mentioned in Chapter 1, similar approaches in which either the limit $h \to 0$ was not explicitly taken or $O(h^2)$ diffusive terms were retained were used in Hywood et al. (2013); Ross et al. (2015); Davies et al. (2014) to derive PDE approximations to discrete agent-based models. Alternatively, we note that we could have considered how the transition probabilities $(P_m, P^{x\pm}, P^{y\pm})$ scale with the lattice spacing h (represents the (dimensionless) diameter of a cell in our framework). In particular, we could follow the approach outlined in Spill et al. (2015); they consider a mesoscale framework (the lattice spacing h is larger than the size of a cell) in which the diffusion and chemotactic transition probabilities scale with $1/h^2$. Considering the scaling could also provide additional physical insight into the system. For example, in the case of diffusive motion, the $1/h^2$ scaling arises due to the path length associated with Brownian motion (see Spill et al. (2015)). We postpone such investigations in our framework to future work.

We have neglected terms of $O(h^4)$ and higher in our model; we will show later that when these higher-order terms are neglected, the PDEs approximate the discrete model well.

We approximate the boundary conditions in the discrete model by imposing no flux boundary conditions on equations (2.21) and (2.22), assuming that anastomosis and branching are negligible there. With these boundary conditions, our PDE model remains valid until the TC front reaches $x = 1$.

The initial conditions for the TCs in the discrete model (see equation (2.10)) are discontinuous. We instead use averaged CA simulation results for the TCs and ECs at some later discrete time step $\bar{K}_{IC}$, $n_{i,j}(\bar{K}_{IC})$ and $e_{i,j}(\bar{K}_{IC})\,\forall i, j$ (ensemble averages defined in equation (2.11)), respectively, to initialise the continuum model. Here, t_{IC} is related to the discrete time step K_{IC} by $t_{IC} = \tau \bar{K}_{IC}$.

Our continuum model, valid for $t \geq t_{IC}$, can now be written as:

$$\begin{aligned}
\frac{\partial n}{\partial t} &= (1 - a_n n - a_e e)\left(D\nabla^2 n - \chi\nabla\cdot(n\nabla c)\right) \\
&\quad -\mu(a_n n^2 + a_e n e) + c\left(\lambda n + D_b\frac{\partial^2 n}{\partial y^2}\right), \qquad (2.26)\\
\frac{\partial e}{\partial t} &= \mu n + a_n n\left(\mu n + D\nabla^2 n - \chi\nabla\cdot(n\nabla c)\right), \qquad (2.27)
\end{aligned}$$

subject to

$$\begin{aligned}
D\frac{\partial n}{\partial x} - \chi n\frac{\partial c}{\partial x} &= 0, \text{ at } x = 0, 1, 0 \leq y \leq 1, \qquad (2.28)\\
D\frac{\partial n}{\partial y} - \chi n\frac{\partial c}{\partial y} &= 0, \text{ at } y = 0, 1, 0 \leq x \leq 1, \qquad (2.29)
\end{aligned}$$

with

$$\begin{aligned}
n(x, y, t_{IC})\ \forall x, y &= n_{i,j}(\bar{K}_{IC})\ \forall i, j, \qquad (2.30)\\
e(x, y, t_{IC})\ \forall x, y &= e_{i,j}(\bar{K}_{IC})\ \forall i, j. \qquad (2.31)
\end{aligned}$$

It is clear that terms multiplied by D or χ only arise from the diffusive and chemotactic motion of the TCs, terms multiplied by λ and D_b arise from TC branching, and terms multiplied by a_n or a_e arise from tip-to-tip and tip-to-sprout anastomosis, respectively. The EC population is created predominantly through TC movement, via random motion and/or chemotaxis, as indicated by the source term μn on the right-hand side of equation (2.27). Here μ can be interpreted as the TC motility rate. We also note that given the form of equation (2.27), we need only specify an initial condition for $e(x, y, t)$. Equations (2.26)-(2.31) constitute a new (non-dimensional) snail-trail model of angiogenesis. Whilst the terms that govern TC diffusion and chemotaxis are standard (see Byrne and Chaplain (1995a); Balding and McElwain (1985); Anderson and Chaplain (1998); Orme and Chaplain (1997)), the terms as-

sociated with anastomosis (flux terms), TC branching in two dimensions, and most notably, EC creation, are new.

We note that the diffusive term due to branching would read $D_b\nabla^2 n$ had we implemented branching in the x-direction. Recall that we assumed that branching occurs only in the direction perpendicular to the direction of propagation of the vascular front (i.e. in y only). We also assumed that branching does not create ECs, and therefore equation (2.27) does not contain source terms arising from branching. Our implementation of branching at the microscale gives rise to a branching term, λcn, at the macroscale that is consistent with those used in existing continuum models (Byrne and Chaplain, 1995a; Spill et al., 2015). To summarise, there are many ways to implement branching, further, the leading order branching term, λcn, could describe a multitude of branching processes on the microscale (see Simpson et al. (2010a)). We also note that with $c(x, y) = x$, $\partial c/\partial y = 0$ in the no flux boundary condition in y (equation 2.29).

2.3.1 One-Dimensional Model

We now reduce our PDE model from two spatial dimensions to one so as to compare the solutions to the one-dimensional BC model. To this end, we define the following variables:

$$N(x,t) = \int_0^1 n(x,y,t)dy, \quad E(x,t) = \int_0^1 e(x,y,t)dy.$$

Integrating equations (2.26) and (2.27) with respect to y, and using the definitions above, we find that for $t \geq t_{IC}$, $N(x,t)$ and $E(x,t)$ satisfy

$$\begin{aligned} \frac{\partial N}{\partial t} &= (1 - a_n N - a_e E)\left(D\frac{\partial^2 N}{\partial x^2} - \chi\frac{\partial}{\partial x}\left(N\frac{\partial c}{\partial x}\right)\right) \\ &\quad -\mu(a_n N^2 + a_e NE) + \lambda c N, \end{aligned} \tag{2.32}$$

$$\frac{\partial E}{\partial t} = \mu N + a_n N\left(\mu N + D\frac{\partial^2 N}{\partial x^2} - \chi\frac{\partial}{\partial x}\left(N\frac{\partial c}{\partial x}\right)\right), \tag{2.33}$$

subject to

$$D\frac{\partial N}{\partial x} - \chi N\frac{\partial c}{\partial x} = 0, \text{ at } x = 0, 1, \tag{2.34}$$

with

$$N(x, t_{IC}) = N_i(\bar{K}_{IC}),\ E(x, t_{IC}) = E_i(\bar{K}_{IC}),\ \forall x, i, \tag{2.35}$$

where N_i and E_i are column ensemble averages as defined in equations (2.12) and (2.13), respectively. In equations (2.32) and (2.33), we assume a general mean-field approximation

$$\int_0^1 f_1 f_2\, dy \approx \left(\int_0^1 f_1(x,y,t)dy\right) \times \left(\int_0^1 f_2(x,y,t)dy\right), \tag{2.36}$$

where f_1 and f_2 represent functions of x, y and t, which, for example, lead to approximations of the form

$$\begin{aligned} \int_0^1 n^2\, dy &\approx \left(\int_0^1 n(x,y,t)dy\right) \times \left(\int_0^1 n(x,y,t)dy\right), \\ \int_0^1 ne\, dy &\approx \left(\int_0^1 n(x,y,t)dy\right) \times \left(\int_0^1 e(x,y,t)dy\right). \end{aligned} \tag{2.37}$$

We will show later that, with these approximations, equations (2.32) and (2.33) are a good approximation of the discrete model (when the mean-field approximation holds). We can also derive the one-dimensional equations directly from the DCEs, equations (2.16) and (2.17), by summing over j, and using the discrete analogue of the approximations above (mean-field approximation); this is equivalent to replacing the ensemble averages with their column averages (Simpson et al., 2009a) (i.e. replacing n and e with N and E in equations (2.26) and (2.27), see Simpson et al. (2009a)). In the next chapter, we will directly formulate one-dimensional PDEs using column-averaged DCEs.

Equation (2.33) reveals that in the absence of tip-to-tip anastomosis ($a_n = 0$), the spatio-temporal evolution of the EC density is proportional to a source term of TCs, μn. In Spill et al. (2015), their mesoscale approach resulted in a continuum model in which random motion of TCs gave rise to a similar source term of ECs, which is proportional to the TC density. In contrast, one-dimensional phenomenological (Balding and McElwain, 1985; Byrne and Chaplain, 1995a) snail-trail models (see Section 2.1) assume that EC (vessel) creation is proportional to the flux of TCs in the x-direction.

2.3.2 Cell Density

In earlier work by Balding and McElwain (1985); Byrne and Chaplain (1995a) and Spill et al. (2015), tip-to-sprout and tip-to-tip anastomosis, were modelled via terms of the form $-\beta_e ne$ and $-\beta_n n^2$ (see Section (2.1)), respectively. In our model, tip-to-tip and tip-to-sprout anastomosis give rise to flux terms $-n\left(D\nabla^2 n - \chi\nabla\cdot(n\nabla c)\right)$ and $-e\left(D\nabla^2 n - \chi\nabla\cdot(n\nabla c)\right))$ in equation (2.26), respectively, in addition to the standard sink terms $-\mu n^2$ and $-\mu ne$. As mentioned, anastomosis imposes occupancy restrictions on the discrete model. Thus, these effects impose density restrictions on the continuum model. If $a_e = 0$, then our model is well-posed, provided we impose

initial conditions with $0 \leq n \leq 1$. However, if $a_e = 1$, then $(1 - a_n n - a_e e)$ may become negative even if the initial TC/EC densities do not exceed one (resulting in ill-posedness). This may occur when the continuum model deviates from the discrete model due to a break-down of the mean-field assumption. Alternatively, when only tip-to-sprout anastomosis is active ($a_n = 0, a_e = 1$), it may occur due to modelling assumptions in the CA model to reproduce a non-volume excluding model comparable to that of the BC model (we require explicit TC VE in the motility mechanism and VE in the branching mechanism to prevent ill-posedness and adhere to density restrictions, and in the next chapter, we will incorporate this). We conclude that tip-to-sprout anastomosis should be implemented with tip-to-tip anastomosis for the PDE model to remain well-posed when our mean-field approximation holds (we further discuss ill-posedness in Appendix F, Section F.4).

As mentioned, branching has been implemented without any VE and thus may violate cell density (occupancy) restrictions imposed by anastomosis in the continuum (discrete) model. However, provided the branching rate, λc, is low, the model will remain well-posed.

In the next section, we compare our one-dimensional PDE model to the averaged CA simulation results. We will also compare a modified version of the one-dimensional BC model (see below) to the averaged CA simulation results. The original BC model represented the network in terms of vessel length per unit area, ρ (i.e. not EC density, see Section 2.1). To relate the vessel density to EC density extracted from the CA model, measured in units of number of ECs averaged over the y-direction (i.e per unit area), we convert vessel density from a length to a number density. The length of a cell is defined by the lattice spacing in our model, h. Thus, to convert vessel density to EC density, we must divide ρ by h such that

$$E = \frac{\rho}{h}. \tag{2.38}$$

The modified BC model is:

$$\frac{\partial N}{\partial t} = D\frac{\partial^2 N}{\partial x^2} - \chi\frac{\partial}{\partial x}\left(N\frac{\partial c}{\partial x}\right) + \lambda N c - \beta_e N E - \beta_n N^2, \tag{2.39}$$

$$\frac{\partial E}{\partial t} = \frac{1}{h}\left|D\frac{\partial N}{\partial x} - \chi N\frac{\partial c}{\partial x}\right|, \tag{2.40}$$

$$c(x) = x, \tag{2.41}$$

Following Spill et al. (2015), we use the absolute value of the TC flux in equation (2.40) to guarantee that the source of ECs generated by the TC flux is non-negative. We also neglect branching from ECs and vessel regression. We solve equations (2.39) and (2.40) on $(x,t) \in [0,1] \times [0,\infty)$, locating the TAF source at $x = 1$ and the limbus at $x = 0$ (switching the limbus and TAF source location in the original BC model, see Chapter 1). We impose no flux boundary conditions (see equation (2.34)), with initial conditions and linear TAF profile ($c = x$) taken from the CA model.

2.4 Continuum-Discrete Comparisons in One Dimension

2.4.1 Parameter Values

To compare discrete and continuum models, we must relate microscale and macroscale parameters. There are five macroscale parameters: D, χ, λ, μ and t_{IC} and six microscale parameters: R, h, P_m, P_p, τ and k. We set the macroscopic diffusion and chemotactic coefficients (using values from the BC model, see Section 1.2 in Chapter 1), D and χ, and t_{IC}, and the following microscale parameters in the CA model: the size of the lattice, R (which determines the lattice spacing h), and the probabilities P_m, P_p. We then use equation (2.24) to derive values for the microscale parameters

k and τ. The value for k allows us to define $P_{i,j}^{x\pm}$. Given τ, we can calculate μ and λ, from equation (2.23). We must also prescribe a_n and a_e in the CA model to fix which anastomosis processes are active. These parameters, a_n and a_e, also appear in the continuum model. With the chosen values for D and χ, the TC flux is always negative and thus the absolute value in equation (2.40) can be replaced by a negative sign.

The parameter values used in the discrete and DCE-derived continuum models are stated in Table 2.1. Each individual CA simulation is run for $K_{\text{final}} = 320$ discrete time steps (equivalent to 2 time units in the continuum model). The remaining parameter values for the BC model, $\lambda, \beta_n = a_n\mu$ and $\beta_e = a_e\mu$ are chosen to be consistent with the values used in our continuum model.

Table 2.1: CA and DCE-derived PDE model parameters

R	P_m	P_p	h	τ	k	g_x	g_y	$P_{x\pm}$	$P_{y\pm}$	D	χ	λ	μ	t_{IC}
200	1	10^{-3}	$\frac{1}{200}$	$\frac{1}{160}$	100	1	0	$\frac{1}{2}, 0$	$\frac{1}{4}$	10^{-3}	0.4	0.16	160	0.2

2.4.2 Comparisons

We compare solutions of the one-dimensional equations (2.32) and (2.33) and solutions to the one-dimensional BC model (equations (2.39) and (2.40)) to averaged CA simulation results defined in equations (2.12) and (2.13). Lattice site occupancy is averaged over $M = 200$ realizations and $R = 200$ columns. We outline the numerical schemes below (further details can be found in Appendix A).

The PDEs are solved numerically using the method of lines with a finite difference scheme in space (upwinding for equation (2.40)). The resulting time-dependent ordinary differential equations are solved over $t \in [0.2, 2]$ using MATLAB's *ode15s* solver, which implements adaptive time-stepping (Shampine and Reichelt, 1997). The solutions are then linearly interpolated in time (using MATLAB's *interp1*) to find the solutions at $t \in [0.2, 2]$ in 0.2 increments.

In Fig. 2.4, we illustrate how network morphology changes when we incorporate different processes in the CA model. A dense vessel network forms as TCs migrate via diffusion and chemotaxis, with new TCs introduced through branching (see Fig. 2.4a). Individual sprouts fuse through tip-to-tip anastomosis (which annihilates TCs), thereby producing a sparser vessel network than when tip-to-tip anastomosis is inactive (compare Figs. 2.4b and 2.4a). Tip-to-sprout anastomosis annihilates all TCs, as TCs fuse with ECs within their own sprout (see Fig. 2.4c). In Fig. 2.5, we compare the averaged CA simulations with PDE model solutions using the same CA parameter values considered in Fig. 2.4.

We see good agreement between the CA simulation results and the DCE-derived PDEs (solutions fall within the standard deviation (not shown) of the averaged CA simulation results) for both the TC and EC densities when anastomosis is neglected (Figs. 2.5a, 2.5b) and when tip-to-tip anastomosis is active (Figs. 2.5c, 2.5d). However, the agreement is poor when both tip-to-tip and tip-to-sprout anastomosis are active (Figs. 2.5e, 2.5f). The removal of TCs associated with anastomosis results in a decrease in the TC density. The effect is more pronounced for tip-to-sprout anastomosis, with all TCs lost and propagation of the vascular front halted for $t \geq 0.4$.

When comparing the BC model to the CA simulation results (see Figs. 2.5a-2.5f), we rescaled the EC density (equation (2.40)) by 2 such that

$$\frac{\partial e}{\partial t} = \frac{2}{h}\left| D\frac{\partial n}{\partial x} - \chi n \frac{\partial c}{\partial x}\right|. \tag{2.42}$$

In the BC model, the vessel/EC density is proportional to the flux of TCs in the x-direction. However, TCs also walk randomly in the y-direction (recall that in the CA model, a TC can move in the positive x-direction with probability $1/2$ and in the y-direction with probability $1/2$ (see Table 3.4)). This means that TCs leave behind ECs as they move in the y-direction. This effect is not included in the BC model and,

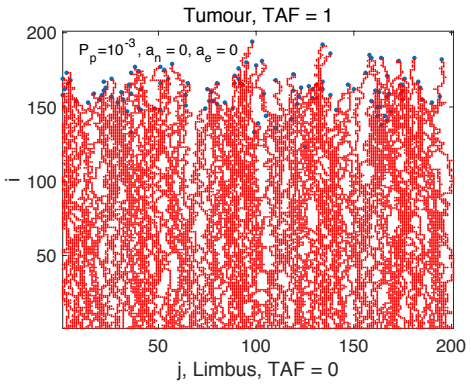

(a) no anastomosis

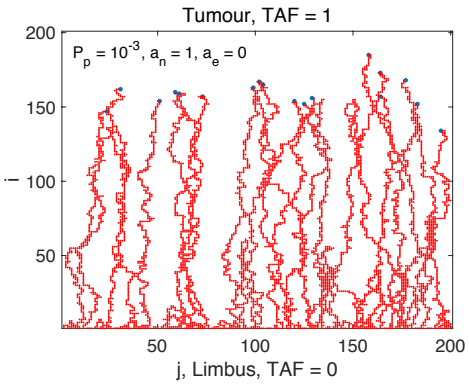

(b) tip-to-tip anastomosis

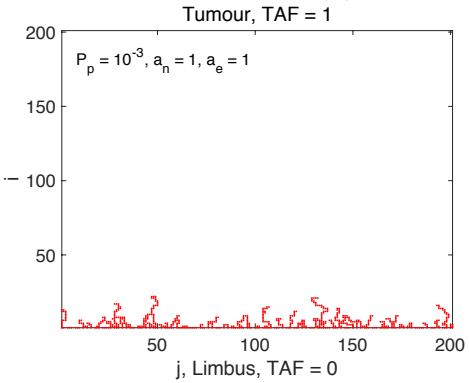

(c) tip-to-tip anastomosis and tip-to-sprout anastomosis

Figure 2.4: Individual CA simulations (after 320 time steps). (a) TCs (blue) migrate via diffusion and chemotaxis towards the TAF source at $x = 1$, leaving behind a trail of ECs (red), and creating a dense network. (b) Tip-to-tip anastomosis creates connections between individual sprouts, and annihilates TCs, producing a sparser network than in (a). (c) Tip-to-sprout anastomosis annihilates all TCs, as TCs anastomose with ECs in their own sprout.

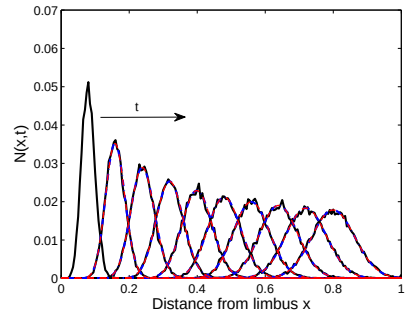

(a) no anastomosis

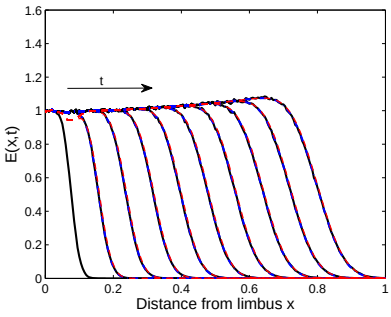

(b) no anastomosis

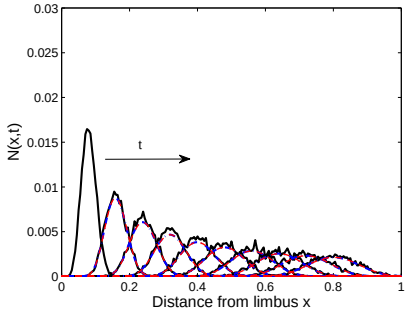

(c) tip-to-tip anastomosis

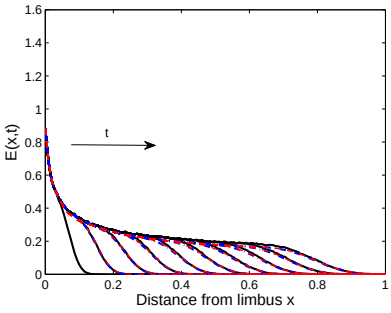

(d) tip-to-tip anastomosis

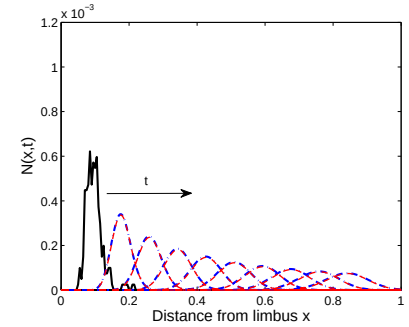

(e) tip-to-tip and tip-to-sprout anastomosis

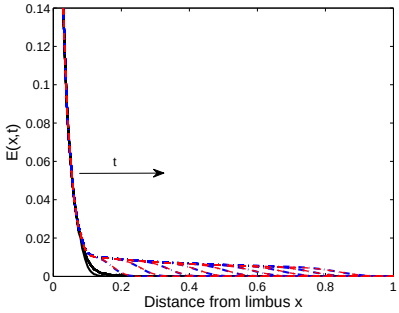

(f) tip-to-tip and tip-to-sprout anastomosis

Figure 2.5: Comparison of PDEs solutions to averaged CA simulation results. Left panel: TC density; right panel: EC density. (a), (b) TCs migrate via diffusion and chemotaxis towards the TAF source at $x = 1$, leaving behind a trail of ECs. (c), (d) Tip-to-tip anastomosis annihilates TCs as they migrate towards the TAF source. (e), (f) Tip-to-sprout anastomosis annihilates all TCs causing the vascular front to halt. Column-averaged CA simulation results (black solid curve) are shown at time $t = 0.2, 0.4, \ldots, 2.0$ (arrow shows direction of increasing time). The averaged CA simulation results at $t_{IC} = 0.2$ initialise the DCE-derived PDE model (blue dashed-dot curve), equations (2.32) and (2.33), and the BC model (red dashed curve), equations (2.39) and (2.42), with the PDE solutions shown from $t = 0.4$ to $t = 2$. Parameter values are given in Table 3.4 except for the anastomosis parameters specified in the DCE-derived PDE model as (a), (b) $a_n = a_e = 0$, (c), (d) $a_n = 1, a_e = 0$, (e), (f) $a_n = a_e = 1$. The anastomosis parameters for the BC model are $\beta_n = 160a_n$ and $\beta_e = 160a_e$. (a)-(f) has been published in Pillay et al. (2017) (S. Pillay, H. M. Byrne and P. K. Maini, Modelling Angiogenesis: A Discrete to Continuum Description, Physical Review E, 95, 012410, 2017), Copyright 2017 American Physical Society (APS).

therefore, equation (2.40) underestimates the true EC density by a half. We note further that in the discrete model, if the probabilities for TC movement in the x- and y-directions, $P^{x\pm}$ and $P^{y\pm}$, respectively, were different to what we have chosen (see Table 3.4), then the path of the TCs would be different and the EC density would have to be rescaled as

$$\frac{\partial e}{\partial t} = \frac{\kappa}{h}\left|D\frac{\partial n}{\partial x} - \chi n\frac{\partial c}{\partial x}\right|, \tag{2.43}$$

where the non-negative parameter κ accounts for EC density created via TC motion in directions other than the positive x-direction. The reader is referred to Appendix B, Section B.1 (see Fig. B.2) for such a case where $P^{x-} \neq 0$ and $\kappa > 2$.

When equation (2.42) is used in place of equation (2.40), there is good agreement between the CA simulation results and solutions to the modified BC model (see Figs. 2.5a-2.5d). We see poor agreement between the CA simulation results and the BC model when both tip-to-tip and tip-to-sprout anastomosis are active (see Figs. 2.5e, 2.5f).

The proximity of cells affects the chances of an anastomosis event, and thus, the assumption that the occupancy of lattice sites are independent may no longer hold. This is most likely why our continuum model, derived using a mean-field approximation, does not capture the rapid rate of tip-to-sprout anastomosis (see Figures 2.5e, 2.5f). In deriving our PDE model, we neglected terms that involve higher-order derivatives of n ($O(h^4)$ and higher), which describe a boundary layer in which the TC density changes rapidly. Thus, it is unlikely that these higher-order derivative terms capture the rapid rate of tip-to-sprout anastomosis which removes all TCs and prevents propagation of the vascular front in the CA model. Since including correlations in our framework would be intractable (see Baker and Simpson (2010)), we opt instead to make our CA model more biologically realistic by modifying the tip-to-sprout anastomosis rules to prevent annihilation of all TCs (explained further in the next section). We capture this more realistic behaviour with our PDE model

through parameter fitting.

2.5 Tip-to-Sprout Anastomosis: Excluding Self-Loops

In our CA model, tip-to-sprout anastomosis occurs when a TC encounters an EC. Extensive simulations (results not shown) reveal that eventually all TCs are annihilated even if they are initially well separated. We deduce that diffusive motion of the TCs in the y-direction and, in general, in directions other than the positive x-direction, causes TCs to anastomose with ECs in their own sprout (self-loops), creating a stunted sprout. All TCs are annihilated through these self-loops. In practice, such stunted sprouts will likely regress (Carmeliet and Jain, 2011) or be remodelled away. We modify our CA model to preclude self-loops during tip-to-sprout anastomosis in the following way. When a TC attempts to move to a site occupied by an EC (identified as the last EC to be created at that site), the move is aborted if that EC belongs to the same sprout as the TC. If the EC belongs to a different sprout, then anastomosis occurs.

We must account for this modification to the CA model in our PDE model. As it would be intractable to keep track of ECs in a particular sprout in our DCE-framework, we instead allow a_e, the parameter that controls the rate of tip-to-sprout anastomosis, to vary and estimate it by fitting PDE solutions to averaged CA simulations results with self-loops excluded.

2.5.1 Model Fitting

When we fit our PDE model to the averaged CA simulation results, we fix $a_n = 1$ and allow a_e to vary so that $0 < a_e \leq 1$. In the same way, when fitting the BC model, we fix $\beta_n = 160$ and suppose $0 < \beta_e \leq 160$. We carry out the parameter estimation using

a non-linear least squares fitting procedure using MATLAB's *lsqnonlin* routine (with a tolerance of 10^{-6}), which implements a trust-region-reflective algorithm (Coleman and Li, 1996, 1994), with the PDEs solved as described earlier (see also Appendix A). We estimate the parameters using TC and EC densities from averaged CA simulation results at times $t = 0.4, 0.6, \ldots, 2.0$.

The resulting parameter estimates and the 95% confidence intervals (calculated using MATLAB's *nlparci* using the Jacobian output from *lsqnonlin*) are stated in Table 2.2. We note that the optimization problem is constrained as all other parameters in both PDE models are fixed (see Section 2.4.1), and thus the confidence intervals are tight. With $a_e = 0.0343$ in equations (2.32) and (2.33) (and $\beta_e = 5.0648$ in equations (2.39) and (2.42)), there is good agreement between the PDE models and the CA simulation results (see Fig. 2.6). Furthermore, when self-loops are excluded, the vascular front continues to propagate towards the TAF source as the TCs are not exhausted (see Figs. 2.5e, 2.5f and individual simulation in Fig. 2.6a).

Table 2.2: Least squares fit: tip-to-sprout anastomosis parameters

Parameter (Model)	Value	95% Confidence Interval
a_e (DCE-derived)	0.0343	± 0.0003
β_e (BC Model)	5.0648	± 0.0423

2.6 Discussion

In this chapter, we have systematically derived continuum snail-trail models of angiogenesis. Specifically, we developed a two-dimensional CA model of angiogenesis in the corneal assay (based on the snail-trail process), and using a mean-field approximation and DCEs, we derived new PDE models (in one and two dimensions) for the spatio-temporal evolution of the TC and EC densities (which differ from existing phenomenological PDE models). We compared solutions of our one-dimensional PDEs

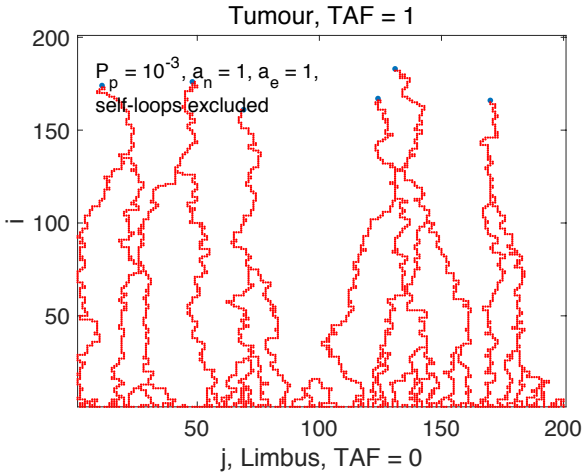

(a) Individual simulation

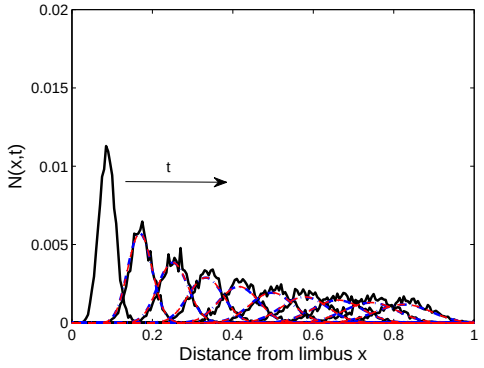

(b) TC density (tip-to-tip and tip-to-sprout anastomosis)

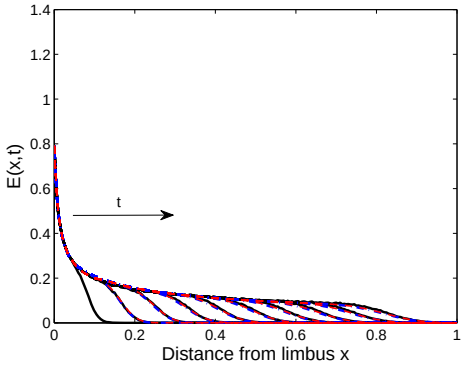

(c) EC density (tip-to-tip and tip-to-sprout anastomosis)

Figure 2.6: Self-loops excluded during tip-to-sprout anastomosis: individual simulations and model comparisons. (a) When self-loops are excluded, the TC front continues to propagate, with individual sprouts connecting through tip-to-tip and tip-to-sprout anastomosis. (b), (c) Tip-to-sprout anastomosis decreases TC and EC densities. Column-averaged CA simulation results (black solid curve) are plotted at times $t = 0.2, 0.4, \ldots, 2.0$ (the arrow shows the direction of increasing time). Solutions to the DCE-derived PDE model (blue dashed-dot curve, equations (2.32) and (2.33)), and the modified BC model (red dashed curve, equations (2.39) and (2.42)), are shown at $t = 0.4, 0.6, \cdots, t = 2$ with the averaged CA simulation results at $t_{IC} = 0.2$ used as the initial conditions. Parameter values are given in Table 3.4 except $a_e = 0.0343$ and $\beta_e = 5.0648$ in the DCE-derived PDE model and the BC model, respectively. (b)-(c) has been published in Pillay et al. (2017) (S. Pillay, H. M. Byrne and P. K. Maini, Modelling Angiogenesis: A Discrete to Continuum Description, Physical Review E, 95, 012410, 2017), Copyright 2017 American Physical Society (APS).

and the phenomenological BC model (Byrne and Chaplain, 1995a) to averaged CA simulation results and, in so doing, determined how microscale behaviour manifests at the macroscale, and elucidated the microscale assumptions underpinning the BC model.

We found that EC creation due to TC movement can be modelled as a source term of TCs on the macroscale. In contrast, phenomenological models (Balding and McElwain, 1985; Byrne and Chaplain, 1995a) assume that EC creation is proportional to the flux of TCs in the direction of increasing TAF concentration (i.e. towards the TAF source). We have found that these snail-trail (Byrne and Chaplain, 1995a; Spill et al., 2015) models can qualitatively account for vessel formation (EC creation) in two dimensions. However, for these models to accurately account for vessel formation in two dimensions, the PDEs for EC density must be rescaled to account for TC motility in directions other than towards the TAF source. This scaling factor and, therefore vessel formation, depends on the microscale behaviour of TCs. We note that this result is explainable by the fact that the TC flux is a vector, and thus, describes net TC movement in the positive x-direction. Therefore the PDE for the EC density in the BC model does not account for movement of the TCs in other directions, which is rectified by including a scaling factor. Once modified, the BC model and our systematically-derived model agree when compared to averaged CA simulation results.

Additionally, we found that anastomosis imposes cell occupancy and density restrictions on the discrete and continuum models, respectively. As a result, for our continuum model to remain well-posed, tip-to-sprout anastomosis should be implemented when tip-to-tip anastomosis is active. The density restrictions are as follows:

- when tip-to-tip anastomosis is active, the TC density should not exceed one, and
- when both tip-to-tip and tip-to-sprout anastomosis are active, the combined

cell density (TC and EC) should not exceed one.

These findings differ from existing continuum models (Byrne and Chaplain, 1995a; Balding and McElwain, 1985; Spill et al., 2015), in which anastomosis is modelled via sink terms only, with no restrictions on cell density. Branching was implemented as a separate process to movement in our model and, thus, may not adhere to the density restrictions imposed by anastomosis. However, provided the branching rate is low, the continuum model will remain well-posed. The potential for ill-posedness arises from assumptions made in the CA model to derive a non-volume excluding model comparable to the BC model. We found that implementing anastomosis on the microscale in the CA model is inconsistent with implementing branching and motility without VE. We will rectify this inconsistency in the next chapter.

When both tip-to-tip and tip-to-sprout anastomosis are active, our PDE model does not agree with the CA model; our PDE model does not capture the rapid rate of tip-to-sprout anastomosis which annihilates all TCs in the CA model. This TC exhaustion is due to the formation of self-loops in the CA model. We postulate that the discrepancy between the discrete and continuum models is due to a break-down of the independence assumption (mean-field approximation) introduced by tip-to-sprout anastomosis. In order to produce a more realistic discrete model of angiogenesis (a TC front which propagates towards the TAF source), we modified our CA model to prevent the formation of self-loops during tip-to-sprout anastomosis. As it would have been intractable to use our DCE-framework to account for self-loops, we estimated the parameter in the continuum model that controls the rate of tip-to-sprout anastomosis, a_e, by fitting the PDE model to averaged CA simulations with self-loops excluded. We note that in pathological conditions, self-loops, different to those discussed in this chapter, are possible (see Tong and Yuan (2001) for modelling of such self-loops in a discrete model). By allowing TCs to move in the negative $x-$direction, and including length-mediated anastomosis (i.e. a TC anastomoses with an EC within in its sprout,

if the EC is located a prescribed number of cell lengths away from the TC, thereby forming a loop), we could incorporate a non-zero probability of self-loop formation.

Our PDE models were derived by assuming that the lattice spacing h is small ($h \ll 1$) and terms of $O(h^4)$ and higher were negligible. (The reader is referred to Appendix B for a comparison of PDE solutions to averaged CA simulation results generated with alternative lattice spacings). In addition, the occupancies of lattice sites were assumed to be independent. These assumptions constrain the probabilities for movement, P_m, and branching (TC proliferation), P_p, in the CA model. Anastomosis may also lead to a break-down of the independence assumption. However, we can account for the complexity introduced by anastomosis if we estimate the relevant parameters in the PDE model by fitting to averaged CA simulation results. We have used a linear TAF profile throughout this chapter, motivated by the assumption that the TAF profile relaxes rapidly to a steady-state on the timescales considered here. We also note that the linear TAF profile preserves the qualitative behaviour of TCs in the discrete and continuum models. We could relax this assumption and consider a two-dimensional TAF field whose evolution is coupled to that of the TCs and ECs. However, we stress that our focus is in determining how microscale cell behaviour influences macroscale effects, and a linear TAF profile enables us to focus on the cell dynamics.

In this chapter, we derived a non-volume excluding snail-trail PDE model of angiogenesis, our aim being to evaluate the phenomenologically derived BC model. In so doing, we elucidated the following underlying implicit assumptions in the BC model:

- The BC model implicitly views cells as point particles; the functional forms that describe branching and motility do not account for VE. This leads to inconsistencies in our PDE model because of the way in which we implement anastomosis in the CA model.

- The EC density is proportional to TC flux in the positive x-direction only, and therefore, the BC model implicitly assumes that TCs move in the direction of

increasing TAF concentration only.

In the next chapter, we will extend the CA framework to explicitly account for TC and EC volume in the motility and branching mechanism. By upscaling, we will determine how VE incorporated on the microscale affects the population behaviour of TCs and ECs, as well as the structure of the PDE models. From here on, we refer to the PDEs derived in this chapter as the Model 0 PDEs, and the CA model as CA Model 0.

Chapter 3

Single and Multi-Species Volume Exclusion

In the previous chapter, we derived a one-dimensional PDE model from a two-dimensional CA model of angiogenesis (based on the snail-trail process) in the corneal assay. We did not explicitly account for cell volume, but found that anastomosis places occupancy and density restrictions on the discrete and continuum models, respectively. We neglected volume exclusion (VE) in our derivation of the PDE model as our intention was to compare it to the well-known phenomenological model of Byrne and Chaplain (BC), which does not account for VE explicitly. In this chapter, we account explicitly for cell volume in our framework in order to determine how it affects our discrete and continuum angiogenesis models. To this end, we derive two one-dimensional PDE models from two-dimensional CA models of the snail-trail process, incorporating TC VE (Model 1) and TC and EC VE (Model 2), respectively. By deriving and comparing these two models, we aim to increase our understanding of the effects of VE in general and the specific effects arising from each cell species. Further, we highlight some of the limitations of the mean-field approximation which arise as we introduce VE into our PDE models.

3.1 Introduction

In this chapter, we explicitly incorporate VE through single and multi-species exclusion processes i.e. aborted TC moves due to occupancy of the target site. We will introduce CA Models 1 and 2, which incorporate TC VE and TC VE and EC VE, respectively. Anastomosis occurs when a TC moves to a site that is occupied. Therefore, anastomosis and VE are essentially mutually exclusive processes: only one process can occur during an attempted TC move to an occupied site.

In keeping with the literature (e.g. Stokes and Lauffenburger (1991); Anderson and Chaplain (1998); Tong and Yuan (2001)), in Chapter 2, we assumed that anastomosis occurred every time a TC encountered another cell (except when self-loops occur). We retain this implementation in this chapter, and note that this implies that either anastomosis or VE occurs (i.e only one process can occur due to mutual exclusivity).

Non-linear PDEs models describing multi-species exclusion processes have been derived using a mean-field approximation (see e.g. Simpson et al. (2009a); Dyson and Baker (2015)). Thus, we will continue to derive PDE models in this chapter using a mean-field approximation (as in Chapter 2). We note, however, that this methodology can lead to inconsistencies (discussed in this chapter), which we aim to circumvent in Chapter 4. This chapter contains material that is necessary to develop in order to motivate the methodologies used in Chapter 4. As such, there is some overlap between content in this chapter and the next/last chapter, which will be noted in the text.

In Fig. 3.1, we highlight the importance of VE, and its effect on network structure. TC VE prevents forward movement of TCs, and thus fewer TCs appear in the boxed area in Fig. 3.1b than in Fig. 3.1a. Additionally, Fig. 3.1c shows that EC VE renders TCs immobile at early times, so that fewer TCs branch and propagate towards the TAF source, producing networks that are sparser than those for which EC VE is inactive (see Figs. 3.1a and 3.1b).

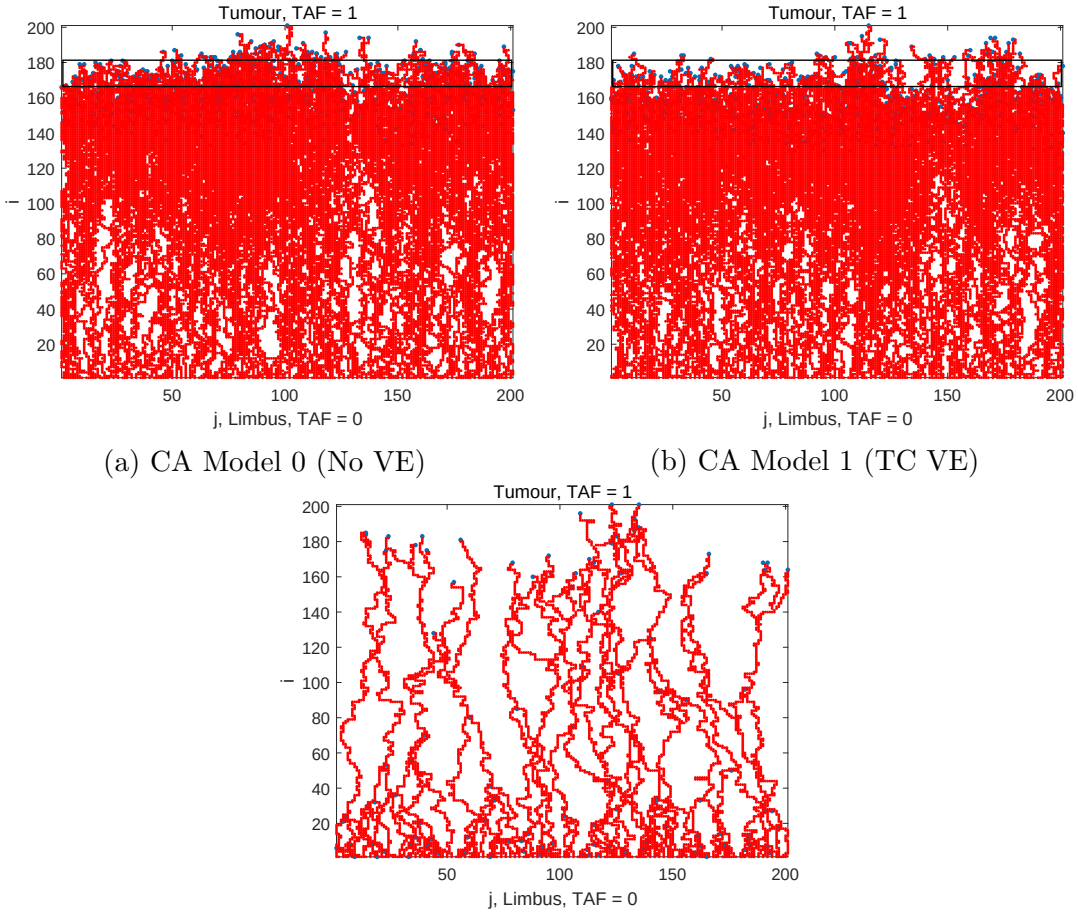

(a) CA Model 0 (No VE)

(b) CA Model 1 (TC VE)

(c) CA Model 2 (TC and EC VE)

Figure 3.1: Effects of VE on individual simulations from CA model. (a)-(c) $a_n = 0, a_e = 0, P_p = 2 \times 10^{-2}$. There are fewer TCs (blue dots) within the boxed area in (b) than in (a) as TC VE prevents TCs from moving forward. EC VE renders many TCs immobile in (c), and thus fewer TCs propagate towards the TAF source, resulting in a sparser network than in (a) and (b). Model 0 refers to a non-volume excluding model developed in Chapter 2. (b)-(c) Models 1 and 2 refer to the volume-excluding models that will be introduced in this chapter.

From the clear differences in network structure in Fig. 3.1, we deduce that the behaviour of TC and EC densities can change significantly when VE is included. It is this behaviour that we explore in this chapter and the next.

3.2 Modifications to CA Model

The reader is referred to Chapter 2, Section 2.2 for details of the CA model. Here, we outline the modifications required to incorporate VE into our CA model.

As in Chapter 2, the positions of TCs are updated using a random sequential update (see Section 2.2). Unlike in Chapter 2, a chosen TC at site (i, j) may move to sites within its von Neumann neighbourhood $(i \pm 1, j \pm 1)$, and may undergo exclusion or anastomosis (see later for details), based on the probabilities $P_{i,j}^{x\pm}$ and $P_{i,j}^{y\pm}$ (see equation (3.1) below). Furthermore, a chosen TC may branch, provided the target sites are unoccupied.

We reiterate the movement probabilities (using a linear TAF, $c_{i,j} = c_i$):

$$P_{i,j}^{x\pm} = \frac{1}{4} \pm \frac{k\left(c_{i+1} - c_{i-1}\right)}{4}, \quad P_{i,j}^{y\pm} = \frac{1}{4}. \tag{3.1}$$

Movement, tip-to-tip anastomosis and tip-to-spout anastomosis are described in Chapter 2, Section 2.2.1 and Figs. 2.2a and 2.2b. As in Chapter 2, we implement anastomosis using two binary variables, a_n and a_e. To be specific, if a TC attempts to move to a site that is occupied by a TC or EC, an anastomosis event occurs if $a_n = 1$ or $a_e = 1$, respectively. If $a_n = 0$ or $a_e = 0$, then the move is aborted (TC VE and EC VE, respectively). Thus, anastomosis and VE are linked in our model. In Chapter 2, we assumed that a TC must move to a site that is occupied by a TC (tip-to-tip anastomosis) or an EC (tip-to-sprout anastomosis) for an anastomosis event to occur. Naturally, therefore, if an anastomosis process is active, an exclusion process in which TC moves are aborted if target sites are occupied must be inactive. Thus, tip-to-tip anastomosis and TC VE and tip-to-sprout and EC VE are mutually exclusive events in our model.

As in the previous chapter, we prohibit self-loops (a TC anastomosing with an EC in its own sprout, i.e. an EC it has left behind) during tip-to-sprout anastomosis.

If a self-loop is prohibited, then the TC move is aborted (EC VE). This differs to the outcome in the previous chapter, where the TC move occurs without causing anastomosis.

Branching is described in Chapter 2, Section 2.2 (see Fig. 2.3). However, in this chapter, branching only occurs provided the target sites are unoccupied. Alternative branching methodologies (e.g. TCs sprout from ECs behind the leading TC) are outlined in Appendix C, Section C.4.

3.2.1 Two Cases

We will now define two cases of our CA model, one in which only TC VE and tip-to-tip anastomosis are active (named CA Model 1), and one in which TC VE, EC VE, tip-to-tip and tip-to-sprout anastomosis are active (named CA Model 2). If we only considered the multi-species VE case, we would not be able to discern how TC VE alone affects the CA model dynamics. Therefore, when considering both TC VE and EC VE, it would be unclear which species accounts for which VE effects at the macroscale (once CA simulations are averaged). CA Model 1 incorporates TC interaction with TCs only and, in this case, the ECs are essentially a history of where the TCs have been. CA Model 2 extends CA Model 1 by incorporating TC interaction with ECs through tip-to-sprout anastomosis and EC VE. By comparing these two models we are able to better understand how TC interaction with ECs affects the vessel network. As outlined in Chapter 1, many models of angiogenesis neglect this interaction by modelling the TC population only.

In CA Model 1, branching incorporates TC VE, while in CA Model 2, branching incorporates multi-species exclusion. Thus, in CA Model 1, a lattice site can be occupied by at most 1 TC, but can be occupied by multiple ECs. In CA Model 2, a lattice site can be occupied by at most one TC or one EC. The two model cases, and corresponding anastomosis variables, are given in Table 3.1.

Table 3.1: CA Model Cases

Model	a_n	a_e	Branching	Occupancy Restriction
Model 1	0 or 1	N/A	TC VE	1 TC, ECs ≥ 1
Model 2	0 or 1	0 or 1	TC, EC VE	1 TC or 1 EC

The initial conditions (TCs placed along $i = 0$ at alternating lattice sites) are the same as those implemented in Chapter 2 (see Section 2.2.3). As before, we implement no flux conditions on the domain boundaries (see Chapter 2, 2.2.1).

We outline the CA algorithm (see Algorithm 2), with modifications relating to CA Model 1 and 2 shown in bold text.

3.3 Derivation of Continuum Models

As before, we formulate DCEs that relate the average TC and EC occupancies at site (i, j) at time $\bar{K} + 1$, $n_{i,j}(\bar{K} + 1)$ and $e_{i,j}(\bar{K} + 1)$ (ensemble averages defined in equation (2.11)), respectively, to the average occupancies at site (i, j) at time $\bar{K}$ and the change in occupancy during a discrete time step. Defining $\delta n_{i,j}$ and $\delta e_{i,j}$ as follows

$$\delta n_{i,j} = n_{i,j}(\bar{K} + 1) - n_{i,j}(\bar{K}), \tag{3.2}$$

$$\delta e_{i,j} = e_{i,j}(\bar{K} + 1) - e_{i,j}(\bar{K}), \tag{3.3}$$

Algorithm 2 CA Model 1 and 2 algorithm for updating TCs after initialisation

While $\bar{K} \leq \bar{K}_{\text{final}}$

1. Choose $\bar{N}$ TCs at random with replacement

   Loop 1 (Movement): For 1 to $\bar{N}$

   (a) Choose a random number, $\bar{T} \in [0, 1]$

   (b) If $\bar{T} \leq P_m$, then the TC attempts to move as follows:

   - A random number $\bar{S} \in [0, 1]$ is chosen
   - The TC moves according to probabilities $P^{x\pm}, P^{y\pm}$ (determines target site)
   - **Model 1 and 2**: If target site is occupied by TCs and $a_n = 1$, then tip-to-tip anastomosis occurs, else TC move is aborted
   - **Model 2**: If target site is occupied by ECs and $a_e = 1$, then tip-to-sprout anastomosis occurs (no self-loops), else TC move is aborted. If a self-loop is prohibited, then the TC move is aborted.
   - If a TC move has occurred, then an EC is placed at the site of the TC before the move

   End Loop 1

2. Choose $\bar{N}$ TCs at random with replacement

   Loop 2 (Branching): For 1 to $\bar{N}$

   (a) Choose a random number, $\bar{R} \in [0, 1]$

   (b) If $\bar{R} \leq P_b = P_p c$, then branching occurs, **provided neighbouring sites are unoccupied by TCs (Model 1 and 2) or by ECs (Model 2)**

   End Loop 2

3. Increment time step: $\bar{K} = \bar{K} + 1$

End While Loop

for Model 1, the DCEs for the TC and EC population are, respectively,

$$
\begin{aligned}
&\delta n_{i,j} = \\
&P_m \Bigg(\underbrace{\left[P^{x+}_{i-1,j} n_{i-1,j} + P^{x-}_{i+1,j} n_{i+1,j} + P^{y+}_{i,j-1} n_{i,j-1} + P^{y-}_{i,j+1} n_{i,j+1}\right](1-n_{i,j})}_{\text{1.movement into } (i,j)} \\
&\underbrace{- \left[P^{x+}_{i,j}(1-(1-a_n)n_{i+1,j}) + P^{x-}_{i,j}(1-(1-a_n)n_{i-1,j})\right.}_{\text{2.movement out of } (i,j)} \\
&\underbrace{\left. + P^{y+}_{i,j}(1-(1-a_n)n_{i,j+1}) + P^{y-}_{i,j}(1-(1-a_n)n_{i,j-1})\right] n_{i,j}}_{\text{2.movement out of } (i,j)} \Bigg) \\
&\underbrace{+ P_p c_{i,j} \left[n_{i,j-1}(1-n_{i,j})(1-n_{i,j-2}) + n_{i,j+1}(1-n_{i,j})(1-n_{i,j+2})\right.}_{\text{3.branching into (i,j)}} \\
&\underbrace{\left. - n_{i,j}(1-n_{i,j+1})(1-n_{i,j-1})\right]}_{\text{4.branching out of (i,j)}}
\end{aligned}
\tag{3.4}
$$

and

$$
\begin{aligned}
\delta e_{i,j} \;=\; & P_m n_{i,j} \Bigg(\underbrace{\left(P^{x+}_{i,j}(1-(1-a_n)n_{i+1,j}) + P^{x-}_{i,j}(1-(1-a_n)n_{i-1,j})\right.}_{2'.\text{movement out of } (i,j)} \\
& \underbrace{\left. + P^{y+}_{i,j}(1-(1-a_n)n_{i,j+1}) + P^{y-}_{i,j}(1-(1-a_n)n_{i,j-1})\right)}_{2'.\text{movement out of } (i,j)} \\
& + \underbrace{a_n \left(P^{x+}_{i-1,j} n_{i-1,j} + P^{x-}_{i+1,j} n_{i+1,j} + P^{y+}_{i,j-1} n_{i,j-1} + P^{y-}_{i,j+1} n_{i,j+1}\right)}_{5'.\text{tip}-\text{to}-\text{tip anastomosis}} \Bigg) .
\end{aligned}
\tag{3.5}
$$

For Model 2, we have

$$
\begin{aligned}
&\delta n_{i,j} = \\
&P_m \Bigg(\underbrace{\left[P^{x+}_{i-1,j} n_{i-1,j} + P^{x-}_{i+1,j} n_{i+1,j} + P^{y+}_{i,j-1} n_{i,j-1} + P^{y-}_{i,j+1} n_{i,j+1}\right](1 - n_{i,j} - e_{i,j})}_{\text{1.movement into } (i,j)} \\
&\underbrace{- \left[P^{x+}_{i,j}(1 - (1-a_n) n_{i+1,j} - (1-a_e) e_{i+1,j})\right.}_{\text{2.movement out of } (i,j)} \\
&\underbrace{+ P^{x-}_{i,j}(1 - (1-a_n) n_{i-1,j} - (1-a_e) e_{i-1,j})}_{\text{2.movement out of } (i,j)} \\
&\underbrace{+ P^{y+}_{i,j}(1 - (1-a_n) n_{i,j+1} - (1-a_e) e_{i,j+1})}_{\text{2.movement out of } (i,j)} \\
&\underbrace{\left. + P^{y-}_{i,j}(1 - (1-a_n) n_{i,j-1} - (1-a_e) e_{i,j-1})\right] n_{i,j}}_{\text{2.movement out of } (i,j)} \Bigg) \\
&\underbrace{+ P_p c_{i,j} \left[n_{i,j-1}(1 - n_{i,j} - e_{i,j})(1 - n_{i,j-2} - e_{i,j-2})\right.}_{\text{3.branching into site (i,j)}} \\
&\underbrace{+ n_{i,j+1}(1 - n_{i,j} - e_{i,j})(1 - n_{i,j+2} - e_{i,j+2})}_{\text{3.branching into site (i,j)}} \\
&\underbrace{- n_{i,j}(1 - n_{i,j+1} - e_{i,j+1})(1 - n_{i,j-1} - e_{i,j-1})\right]}_{\text{4.branching out of site (i,j)}}, \qquad (3.6)
\end{aligned}
$$

and

$$\delta e_{i,j} =$$

$$P_m n_{i,j} \Bigg(\underbrace{P^{x+}_{i,j}(1-(1-a_n)n_{i+1,j}-(1-a_e)e_{i+1,j})}_{2'.\text{movement out of } (i,j)}$$

$$\underbrace{+P^{x-}_{i,j}(1-(1-a_n)n_{i-1,j}-(1-a_e)e_{i-1,j})}_{2'.\text{movement out of } (i,j)}$$

$$\underbrace{+P^{y+}_{i,j}(1-(1-a_n)n_{i,j+1}-(1-a_e)e_{i,j+1})}_{2'.\text{movement out of } (i,j)}$$

$$\underbrace{+P^{y-}_{i,j}(1-(1-a_n)n_{i,j-1}-(1-a_e)e_{i,j-1})n_{i,j}}_{2'.\text{movement out of } (i,j)}$$

$$\underbrace{+a_n\left[P^{x+}_{i-1,j}n_{i-1,j}+P^{x-}_{i+1,j}n_{i+1,j}+P^{y+}_{i,j-1}n_{i,j-1}+P^{y-}_{i,j+1}n_{i,j+1}\right]}_{5'.\text{tip-to-tip anastomosis}} \Bigg), \qquad (3.7)$$

respectively.

When anastomosis is inactive ($a_n, a_e = 0$), the $(1 - n_{i,j})$ and $(1 - n_{i,j} - e_{i,j})$ represent VE from TCs (Model 1) and TCs or ECs (Model 2), respectively. When anastomosis is active ($a_n, a_e = 1$), the terms $(1 - n_{i,j})$ and $(1 - n_{i,j} - e_{i,j})$ remain, as they represent penalty terms due to anastomosis (as in Chapter 2, see Section 2.3). Thus, the terms that represent movement into a site are the same whether tip-to-tip (tip-to-sprout) anastomosis is active or inactive.

Anastomosis and VE affect the movement of TCs out of a site differently. If anastomosis is inactive, then TCs can only move out of a site if the neighbouring sites are vacant (see terms 2 in equations (3.4) and (3.6)). If anastomosis is active ($a_n, a_e = 1$), then TCs are always allowed to move out of a site (no aborted moves), with the outcome depending on the occupancy of the target site. Thus, a TC can only move into a site and remain a TC if the target site is vacant.

Branching always incorporates VE, and in Model 1, branching is allowed if neighbouring sites are unoccupied by TCs (see term 3 of equation (3.4)), and in Model 2,

branching is allowed if neighbouring sites are vacant i.e. no TCs or ECs (see term 3 of equation (3.6)). The branching terms in equations (3.4) and (3.6) represent branching into the site (i, j) from a TC located at $(i, j-1)$ or $(i, j+1)$ (source terms), and the loss of a TC from site (i, j) if it branches into neighbouring sites (sink term).

As before, ECs are created when a TC moves out of a site and via tip-to-tip anastomosis (see equations (3.5) and (3.7)). These source terms are the positive counterparts of sink terms in equations (3.4) and (3.6), which now incorporate VE.

3.3.1 Column-Averaged DCEs

In the previous chapter, we derived one-dimensional PDEs from two-dimensional PDEs. In this chapter, we will derive a one-dimensional PDE directly by formulating the DCEs in terms of column averages. For the motility mechanism, we could either directly write down the terms that affect column averages, or multiply both sides of equations (3.4)-(3.7) by $1/R$ and sum over the column index j, and apply a mean-field approximation for column averages (see Simpson et al. (2009a)). The reader is directed to Appendix C where these approximations are explained in detail. We note that this approach is appropriate here as the transition probabilities, $P_{i,j}^{x\pm}, P_{i,j}^{y\pm}$, do not depend on j (see equations (3.1)). Under these approximations, the column-averaged DCEs for the TC and EC densities in Model 1 are

$$\begin{aligned}\delta N_i &= P_m \Bigg(\underbrace{\left(P_{i-1}^{x+}N_{i-1} + P_{i+1}^{x-}N_{i+1}\right)\left(1-(1-a_n)N_i\right)}_{\text{1.movement into } i} \\ &\quad \underbrace{-N_i\left(P_i^{x+}(1-(1-a_n)N_{i+1}) + P_i^{x-}(1-(1-a_n)N_{i-1})\right)}_{\text{2.movement out of } i} \\ &\quad \underbrace{-a_n\left(P_{i-1}^{x+}N_{i-1} + P_{i+1}^{x-}N_{i+1} + P_i^{y+}N_i + P_i^{y-}N_i\right)}_{\text{3.tip}-\text{to}-\text{tip anastomosis}} \Bigg) \\ &\quad \underbrace{+P_p c_i\left(N_i(1-N_i)(1-N_i)\right)}_{\text{4.branching}}, \end{aligned} \tag{3.8}$$

and

$$\begin{aligned}\delta E_i &= P_m N_i \Bigg(\underbrace{P_i^{x+}(1-(1-a_n)N_{i+1}) + P_i^{x-}(1-(1-a_n)N_{i-1})}_{2'.\text{movement out of } i} \\ &\quad \underbrace{+P_i^{y+}(1-(1-a_n)N_i) + P_i^{y-}(1-(1-a_n)N_i)}_{2''.\text{movement out of } j \text{ within a column}} \\ &\quad \underbrace{+a_n\left(P_{i-1}^{x+}N_{i-1} + P_{i+1}^{x-}N_{i+1} + P_i^{y+}N_i + P_i^{y-}N_i\right)}_{3'.\text{tip}-\text{to}-\text{tip anastomosis}} \Bigg). \end{aligned} \tag{3.9}$$

For Model 2, we have

$$\begin{aligned}\delta N_i &= P_m \Bigg(\underbrace{\left[P_{i-1}^{x+}N_{i-1} + P_{i+1}^{x-}N_{i+1}\right](1-(1-a_n)N_i-(1-a_e)E_i)}_{\text{1.movement into } i} \\ &\quad \underbrace{-\left[P_i^{x+}(1-(1-a_n)N_{i+1}-(1-a_e)E_{i+1})\right.}_{\text{2.movement out of } i} \\ &\quad \underbrace{\left.+P_i^{x-}(1-(1-a_n)N_{i-1}-(1-a_e)E_{i-1})\right]N_i}_{\text{2.movement out of } i} \\ &\quad \underbrace{-a_n N_i\left[P_{i-1}^{x+}N_{i-1} + P_{i+1}^{x-}N_{i+1} + P_i^{y+}N_i + P_i^{y-}N_i\right]}_{\text{3.tip-to-tip anastomosis}} \\ &\quad \underbrace{-a_e E_i\left[P_{i-1}^{x+}N_{i-1} + P_{i+1}^{x-}N_{i+1} + P_i^{y+}N_i + P_i^{y-}N_i\right]}_{\text{4.tip-to-sprout anastomosis}}\Bigg) \\ &\quad + \underbrace{P_p c_i\left[N_i(1-N_i-E_i)(1-N_i-E_i)\right]}_{\text{5.branching}}, \end{aligned} \tag{3.10}$$

and

$$\begin{aligned}\delta E_i &= P_m N_i \Bigg(\underbrace{P_i^{x+}(1-(1-a_n)N_{i+1}-(1-a_e)E_{i+1})}_{1'.\text{movement out of } i} \\ &\quad \underbrace{+P_i^{x-}(1-(1-a_n)N_{i-1}-(1-a_e)E_{i-1})}_{2'.\text{movement out of } i} \\ &\quad + \underbrace{P_i^{y+}(1-(1-a_n)N_i-(1-a_e)E_i) + P_i^{y-}(1-(1-a_n)N_i-(1-a_e)E_i)}_{2''.\text{movement out of } j \text{ within a column}} \\ &\quad \underbrace{+a_n\left[P_{i-1}^{x+}N_{i-1} + P_{i+1}^{x-}N_{i+1} + P_i^{y+}N_i + P_i^{y-}N_i\right]}_{3'.\text{tip-to-tip anastomosis}}\Bigg), \end{aligned} \tag{3.11}$$

respectively. When considering column averages, it is clear that movements within a column (in y) excluding anastomosis do not affect the TC density (see equations (3.8) and (3.10)). For anastomosis, movements in both directions (x and y) affect the TC density through TC annihilation and, therefore, movements in both directions are accounted for. The branching terms incorporate changes in TC density in the y-

direction only, and the form of the term is intuitive (derived by summing the branching terms in equations (4.5) over j and applying a mean-field approximation for column averages).

ECs are created once a TC leaves a site or through tip-to-tip anastomosis. Thus, in equations (3.9) and (3.11), TC movements in the y-direction (i.e. within a column) have been retained, and the tip-to-tip anastomosis term is the positive counterpart of the term in equations (3.8) and (3.10), respectively.

As in Chapter 2, we relate the DCEs to PDEs by expanding all dependent variables in equations (3.8)-(3.11) in Taylor series about the site i. We set $x_i \to x, N_i(\bar{K}) \to N(x,t), E_i(\bar{K}) \to E(x,t)$, divide the resulting expressions by τ ($t = \bar{K}\tau$, τ relates the discrete and continuum time scales), and take the limit as $\tau \to 0$, neglecting terms of $O(h^4)$ and higher. In this way, we deduce that for Model 1, $N(x,t)$ and $E(x,t)$, satisfy the following PDEs:

$$\begin{aligned}
\frac{\partial N}{\partial t} &= (1-a_nN)\left(D\nabla^2 N - \chi\nabla\cdot[N(1-(1-a_n)N)\nabla c]\right) - \mu a_n N^2 \\
&\quad +\lambda c N(1-N)^2, \qquad (3.12)\\
\frac{\partial E}{\partial t} &= \mu N(1-(1-a_n)N + a_nN) - N\left([1-2a_n]D\nabla^2 N + \chi\left[\nabla c\cdot\nabla((1-a_n)N)\right.\right. \\
&\quad \left.\left. +a_n\nabla\cdot(N\nabla c)\right]\right), \qquad (3.13)
\end{aligned}$$

while for Model 2, they satisfy

$$\begin{aligned}
\frac{\partial N}{\partial t} &= D\left([1-N-E]\nabla^2 N + N\left[(1-a_n)\nabla^2 N + (1-a_e)\nabla^2 E\right]\right) \\
&\quad -\chi\left([1-a_nN-a_eE]\nabla\cdot[N(1-(1-a_n)N-(1-a_e)E)\nabla c]\right) \\
&\quad -a_n(1-a_na_e)\chi\left[(1-N)\nabla\cdot\nabla(NE\nabla c) - E\nabla\cdot(N\nabla c) - N\nabla E\cdot\nabla c\right] \\
&\quad -a_e(1-a_na_e)\chi\left[(1-E)\nabla\cdot(N^2\nabla c) - N\nabla\cdot(N\nabla c) - N\nabla N\cdot\nabla c\right] \\
&\quad -\mu\left(a_nN^2 + a_eNE\right) + \lambda c N(1-N-a_eE)^2, \qquad (3.14)
\end{aligned}$$

and

$$\begin{aligned}\frac{\partial E}{\partial t} &= \mu N\left(1-(1-a_n)N-(1-a_e)E+a_nN\right)\\ &\quad -ND\left((1-a_n)\nabla^2N-a_n\nabla^2N+(1-a_e)\nabla^2E\right)\\ &\quad -\chi N\left(\nabla c\cdot\nabla[(1-a_n)N+(1-a_e)E]+a_n\nabla\cdot[N\nabla c]\right). \qquad (3.15)\end{aligned}$$

The expressions for D, χ, λ and μ coincide with those found in the previous chapter (see equations (2.24) and (2.23)). We note that for the Model 1 PDEs, $N \leq 1$, while for the Model 2 PDEs, $N + E \leq 1$. These are the continuum analogues of the occupancy restrictions in the discrete model. As in Chapter 2, we use column-averaged CA simulation results at some later discrete time step to initialise the PDEs (see equation (2.35) in Section 2.3.1 in Chapter 2)

3.4 Structure of Continuum Models

To better explain the form of the PDEs and meaning of terms, we explicitly consider all continuum models for all cases (along with boundary conditions).

3.4.1 Model 1 PDEs

In Model 1, there is no interaction between TCs and ECs, and TCs interact with other TCs via tip-to-tip anastomosis ($a_n = 1$) or TC VE ($a_n = 0$). With $a_n = 0$, we have

$$\frac{\partial N}{\partial t} = D\nabla^2N-\chi\nabla\cdot(N(1-N)\nabla c)+\lambda cN(1-N)^2, \qquad (3.16)$$

$$\frac{\partial E}{\partial t} = \mu N(1-N)-DN\nabla^2N-N\chi\nabla c\cdot\nabla N, \qquad (3.17)$$

$$D\nabla N-\chi N(1-N)\nabla c\,|_{x=0,1}=0, \qquad (3.18)$$

and for $a_n = 1$ (active tip-to-tip anastomosis), we have

$$\frac{\partial N}{\partial t} = (1-N)\left(D\nabla^2 N - \chi\nabla\cdot(N\nabla c)\right) - \mu N^2 + \lambda c N(1-N)^2, \quad (3.19)$$

$$\frac{\partial E}{\partial t} = \mu N(1+N) + DN\nabla^2 N - \chi N\nabla\cdot(N\nabla c)\,, \quad (3.20)$$

$$D\nabla N - \chi N\nabla c\,|_{x=0,1} = 0. \quad (3.21)$$

As in Chapter 2, we impose no flux boundary conditions (see equations (3.18) and (3.21), different forms depending on whether TC VE is active or inactive).

Equation (3.16) for the TC density when TC VE is active, is consistent with results for biased random walks, where the diffusion term is linear, but the chemotaxis term is non-linear (Simpson et al., 2010a, 2009a; Penington et al., 2011; Liggett, 1999). We note also that equation (3.16) is similar to a viscous Burgers' equation; we will comment on this further in Chapter 4. Equation (3.19) for TC density when tip-to-tip anastomosis is active is the same as that derived in Chapter 2 for a non-volume excluding model barring the branching term i.e motility only. This is expected; when an anastomosis process is active, the corresponding VE process is inactive. As in Chapter 2, the non-linear sink term $-\mu N^2$ and the $(1-N)$ term pre-multiplying the diffusion and chemotaxis terms arise from tip-to-tip anastomosis. The non-linear branching term in Model 1 incorporates TC VE and agrees with a result derived by Simpson et al. (2010a), where the macroscopic description depends on the separation distance, which in this case is 1; TCs branch into vacant neighbouring sites. To enforce $N \leq 1$, the branching rate, λ should be set to zero if $N = 1$. (We have conducted an analysis (see Appendix F, Section F.4) to illustrate that the Model 1 PDEs will remain well-posed.)

As found in Chapter 2, ECs are created either via TC motility incorporating VE or through TC motility and tip-to-tip anastomosis. In equations (3.17) and (3.20), μ

can be interpreted as the TC motility rate and, in effect, this term is a proliferation term. This is biologically realistic as ECs proliferate behind the leading TCs (see Chapter 1 for biological overview of angiogenesis). When tip-to-tip anastomosis is active ($a_n = 1$), equation (3.20) is the same as that found in Chapter 2. When tip-to-tip anastomosis is inactive ($a_n = 0$), the EC density (equation (3.17)) is proportional to the sum of a source term incorporating TC VE and negative flux terms that account for TC VE. Fewer ECs are produced when TC VE is active, as opposed to a non-volume excluding model (see Chapter 2, Section 2.3.1).

A discussion of the steady-state behaviour of equations (3.16)-(3.21), and similarity to Burgers equation, is presented in Appendix F, Sections F.1, F.2 and F.3.

3.4.2 Model 2 PDEs

For Model 2, we consider four cases: $(a_n, a_e) = (0,0)$, $(1,0)$, $(0,1)$ and $(1,1)$. For active anastomosis ($a_n = 1, a_e = 1$), the equations for the TC and EC density are

$$\frac{\partial N}{\partial t} = (1-N-E)\left(D\nabla^2 N - \chi\nabla\cdot(N\nabla c)\right) - \mu NE$$
$$-\mu N^2 + \lambda c N(1-N-E)^2, \tag{3.22}$$
$$\frac{\partial E}{\partial t} = \mu N(1+N) + DN\nabla^2 N - \chi N\nabla\cdot(N\nabla c), \tag{3.23}$$
$$D\nabla N - \chi N\nabla c\,|_{x=0,1} = 0, \tag{3.24}$$

respectively, whereas for active tip-to-sprout anastomosis and TC VE ($a_n = 0, a_e = 1$), we have

$$\frac{\partial N}{\partial t} = D(1-E)\nabla^2 N - \chi(1-N-E)\nabla\cdot(N\nabla c) + \chi N\nabla N\cdot\nabla c$$
$$-\mu NE + \lambda c N(1-N-E)^2, \tag{3.25}$$
$$\frac{\partial E}{\partial t} = \mu N(1-N) - DN\nabla^2 N - \chi N\nabla c\cdot\nabla N, \tag{3.26}$$
$$D\nabla N - \chi N(1-N)\nabla c\,|_{x=0,1} = 0. \tag{3.27}$$

Once again, we impose no flux boundary conditions on equations (3.22) and (3.25). When both anastomosis processes are active in Model 2, equation (3.22), the model (excluding branching) reduces to the non-volume excluding model derived in Chapter 2 (see Section 2.3.1). This is expected, as active anastomosis implies VE is inactive.

We note that equation (3.25) ($a_n = 0, a_e = 1$), is a combination of equations (3.22) and (3.16): tip-to-sprout anastomosis produces the non-linear diffusion term $D(1 - E)\nabla^2 N$ and a non-linear contribution to the chemotactic term $\chi E \nabla \cdot (N \nabla c)$, while TC VE introduces an additional non-linear chemotactic term $-\chi \nabla (N(1 - N)\nabla c)$. This is easily observed if $-\chi(1 - N - E)\nabla(N\nabla c) + \chi \nabla N \nabla N \cdot \nabla c$ is rewritten as $-\chi \nabla \cdot (N(1 - N)\nabla c) + \chi E \nabla \cdot (N \nabla c)$. The sink term in equation (3.26) arises from tip-to-sprout anastomosis. The branching term in Model 2 is an extension of the term in Model 1 to include VE from the ECs. To adhere to density restrictions in Model 2, $N + E \leq 1$, the branching rate, λ should be set to zero if $N + E = 1$. We have conducted an analysis (see Appendix F, Section F.4) to illustrate that equations (3.22)-(3.27) will remain well-posed. Recall that in the previous chapter, we were unable to use the PDE model derived when tip-to-sprout anastomosis was active whilst tip-to-tip anastomosis was inactive, as this could potentially lead to ill-posedness. We have resolved this issue in the Model 2 PDEs ($a_n = 0, a_e = 1$) by incorporating TC VE explicitly in the motility and branching terms.

As TC motility, TC VE and tip-to-tip anastomosis are the only processes that affect EC density, equations (3.23) and (3.27) are identical to equations (3.17) and (3.20). As in Chapter 2, we have not explicitly accounted for prohibited self-loops (and subsequent aborted moves) during tip-to-sprout anastomosis in the PDE derivation.

For inactive anastomosis ($a_n = a_e = 0$), the equations for the TC and EC densities

are

$$\begin{aligned}\frac{\partial N}{\partial t} &= D(1-N-E)\nabla^2 N + DN\nabla^2(N+E) - \chi\nabla\cdot(N(1-N-E)\nabla c) \\ &\quad +\lambda c N(1-N-E)^2, \qquad (3.28)\\ \frac{\partial E}{\partial t} &= \mu N(1-N-E) - DN(\nabla^2 N + \nabla^2 E) - \chi N\nabla c\cdot\nabla(N+E), \qquad (3.29)\end{aligned}$$

respectively, whereas for active tip-to-tip anastomosis and EC VE ($a_n = 1, a_e = 0$), they are

$$\begin{aligned}\frac{\partial N}{\partial t} &= D(1-N-E)\nabla^2 N + DN\nabla^2 E - \chi(1-N-E)\nabla\cdot(N\nabla c) + \chi N\nabla E\cdot\nabla c \\ &\quad -\mu N^2 + \lambda N(1-N-E)^2, \qquad (3.30)\\ \frac{\partial E}{\partial t} &= \mu N(1+N-E) + DN(\nabla^2 N - \nabla^2 E) - \chi N\nabla\cdot(N\nabla c) - \chi N\nabla E\cdot\nabla c. \\ &\qquad (3.31)\end{aligned}$$

Equation (3.28) agrees with that of Simpson et al. (2009a) for VE from two species, and can be interpreted in the sense that the diffusive and chemotactic fluxes are reduced by exclusion from both species. Alternatively, we can rewrite the first two terms as $D(1-E)\nabla^2 N + DN\nabla^2 E$, which can be interpreted as the diffusive flux being reduced by exclusion from the ECs only, and an additional advection term representing the flux of TCs down the gradient of ECs. This differs from Model 1 (single species exclusion) in which the diffusion term is linear (see equation (3.16)).

Equation (3.30) for the TC density when tip-to-tip anastomosis and EC VE is active is an intermediate case between equations (3.28) and (3.22). EC VE introduces the non-linear diffusion terms (as in equation (3.28)), while tip-to-tip anastomosis introduces a non-linear chemotaxis term $\chi N\nabla\cdot(N\nabla c)$ and EC VE produces the non-linear chemotactic term $-\chi\nabla\cdot(N(1-E)\nabla c)$. This is easily observed as $-\chi(1-N-E)\nabla\cdot(N\nabla c) + \chi N\nabla E\cdot\nabla c$ can be written as $-\chi\nabla\cdot(N(1-E)\nabla c) + \chi N\nabla(N\nabla c)$.

We note that equations (3.29) and (3.31) include backward diffusion terms. We note also that equations (3.29) and (3.31) for EC density are the natural extension of equations (3.17) and (3.20) in Model 1, where each flux term and the source term now includes exclusion from the ECs. These generalisations from Model 1 to Model 2 are indicated in Table 3.2 (resulting in backwards heat equations).

Table 3.2: Generalisation of Terms from Model 1 to 2

TCs	Chemotaxis	Branching
Model 1 (equation (3.16))	$\chi\nabla\cdot(N(1-N)\nabla c)$	$\lambda N(1-N)^2$
Model 2 (equation (3.28))	$\chi\nabla\cdot(N(1-N-E)\nabla c)$	$\lambda N(1-N-E)^2$
Model 1 (equation (3.19))	$\chi(1-N)\nabla\cdot(N\nabla c)$	$\lambda N(1-N)^2$
Model 2 (equation (3.30))	$\chi(1-N-E)\nabla\cdot(N\nabla c)$	$\lambda N(1-N-E)^2$
ECs	**Source term**	**Motility**
Model 1 (equation (3.17))	$\mu N(1-N)$	$-DN\nabla^2 N$ $-\chi N\nabla c\cdot\nabla N$
Model 2 (equation (3.29))	$\mu N(1-N-E)$	$-DN(\nabla^2 N+\nabla^2 E)$ $-\chi N\nabla c\cdot\nabla(N+E)$
Model 1 (equation (3.20))	$\mu N(1+N)$	$DN\nabla^2 N$ $-\chi N\nabla\cdot(N\nabla c)$
Model 2 (equation (3.31))	$\mu N(1+N-E)$	$DN(\nabla^2 N-\nabla^2 E)$ $-\chi N\nabla\cdot(N\nabla c)$ $-\chi N\nabla c\cdot\nabla E$

We postulate that correlations arise when EC VE is active since migrating TCs leave behind ECs. In other words, TCs are excluded by ECs, which they generate, causing the mean-field approximation to break down. A similar result was reported in Chapter 2 when tip-to-sprout anastomosis was active. There the equations were amenable to fitting so the parameter, a_e, which controls tip-to-sprout anastomosis, could be estimated. By contrast, in this case, the mean-field approximation has led to a backwards heat equation. This example highlights how this methodology can break down when added complexity is incorporated on the microscale.

The reader is directed to Appendix C for a discussion of our attempts to formulate a well-posed model. In all cases, the resulting PDEs fail to replicate the averaged CA

Table 3.3: PDE Model Cases, and corresponding CA model parameters in Model 2

Model	a_n	PDE $\tilde{a}_e$/CA a_e	Branching
1 (Non-EC interacting)	0 or 1	N/A	$\lambda cN(1-N)^2$
2 (EC interacting)	0 or 1	$(0,1]$ (Estimated)/ 1	$\lambda cN(1-N-E)^2$

simulation results. In the next chapter, we will devise a methodology to account for EC VE and produce a well-posed continuum model.

In the next section, we compare our well-posed one-dimensional PDE models to averaged CA simulation results. The cases we consider are given in Table 3.3. For Model 1, we consider equations (3.16)-(3.21) with $a_n = 0, 1$. For Model 2, we consider, equations (3.22)-(3.27), for which tip-to-sprout anastomosis (prohibiting self-loops) is active ($a_e = 1$) and tip-to-tip anastomosis is either active or inactive ($a_n = 1$ or 0). Recall that we modified our CA model such that a TC move is aborted when we prohibit a self-loop, representing an EC VE effect. As we are departing from our systematic PDE derivation by prohibiting self-loops (recall that we cannot keep track of which ECs belong to which sprout, see previous Chapter 2, Section 2.5), we estimate the parameter a_e, now renamed to $\tilde{a}_e$ in the Model 2 PDEs, by fitting the PDE models to averaged CA simulation results.

3.5 One-Dimensional Comparisons

The reader is referred to Chapter 2, Section 2.4.1 for an explanation and derivation of parameters given in Table 3.4. The parameter, a_n (either 1 or 0) controlling tip-to-tip anastomosis, must be set in the CA and PDE models. The parameter, a_e, controlling tip-to-sprout anastomosis, must be set in the CA model to either 1 or 0. In the PDE model, this parameter, renamed $\tilde{a}_e$, is estimated by fitting the PDE models to the averaged CA simulations results when $a_e = 1$ (see Table 3.3).

We use the methodology as outlined in Chapter 2 to solve equations (3.16)-(3.21) and (3.22)-(3.27) numerically and estimate $\tilde{a}_e$ (see Sections 2.4.2 and 2.5.1).

Table 3.4: CA and DCE-derived PDE model parameters

R	P_m	P_p	h	τ	k	$P_{x\pm}$	$P_{y\pm}$	D	χ	λ	μ	t_{IC}
200	1	10^{-3}	$\frac{1}{200}$	$\frac{1}{160}$	100	$\frac{1}{2}, 0$	$\frac{1}{4}$	10^{-3}	0.4	0.16	160	0.2

The solutions to the PDEs are compared against column-averaged CA simulation results (see equations (2.12) and (2.13)), where the occupancy of lattice sites has been averaged over $R = 200$ columns and over $M = 200$ realizations in all cases except where EC VE is explicitly incorporated in the motility mechanism, in which case, $M = 400$ (we perform additional realizations here to obtain a smoother distribution).

3.5.1 Individual CA Simulations and Comparisons

Fig. 3.2 compares the TC and EC density distribution when tip-to-tip anastomosis is inactive ($a_n = 0$, active TC VE) in Models 1 and 2. Tip-to-sprout anastomosis has a marked effect on the TC and EC density profiles. It annihilates TCs, so a less dense vessel network forms (compare Figs. 3.2b, 3.2d, 3.2f to 3.2a, 3.2c, 3.2e). EC VE (aborted TC move during prohibited self-loops) lowers the cell densities further, as aborted TC moves reduce the number of ECs created. The solutions to equations (3.16)-(3.18) and equations (3.25)-(3.27) agree well with the averaged CA simulation results. We consider TC moves without tip-to-sprout anastomosis occurring when prohibiting self-loops in Appendix C.

We also note that our results for Model 1 with TC VE in the motility mechanism (see Figs. 3.2c, 3.2e) are essentially the same as in Chapter 2 for the non-volume excluding model (see Figs. 2.5a and 2.5b). This occurs for two reasons. Firstly, the TC densities we consider are low (as a result of the initial condition, and the low branching rate). Secondly, TCs mainly interact with each other laterally (they are unable to move in negative x, as $P^{x-} = 0$ (see Table 3.4), and are clustered together at the leading edge of the front) and therefore, TC VE is more pronounced within a column. As we consider low density column-averaged results only, the distribution of

TCs as a result of TC VE and the effects of TC VE are not significant. In the next chapter, we consider cases for which TC VE effects are non-negligible.

In Fig. 3.3, tip-to-tip anastomosis is active. TC annihilation via tip-to-tip anastomosis results in fewer TCs propagating towards the TAF source and, thus, the EC density is lower (fewer ECs are created) than when TC VE is active (compare TC densities in Figs. 3.3 and 3.2). Tip-to-sprout anastomosis further annihilates TCs, and thus the TC and EC densities are lower in Figs. 3.3d-3.3f, than in Figs. 3.3c and 3.3e. Additionally, tip-to-sprout anastomosis does not annihilate TCs to the same extent as in Fig. 3.2, as there are fewer TCs (annihilated by tip-to-tip anastomosis) to interact with ECs. Our results indicate that interactions with ECs, through tip-to-sprout anastomosis and EC VE (see Figs. 3.2 and 3.3) are important, as they affect the distributions of the TC and EC densities, producing a less dense vessel network. We also note that the solutions to equations (3.19)-(3.21) and equations (3.22)-(3.24) agree well with the averaged CA simulation results.

Finally, we consider the averaged CA simulation results (see Fig. 3.4) to determine the population behaviour for cases for which we were unable to derive well-posed PDEs: active EC VE (($a_e = 0$) in the CA model, tip-to-sprout anastomosis inactive). Fig. 3.4 shows that the TC density drops off rapidly when EC VE is active. This is because TCs cannot move as their neighbouring sites are occupied by other cells, mainly ECs. TCs become 'stuck', creating long tails in the TC density. As a result, few TCs propagate towards the TAF source, and the vessel network (EC density) is considerably less dense than, and the density distribution is markedly different to, the cases considered in Figs. 3.2 and 3.3. Our simulations indicate that EC VE significantly impacts the vessel network as fewer TCs can move freely, and thus fewer vessels form. It is possible that, in practice, Delta-Notch signalling will dynamically select TCs and ECs so TCs are not rendered immobile.

Since we used a low branching rate ($\lambda = 0.16$) in all simulations, the TC and

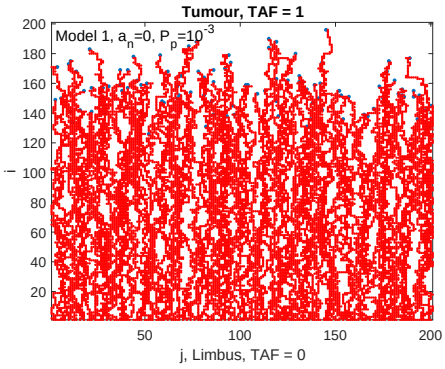

(a) Model 1, $a_n = 0$, a_e N/A

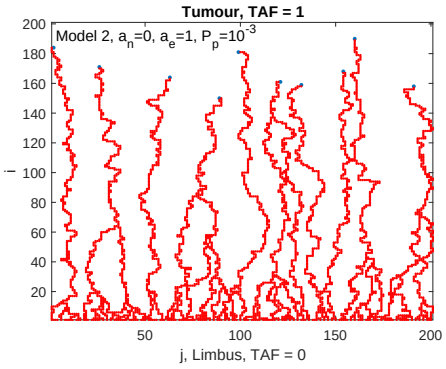

(b) Model 2, $a_n = 0$, $a_e = 1$

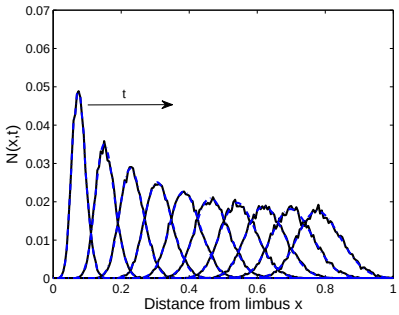

(c) Model 1, $a_n = 0$, a_e N/A

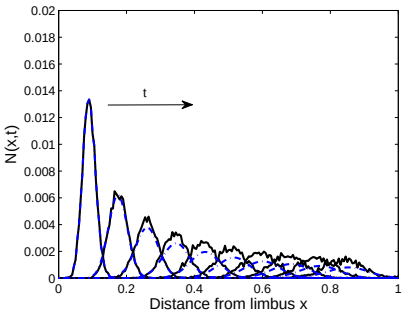

(d) Model 2, $a_n = 0$, $\tilde{a}_e = 0.1307$

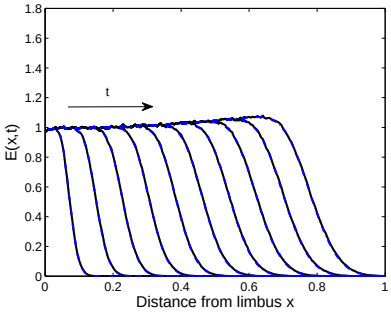

(e) Model 1, $a_n = 0$, a_e N/A

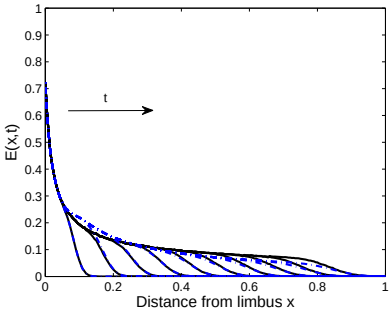

(f) Model 2, $a_n = 0$, $\tilde{a}_e = 0.1307$

Figure 3.2: Effect of TC VE on network morphology and population behaviour. TCs migrate via diffusion and chemotaxis incorporating TC VE ($a_n = 0$) towards the TAF source at $x = 1$, leaving behind a trail of ECs. CA Model 1: (a) individual simulation, (c) TC density (e) EC density. CA Model 2: (b) individual simulation, (d) TC density (f) EC density. (b), (d), (f) Tip-to-sprout anastomosis excluding self-loops with aborted TC moves (EC VE). Comparing (a), (c), (e) to (b), (d), (f), it is clear that TC interaction with ECs through tip-to-sprout anastomosis results in a loss of TCs, and therefore a less dense vessel network (EC density), and a marked change in the EC density profile. (c)-(f) Column-averaged CA simulation results (black solid curve) are shown from $t = 0.2, 0.4, \ldots, 2.0$ (arrow shows direction of time). The CA simulation results at $t_{IC} = 0.2$ are used as the initial conditions in the DCE-derived PDE models (blue dashed-dot curve) (equations (3.16)-(3.18) (Model 1 PDEs) and equations (3.25)-(3.27) (Model 2 PDEs)), which agree with the averaged CA simulations. Discrete and PDE model parameters are given in Table 3.4 with the parameters controlling tip-to-sprout anastomosis as follows: (d), (f) $\tilde{a_e} = 0.1307 \pm 0.0012$. (a), (b): red = ECs, blue = TCs.

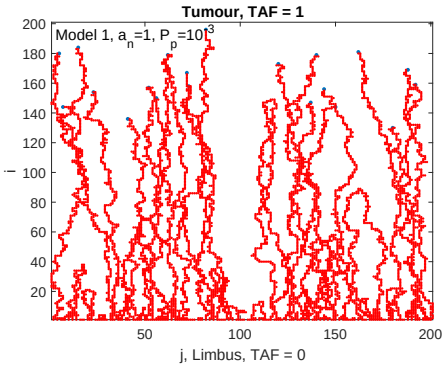

(a) Model 1, $a_n = 1$, a_e N/A

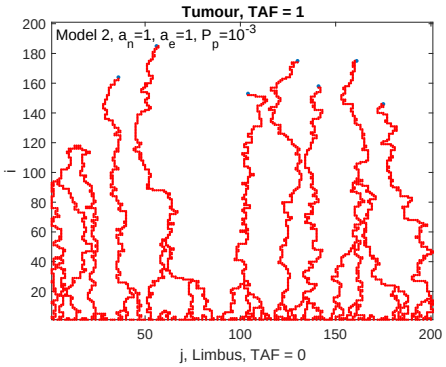

(b) Model 2, $a_n = 1$, $a_e = 1$

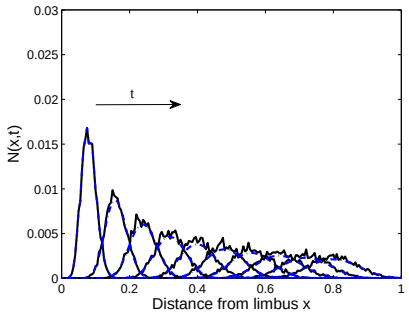

(c) Model 1, $a_n = 1$, a_e N/A

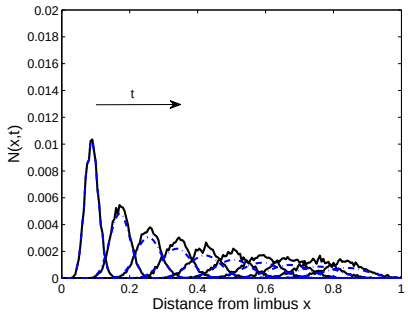

(d) Model 2, $a_n = 1$, $\tilde{a}_e = 0.0825$

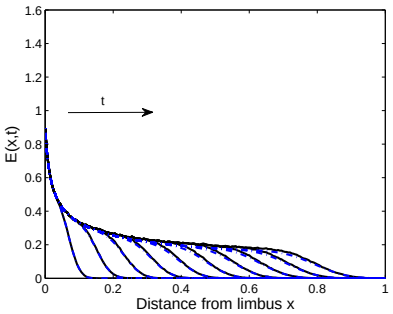

(e) Model 1, $a_n = 1$, a_e N/A

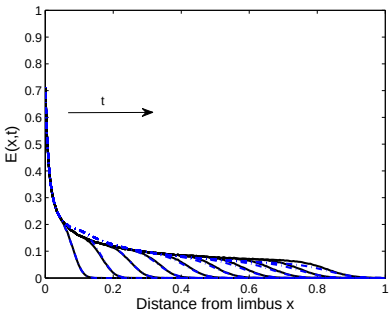

(f) Model 2, $a_n = 1$, $\tilde{a}_e = 0.0825$

Figure 3.3: Effect of tip-to-tip anastomosis on network morphology and population behaviour. Tip-to-tip anastomosis ($a_n = 1$) annihilates TCs, and thus the TC density is lower than in Fig. 3.2. As a result, the EC densities are also lower when tip-to-tip anastomosis is active. Model 1: (a) individual simulation, (c) TC density, (e) EC density. Model 2: (b) individual simulation, (d) TC density, (f) EC density. (b), (d), (f) Tip-to-sprout anastomosis excluding self-loops with aborted TC moves (EC VE). Tip-to-sprout anastomosis (b), (d), (f), results in a lower TC density, and lower EC density, and overall a less dense vessel network. (c)-(f) Column-averaged CA simulation results (black solid curve) are shown from $t = 0.2, 0.4, \ldots, 2.0$ (arrow shows direction of increasing time). The CA simulation results at $t_{IC} = 0.2$ are used as the initial conditions in the DCE-derived PDE models (blue dashed-dot curve) (equations (3.19)-(3.21) (Model 1 PDEs) and equations (3.22)-(3.24) (Model 2 PDEs)) with the PDE solutions shown from $t = 0.4 - 2$. Discrete and PDE model parameters are given in Table 3.4 with the parameters controlling tip-to-sprout anastomosis as follows: (d), (f) $\tilde{a_e} = 0.0825 \pm 0.0010$. (a), (b): red = ECs, blue = TCs.

EC densities are low and, thus, VE effects arising from branching are minimal (see Figs. 3.2-3.4). Consequently, branching is omitted from the discussions above.

3.6 Discussion

We have developed two-dimensional CA models of angiogenesis based on the snail-trail process in the corneal assay accounting for the volume of TCs and ECs. Using the transition probabilities in the discrete model, along with a mean-field approximation and column-averaged DCEs, we derived one-dimensional PDE models for the TC and EC densities for two cases, a model accounting for the interaction of TCs with ECs (Model 2), and one in which TCs do not interact with ECs (Model 1). In Model 1, TCs interact with each other through TC VE and tip-to-tip anastomosis; in Model 2, TCs interact with ECs through EC VE and tip-to-sprout anastomosis. In each case, VE consistent with the motility mechanism is applied in the branching process (i.e. TC VE in Model 1 and, additionally, EC VE in Model 2). We considered these two cases in order to elucidate the macroscale effects of TC VE and EC VE.

We note that, unlike the previous chapter, we formulated the PDEs in one dimension directly, instead of deriving two-dimensional PDEs first. We remark that the difference between the one- and two-dimensional PDEs is additional branching terms involving higher-order derivatives in the y-direction. This is similar to what we found in Chapter 2 in the two-dimensional case, and the additional branching terms involving derivatives in y were eliminated in the one-dimensional PDE (by integrating over y). We have directly formulated our PDEs in one dimension in this chapter (and in the next) as the additional branching terms are not relevant for our purposes (and are given in Appendix C, Section C.4 for reference).

In our CA model, an anastomosis event occurs every time a TC meets another TC or EC (except where self-loops are prohibited). We have modelled anastomosis

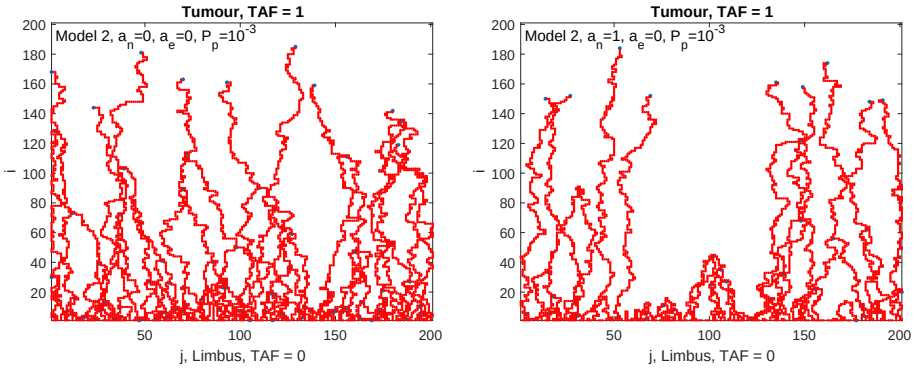

(a) Model 2, $a_n = 0$, $a_e = 0$ (b) Model 2, $a_n = 1$, $a_e = 0$

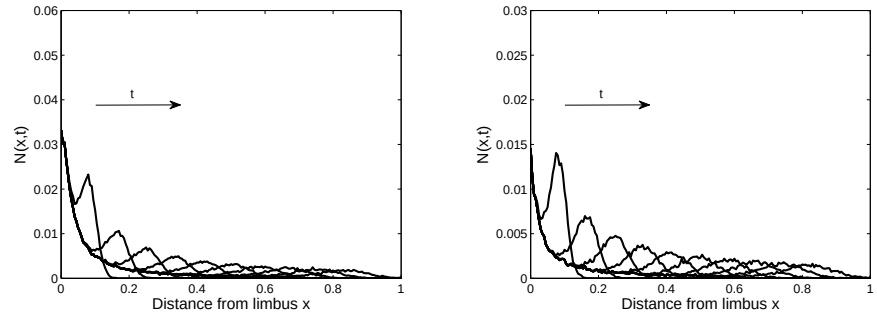

(c) Model 2, $a_n = 0, a_e = 0$ (d) Model 2, $a_n = 1, a_e = 0$

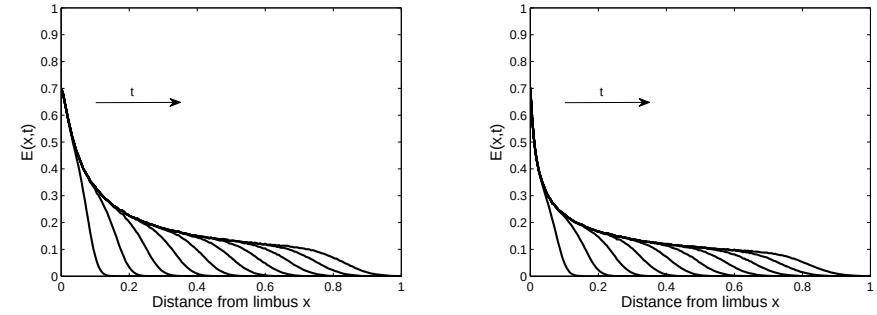

(e) Model 2, $a_n = 0, a_e = 0$ (f) Model 2, $a_n = 1, a_e = 0$

Figure 3.4: Effects of EC VE in CA Model 2: (a), (b) individual simulations (red = ECs, blue = TCs), (c)-(f) column-averaged CA simulation results (black solid curve) shown from $t = 0.2, 0.4, \ldots, 2.0$ (arrow shows direction of increasing time), over $M = 400$ runs. TC motility with EC VE and (a), (c), (e) TC VE and (b), (d), (f) tip-to-tip anastomosis. Even when tip-to-tip anastomosis is active, EC VE prohibits TC movement, and thus the TC density distributions in (c) and (d), particularly at early times $t = 0.2, 0.4$ are different to the TC densities in Figs. 3.2 and 3.3. TC movement is restricted by EC VE as neighbouring sites are more likely to be occupied by ECs. This effect is particularly pronounced at early times where TCs are unable to move to neighbouring sites, creating a long tail in the TC density as the TC front propagates.

so that anastomosis and VE are mutually exclusive events, in keeping with other discrete models of angiogenesis (Tong and Yuan, 2001; Stokes and Lauffenburger, 1991). Anastomosis and VE impose the same occupancy and density restrictions on the discrete and continuum models, respectively. In Model 1, tip-to-tip anastomosis and TC VE imply that TC occupancy and density cannot exceed 1; in Model 2, anastomosis and VE imply that the total cell occupancy/density cannot exceed 1. As we imposed VE in the branching mechanisms consistent with anastomosis, the potential for ill-posedness discussed in Chapter 2 is essentially eliminated in this chapter.

Whenever anastomosis is active, the motility terms in our PDEs reduce to the non-volume excluding model derived in Chapter 2 (branching terms incorporate VE which differs from the previous chapter). This is expected, as anastomosis and VE are mutually exclusive. Our PDEs indicate that fewer ECs are formed when TC VE is active. Further, our PDEs for single (Model 1) and multi-species exclusion (Model 2) (summarised in Table 3.5) agree with existing results (e.g. Simpson et al. (2010a, 2009a)). However, the mean-field approximation led directly to a backwards heat equation for the EC density when EC VE is active. We postulate that this occurs as a result of a break down of the mean-field approximation. Given the complexity of the $O(h^4)$ terms in our derivation, we were unable to regularise these equations using these higher order terms. Furthermore, we opted not to correct our mean-field models using moment dynamics models given their intractability. We conclude that an alternative methodology is required to systematically derive PDE models incorporating EC VE. In the next chapter, we consider a way of incorporating EC VE using the equations we have derived.

The solutions to the Model 1 and well-posed Model 2 PDEs agree with averaged CA simulations. TC VE effects were negligible at the densities considered. In the next chapter, we consider pronounced TC VE effects, which occur at higher TC density.

Table 3.5: Summary of PDE Models 1 and 2 (equations (3.16)-(3.31)). TC VE corresponds to $a_n = 0$, tip-to-tip anastomosis to $a_n = 1$, EC VE to $a_e = 0$ and tip-to-sprout anastomosis to $a_e = 1$. TC-TC interactions refer to TC VE and tip-to-tip anastomosis and TC-EC interactions refer to EC VE and tip-to-sprout anastomosis.

Model	a_n	a_e	Ill-posed?
1 (TC-TC interactions)	1 or 0	N/A	No
2 (TC-TC, EC VE)	1 or 0	0	Yes (backward heat)
2 (TC-TC, tip-to-sprout anastomosis)	1 or 0	1	Can become ill-posed

For the EC VE cases in Model 2 for which we were unable to derive well-posed PDEs (generated backward heat equations), we used the averaged CA simulation to determine population behaviour. We found that EC VE renders TCs immobile, as neighbouring sites are occupied by ECs. This creates long tails in the TC density and as a result, fewer TCs propagate, and fewer ECs are formed.

In general, we found that TC-EC interactions alter the density profile of the vessel network and produce a less dense vessel network. Many models neglect such interactions, modelling only TCs (Chaplain and Stuart, 1993; Chaplain, 1995, 1996) (assuming that vessels are TC trajectories).

Our PDEs were derived assuming a mean-field approximation, a small lattice spacing $h \ll 1$ (see Appendix B for comparisons of PDE solutions with averaged CA results produced with different lattice spacings) and that $O(h^4)$ terms and higher were negligible. The mean-field approximation places constraints on the CA model, and thus we kept the branching rate low in comparison to the motility rate. However, under these restrictions, we are unable to reproduce the brush-border effect, in which the TC density increases as the front approaches the TAF source. Additionally, we assumed that anastomosis occurs whenever a TC encounters another cell. The high rate of TC annihilation through anastomosis also prevents us from qualitatively reproducing the brush-border effect. In the next chapter, we resolve these issues by implementing a higher branching rate, and assigning probabilities to the occurrence of anastomosis events. Further, we will account for active EC VE through the pa-

rameters in our Model 2 PDEs, thereby circumventing the backward heat equations derived in this chapter.

Chapter 4

The Impact of Exclusion Processes on Angiogenesis Models

In the previous chapter, we systematically derived one-dimensional PDE models from two-dimensional CA models of angiogenesis (based on the snail-trail process) in the corneal assay, incorporating TC VE as well as TC and EC VE. We found that TC interaction with ECs (Model 2) produced a less dense vessel network than when these interactions were omitted (Model 1). The effects of TC VE were insignificant as we considered low TC densities. We found good agreement between the (well-posed) PDEs and averaged CA simulation results. The Model 2 PDEs with active EC VE were ill-posed, with a backwards heat equation for the EC density. We were unable to regularise this equation as the fourth order terms were intractable. Additionally, a moment dynamics approach to correct these mean-field models would also have been intractable.

In this chapter, we use the well-posed Model 2 PDEs derived to account for EC VE by estimating the parameters that control the interactions between TCs and ECs by fitting the PDEs to averaged CA simulation results. Further, in the discrete model, we consider a higher branching rate (relaxing mean-field restrictions), and suppose

that anastomosis occurs with a certain probability (instead of occurring whenever a TC meets another cell). We also compare the phenomenological BC model (Byrne and Chaplain, 1995a), linear in the diffusive, chemotactic and branching terms to the averaged CA simulation results to assess agreement. This will enable us to determine whether linear models can account for VE effects at the macroscale, or whether our non-linear PDE models are necessary to capture macroscale VE effects.

Note: A version of this chapter, entitled 'The Impact of Exclusion Processes on Angiogenesis Models' by S. Pillay, H. M. Byrne and P. K. Maini, is under review for publication in the Journal of Mathematical Biology, Karl Hadeler Special Issue.

4.1 Introduction

We know, from the work of Simpson and Baker (2011), that when movement and birth and death processes occur, correlations arise that do not cancel at the macroscale, and that corrected models outperform mean-field models in such cases. Branching is essentially a TC birth process, while anastomosis, which annihilates TCs, is a death process. Thus, our snail-trail model of angiogenesis is effectively a biased motility mechanism with birth and death processes, and we know that this gives rise to correlations. Further, VE and anastomosis are linked (mutually exclusive events) in our framework, and thus VE may also give rise to correlations. This potential break down of the mean-field is compounded by the fact that TC movement generates ECs via the snail-trail.

Thus far, our mean-field models have agreed well with averaged CA simulation results, except when we allowed self-loops during tip-to-sprout anastomosis. By prohibiting self-loops, and fitting the parameter that controlled tip-to-sprout anastomosis to the averaged CA simulation results, we were able to find agreement between the PDE model solutions and the averaged CA simulation results. Further, in keep-

ing with mean-field restrictions, we kept the branching rate low in the CA model ($P_p \ll P_m$), and implemented anastomosis and VE in the simplest way possible (anastomosis occurs every time a TC encounters another cell). However, this meant that few TCs were produced by branching, and that many TCs were annihilated by anastomosis, both effects caused the TC density to fall as the TC front approached the TAF source. In this chapter, we aim to reproduce the brush-border effect (TC density increases as the TC front approaches the TAF source) by relaxing mean-field restrictions. Further, we aim to account for EC VE in our PDE models (produced backwards heat equations in the last chapter).

To accomplish this, we will estimate macroscale parameters by fitting the PDE models to averaged CA simulation results. This may seem counterintuitive, as our discrete to continuum framework directly relates discrete and continuum parameters. However, this framework places many restrictions on our system that do not allow us to capture biologically realistic behaviour. As moment dynamics models are intractable, we exploit the structure of our mean-field PDE models to capture population behaviour by estimating macroscale parameters that arise from processes that may lead to correlations (by fitting the PDE models to averaged CA simulation results). This approach is similar to that used to account for prohibited self-loops (see Chapter 2). For comparison, we will also fit the BC model to our averaged CA simulation results to determine whether a model linear in the diffusive, chemotactic and branching terms, can account for VE effects at the macroscale.

4.2 Modifications to CA Model

Here we outline the changes to the CA algorithm discussed in Chapter 3 (see Section 3.2, Algorithm 2). As before, we implement anastomosis using the variables a_n and a_e, which control tip-to-tip and tip-to-sprout anastomosis, respectively. In contrast to

Table 4.1: Summary of variables and rules used in CA Models 1 and 2.

Model	VE	Anastomosis	Max Occupancy	a_n	a_e
1	TC	Tip-to-tip	1 TC, ECs ≥ 1	[0,1]	N/A
2	TC, EC	Tip-to-tip, Tip-to-sprout	1 TC or EC	[0,1]	[0,1]

Chapter 3 (see Table 3.1), we allow a_n and a_e to vary between 0 and 1. This implies that tip-to-tip (tip-to-sprout) anastomosis occurs with probability a_n (a_e) and TC VE (EC VE) occurs with probability $1 - a_n$ ($1 - a_e$). Therefore, tip-to-tip (tip-to-sprout) anastomosis does not occur every time a TC encounters a TC (EC), though tip-to-tip (tip-to-sprout) anastomosis and TC VE (EC VE) are still mutually exclusive (they cannot occur simultaneously).

We modify the following lines of the CA model pseudocode (pertaining to motility and anastomosis) in Chapter 3, Section 3.2, Algorithm 2 as follows:

- Model 1 and 2: Choose a random number $P_{tt} \in [0, 1]$. If target site is occupied by TCs and $P_{tt} < a_n$, tip-to-tip anastomosis occurs, else TC move is aborted
- Model 2: Choose a random number $P_{ts} \in [0, 1]$. If target site is occupied by ECs and $P_{ts} < a_e$, tip-to-sprout anastomosis occurs (no self-loops), else TC move is aborted

---

The rules for motility, anastomosis and branching in Model 2 imply that a lattice site can be occupied by at most one cell (i.e. it cannot be occupied by two cells of any type). In contrast, in Model 1, at most one TC can occupy a lattice site, but there are no restrictions on EC occupancy (i.e. many ECs or a TC and several ECs may occupy the same lattice site). Models 1 and 2, and the corresponding variables, are summarized in Table 4.1.

These are the only changes to the CA model, and the reader is referred to Chapter 3, Section 3.2, for remaining details of the CA model including algorithm, branching, boundary and initial conditions, and ensemble averages.

4.3 Derivation of Continuum Models

In this section, we will derive continuum models for $a_n \in [0,1]$ in Model 1, and additionally, in Model 2, $a_e = 1$, i.e. in Model 2, we derive a PDE model for which tip-to-sprout anastomosis occurs with probability 1. Recall that in the previous chapter, we found that if $a_e \neq 1$, our mean-field framework leads to a backwards heat equation for the EC density, and this is the reason why we restrict the derivation to $a_e = 1$. We will show how to use the PDE model, derived with $a_e = 1$, to capture a wider range of interactions later on.

The DCEs for Model 1 are unchanged from Chapter 3, except that a_n is no longer binary (see equations (3.4) and (3.5)). Similarly, in the DCEs for Model 2, a_n is no longer binary, with $a_e = 1$ (see equations (3.6) and (3.7)). We reiterate these equations below, but in this case, we combine the DCEs for both models by using the variable B to distinguish models,

$$B = \begin{cases} 0, & \text{Model 1,} \\ 1, & \text{Model 2.} \end{cases} \tag{4.1}$$

The variable B controls the VE incorporated in the branching term (EC VE in Model 2, only TC VE in Model 1), and also whether tip-to-sprout anastomosis is included (Model 2) or not (Model 1). The DCEs for the TC and EC density, are, respectively

$$
\begin{aligned}
&\delta n_{i,j} = \\
&P_m \Bigg(\underbrace{\left[P^{x+}_{i-1,j} n_{i-1,j} + P^{x-}_{i+1,j} n_{i+1,j} + P^{y+}_{i,j-1} n_{i,j-1} + P^{y-}_{i,j+1} n_{i,j+1}\right](1 - n_{i,j} - a_e B e_{i,j})}_{\text{1.movement into } (i,j)} \\
&\underbrace{- \left[P^{x+}_{i,j}(1-(1-a_n)n_{i+1,j}) + P^{x-}_{i,j}(1-(1-a_n)n_{i-1,j})\right.}_{\text{2.movement out of } (i,j)} \\
&\underbrace{\left. + P^{y+}_{i,j}(1-(1-a_n)n_{i,j+1}) + P^{y-}_{i,j}(1-(1-a_n)n_{i,j-1})\right] n_{i,j}}_{\text{2.movement out of } (i,j)} \Bigg) \\
&\underbrace{+ P_p c_{i,j} \left[n_{i,j-1}(1 - n_{i,j} - B e_{i,j})(1 - n_{i,j-2} - B e_{i,j-2})\right.}_{\text{3.branching into (i,j)}} \\
&\underbrace{+ n_{i,j+1}(1 - n_{i,j} - B e_{i,j})(1 - n_{i,j+2} - B e_{i,j+2})}_{\text{3.branching into (i,j)}} \\
&\underbrace{\left. - n_{i,j}(1 - n_{i,j+1} - B e_{i,j+1})(1 - n_{i,j-1} - B e_{i,j-1})\right]}_{\text{4.branching out of (i,j)}}
\end{aligned}
\tag{4.2}
$$

and

$$
\begin{aligned}
\delta e_{i,j} \;=\; & P_m n_{i,j} \underbrace{\left(P^{x+}_{i,j}(1-(1-a_n)n_{i+1,j}) + P^{x-}_{i,j}(1-(1-a_n)n_{i-1,j})\right.}_{2'.\text{movement out of } (i,j)} \\
& \underbrace{+ P^{y+}_{i,j}(1-(1-a_n)n_{j+1}) + P^{y-}_{i,j}(1-(1-a_n)n_{i,j-1})}_{2'.\text{movement out of } (i,j)} \\
& \left. + \underbrace{a_n \left(P^{x+}_{i-1,j} n_{i-1,j} + P^{x-}_{i+1,j} n_{i+1,j} + P^{y+}_{i,j-1} n_{i,j-1} + P^{y-}_{i,j+1} n_{i,j+1}\right)}_{5'.\text{tip-to-tip anastomosis}} \right) .
\end{aligned}
\tag{4.3}
$$

Before proceeding, we explain why these equations describe motility with tip-to-tip anastomosis with probability a_n and TC VE with probability $1 - a_n$. We can

rewrite the first line of equation (4.2) as follows

$$\begin{aligned}
&\left[P^{x+}_{i-1,j}n_{i-1,j} + P^{x-}_{i+1,j}n_{i+1,j} + P^{y+}_{i,j-1}n_{i,j-1} + P^{y-}_{i,j+1}n_{i,j+1}\right](1-(1-a_n)n_{i,j}) \\
&-a_n n_{i,j}\left[P^{x+}_{i-1,j}n_{i-1,j} + P^{x-}_{i+1,j}n_{i+1,j} + P^{y+}_{i,j-1}n_{i,j-1} + P^{y-}_{i,j+1}n_{i,j+1}\right] \\
&-a_e B e_{i,j}\left[P^{x+}_{i-1,j}n_{i-1,j} + P^{x-}_{i+1,j}n_{i+1,j} + P^{y+}_{i,j-1}n_{i,j-1} + P^{y-}_{i,j+1}n_{i,j+1}\right]. \qquad (4.4)
\end{aligned}$$

The term $(1-(1-a_n)n_{i,j})$ describes movement from neighbouring sites into (i,j) where TC VE occurs with probability $(1-a_n)$ if site (i,j) is occupied by a TC; the terms $-a_n n_{i,j}$ and $-Ba_e e_{i,j}$ are penalty terms (as in Chapters 2 and 3) for movement from neighbouring sites into (i,j) if site (i,j) is occupied by a TC or EC, respectively. Thus these terms represent tip-to-tip and tip-to-sprout anastomosis which occur with probabilities a_n and a_e, respectively. The term $(1-n_{i,j}-Ba_e e_{i,j})$ ensures that a TC can only move into site (i,j) and remain a TC if that site is vacant.

Anastomosis and VE affect TC movement out of a site differently. TCs move out of a site into neighbouring sites where TC VE occurs with probability $1-a_n$ (see terms 2 of equation (4.2)) if the target site is occupied by a TC. If $a_n = 1$, then TCs are always allowed to move out of a site, and the outcome depends on the occupancy of the target site.

The equation for the EC density is unchanged from Chapter 3 as only tip-to-tip anastomosis and movement out of a site affect EC density.

As in Chapter 3, branching incorporates VE; it can only occur if neighbouring sites are unoccupied by TCs (Models 1 and 2) or ECs (Model 2) (see terms 4 and 5 in equation (4.2)).

As in Chapter 3, we formulate the DCEs in terms of column averages, so that the resulting PDEs are one-dimensional. The column-averaged DCEs for the TCs and

ECs are, respectively,

$$\begin{aligned}\delta N_i &= P_m \Bigg(\underbrace{\left(P_{i-1}^{x+}N_{i-1} + P_{i+1}^{x-}N_{i+1}\right)\left(1-(1-a_n)N_i\right)}_{\text{movement into } i} \\ &\quad \underbrace{-N_i\left(P_i^{x+}(1-(1-a_n)N_{i+1}) + P_i^{x-}(1-(1-a_n)N_{i-1})\right)}_{\text{movement out of } i} \\ &\quad \underbrace{-a_n N_i\left(P_{i-1}^{x+}N_{i-1} + P_{i+1}^{x-}N_{i+1} + P_i^{y+}N_i + P_i^{y-}N_i\right)}_{\text{tip}-\text{to}-\text{tip anastomosis}} \\ &\quad \underbrace{-a_e BE_i\left(P_{i-1}^{x+}N_{i-1} + P_{i+1}^{x-}N_{i+1} + P_i^{y+}N_i + P_i^{y-}N_i\right)}_{\text{tip}-\text{to}-\text{sprout anastomosis}} \Bigg) \\ &\quad \underbrace{+P_p c_i\left(N_i(1-N_i-BE_i)(1-N_i-BE_i)\right)}_{\text{branching}}, \end{aligned} \tag{4.5}$$

and

$$\begin{aligned}\delta E_i &= P_m N_i \Bigg(\underbrace{P_i^{x+}(1-(1-a_n)N_{i+1}) + P_i^{x-}(1-(1-a_n)N_{i-1})}_{\text{movement out of } i} \\ &\quad \underbrace{+P_i^{y+}(1-(1-a_n)N_i) + P_i^{y-}(1-(1-a_n)N_i)}_{\text{movement out of } j \text{ within a column}} \\ &\quad \underbrace{+a_n\left(P_{i-1}^{x+}N_{i-1} + P_{i+1}^{x-}N_{i+1} + P_i^{y+}N_i + P_i^{y-}N_i\right)}_{\text{tip}-\text{to}-\text{tip anastomosis}} \Bigg). \end{aligned} \tag{4.6}$$

These equations are the same as those derived in Chapter 3, see equations (3.8), (3.9), (3.10) and (3.11) except that $a_n \in [0,1]$ and $a_e = 1$. An explanation of terms in these equations can be found in Section 3.3.1

As before (see Chapter 3, Section 3.3.1), we derive from the DCEs the following

PDEs for $N(x,t)$ and $E(x,t)$, respectively:

$$\begin{aligned}\frac{\partial N}{\partial t} &= D(1-a_nN-Ba_eE)\frac{\partial^2 N}{\partial x^2} \\ &\quad -\chi\left(\frac{\partial}{\partial x}\left(N(1-N)\frac{\partial c}{\partial x}\right)+a_nN\frac{\partial N}{\partial x}\frac{\partial c}{\partial x}-Ba_eE\frac{\partial}{\partial x}\left(N\frac{\partial c}{\partial x}\right)\right) \\ &\quad -\mu\left(a_nN^2+Ba_eNE\right)+\lambda cN(1-N-BE)^2, \end{aligned} \tag{4.7}$$

and

$$\begin{aligned}\frac{\partial E}{\partial t} &= \mu N\left(1-N+2a_nN\right)-D(1-2a_n)N\frac{\partial^2 N}{\partial x^2} \\ &\quad -\chi N\left((1-a_n)\frac{\partial c}{\partial x}\frac{\partial N}{\partial x}+a_n\frac{\partial}{\partial x}\left(N\frac{\partial c}{\partial x}\right)\right), \end{aligned} \tag{4.8}$$

with no flux boundary conditions

$$D\frac{\partial N}{\partial x}-\chi N(1-(1-a_n)N)\frac{\partial c}{\partial x}\mid_{x=0,1}=0, \tag{4.9}$$

where D, χ, μ and λ defined as in the previous chapters (see equations (2.23) and (2.24)) and are restated here:

$$D=\frac{\mu h^2}{4}=\lim_{\tau\to 0}\frac{P_mh^2}{4\tau},\ \chi=\mu kh^2=\lim_{\tau\to 0}\frac{P_mkh^2}{\tau},\ \mu=\lim_{\tau\to 0}\frac{P_m}{\tau},\ \lambda=\lim_{\tau\to 0}\frac{P_p}{\tau}. \tag{4.10}$$

Once again, we use the column-averaged CA simulation results at discrete time step $\bar{K}_{IC}$, $N_i(\bar{K}_{IC})$ and $E_i(\bar{K}_{IC})\,\forall i$ to initialise our PDEs (see equation (2.35) in Chapter 2).

4.3.1 Structure of Continuum Models

When $a_n=0,1$, equations (4.7)-(4.8) reduce to those derived in Chapter 3. We first consider Model 1, by setting $B=0$ in equation (4.7). For $a_n=0$, the equation for

the TC density (excluding branching i.e. $\lambda = 0$) satisfies

$$\frac{\partial N}{\partial t} + \chi \frac{\partial}{\partial x}\left(N(1-N)\frac{\partial c}{\partial x}\right) = D\frac{\partial^2 N}{\partial x^2}, \tag{4.11}$$

(wherein $\frac{\partial c}{\partial x} = 1$), which is consistent with well-known results for biased motility mechanisms (Simpson et al., 2010a, 2009a). We note also that equation (4.11) is similar to a viscous Burgers' equation Whitham (1974),

$$\frac{\partial N}{\partial t} + N\frac{\partial N}{\partial x} = D\frac{\partial^2 N}{\partial x^2}, \tag{4.12}$$

where the advection term is of the form $(1-2N)\frac{\partial N}{\partial x}$. The inviscid Burgers' equation can generate shocks, which are smoothed by the viscous Burgers' equation (see Whitham (1974), pg 103). We anticipate similar behaviour in equation (4.11). To illustrate this behaviour, we solve equation (4.11) using a Gaussian initial condition (see Fig. 4.1). The steepening behaviour shown in Fig. 4.1 can be explained by neglecting the diffusion term in equation (4.11) as D is small (inviscid limit), thereby arriving at a purely advective equation. To a first approximation, therefore, the wave speed, w, is $w \approx 1-2N$, which decreases as N increases. Furthermore, $w < 0$ for $N > 0.5$, $w = 0$ for $N = 0.5$ and $w > 0$ for $N < 0.5$, indicating that the top part of the wave moves in the negative x-direction, while the bottom part moves in the positive x-direction, creating the steepening behaviour at the back of the TC front (see Fig. 4.1). We comment on this behaviour further when discussing averaged CA simulation results later on. An analysis of this steepening behaviour is presented in Appendix F.

From equation (4.7), we see that the difference between the $a_n = 0$ and $a_n = 1$ cases is an additional $N\chi\frac{\partial N}{\partial x}\frac{\partial c}{\partial x}$ term. Thus, when we allow a_n to take on values between 0 and 1, there is a chemotactic term of the form $-\chi(1-2N+a_nN)\frac{\partial N}{\partial x}\frac{\partial c}{\partial x}$, and a second chemotactic term involving the second derivative of c, $-\chi N(1-N)\frac{\partial^2 c}{\partial x^2}$. When

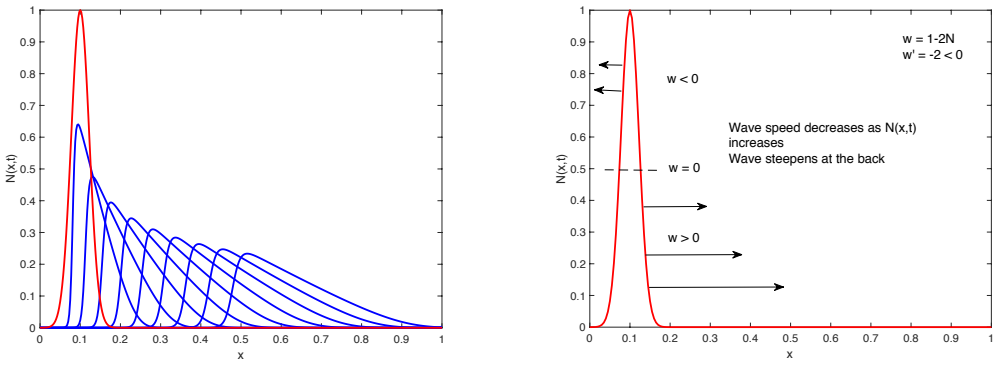

(a) (b)

Figure 4.1: (a) Solution to equation (4.11), using a Gaussian initial condition (red curve) centred on $x = 0.1$ with a variance of $\sigma^2 = 0.0005$. The solutions are shown at $t = 0.2, 0.4, \cdots 2.0$. We see that the TC front steepens on the left, and develops a triangular travelling wave type shape. This steepening of the front at the back is caused by the non-linearity of the chemotactic term $(1-2N)\frac{\partial N}{\partial x}$, which implies that the wave speed decreases as N increases, as illustrated in the schematic in (b).

a_n is non-zero, we also introduce non-linearity into the diffusion term $(1-a_nN)D\frac{\partial^2 N}{\partial x^2}$ and a sink term of the form $-\mu a_n N^2$, as before, except now the coefficients of these non-linear terms can take on a wider range of values as $a_n \in [0,1]$.

If tip-to-sprout anastomosis is active, then $a_e = 1$ in equation (4.7) (Model 2 PDEs, with $B = 1$), and additional non-linearities pre-multiply the diffusive and chemotactic terms $(-Ba_eE)$. As in Chapters 2 and 3, there is an additional sink term $(-\mu a_e NE)$ and branching incorporates EC VE when tip-to-sprout anastomosis is active.

Equation (4.8) for the EC density, is identical to that derived in Chapter 3 as only TC VE and tip-to-tip anastomosis affect EC density, except that now $a_n \in [0,1]$.

The Model 1 and 2 PDEs described here (and partly in Chapter 3) remain well-posed, provided appropriate initial conditions and parameters are used, and $\lambda = 0$ once maximum density has been reached ($N = 1$ in Model 1; $N + E = 1$ in Model 2). In Appendix F, Section F.4, we investigate the well-posedness of our PDE models further.

Table 4.2: Summary of dimensionless values of microscale and macroscale model parameters. $P_{i,j}^{x\pm}$ and $P_{i,j}^{y\pm}$ are given in equation (3.1).

CA Parameters	R	h	P_m	k	τ	K_{IC}	$P_{i,j}^{x\pm}$	$P_{i,j}^{y\pm}$
	200	1/200	1	100	1/160	32	$\frac{1}{2}$,0	$\frac{1}{4}$
PDE Parameters	D	χ	μ	t_{IC}				
	10^{-3}	0.4	160	0.2				

In the following sections, we will compare our one-dimensional PDE models to the averaged CA simulation results. We will consider Model 1 ($B = 0$ in equation (4.7)) with $a_n \in [0, 1]$, and Model 2 ($B = 1$ in equation (4.7)), with $a_n = 1, 0$ and $a_e \in (0, 1]$. Apart from a_e, which we know we have to estimate (from prohibiting self-loops), we do not know which other parameters we should estimate. We will consider each model in turn, and motivate which parameters should be estimated in the next section.

4.4 Determining Which Parameters to Estimate

In what follows, the parameters used in the discrete and continuum models, the numerical schemes used to solve the PDE models, and the fitting procedure are identical to those outlined in Chapter 2 (see Sections 2.4.2 and 2.5.1).

We reiterate microscale and macroscale parameters in Table 4.2, while P_p (branching probability), a_n (Model 1 and 2) and a_e (Model 2 only) are fixed for each CA model case we consider. The branching rate, λ, can be calculated from P_p via equation (4.10). We now solve our PDE models and compare their outputs to column-averaged discrete simulation results, averaged over $M = 200$ realizations (each realization run for $\bar{K}_{\text{final}} = 320$ steps).

4.4.1 Model 1

We know that branching (birth) and tip-to-tip anastomosis (death) are likely to generate correlations, if the probability of these events is comparable to the motility probability, $P_m = 1$. Thus, if our PDE models deviate from the averaged CA simulation results in these cases, we postulate that the parameters controlling branching and tip-to-tip anastomosis should be estimated.

In Chapter 3, with $P_p = 10^{-3}$ (controls the branching probability) and $a_n = 1$ or $a_n = 0$, we found agreement between the PDE solutions and averaged CA simulations (see Fig. 3.2 and 3.3). When we increase the branching probability from $P_p = 10^{-3}$ to $P_p = 10^{-2}$, our PDE model, with parameters derived from the discrete-continuum framework, agrees well with the averaged CA simulation results when $a_n = 0$ (see Fig. 4.2). When $a_n = 1$, Figs. 4.2c-4.2d show that the CA model produces a flatter increase in TC density and, consequently, EC density, while the PDE model, with $\lambda = 1.6$, determined from the discrete-continuum framework (see equation (4.10)), produces a larger increase in the TC density as the front approaches the TAF source. We conclude that the higher branching probability combined with tip-to-tip anastomosis causes the mean-field approximation to break down. To generate agreement between the PDE solutions and averaged CA simulation results, we postulate that we should decrease the branching rate as we cannot increase the value of a_n (in the PDE model); it is already set to its maximum value ($a_n = 1$). When we estimate the branching rate by fitting the PDE model to averaged CA simulation results, we rename λ by $\tilde{\lambda}$ and find that when $\tilde{\lambda} = 0.8582 \pm 0.0083$ (see Fig. 4.2e, 4.2f), there is good agreement between the PDE model and the averaged CA simulation results.

Now we consider $a_n = 0.2$ with $P_p = 10^{-3}$ and $P_p = 10^{-2}$. Using the parameters from the discrete and continuum framework, the PDE model fails to capture the CA simulation results when $P_p = 10^{-2}$. For $P_p = 10^{-3}$, the agreement is good for the TC density, and poorer for the EC density (but acceptable) (see Figs. 4.3a-4.3d).

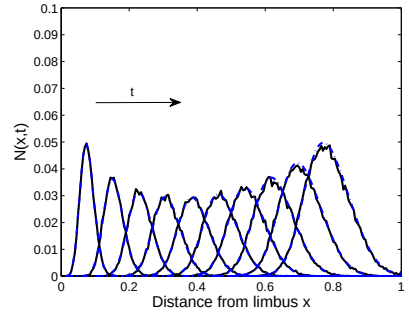

(a) $P_p = 10^{-2}, a_n = 0$

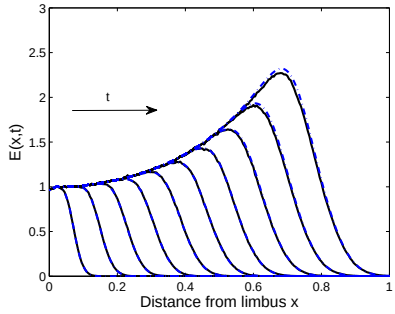

(b) $P_p = 10^{-2}, a_n = 0$

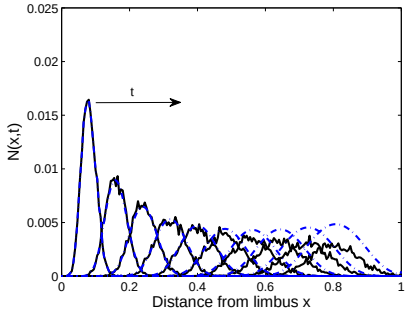

(c) $P_p = 10^{-2}, a_n = 1$

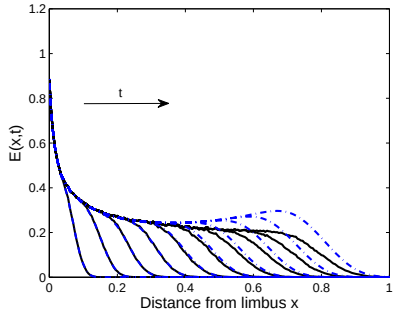

(d) $P_p = 10^{-2}, a_n = 1$

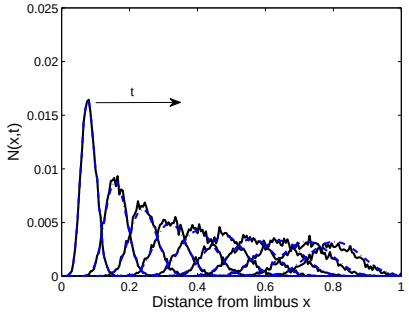

(e) $\tilde{\lambda} = 0.8582 \pm 0.0083, a_n = 1$

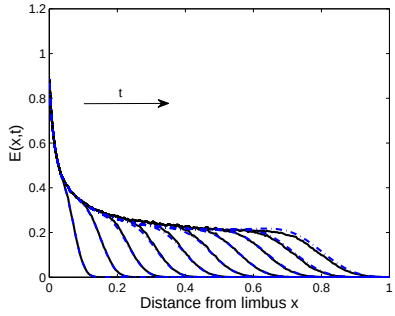

(f) $\tilde{\lambda} = 0.8582 \pm 0.0083, a_n = 1$

Figure 4.2: Model 1: Effect of branching rate on agreement between PDE model (equations (4.7) and (4.8) with $B = 0$) solutions (blue dot-dashed curves) and averaged CA simulation results (black curves). (Left panel) Tip cell (TC) density, (Right panel) Endothelial cell (EC) density. In the CA model, we implement TC motility with tip-to-tip anastomosis with probability a_n and TC VE with probability $1 - a_n$ and branching with probability P_p. $P_p = 10^{-2}$ corresponds to continuum branching rate of $\lambda = 1.6$. (a)-(b) We see good agreement between the PDE and discrete model when $a_n = 0$. (c)-(d) If we set $a_n = 1$, the agreement is poor, likely due to a break down of the mean-field approximation. (e)-(f) For the $a_n = 1$ case, if we estimate $\tilde{\lambda}$ though fitting, the agreement is improved.

For $P_p = 10^{-2}$, if we fit for both a_n and λ (renamed $\tilde{a}_n$ and $\tilde{\lambda}$ for clarity), we find agreement (see Figs. 4.3e-4.3f).

The results presented in Figs. 4.2 and 4.3 reveal that when we estimate parameters in the continuum model, good agreement between the solutions of the PDE model and the CA simulation results can be found. When $a_n = 0$ (minimum value) or $a_n = 1$ (maximum value) in the CA, we estimate only $\tilde{\lambda}$ in the continuum model. When $0 < a_n < 1$, both $\tilde{a}_n$ and $\tilde{\lambda}$ must be estimated in the continuum model to find good agreement.

By fitting $\tilde{a}_n$ and $\tilde{\lambda}$, we could include additional processes in the CA model and capture them in the PDE model. For example, we could implement a minimum branching or a minimum tip-to-tip anastomosis length in the CA model (see Fig. 4.4). Estimating $\tilde{\lambda}$ and $\tilde{a}_n$ allows us to include a wider range of interactions in the CA model that would have been intractable to include in the DCE framework.

4.4.2 Model 2

As in Chapters 2 and 3, we estimate the parameter controlling tip-to-sprout anastomosis, a_e, now renamed $\tilde{a}_e$, by fitting the PDE model to averaged CA simulation results. This enables us to account for prohibited self-loops, which are not explicitly accounted for in the DCE framework. This is why we retained the parameter a_e in the PDE derivation. For $P_p = 10^{-3}$, $a_n = 1$ or 0, and $a_e = 1$ in the CA model, the PDE model solutions agree well with the averaged CA simulations when we estimate $\tilde{a}_e$ (see previous chapter, Figs. 3.2 and 3.3).

Thus far, we have not derived a well-posed PDE model for which $a_e < 1$ in the CA model (recall backward heat equations in the previous chapter). In the CA model, as a_e is decreased below one, the probability of aborted TC moves due to EC VE, $1 - a_e$, increases. This leads to a multi-species exclusion process (exclusion from TCs and ECs). As we are already estimating the parameter $\tilde{a}_e$ by fitting the PDE

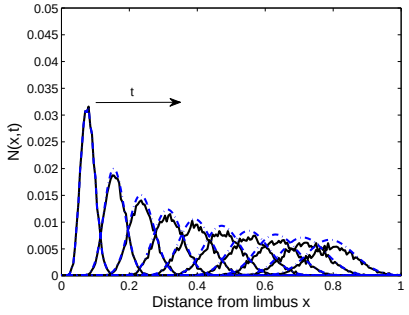

(a) $P_p = 10^{-3}, a_n = 0.2$

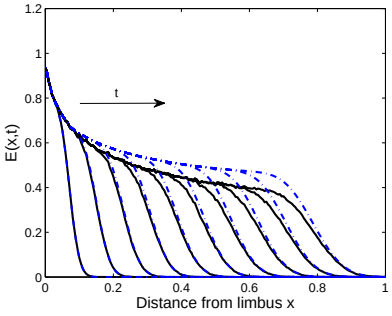

(b) $P_p = 10^{-3}, a_n = 0.2$

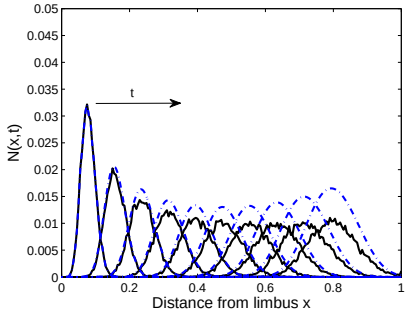

(c) $P_p = 10^{-2}, a_n = 0.2$

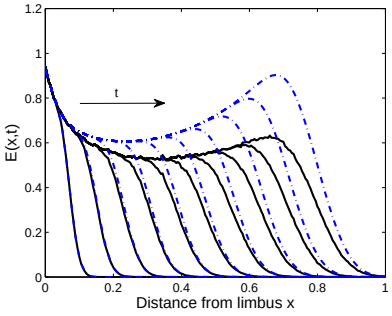

(d) $P_p = 10^{-2}, a_n = 0.2$

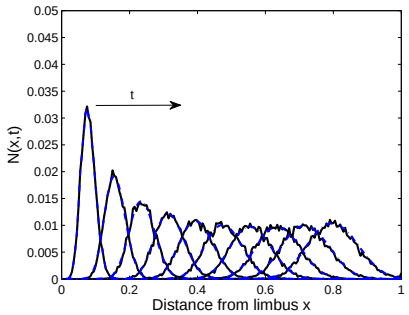

(e) $\tilde{\lambda} = 1.1821 \pm 0.0041, \tilde{a}_n = 0.3001 \pm 0.0008$

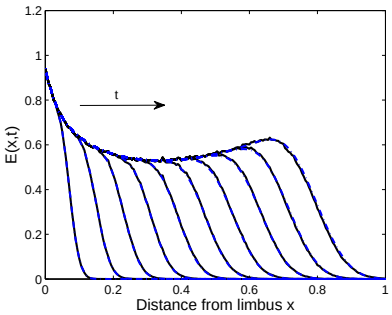

(f) $\tilde{\lambda} = 1.1821 \pm 0.0041, \tilde{a}_n = 0.3001 \pm 0.0008$

Figure 4.3: Model 1: Effect of branching rate and anastomosis on agreement between PDE model (equations (4.7) and (4.8) with $B = 0$) solutions (blue dot-dashed curves) and averaged CA simulation results (black solid curves). (Left panel) Tip cell (TC) density, (Right panel) Endothelial cell (EC) density. In the CA model, we implement TC motility with tip-to-tip anastomosis with probability a_n and TC VE with probability $1 - a_n$ and branching with probability P_p. $P_p = 10^{-3}, 10^{-2}$ corresponds to continuum branching rate of $\lambda = 0.16, 1.6$, respectively. (a)-(b) Solutions agree with averaged CA simulation results, though agreement is poorer for EC density. (c)-(d) PDE model does not agree with the averaged CA simulation results when we use the continuum parameters derived directly from our framework. (e)-(f) For $P_p = 10^{-2}$, when we fit the parameters that control the rate of branching and anastomosis, the PDE models agree with the simulation results.

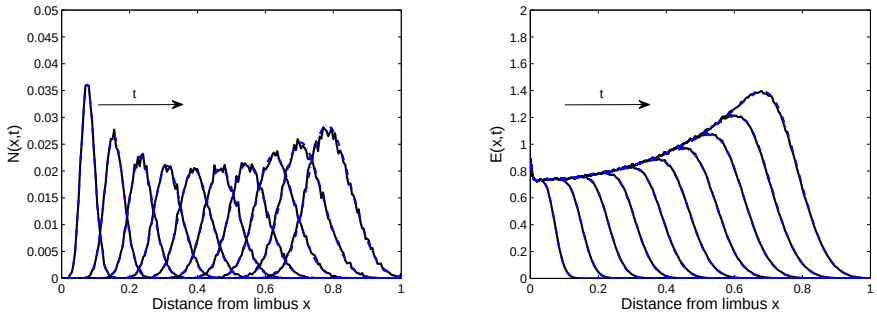

(a) TC density (b) EC density

Figure 4.4: Model 1 ($a_n = 1, P_p = 10^{-2}$): A minimum branching length and a minimum tip-to-tip anastomosis length of 5 cells has been implemented, i..e a TC does not branch or anastomose with another TC, unless there are at least 4 ECs in the sprout of the active TC. As we have not accounted for interactions with these restrictions in our DCE framework, we fit the parameters in the PDE model (equations (4.7) and (4.8) with $B = 0$) that control the rate of branching and anastomosis: $\tilde{\lambda} = 1.2075 \pm 0.0036, \tilde{a}_n = 0.0000 + 0.0004$. (PDE solutions = blue dot-dashed curves, Averaged CA simulations = black solid curves.)

model to averaged CA simulation results, we will also attempt to capture averaged CA simulation results generated with $0 < a_e \leq 1$ through this methodology. Thus, we account for EC VE through parameter estimation, instead of using the DCE framework to derive alternative detailed non-linear PDEs or account for correlations through a moment dynamics approach.

Setting $a_e = 0$ in the CA corresponds to total EC VE and neglect of tip-to-sprout anastomosis. In reality, this is unlikely, as networks produced via angiogenesis show connections between sprouts. Therefore, we consider averaged CA simulations for $a_n = 1, 0$ and $a_e \in (0, 1]$ in Model 2. To reproduce the brush border effect (see Chapter 1), we use a high branching probability of $P_p = 10^{-1}$ in the CA model. Guided by the discussion on potential mean-field break-down in Model 1, in Model 2, we estimate $\tilde{\lambda}$ and $\tilde{a}_e$. We expect there will be a threshold value of a_e in the CA model below which the Model 2 PDEs fail to capture the population behaviour due to the increasing effects of EC VE. In Section 4.5, we compare solutions to equations (4.7) and (4.8) with parameters estimated through fitting to column-averaged CA simulation results to assess agreement.

BC Model

We will also compare (in Section 4.5) the modified BC model to the averaged CA simulation results. Recall from Chapter 2, that the modified BC model is given by:

$$\frac{\partial N}{\partial t} = D_{\mathrm{BC}}\frac{\partial^2 N}{\partial x^2} - \chi_{\mathrm{BC}}\frac{\partial}{\partial x}\left(N\frac{\partial c}{\partial x}\right) + \lambda_{\mathrm{BC}}Nc - \beta_e NE - \beta_n N^2, \tag{4.13}$$

$$\frac{\partial E}{\partial t} = \frac{2}{h}\left|D_{\mathrm{BC}}\frac{\partial N}{\partial x} - \chi_{\mathrm{BC}}N\frac{\partial c}{\partial x}\right|, \tag{4.14}$$

subject to

$$D_{\mathrm{BC}}\frac{\partial N}{\partial x} - \chi_{\mathrm{BC}}N\frac{\partial c}{\partial x}\ |_{x=0,1} = 0, \tag{4.15}$$

where h is the lattice spacing from the CA model. We estimate the parameters ($D_{\mathrm{BC}}, \chi_{\mathrm{BC}}, \lambda_{\mathrm{BC}}, \beta_e$ and β_n) by fitting the BC model to averaged CA simulation results. In so doing, we determine whether non-linear interactions and VE can be adequately described by a linear (in N) model (through the parameters). Recall, as mentioned in Chapter 2, the spatio-temporal evolution of EC density is proportional to the TC flux, whilst in our PDE models, it is proportional to a source term and additional flux terms accounting for anastomosis and/or TC VE.

4.5 One-Dimensional Comparisons

In Table 4.3, we outline the CA (see Table 4.1) and PDE models we will compare (see Table 4.2 for values of other model parameters). For Models 1 and 2, we have used high branching probabilities (relative to the motility probability $P_m = 1$) to ensure that the TC density increases as the TC front approaches the TAF source and thereby qualitatively reproduce the brush border effect.

We compare solutions of the one-dimensional equations (4.7)-(4.9) and the BC model (equations (4.13)-(4.15)) to averaged CA simulation results (see equations

(2.12) and (2.13)), where lattice site occupancy has been averaged over $M = 200$ realizations and $R = 200$ columns. As before, initial conditions for the continuum models are the column-averaged CA simulation results at $t = 0.2$ (see equations (2.35) in Chapter 2).

We measure the goodness of fit in terms of root mean square error (RMSE), a measure of the deviation between the PDE solutions and the averaged CA results. For the TC and EC densities we define

$$\text{TC RMSE} = \sqrt{\frac{\sum_{i=1}^{P}(N_{PDE}^{i} - N_{CA}^{i})^2}{P}}, \tag{4.16}$$

$$\text{EC RMSE} = \sqrt{\frac{\sum_{i=1}^{P}(E_{PDE}^{i} - E_{CA}^{i})^2}{P}}, \tag{4.17}$$

where P is the total number of points (all lattice points for times $t = 0.4 - 2.0$ in increments of $t = 0.2$, $P = 1809$) and N_{PDE} and E_{PDE} and N_{CA} and E_{CA} are the PDE and CA model TC and EC densities, respectively. We also calculate the cell mass, defined as the spatial integral of TC and EC densities at $t = 2.0$ (final time point). We compare the mass calculated from each PDE model to that calculated from the averaged CA simulations. We visualise mass calculated from the averaged CA simulations as a continuum (straight line connecting data points) for comparison. We visualise the RMSEs as functions of total cell mass (TC and EC mass) calculated from the averaged CA simulation results, as the cell mass provides us with a single data point for each set of CA model parameters used.

We perform the fitting using 30 random start points generated using MATLAB's optimization toolbox (*createOptimProblem*) and *lsqnonlin*. The random start points are generated within the pre-defined bounds set for the parameters. For Model 1 (Model 2): $\tilde{\lambda} \in [0, 30]$ and $\tilde{a}_n = [0, 1]$ ($\tilde{a}_e \in [0.08, 1]$). For the BC model: $\tilde{D}_{BC} \in [10^{-4}, 10^{-2}], \tilde{\chi}_{BC} \in [0.2, 0.5], \tilde{\lambda}_{BC} \in [0, 30]$ and $\tilde{\beta}_n \in [0.80]$ ($\tilde{\beta}_e \in [0, 80]$). We also used the continuum analogue of the discrete parameters calculated using equation

Table 4.3: Cases for CA and PDE models: We give the CA model parameters, and the corresponding parameters in the continuum model. In the PDE models, the parameters are estimated by fitting the PDE models to averaged CA simulation results, with the exception of $\tilde{a}_n$ in Model 2, which is the direct analogue of a_n in the CA model.

CA Model	a_n	a_e	P_p
1	$[0,1]$	N/A	$10^{-2}, 4\times10^{-2}$
2	0 or 1	$(0,1]$	10^{-1}
PDE Model	$\tilde{a}_n$	$\tilde{a}_e$	$\tilde{\lambda}$
1 ($B=0$ in equation (4.7))	[0,1]	N/A	$[0,1.6],[0,6.4]$
2 ($B=1$ in equation (4.7))	0 or 1	$(0,1]$	$[0,16]$

(4.10) as a start point and confirmed that the fitted parameter values were within the confidence intervals of the parameters found using the optimization toolbox.

4.5.1 Model 1 Comparisons

In Figs. 4.5 and 4.6, we compare Model 1 PDEs and the BC model to averaged CA simulation results for which tip-to-tip anastomosis occurs with probability a_n, and TC VE with probability $1-a_n$. We use branching probabilities of $P_p = 10^{-2}$ and $P_p = 4\times10^{-2}$ for each of $a_n = 0.02, 0.05, 0.1, 0.15, 0.2$. We see that as the probability of tip-to-tip anastomosis decreases, and the branching probability increases, the TC and EC densities at later time points increase due to reduced TC death rate and increased TC birth rate (compare Figs. 4.5a, 4.5b to 4.5c, 4.5d). The larger population of TCs causes the TC density (see Figs. 4.5c-4.5d) to steepen at the back and extend to the left as forward TC movement is prevented by TC VE (contrast this behaviour with that depicted in Figs. 4.5a- 4.5b). As discussed earlier, steepening of the TC front can be understood by considering the PDE for the TC density. When $a_n = 0$, a factor of $1-2N$ pre-multiplies the chemotactic term $\frac{\partial N}{\partial x}$ in equation (4.7). We can approximate the wave speed as $1-2N$, which decreases as N increases, causing the TC front to steepen at the back. This is analogous to the steepening behaviour that occurs in the viscous Burgers' equation (see Whitham (1974)). Thus, as we reduce

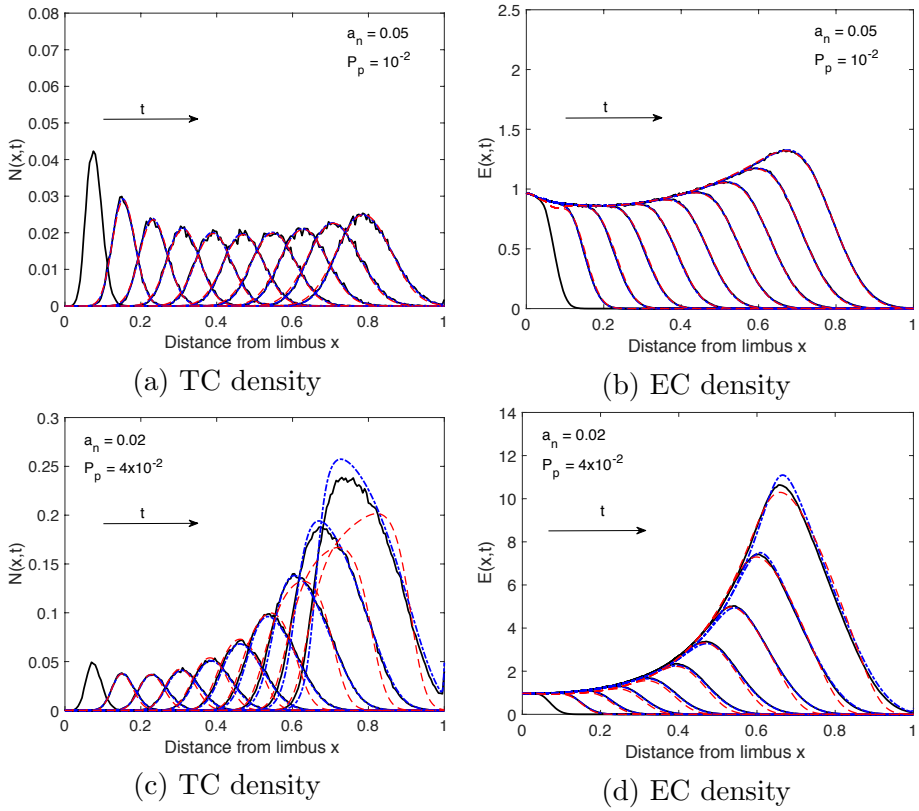

(a) TC density (b) EC density

(c) TC density (d) EC density

Figure 4.5: Model 1 Comparisons. TC and EC densities increase as the probability of tip-to-tip anastomosis, a_n, decreases and the branching probability, P_p increases. (a)-(d) Column-averaged CA simulation results (black solid curves) are shown at times $t = 0.2, 0.4, \cdots, 2.0$ (arrow shows direction of increasing time). The TC front steepens at the back (see (c)), as TC VE prevents the forward movement of TCs as the TC density increases. Model 1 PDE (blue dashed-dot curves, equations (4.7)-(4.9) with $B = 0$) and BC model solutions (red dashed curve, equations (4.13)-(4.15)) are shown from $t = 0.4 - 2.0$. The PDE models agree with the averaged CA simulations when the TC density is low, but the BC model deviates from the CA simulation results as the cell density increases.

a_n in our CA model, if the cell density is high, a front that steepens at the back will develop. A model that is linear in the chemotactic term will not generate this behaviour. Thus, the BC model, in which the chemotactic term ($\frac{\partial N}{\partial x}$) is linear in N cannot capture this steepening behaviour and, therefore, deviates from the averaged CA simulation results (see Fig. 4.5c).

The RMSE increases for both models as the total cell mass (integral of cell densities in x at $t = 2.0$, mass calculated from CA simulation results visualised as a continuum) increases (see Figs. 4.6a and 4.6b). Therefore, the difference between the

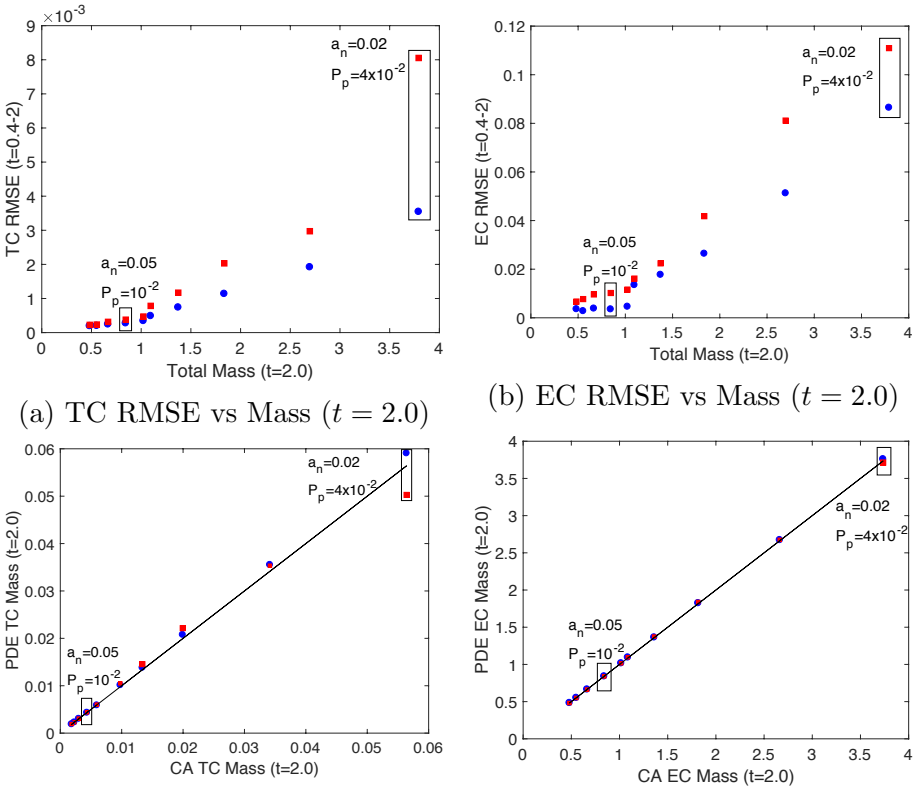

(a) TC RMSE vs Mass ($t = 2.0$)

(b) EC RMSE vs Mass ($t = 2.0$)

(c) TC Mass ($t = 2.0$)

(d) EC Mass ($t = 2.0$)

Figure 4.6: Model 1 Comparisons. TC and EC densities increase as the probability of tip-to-tip anastomosis, a_n, decreases and the branching probability, P_p increases. (a)-(b) The relative difference between the RMSEs for the Model 1 PDEs (blue circles) and the BC model (red squares) increases as mass (integral of cell densities in x) at $t = 2.0$ increases. (c)-(d) Mass from the PDE models at $t = 2.0$ agrees with CA model mass (black line), except at high TC density when TC VE takes effect. The PDE models agree with the averaged CA simulations when the TC density is low, but the modified BC model deviates from the CA simulation results as the cell density increases, seen in (a) and (c). (a)-(d) Boxed data points correspond to annotated parameter values in Fig. 4.5.

RMSE for each model should be used to determine which model is a better fit (lower RMSE). When the mass is low and TC VE effects are negligible, both the Model 1 PDEs and the BC model agree well with the averaged CA simulation results, and the RMSEs for both models are clustered together. As the TC density increases, the BC model deviates from the averaged CA simulation results (see Fig. 4.5c where TC VE effects are visible) and the relative difference between the RMSEs increases. Both models capture total cell mass at $t = 2.0$ well except when TC VE effects are noticeable (see Figs. 4.6c-4.6d). To summarize, as the TC density increases (for higher branching rates), the Model 1 PDEs better capture the non-linear behaviour in the TC density that arises from TC VE than the BC model.

The fitted parameter values for Model 1 and the BC model are given in Appendix D in Tables D.1 and D.2, respectively. In Fig. 4.7, we show how estimated branching rates ($\tilde{\lambda}, \tilde{\lambda}_{\text{BC}}$) and tip-to-tip anastomosis parameters ($\tilde{a}_n, \tilde{\beta}_n\mu$) for the Model 1 PDEs and the BC model change as the tip-to-tip anastomosis parameter (a_n) in the CA model is varied.

In Fig. 4.7a, for $\lambda = 1.6$ (calculated value of the branching rate from the CA branching probability, P_p, using equation (4.10)), the estimated branching rates for the Model 1 PDEs are less than the calculated value. This is also true for the BC model, except for $\lambda = 6.4$ and $a_n = 0.05, 0.02$, where the estimated branching rates in the BC model are higher than the calculated value. Further, as a_n increases, the values of $\tilde{\lambda}$ and $\tilde{\lambda}_{\text{BC}}$ decrease. This is reasonable as more TCs are annihilated via tip-to-tip anastomosis as a_n increases and, therefore, the branching rate should decrease.

The estimated tip-to-tip anastomosis parameter, $\tilde{a}_n$, in the Model 1 PDEs, is higher than the CA values (see Fig. 4.7b and 4.7c). This is also true for the estimated tip-to-tip anastomosis parameter in the BC model, $\tilde{\beta}_n$, though for $\lambda = 6.4$ and $a_n = 0.05, 0.02$, the estimated values in the BC model are significantly higher than the

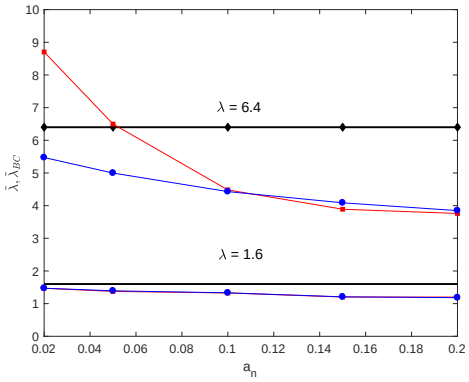

(a) Estimated branching rate compared to calculated value

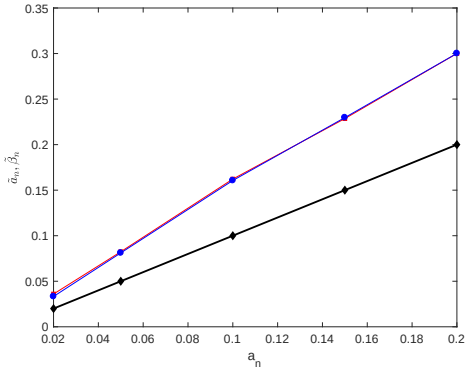

(b) Estimated tip-to-tip anastomosis rates for $\lambda = 1.6$

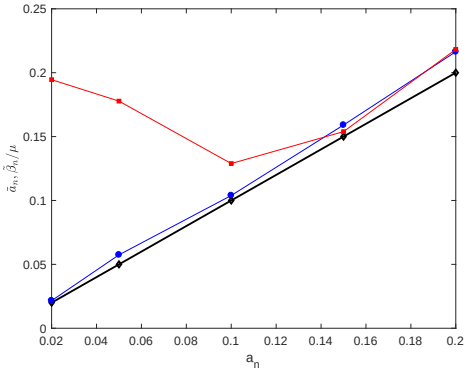

(c) Estimated tip-to-tip anastomosis rates for $\lambda = 6.4$

Figure 4.7: Model 1: Comparisons between estimated branching and anastomosis parameters and calculated values. (a) For $\lambda = 1.6$, the estimated branching rates in both models are less than the calculated branching rate. For $\lambda = 6.4$, the estimated branching rates in the Model 1 PDEs are less than the calculated branching rate, while the estimated rate for the BC model is higher than the calculated rate for $a_n = 0.02$ and 0.05. The estimated branching rates for both models are similar except for $\lambda = 6.4$ and $a_n = 0.05, 0.02$ (when TC VE effects non-negligible). (b) Estimated anastomosis parameters for both models are similar and higher than the CA values (black line, visualised as a continuum for comparison). (c) The estimated anastomosis parameter for the BC model is higher than that for the Model 1 PDEs and the CA values. Model 1 PDEs = blue circles, BC Model = red squares, Actual parameter values calculated from the CA = black.

values from the CA and the estimated values from the Model 1 PDEs. (Recall that $\beta_n = \mu a_n$, see Chapter 2.)

The estimated diffusion coefficient for the BC model (see Table D.2 in Appendix D)) is approximately 10^{-3}. In the Model 1 PDEs, the diffusion coefficient $D = 10^{-3}$ is multiplied by a $(1 - a_n N)$ term (see equation (4.7)), and thus $\tilde{D}_{\text{BC}}$ should decrease as a_n decreases when the TC density is high, which is not observed. The $(1 - 2N + a_n N)$ term pre-multiplies the chemotactic term in the Model 1 PDEs, so we expect the estimated chemotactic coefficient for the BC model to be less than $\chi = 0.4$ (value used in the Model 1 PDEs) and to increase as a_n increases, which is evident in the values for $\tilde{\chi}_{\text{BC}}$ in Table D.2. Overall, the estimated parameters from the BC model are similar to those from the Model 1 PDEs, except when TC VE effects are significant and the BC model deviates from the averaged CA simulation results (see Fig. 4.5c).

4.5.2 Model 2 Comparisons

We compare the Model 2 PDEs and the modified BC model to averaged CA simulation results where tip-to-sprout anastomosis occurs with probability a_e, and EC VE with probability $1 - a_e$. In this case branching incorporates two species exclusion. Additionally, any attempts at tip-to-sprout anastomosis within the same sprout are aborted, incorporating an additional EC VE effect. In what follows, we consider two cases, one in which tip-to-tip anastomosis is neglected ($a_n = 0$), and a second case in which tip-to-tip anastomosis occurs with probability 1 ($a_n = 1$). We use a branching probability of $P_p = 10^{-1}$ for each of $a_e = 0.1, 0.2, 1$ in the CA.

4.5.2.1 Case 1: TC VE occurs with probability 1 ($a_n = 0$ in the CA model)

As the probability of tip-to-sprout anastomosis, a_e, decreases, the cell densities/mass at $t = 2.0$ (see Figs. 4.8a-4.9d) increase as fewer TCs are annihilated. This implies a larger EC VE effect, as TCs create and interact with more ECs. This EC VE leads

to long tails in the TC density (see Fig. 4.8c) as TCs are rendered immobile behind the migrating TC front (within the EC front). This behaviour contrasts with the TC VE effect in Model 1, where forward movement of TCs is restricted by TCs located ahead of the EC front (and therefore TCs are located within the TC front).

The Model 2 PDEs and BC model are consistent with the averaged CA simulations when $a_e = 1$ (see Figs. 4.8a-4.8b and Figs. 4.9a-4.9d). As a_e decreases (EC VE more pronounced), the RMSE for the Model 2 PDEs increases more rapidly than for the BC model. The Model 2 PDEs produce a TC front that is out of phase with the averaged CA results at $t = 2.0$ (see Fig. 4.8c for $a_e = 0.1$). For $t < 2.0$, the Model 2 PDEs agree better with the averaged CA simulation results. In terms of EC mass at $t = 2.0$, the Model 2 PDEs and the BC model agree well with the CA EC mass (see Fig. 4.9d). For $P_p = 10^{-1}, a_e = 1$ and $P_p = 10^{-2}, a_e = 1$ (results not shown), both PDE models are in good agreement with the averaged CA simulation results. For $P_p = 10^{-1}, a_e = 0.2, 0.1$, the BC model captures the averaged CA simulation results better, according to the RMSE and TC mass metrics at $t = 2.0$ (see Figs. 4.9a-4.9d). For $P_p = 10^{-2}, a_e = 0.2, 0.1$, the Model 2 PDEs capture the averaged CA simulation results better, according to the RMSE and TC mass metrics (results not shown). For values of a_e below 0.1, as the effects of EC VE increase, neither model gives good agreement with the averaged CA simulation results (results not shown).

The TC density for Model 2 is much lower than the TC density for Model 1 (see Fig. 4.5 and Fig. 4.6) for two reasons. Firstly, EC and TC VE in the branching process mean that fewer TCs are produced, even though the branching probability is higher than for Model 1. Secondly, TC-EC interactions annihilate many TCs via tip-to-sprout anastomosis. As the TC mass remains low, the TC VE effect seen in Model 1 (steepening of TC front) is not observed in Model 2.

The estimated parameters (with $a_n = 0$) for the Model 2 PDEs and the BC Model are given in Tables D.3 and D.4 in Appendix D, respectively. In Fig. 4.10,

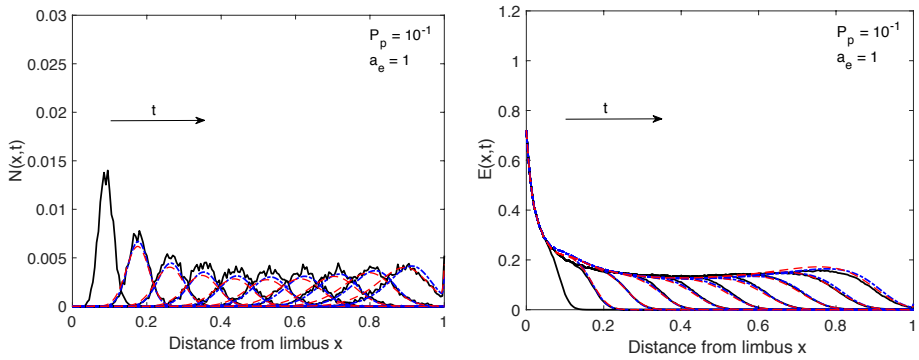

(a) TC density (b) EC density

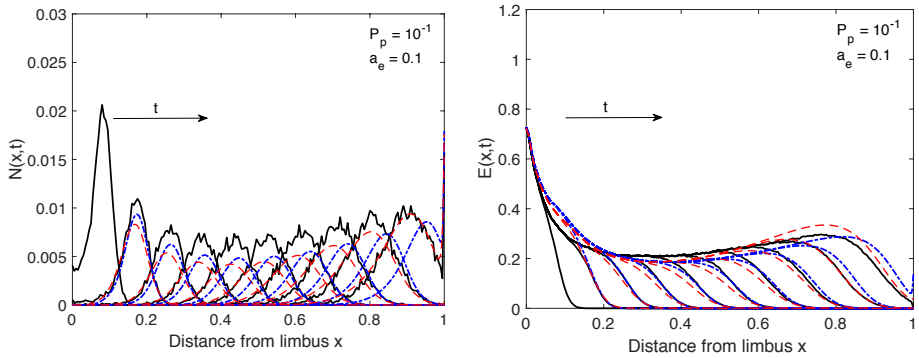

(c) TC density (d) EC density

Figure 4.8: Model 2 ($a_n = 0$) Comparisons. TCs interact with ECs through tip-to-sprout anastomosis and EC VE, and with TCs through TC VE. TC and EC densities increase as the probability of tip-to-sprout anastomosis, a_e, decreases. The branching probability is $P_p = 10^{-1}$. (a)-(d) Column-averaged CA simulation results (black solid curve) are shown at times $t = 0.2, 0.4, \cdots, 2.0$ (arrow shows direction of increasing time). The migrating TC front exhibits long tails (see (c)), as EC VE prevents movement of TCs as the EC density increases. Model 2 PDE (blue dashed-dot curve, equations (4.7)-(4.9) with $B = 1$) and modified BC model (red dashed curve, equations (4.13)-(4.15)) solutions shown from $t = 0.4 - 2.0$. The BC model agrees better with the CA simulation results for $a_e = 0.1$.

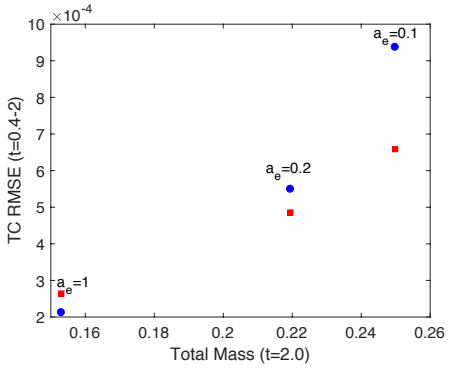

(a) TC RMSE vs Mass ($t = 2.0$)

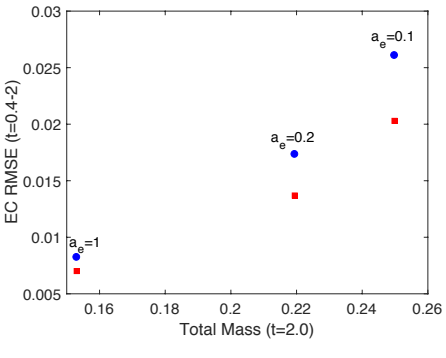

(b) EC RMSE vs Mass ($t = 2.0$)

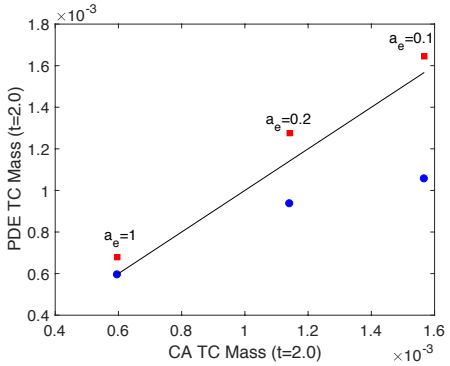

(c) TC Mass ($t = 2.0$)

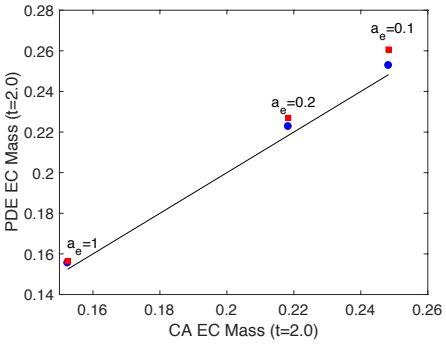

(d) EC Mass ($t = 2.0$)

Figure 4.9: Model 2 ($a_n = 0$) Comparisons. TCs interact with ECs through tip-to-sprout anastomosis and EC VE, and with TCs through TC VE. TC and EC densities increase as the probability of tip-to-sprout anastomosis, a_e, decreases. The branching probability is $P_p = 10^{-1}$. (a)-(d) Model 2 PDEs = blue circles, BC Model = red squares. (a)-(b) The relative difference between the RMSE for each model increases as mass at $t = 2.0$ increases. (c)-(d) Model 2 PDEs deviate from the CA TC mass (black line, visualised as a continuum) at $t = 2.0$ as stronger EC VE takes effect ($a_e = 0.1$). The BC model agrees better with the CA simulation results for $a_e = 0.1$.

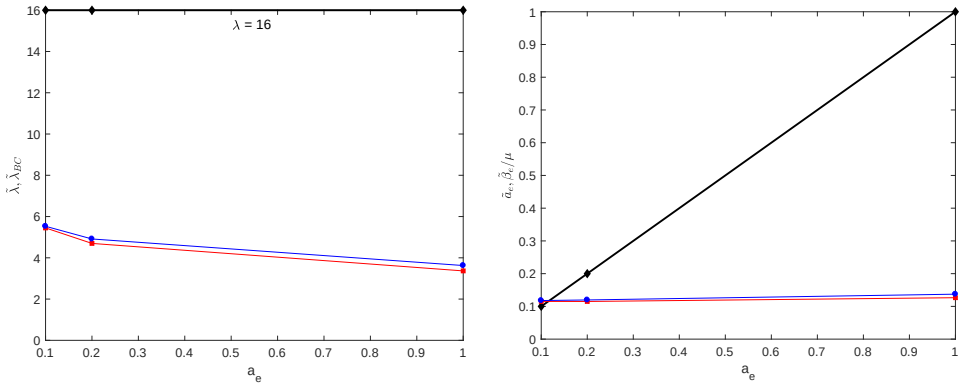

(a) Estimated branching rate compared to calculated value

(b) Estimated tip-to-sprout anastomosis rate vs CA values

Figure 4.10: Model 2 ($a_n = 0$): Comparisons between estimated branching and anastomosis parameters and calculated values. (a) The estimated branching rates in both models are less than the calculated branching rate, and are similar. (b) Estimated anastomosis parameters for both models are similar and much lower than the CA values (black line). Note that the CA value for a_e does not incorporate aborted self-loops which are implemented through rules in the CA model, while the estimated parameters do account for aborted self-loops, and thus the estimated parameter values are much lower than the CA values. Model 1 PDEs = blue circles, BC Model = red squares, Actual parameter values from the CA= black.

we plot the estimated branching $(\tilde{\lambda}, \tilde{\lambda}_{\mathrm{BC}})$ and tip-to-sprout anastomosis parameters $(\tilde{a}_e, \tilde{\beta}_e)$ for the Model 2 PDEs and the BC model against the tip-to-sprout anastomosis parameter, a_e, from the CA model. (Recall that $\beta_e = \mu a_e$ see Chapter 2.)

The estimated branching rates for the BC model and the Model 2 PDEs decrease as a_e increases (see Fig. 4.10a). This is reasonable, given that as a_e increases, more TCs are annihilated via tip-to-sprout anastomosis resulting in a lower branching rate. The estimated values for $\tilde{\lambda}_{\mathrm{BC}}$ are slightly less than the values for $\tilde{\lambda}$, as the value of $\tilde{\lambda}_{\mathrm{BC}}$ must account for the $(1 - N - E)^2$ in the branching term in the Model 2 PDEs. The estimated values for $\tilde{\beta}_e/\mu$ are similar to those for $\tilde{a}_e$, and further, both estimates are much lower than the CA values for a_e. This is because in the CA, a_e does not incorporate prohibited self-loops directly (implemented through rules), while the estimated tip-to-sprout anastomosis parameters do account for prohibited self-loops.

In the BC Model, the estimated diffusion coefficient $\tilde{D}_{\mathrm{BC}}$ is about approximately

twice as large as the coefficient used in the Model 2 PDEs ($D = 10^{-3}$). Further, $\tilde{D}_{BC}$ increases as a_e decreases. This occurs as the BC model attempts to capture the long tails in TC density that occur due to EC VE as a_e decreases. The chemotactic coefficient, $\tilde{\chi}_{\mathrm{BC}}$, increases as a_e increases.

4.5.2.2 Case 2: Tip-to-tip anastomosis occurs with probability 1 ($a_n = 1$ in the CA model)

In Figs. 4.11 and 4.12, tip-to-tip anastomosis occurs with probability $a_n = 1$, and TC VE is neglected. Both PDE models give good agreement with the averaged CA simulation results. For $a_e = 0.1$, EC VE produces short tails in TC density (see Fig. 4.11c). However, TC annihilation caused by tip-to-tip anastomosis means the EC VE is less pronounced than when tip-to-tip anastomosis is inactive (see Fig. 4.8c). We have also confirmed that both PDE models agree with the averaged CA simulation results for $P_p = 10^{-2}$ (results not shown). Based on the TC mass metrics (integral of TC density in x at $t = 2.0$) and TC RMSE (see Figs. 4.12a and 4.12c-4.12d), we conclude that the Model 2 PDEs agree slightly better with the averaged CA simulation results than the BC model. When $0 < a_e < 0.1$, neither model captures the long tails in the TC density caused by EC VE (results not shown).

The estimated branching rates for the BC model and the Model 2 PDEs decrease as a_e increases (results not shown). This is reasonable, given that as a_e increases, more TCs are annihilated via tip-to-sprout anastomosis resulting in a lower branching rate. Further, the estimated branching rates are much lower than the calculated rate. The estimated values for $\tilde{\lambda}_{\mathrm{BC}}$ are slightly less than the values for $\tilde{\lambda}$, as the BC model must compensate for the non-linear term $(1 - N - E)^2$ which appears in the branching term in the Model 2 PDEs (but not in the BC model). As in the previous case, the estimated values for $\tilde{\beta}_e/\mu$ are very close to those for $\tilde{a}_e$ and, further, are much lower than the CA values for a_e.

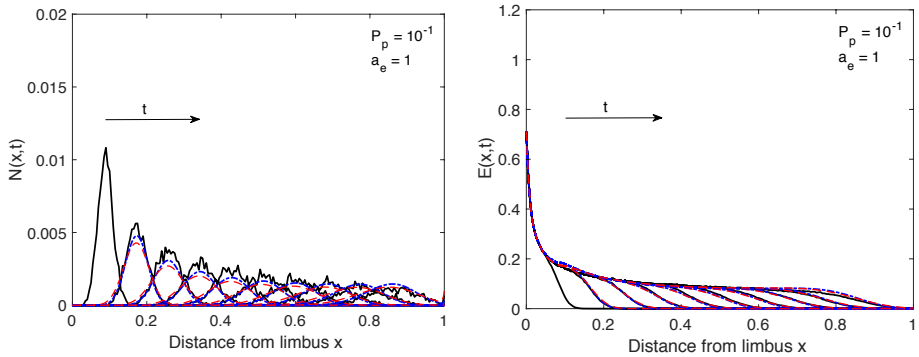

(a) TC density (b) EC density

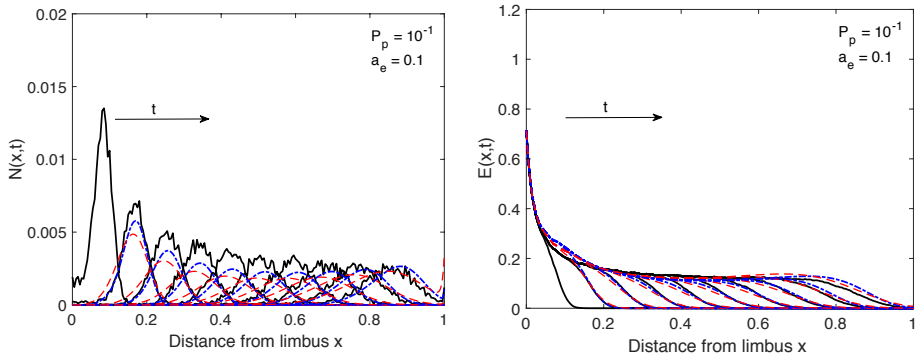

(c) TC density (d) EC density

Figure 4.11: Model 2, TC VE neglected ($a_n = 1$) Comparisons. TCs interact with ECs through tip-to-sprout anastomosis and EC VE, and TCs are annihilated through tip-to-tip anastomosis. TC and EC densities increase as the probability of tip-to-sprout anastomosis, a_e, decreases. The branching probability is $P_p = 10^{-1}$. (a)-(d) Column-averaged CA simulation results (black solid curve) are shown at times $t = 0.2, 0.4, \cdots, 2.0$ (arrow shows direction of increasing time). The migrating TC front exhibits short tails at early time points (t=0.4-0.8) (see (c)), as EC VE prevents movement of TCs. Model 2 PDEs (blue dashed-dot curve, equations (4.7)-(4.9)), and modified BC model (red dashed curve, equations (4.13)-(4.15)) solutions shown from $t = 0.4 - 2.0$. Both models agree with the CA simulation results.

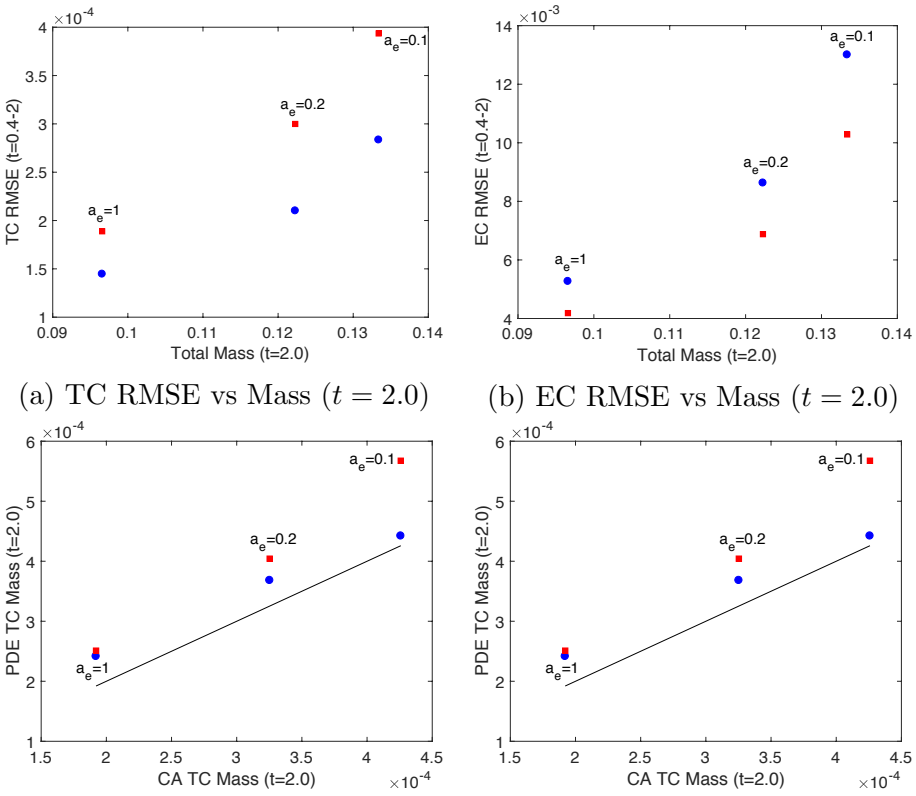

(a) TC RMSE vs Mass ($t = 2.0$)

(b) EC RMSE vs Mass ($t = 2.0$)

(c) TC Mass ($t = 2.0$)

(d) EC Mass ($t = 2.0$)

Figure 4.12: Model 2, TC VE neglected ($a_n = 1$) Comparisons. TCs interact with ECs through tip-to-sprout anastomosis and EC VE, and TCs are annihilated through tip-to-tip anastomosis. TC and EC densities increase as the probability of tip-to-sprout anastomosis, a_e, decreases. The branching probability is $P_p = 10^{-1}$. (a)-(d) Model 2 PDEs = blue circles, BC Model = red squares. (a)-(b) The relative difference between the RMSEs are comparable for $a_e = 0.2$ and $a_e = 0.1$, but larger than for $a_e = 1$. (c)-(d) The mass calculated from both models are comparable to the CA mass (black line). Both models agree with the CA simulation results.

In the BC Model, the estimated diffusion coefficient $\tilde{D}_{\mathrm{BC}}$ is approximately twice the value of the diffusion coefficient used in the Model 2 PDEs ($D = 10^{-3}$) and increases as a_e decreases, as the BC model attempts to capture the long tails in the TC density that arise due to EC VE. The chemotactic coefficient, $\tilde{\chi}_{\mathrm{BC}}$ increases as a_e increases.

4.6 Discussion

We have developed two-dimensional CA models of corneal angiogenesis based on the snail-trail process that account for TC VE (Model 1) and, additionally, EC VE (Model 2). In Model 1, TCs interact with TCs via tip-to-tip anastomosis with probability $a_n \in [0, 1]$ and TC VE with probability $(1 - a_n)$. In Model 2, in addition to TC interaction with TCs, TCs interact with ECs via tip-to-sprout anastomosis with probability $a_e \in [0, 1]$ and EC VE with probability $(1 - a_e)$. As in Chapters 2 and 3, we derived one-dimensional PDE models for the TC and EC densities associated with CA Models 1 and 2. For Model 2, we derived PDEs for the case $a_e = 1$, with $a_n = 1$ or 0. We compared our PDE models and the BC model to averaged CA simulation results to assess agreement and distinguish the effects of VE.

We note that the PDE models are derived using a mean-field approximation, which places constraints on the probabilities with which interactions can occur in the CA model. It is well known that high birth (branching) and death (anastomosis) rates (relative to the motility rate) give rise to correlation effects that cannot be captured by mean-field continuum models. Thus, we postulate that deviations of our PDE model solutions from the averaged CA simulation results, which occur for high branching rates and/or active anastomosis, are caused by a break down in the mean-field assumption. We rectified this discrepancy by fitting the PDE models to averaged CA simulation results and estimating parameters in the PDE models

that control processes from which correlations arise. In particular, we estimated the branching rate, and the parameters that control tip-to-tip anastomosis and tip-to-sprout anastomosis, in Model 1 and 2, respectively. We also used this approach to capture EC VE effects instead of deriving more complicated non-linear mean-field PDE models (which we found in the previous chapter led to backward heat equations).

We found that our Model 1 PDEs and the BC model were in good agreement with averaged CA Model 1 simulation results when TC mass is low, and TC VE effects negligible. However, when the TC mass is high, averaged CA simulations indicate that TC VE produces a front that steepens at the back as TCs are prevented from moving towards the TAF source by other TCs. As the TC mass increases, the BC model is unable to capture the increasing effects of TC VE, while the non-linear chemotactic terms in the Model 1 PDEs have been derived for this purpose.

Both the BC Model and the Model 2 PDEs capture the averaged CA Model 2 simulation results when EC VE effects are negligible. As we reduce the probability of tip-to-sprout anastomosis in the CA model, thus increasing macroscale EC VE effects, long tails in the TC density form, as TCs are rendered immobile behind the migrating TC front (within the EC front). This behaviour contrasts with TC VE effects, where forward movement of TCs is restricted by other TCs located ahead of the EC front (therefore, TCs are located within the TC front). Neither PDE model captures the increasingly long tails in the TC density due to EC VE. In the context of angiogenesis, however, network connections are prevalent, and thus, strong EC VE effects, which prevent connections via tip-to-sprout anastomosis, may not be relevant. In general, however, the differences in PDE model performance are not significant enough to distinguish which PDE models perform better, as differences can be attributed to noise (accuracies of fitting method, PDE solutions etc.), and thus we conclude that both models perform well.

In general, we conclude that our non-linear model should be used when single-

species exclusion effects are pronounced, while linear or non-linear models can be used when single or multi-species exclusion effects are negligible at the macroscale. More generally, we note that TC-EC interactions in the CA and PDE models produce less dense networks than when TCs interact with TCs only, as tip-to-sprout anastomosis annihilates TCs, and EC VE further prohibits TC movement. Further, for vessel networks that are less dense, the pronounced effects of TC VE do not arise (as the TC density is low). This should be considered when developing angiogenesis models, as including or excluding TC-EC interactions has a marked effect on the vessel densities.

We note that by fitting the mean-field PDE models to averaged CA simulation results to estimate parameters, we are able to capture more complicated scenarios in the PDE and CA models. For example, we could implement branching and/or anastomosis when a sprout is of a certain length (i.e. length restrictions) in the CA model. Instead of deriving more complicated non-linear PDE models to capture these interactions, we exploited the structure of the mean-field PDEs and fitted them to CA simulations to estimate the branching rate and parameters controlling anastomosis. This approach enabled us to include a wider range of interactions in the CA model that would have been intractable to include in our discrete to continuum framework. We note, however, that a different approach is required to capture pronounced EC VE effects and, in future work, we intend to derive such a model.

In this chapter, we quantified the descriptive power of continuum models in terms of goodness of fit metrics. An advantage of PDE models is their ability to predict population behaviour. In the next chapter, we use goodness of fit metrics to classify the predictive power of the Model 1 and Model 2 PDEs, as well as the BC model.

Chapter 5

Predictive Power of Continuum Models

In previous chapters, we systematically derived three continuum descriptions from two-dimensional CA implementations of the snail-trail model of corneal angiogenesis. We showed that these PDE models capture various motility mechanisms and interactions, such as VE and anastomosis. We also found that the modified phenomenological snail-trail model of Byrne and Chaplain (Byrne and Chaplain, 1995a) could capture the same macroscopic behaviour as our systematically-derived PDE models except when TC VE effects are non-negligible. In these earlier thesis chapters, we were evaluating the *descriptive* power of PDE models. An important use of PDE models is their ability to *predict* population behaviour, especially as they may provide insight that cannot be determined from experiment. In this chapter, we illustrate how PDE models can be used to predict the behaviour of the averaged CA simulation results. We then use goodness of fit metrics to compare the predictions generated by different PDE models.

5.1 Introduction

In Chapters 2, 3 and 4, we derived three continuum snail-trail models of angiogenesis: Model 0 (no VE), Model 1 (TC VE), Model 2 (TC and EC VE) and compared their solutions and those of the BC model to averaged CA simulation results. We found that our systematically-derived PDEs agree better than the BC model with averaged CA simulation results when TC VE is non-negligible at the macroscale, and that our systematically-derived PDEs and BC model both fail when EC VE is pronounced at the macroscale. In all other instances, our derived PDE models and the BC model are able to capture averaged CA simulation results (see Chapters 2, 3, 4). Thus, in previous chapters, we have been assessing descriptive power; the ability of the PDE models to capture averaged CA simulation results.

PDE models can also be used to predict population behaviour. In this way they may provide insight that cannot easily be determined from experiment, especially if it is impractical to run experiments for long periods of time. PDE models also provide a tractable framework for predicting responses to potential therapeutic strategies early in the drug development process. In this chapter, we will consider the predictive power of our systematically-derived PDE models and the BC model.

To assess predictive power, we fit the PDE models to averaged CA simulation results at a select number of time points. We then use the parameter estimates to simulate the PDE models at later time points. We then quantify the predictive power of the PDE models using goodness of fit metrics to compare our predictions with averaged data from the CA simulations. This process will be explained in detail later.

In Chapter 4, we considered two goodness of fit metrics: RMSEs and mass (calculated from the PDE models compared to that calculated from averaged CA simulation results). In this chapter, we will also include the Akaike Information Criterion (Akaike, 1973) (AIC) as a goodness of fit measure. The AIC (defined mathematically

in detail later) is typically used to discriminate between and to rank models (see, for example, Benzekry et al. (2014); Baker et al. (2005b); Motulsky and Christopoulos (2004); Burnham and Anderson (2002); Burnham et al. (2011); Baker et al. (2005a)). In particular, the model with the lowest AIC value is typically that which best approximates the data (see for example Baker et al. (2005b); Benzekry et al. (2014)). Indeed, it is common to use both RMSEs and the AIC as goodness of fit measures (see Benzekry et al. (2014)). The advantage of the AIC (based on information-theoretic approaches), is that it allows models to be ranked (see Motulsky and Christopoulos (2004); Burnham and Anderson (2002); Burnham et al. (2011)). By comparing the solutions of the different PDE models to averaged CA simulation results, and ranking the models in terms of goodness of fit, we are assessing the predictive power of the PDE models. We note that we use existing methods (developed by others, for example Benzekry et al. (2014)) to discriminate between PDE models rather than developing new ones, as our focus is to assess the predictive power of continuum models developed in this thesis. In the discussion, we outline alternative approaches and possible extensions.

The remainder of this chapter is organised as follows. In the next section, we restate the PDE models derived in previous chapters that form the basis for the comparisons performed in this chapter. Thereafter, we explain how we assess predictive power, and the goodness of fit metrics used to discriminate between the PDE models. We then present our results.

5.2 Continuum Models

In this section, we restate the continuum models that we will compare in this chapter.

Model 0: No VE

In Chapter 2, we derived the non-volume excluding model in which the TC and EC density, respectively, $N(x,t)$, $E(x,t)$ satisfy

$$\begin{aligned}\frac{\partial N}{\partial t} &= (1-a_n^{\mathrm{M0}}N-a_e^{\mathrm{M0}}E)\left(D_{\mathrm{M0}}\frac{\partial^2 N}{\partial x^2}-\chi_{\mathrm{M0}}\frac{\partial}{\partial x}\left(N\frac{\partial c}{\partial x}\right)\right)\\ &\quad -\mu(a_n^{\mathrm{M0}}N^2+a_e^{\mathrm{M0}}NE)+\lambda_{\mathrm{M0}}cN, \qquad (5.1)\\ \frac{\partial E}{\partial t} &= \mu N+a_n^{\mathrm{M0}}N\left(\mu N+D_{\mathrm{M0}}\frac{\partial^2 N}{\partial x^2}-\chi_{\mathrm{M0}}\frac{\partial}{\partial x}\left(N\frac{\partial c}{\partial x}\right)\right), \qquad (5.2)\end{aligned}$$

subject to

$$D_{\mathrm{M0}}\frac{\partial N}{\partial x}-\chi_{\mathrm{M0}}N\frac{\partial c}{\partial x}=0, \text{ at } x=0,1, \qquad (5.3)$$

where the diffusion and chemotactic coefficients, D_{M0} and χ_{M0}, are defined by

$$D_{\mathrm{M0}}=\frac{\mu h^2}{4}=\lim_{\tau\to 0}\frac{P_m h^2}{4\tau}, \quad \chi_{\mathrm{M0}}=\mu k h^2=\lim_{\tau\to 0}\frac{P_m k h^2}{\tau}, \qquad (5.4)$$

and μ and λ_{M0} are defined as

$$\mu=\lim_{\tau\to 0}\frac{P_m}{\tau}, \quad \lambda_{\mathrm{M0}}=\lim_{\tau\to 0}\frac{P_p}{\tau}. \qquad (5.5)$$

In contrast to Chapter 2, we suppose that $a_n^{\mathrm{M0}}\in[0,1]$ and $a_e^{\mathrm{M0}}\in(0,1]$ if $a_n^{\mathrm{M0}}>0$, that is, tip-to-sprout anastomosis cannot be implemented without active tip-to-tip anastomosis, as otherwise this may lead to ill-posedness in the continuum model (see Chapter 2).

Models 1 and 2: TC VE and TC, EC VE

These equations were derived in Chapter 4. We set $B = 0$ for Model 1 and $B = 1$ for Model 2:

$$\begin{aligned}\frac{\partial N}{\partial t} &= D\left((1 - a_n N - Ba_e E)\frac{\partial^2 N}{\partial x^2}\right) - \chi\left((\underbrace{1 - 2N}_{\text{TC VE}} + a_n N - Ba_e E)\frac{\partial N}{\partial x}\frac{\partial c}{\partial x}\right. \\ &\quad \left. + N(1 - N - Ba_e E)\frac{\partial^2 c}{\partial x^2}\right) - \mu\left(a_n N^2 + Ba_e NE\right) + \lambda cN\underbrace{(1 - N - BE)^2}_{\text{VE}}, \end{aligned} \tag{5.6}$$

$$\begin{aligned}\frac{\partial E}{\partial t} &= \mu N\left(\underbrace{1 - N}_{\text{TC VE}} + 2a_n N\right) - N\left(D\underbrace{(1 - 2a_n)}_{\text{TC VE}}\frac{\partial^2 N}{\partial x^2}\right) - \chi N\left((1 - a_n)\underbrace{\frac{\partial c}{\partial x}\frac{\partial N}{\partial x}}_{\text{TC VE}},\right. \\ &\quad \left. + a_n\frac{\partial}{\partial x}\left(N\frac{\partial c}{\partial x}\right)\right), \end{aligned} \tag{5.7}$$

subject to

$$D\frac{\partial N}{\partial x} - \chi N\underbrace{(1 - (1 - a_n)N)}_{\text{TC VE}}\frac{\partial c}{\partial x} \mid_{x=0,1} = 0, \tag{5.8}$$

where D, χ, μ and λ are defined as in equations (5.4) and (5.5).

The equations for Model 1 and 2 differ from those in Model 0 by the TC VE terms in the motility mechanism and the VE term in the branching mechanism, which are indicated by underbraces in equations (5.6) and (5.7). We note that Model 1 with $a_n = 1$, and Model 2 with $a_n = 1, a_e = 1$, reduce to Model 0 with the exception of the branching term, which is linear in Model 0 and non-linear in Models 1 and 2, incorporating TC VE and TC and EC VE, respectively.

BC Model

The modified version of Byrne and Chaplain's (Byrne and Chaplain, 1995a) dimensionless model of angiogenesis introduced in Chapter 2 is given by:

$$\frac{\partial N}{\partial t} = D_{\mathrm{BC}}\frac{\partial^2 N}{\partial x^2} - \chi_{\mathrm{BC}}\frac{\partial}{\partial x}\left(N\frac{\partial c}{\partial x}\right) + \lambda_{\mathrm{BC}}Nc - \beta_e NE - \beta_n N^2, \tag{5.9}$$

$$\frac{\partial E}{\partial t} = \frac{2}{h}\left|D_{\mathrm{BC}}\frac{\partial N}{\partial x} - \chi_{\mathrm{BC}}N\frac{\partial c}{\partial x}\right|, \tag{5.10}$$

subject to

$$D_{\mathrm{BC}}\frac{\partial N}{\partial x} - \chi_{\mathrm{BC}}N\frac{\partial c}{\partial x} \mid_{x=0,1} = 0. \tag{5.11}$$

A discussion of initial conditions and those parameters that will be estimated follows in the next section.

5.3 Methodology: Assessing Predictive Power

As before, our synthetic data comprise column-averaged CA simulation results (averaged over 200 realizations; see equations (2.12) and (2.13) from Chapter 2 for definitions) generated using CA Models 1 and 2. (Descriptions of these CA models can be found in Chapter 4). To reiterate, Model 1 incorporates TC VE with probability $1 - a_n$ and tip-to-tip anastomosis with probability a_n. Model 2 incorporates TC-TC interactions, EC VE with probability $1 - a_e$, and tip-to-sprout anastomosis with probability a_e.

Since, in general, one would not know which mechanisms generated a given set of continuum data, we compare the different PDE models to the cell density in order to determine which PDE model best approximates the synthetic data. We compare solutions of the Model 0 and 1 PDEs and the BC model to averaged simulation results generated using CA Model 1. We will also compare solutions to Model 0 and 2 PDEs

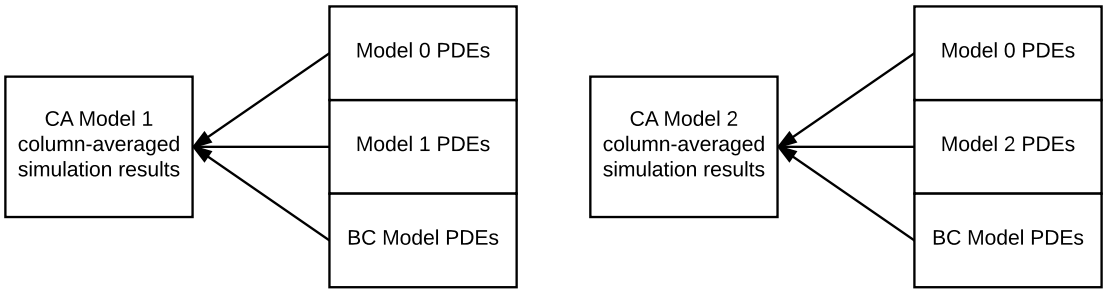

Figure 5.1: Schematic illustrating the PDE models we will compare to averaged CA simulation results to assess predictive power.

and the BC model to averaged simulations generated using CA Model 2. A schematic of the comparisons we make is presented in Fig. 5.1. The purpose of these comparisons is to determine whether non-volume excluding PDE models (Model 0 PDEs and BC model) can account for averaged CA simulations incorporating TC VE (CA Model 1 rules) and additionally, EC VE (CA Model 2 rules) by suitable choice of parameters. We aim also to determine how well the different PDEs we derived predict averaged CA simulation results.

To assess predictive power, we fit each PDE model to averaged CA simulation results at times $t = 0.4, 0.6, 0.8, 1$. Thereafter, we use the parameter estimates to simulate the PDEs at times $t = 1.2, 1.4, 1.6, 1.8, 2.0$ and compare these predictions with data generated from the CA Model 1 and at times $t = 1.2, 1.4, 1.6, 1.8$ for comparison to averaged simulations generated using CA model 2. For CA Model 2, we do not consider time $t = 2.0$ in order to avoid boundary effects which might skew the goodness of fit calculations. The methodology we use is similar to that employed by Benzekry et al. (2014), where ODE models were fit to temporal data and then the estimated parameters used to predict data at later times.

The fitting is performed using MATLAB's *lsqnonlin* with a tolerance of 10^{-6} from 40 randomly chosen initial guesses within parameter bounds (in parallel using 2 to 4 workers). We use *nlparci* to calculate the confidence intervals using the Jacobian

output from *lsqnonlin*. In general, using *lsqnonlin* to estimate the parameters for each of the continuum models, for a single set of averaged simulation results generated by the CA, takes approximately 1 hour (parameter bounds used in the fitting algorithm are stated in Appendix E). The PDE models are solved numerically using the methods introduced in Chapter 2 (see Section 2.4.2).

5.3.1 Estimated Continuum Model Parameters

The parameters that we estimate for each PDE model are listed in Table 5.1. In PDE Models 1 and 2, we estimate the branching rate, λ, and parameters controlling tip-to-tip and tip-to-sprout anastomosis, a_n and a_e, respectively (recall discussions in Chapter 4 motivating the estimation of these parameters due to correlations). In the BC Model, we estimate all parameters: the diffusion coefficient D_{BC}, chemotactic coefficient χ_{BC}, the branching rate λ_{BC}, and the parameters controlling tip-to-tip and tip-to-sprout anastomosis, β_n and β_e, respectively. Similarly, in PDE Model 0, in addition to the branching rate and parameters controlling anastomosis, we estimate the diffusion and chemotactic coefficients, D_{M0} and χ_{M0}, respectively.

From here on, we indicate parameter values estimated through fitting with tildes (e.g. $\tilde{\lambda}$) to distinguish them from parameters that have been calculated directly (or set). Parameter values that have been calculated directly using the discrete to continuum framework developed in this thesis are stated in Table 5.2, along with CA model parameters.

The reader is referred to Chapter 2 for a discussion of the parameter values in Table 5.2. The values of D and χ in Table 5.2 are those used in PDE Model 1 and 2, μ is used in PDE Models 0, 1, and 2, and t_{IC} (initial condition) is used in all continuum models. The remaining CA model parameters (P_p, a_n, a_e) are specified in each result section.

As in previous chapters, we use the column-averaged CA simulation results for

Table 5.1: Continuum model parameters estimated through fitting the models to averaged CA simulation results generated using Model 1 (CA M1) and 2 (CA M2).

Model 0 PDEs				
CA M1	$\tilde{D}_{\mathrm{M0}}$	$\tilde{\chi}_{\mathrm{M0}}$	$\tilde{\lambda}_{\mathrm{M0}}$	$\tilde{a}_n^{\mathrm{M0}}$
CA M2	$\tilde{D}_{\mathrm{M0}}$	$\tilde{\chi}_{\mathrm{M0}}$	$\tilde{\lambda}_{\mathrm{M0}}$	$\tilde{a}_e^{\mathrm{M0}}$
Model 1 and 2 PDEs				
CA M1	$\tilde{\lambda}$	$\tilde{a}_n$		
CA M2	$\tilde{\lambda}$	$\tilde{a}_e$		
BC Model				
CA M1	$\tilde{D}_{\mathrm{BC}}$	$\tilde{\chi}_{\mathrm{BC}}$	$\tilde{\lambda}_{\mathrm{BC}}$	$\tilde{\beta}_n$
CA M2	$\tilde{D}_{\mathrm{BC}}$	$\tilde{\chi}_{\mathrm{BC}}$	$\tilde{\lambda}_{\mathrm{BC}}$	$\tilde{\beta}_e$

Table 5.2: Microscale and Macroscale Model Parameters. $P_{i,j}^{x\pm}$ and $P_{i,j}^{y\pm}$ are movement probabilities defined in equations (2.5) and (2.6).

CA Parameters	R	h	P_m	k	τ	$\bar{K}_{IC}$	$P_{i,j}^{x\pm}$	$P_{i,j}^{y\pm}$
	200	1/200	1	100	1/160	32	$\frac{1}{2}$,0	$\frac{1}{4}$
PDE Parameters	D	χ	μ	t_{IC}				
	10^{-3}	0.4	160	0.2				

the TC and EC densities, $N_i(K_{IC})$ and $E_i(\bar{K}_{IC})\,\forall i$, respectively, at discrete time step $\bar{K}_{IC}$, as initial conditions $(N(x,t_{IC}), E(x,t_{IC}))$ for the continuum models (see equation 2.35).

5.3.2 Goodness of Fit Metrics

Our metrics quantify goodness of fit with respect to spatial and temporal points. We calculate the residuals (squared difference between PDE model solutions and averaged CA simulation results) for each time point, over all spatial points ($0 \leq i \leq R$ for the CA, and $x = ih$ for the continuum models, where R is the number of columns on the lattice and h is the lattice spacing), for which we wish to measure the goodness of fit. We quantify goodness of fit using a modified RMSE and the corrected AIC, $\mathrm{AIC_c}$ (defined below).

In contrast to the RMSE used in Chapter 4, the modified RMSE includes a term of the form $(P - K)$, which penalises models with more parameters (as in Benzekry et al. (2014)):

$$\text{TC RMSE} = \sqrt{\frac{\sum_{l=1}^{P}(N_{\text{PDE}}^{l} - N_{\text{CA}}^{l})^2}{P-K}}, \tag{5.12}$$

$$\text{EC RMSE} = \sqrt{\frac{\sum_{l=1}^{P}(E_{\text{PDE}}^{l} - E_{\text{CA}}^{l})^2}{P-K}}. \tag{5.13}$$

In equations (5.12) and (5.13), P is the number of points at which we quantify goodness of fit (all lattice points for specific times), e.g. if we wanted to calculate the RMSEs for the time points $t = 1.2, 1.4, 1.6, 1.8$, $P = (R+1) * 4 = 201 \times 4$ (R is the number of columns on the lattice in the CA model). In equations (5.12) and (5.13), K is the number of parameters we estimate and N_{PDE}, E_{PDE}, N_{CA} and E_{CA} are the PDE and CA model TC and EC densities, respectively, at each point. Given the relative size of P (minimum of 201, RMSEs calculated for all lattice points for a single time point) and K (maximum of 4, see Table 5.1), the additional $-K$ term in the denominator has little effect on the RMSEs.

The definition of the AIC for the TC and EC densities when using least-squares fitting is as follows:

$$\text{TC AIC} = P \log\left(\frac{\sum_{l=1}^{P}(N_{\text{PDE}}^{l} - N_{\text{CA}}^{l})^2}{P}\right) + 2(K+1) \tag{5.14}$$

$$\text{EC AIC} = P \log\left(\frac{\sum_{l=1}^{P}(E_{\text{PDE}}^{l} - E_{\text{CA}}^{l})^2}{P}\right) + 2(K+1), \tag{5.15}$$

where P and K are defined as in the description of the RMSEs. For small sample sizes (P), it is typical to calculate the corrected AIC value (Sugiura, 1978; Hurvich

and Tsai, 1989), $\mathrm{AIC_c}$,

$$\mathrm{TC\,AIC_c} = \mathrm{TC\,AIC} + \frac{2(K+1)(K+2)}{(P-K-2)}, \tag{5.16}$$

$$\mathrm{EC\,AIC_c} = \mathrm{EC\,AIC} + \frac{2(K+1)(K+2)}{(P-K-2)}, \tag{5.17}$$

where $P > K+2$. It is typical to use the corrected AIC value (see Benzekry et al. (2014); Motulsky and Christopoulos (2004); Burnham and Anderson (2002)), which, for large sample size, converges to the AIC value. We rank models according to their $\mathrm{AIC_c}$ values, the model with the lowest $\mathrm{AIC_c}$ being judged the best model. We note that when using least squares fitting, the $\mathrm{AIC_c}$ is essentially the logarithm of the residuals. Further, we note that since we use residuals (typically $\ll 1$), the $\mathrm{AIC_c}$ values are typically negative and large.

Visualisation of Goodness of Fit Metrics

In what follows, we plot the RMSEs and $\mathrm{AIC_c}$ values for each PDE model against mass determined from the averaged CA simulation results at the final time point. Here, mass is the integral of the cell density over x (spatial variable), and mass determined from the averaged CA simulation results provides us with a single data point for a particular set of CA parameter values. This allows us to visualise the RMSEs and $\mathrm{AIC_c}$ values, as we did in Chapter 4. We note that we cannot compare RMSEs and $\mathrm{AIC_c}$ values calculated for PDE models across averaged CA simulation results generated with different sets of parameter values, as the RMSEs and $\mathrm{AIC_c}$ cannot be normalised in a straightforward manner. It is the relative difference between the $\mathrm{AIC_c}$ and RMSE values for different continuum models that indicate which model is a better fit (lowest value of the RMSE and $\mathrm{AIC_c}$).

We also compare mass calculated from the PDE models to that from the CA model as another goodness of fit measure. When we plot these mass comparisons,

the CA mass is visualised as a continuum (a straight line connecting individual mass data points).

5.4 Model 1: Predictive Power Results

In this section, we compare the Model 0 PDEs, Model 1 PDEs and the BC Model to synthetic data generated using CA Model 1. The branching probabilities and anastomosis probabilities we consider in the CA model are given in Table 5.3. We consider a total of 25 combinations of P_p and a_n.

Table 5.3: Averaged CA Model 1 simulation results: Probabilities governing branching and tip-to-tip anastomosis. We consider each combination of a_n and P_p for a total of 25 combinations.

P_p	10^{-3}	10^{-2}	2×10^{-2}	3×10^{-2}	4×10^{-2}
a_n	0.02	0.05	0.1	0.15	0.2

The goodness of fit metrics are given in Figs. 5.2-5.3. All models approximate the TC and EC masses at time $t = 2$ from the averaged CA simulations well, except at high mass, where the Model 1 PDEs more closely approximate the mass (see Figs. 5.2a and 5.2b). Supporting this finding, we see that the predictions from the Model 0 and the BC model PDEs deviate from the averaged CA simulation results at high mass (see Figs. 5.2c-5.2f). From Figs. 5.3a and 5.3b, we see that at the first prediction point ($t = 1.2$), the TC and EC RMSEs for all models are clustered together and all models approximate the averaged CA simulation results well. At later times ($t = 1.2 - 2.0$), the differences between the RMSEs for each PDE model increase as the mass increases. Further, the RMSEs for the Model 1 PDEs are lower for both the TC and EC densities than those for the Model 0 PDEs and the BC Model. The AIC_c values (see Figs. 5.3e and 5.3f) corroborate these findings. We conclude that the Model 1 PDEs is the better predictive model as the mass increases. Estimated parameter values are given in Tables E.4, E.5 and E.6 of Appendix E.

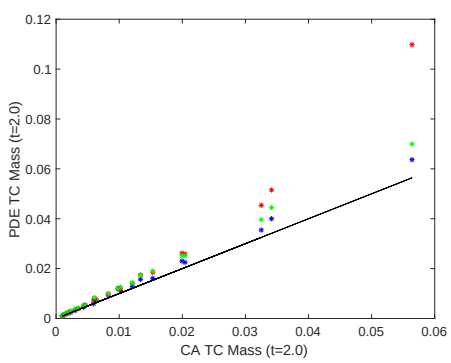

(a) TC Mass ($t = 2.0$)

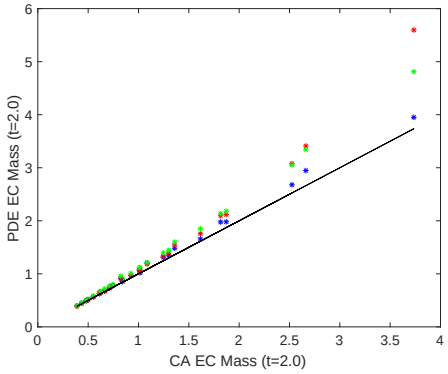

(b) EC Mass ($t = 2.0$)

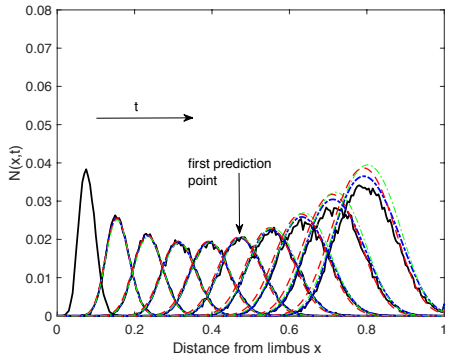

(c) TC density, $(a_n, P_p) = (0.1, 2 \times 10^{-2})$

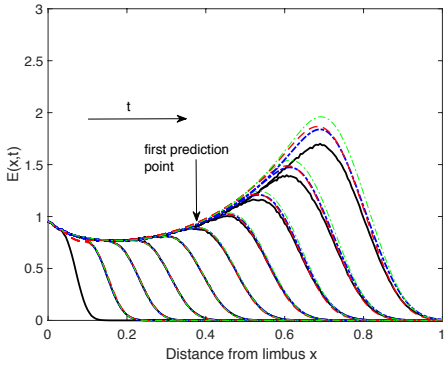

(d) EC density, $(a_n, P_p) = (0.1, 2 \times 10^{-2})$

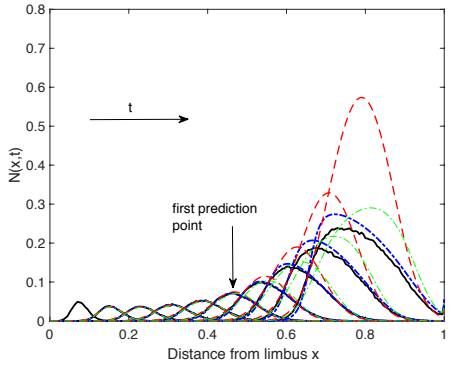

(e) TC density, $(a_n, P_p) = (0.05, 4 \times 10^{-2})$

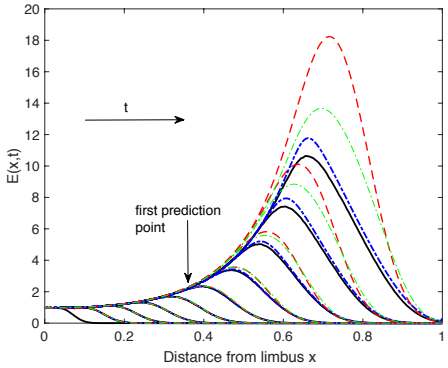

(f) EC density, $(a_n, P_p) = (0.05, 4 \times 10^{-2})$

Figure 5.2: Model 1: PDE Predictions. Key: Black = CA, Blue = Model 1 PDEs, Red = BC Model, Green = Model 0 PDEs. (a), (b) All PDE models approximate the TC and EC mass from the CA model (black line) well, except at high mass, where the Model 1 PDEs outperforms the other models. Each CA mass point corresponds to a distinct set of CA parameter values (see Table 5.3). (c)-(f) TC and EC density predictions ($t = 1.2, 1.4, \cdots, 2.0$) for a particular set of parameter values (indicated in caption). Our results suggest that PDE Model 1 is the best predictive model when the TC density is high (see (e) and (f)); otherwise, all PDE models have similar predictive power.

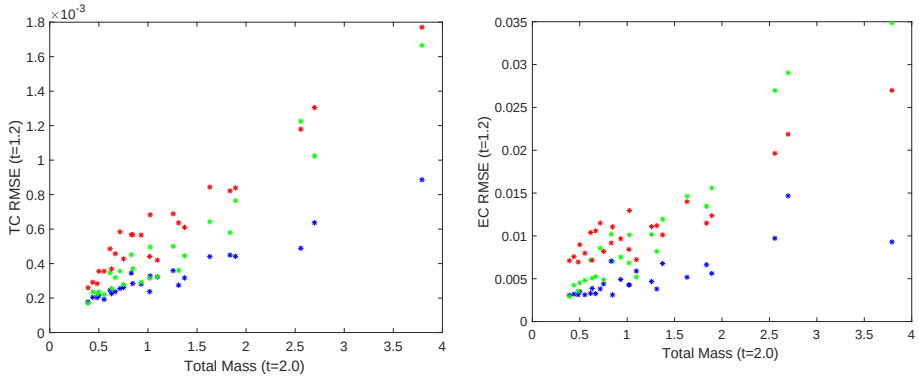

(a) TC RMSE ($t = 1.2$)

(b) EC RMSE ($t = 1.2$)

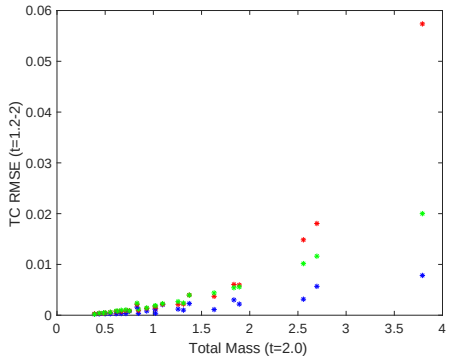

(c) TC RMSE ($t = 1.2 - 2.0$)

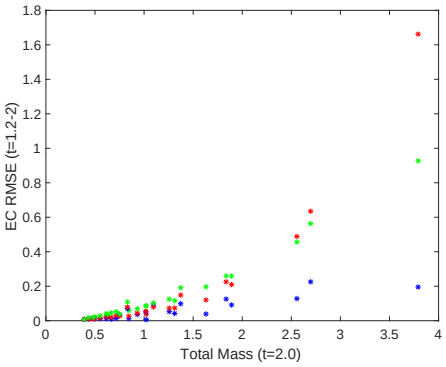

(d) EC RMSE ($t = 1.2 - 2.0$)

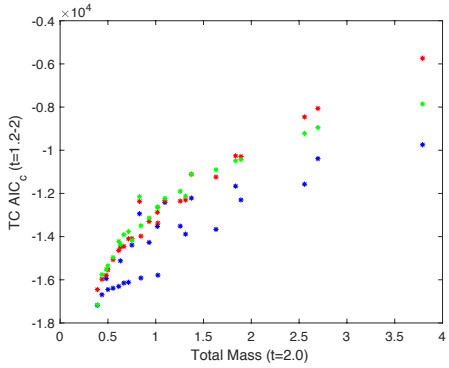

(e) TC AIC_c ($t = 1.2 - 2.0$)

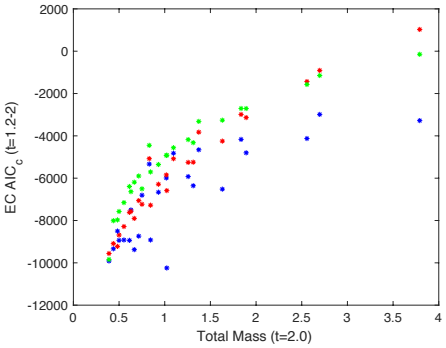

(f) EC AIC_c ($t = 1.2 - 2.0$)

Figure 5.3: Model 1 Predictions: RMSEs and AIC_c values for each PDE model visualised against mass determined from CA model (each mass point corresponds to a particular set of CA model parameters). Key: Blue = Model 1 PDEs, Red = BC Model, Green = Model 0 PDEs. (a), (b) The TC and EC RMSEs are similar at $t = 1.2$ (first prediction) as all models capture the averaged CA simulation results well. (c), (d) At subsequent times, the TC and EC RMSEs are clustered together for all three models, except when the mass increases introducing TC VE effects. (e), (f) The AIC_c values corroborate the RMSE findings in (c) and (d). When TC VE effects are important, the Model 1 PDEs are the better predictive model.

5.5 Model 2: Predictive Power Results

We compare the Model 2 PDEs and the BC Model to data generated from CA Model 2. Thus, the averaged CA simulation results incorporate TC and EC VE during branching, and in the motility mechanism, TC VE occurs with probability $1 - a_n$, and tip-to-sprout anastomosis and EC VE occur with probability a_e and $1 - a_e$, respectively. As in Chapter 4, we consider two values of a_n, $a_n = 1$ (tip-to-tip anastomosis occurs with probability 1) and $a_n = 0$ (no tip-to-tip anastomosis). The branching and anastomosis probabilities are given in Table 5.4. Recall that for the Model 0 PDEs to remain well-posed (see Section 5.2), tip-to-tip anastomosis must be active when tip-to-sprout anastomosis is active, and thus we only consider the predictive power of Model 0 when $a_n = 1$.

Table 5.4: Averaged CA Model 2 simulation results: Branching and tip-to-sprout anastomosis probabilities. We consider each combination of a_e and P_p for a total of 6 combinations.

P_p	10^{-2}	10^{-1}	
a_e	0.1	0.2	1

5.5.1 Model 2, $a_n = 0$ (no tip-to-tip anastomosis)

In Figs. 5.4 and 5.5, we consider predictive power statistics. From Figs. 5.5a and 5.5b, it is clear that both models predict the averaged CA results at time $t = 1.2$ equally well (there is little difference between their RMSEs). This is corroborated by the plots in Figs. 5.4c-5.4f, which show the TC and EC densities at the first, predicted time point (for $a_e = 0.1, 1$ and $P_p = 10^{-1}$). At subsequent time points, the predictions from both models diverge from the averaged CA simulations, with the predictions from the BC model diverging more than those from the Model 2 PDEs. This is supported by the RMSEs and AIC_c values for $t = 1.2 - 1.8$ (see Figs. 5.5c, 5.5d, 5.5e and 5.5f), which are larger for the BC model than the Model 2 PDEs. The PDE models also poorly predict and overestimate the TC and EC mass at $t = 1.8$

(see Figs. 5.4a-5.4b). In general, the worst predictions occur when EC VE effects are important ($a_e = 0.1$ produces longer tails in the TC densities).

We also note that the BC model predicts a wider TC distribution than the Model 2 PDEs (see Figs. 5.4c-5.4f). This is because the estimated diffusion coefficient for the BC model is larger than that of the Model 2 PDEs ($\tilde{D}_{BC} = 20 \times 10^{-3} > D = 10^{-3}$, see Table E.11 in Appendix E for estimated parameter values) as the BC model attempts to capture the long tails in the TC density (see Fig. 5.4e). Estimated parameter values can be found in Tables E.10-E.12 of Appendix E.

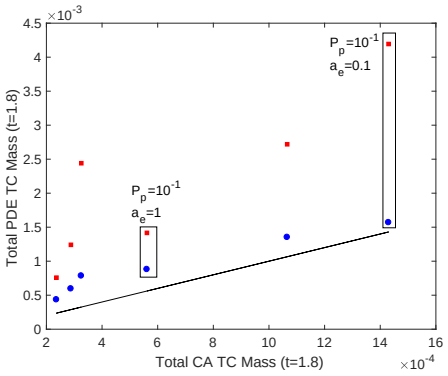

(a) TC Mass ($t = 1.8$)

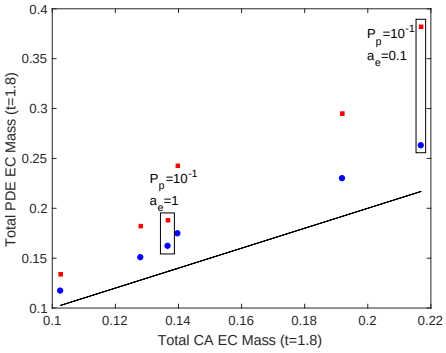

(b) EC Mass ($t = 1.8$)

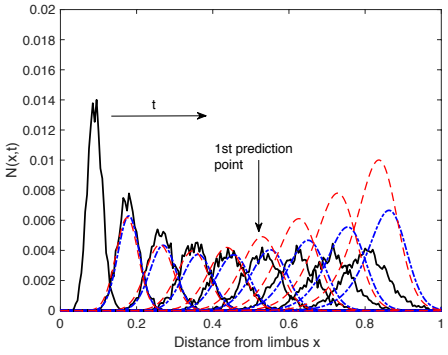

(c) TC density ($a_e = 1, P_p = 10^{-1}$)

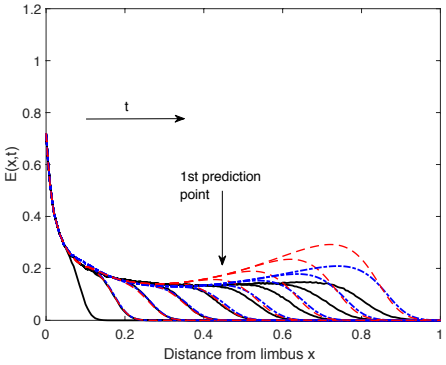

(d) EC density ($a_e = 1, P_p = 10^{-1}$)

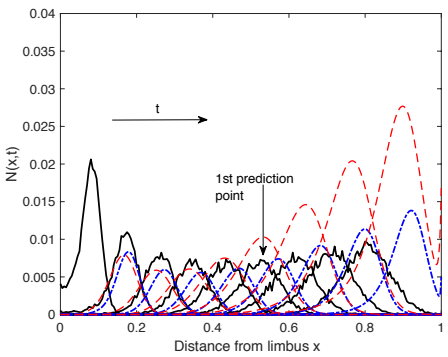

(e) TC density ($a_e = 0.1, P_p = 10^{-1}$)

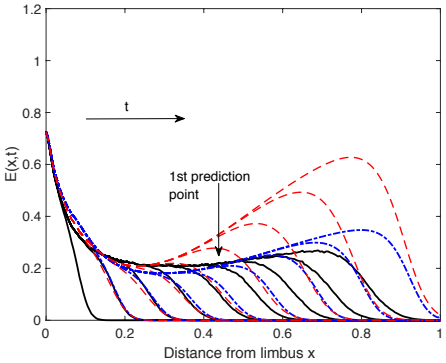

(f) EC density ($a_e = 0.1, P_p = 10^{-1}$)

Figure 5.4: Model 2 ($a_n = 0$): PDE Predictions. Key: Black = CA, Blue = Model 2 PDEs, Red = BC Model. (a), (b) As the CA mass increases, PDE mass predictions deviate from the CA mass (black line), though the Model 2 PDEs more closely predict the CA mass. Each CA mass point corresponds to a distinct set of CA parameter values (see Table 5.4). Boxed data points correspond to CA parameters used in (c)-(f). (c)-(f) TC and EC density predictions ($t = 1.2, 1.4, \cdots, 1.8$) for parameter values given in captions. (c), (d) While both models predict behaviour at $t = 1.2$ well, the predictions deviate at subsequent times and become worse as a_e decreases (see (e), (f)).

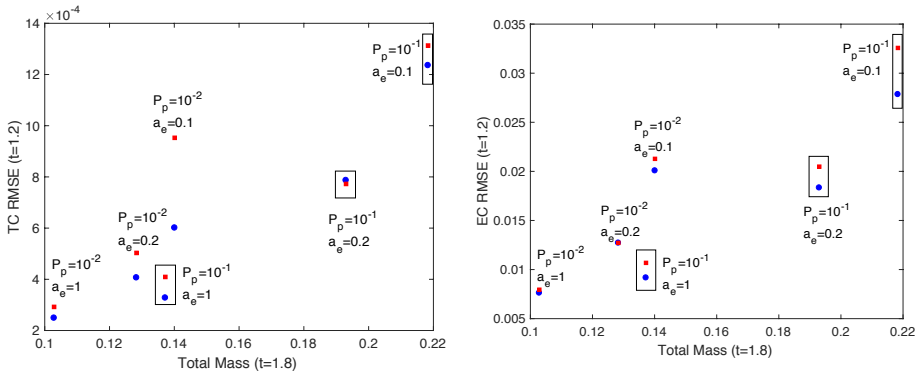

(a) TC RMSE ($t = 1.2$)

(b) EC RMSE ($t = 1.2$)

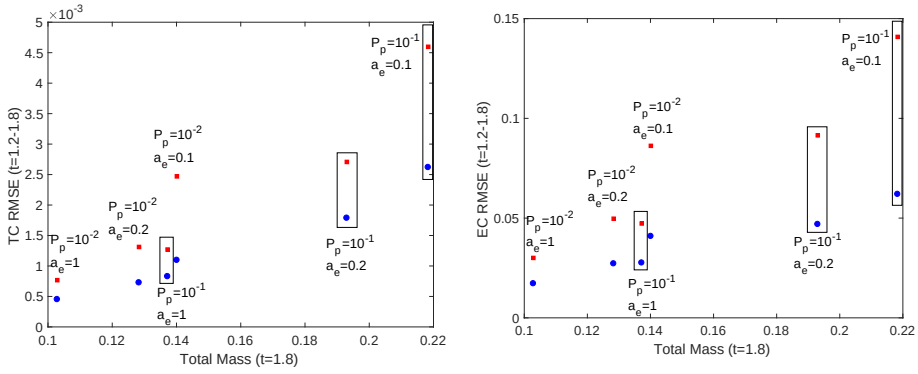

(c) TC RMSE ($t = 1.2 - 1.8$)

(d) EC RMSE ($t = 1.2 - 1.8$)

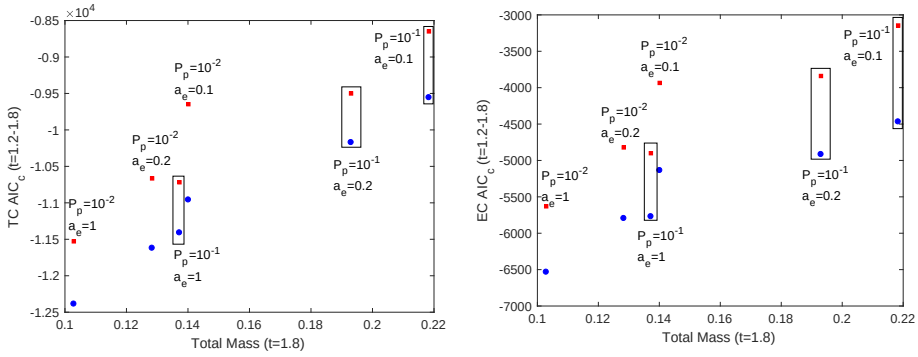

(e) TC AIC_c ($t = 1.2 - 1.8$)

(f) EC AIC_c ($t = 1.2 - 1.8$)

Figure 5.5: Model 2 ($a_n = 0$) Predictions: RMSEs and AIC_c values for each PDE model visualised against mass determined from CA model (each mass point corresponds to a particular set of CA model parameters, see Table 5.4). Key: Blue = Model 2 PDEs, Red = BC Model. (a), (b) Both models predict behaviour at time $t = 1.2$ well, as the difference between the RMSEs at each mass point is small. (c), (d) For $t = 1.2 - 1.8$, the Model 2 PDEs predict the averaged CA simulation results better (lower RMSEs). (e), (f) AIC_c values for each PDE model at each mass point follow the same trend as the RMSEs (see (c) and (d)). CA branching parameters: $P_p = 10^{-1}$ (boxed data), $P_p = 10^{-2}$ (unboxed data).

5.5.2 Model 2, $a_n = 1$ (tip-to-tip anastomosis)

We compare Model 0 and 2 PDEs, and the BC Model to synthetic data generated using CA Model 2, with TC VE neglected in the motility mechanism i.e $a_n = 1$, and tip-to-tip anastomosis occurring with probability 1. The branching and tip-to-sprout anastomosis probabilities in the CA model are unchanged (same as the $a_n = 0$ case, see Table 5.4). In the Model 0 and 2 PDEs, $a_n = 1$, and $\beta_n = \mu a_n$ in the BC model.

At $t = 1.2$, all models approximate the averaged CA results well (similar RMSEs, see Figs. 5.7a and 5.7b), though the fit deteriorates as a_e decreases (compare Figs. 5.6c and 5.6e). For the TC densities, the Model 2 and Model 0 PDEs have lower RMSEs than the BC model, indicating a better fit (and better predictions). At subsequent time points ($t = 1.2 - 1.8$), the agreement between the model predictions and the averaged CA simulation results declines (see Figs. 5.6c-5.6f). The BC model has larger RMSEs and AIC_C values than the Model 0 or 2 PDEs (see Figs. 5.7c-5.7f).

For $a_e = 0.1$, the Model 0 PDEs produce larger TC RMSE and AIC_c values than the Model 2 PDEs, indicating a poorer fit to the TC densities. Given that the Model 0 PDEs and Model 2 PDEs differ only in the branching term (when $a_n = 1$), this is noteworthy. For $a_e = 0.1$, the Model 0 PDEs produce a TC distribution that is narrower and has a higher amplitude than that predicted by the Model 2 PDEs at $t = 1.8$ (see Fig. 5.6e). Considering the estimated parameter values (see Tables E.7-E.12 in Appendix E), the PDE models differ most in the branching rate and the diffusion coefficient. For the Model 0 PDEs, the estimated branching and diffusion parameters are $\tilde{\lambda}_{\text{M0}} = 7.9667$ and $\tilde{D}_{\text{M0}} = 3 \times 10^{-4}$, respectively, whilst for Model 2, they are $\tilde{\lambda} = 6.8856$ and $D = 10^{-3}$. Further, the effective branching rate is actually lower in the Model 2 PDEs, as $\tilde{\lambda} c N$ is multiplied by $(1 - N - E)^2 < 1$. Thus, at times $t = 1.2 - 1.8$, the Model 0 PDEs predict that more TCs are produced via branching than the Model 2 PDEs, and secondly, predicts a narrower TC distribution (due to smaller diffusion coefficient), giving rise to the discrepancy between Model 0 and 2

PDE predictions (see Fig. 5.6e).

For $a_e = 1$, the discrepancy between Model 0 and 2 PDE predictions is negligible (see Fig. 5.6c). A higher value of a_e produces more loops via tip-to-sprout anastomosis, and thus fewer branchings (as many TCs are annihilated by tip-to-sprout anastomosis) and lower total density ($N + E$ lower for $a_e = 1$ than for $a_e = 0.1$). Therefore, the difference in the branching rates for $a_e = 1$ is not as large as for $a_e = 0.1$ (for the Model 0 PDEs, $\tilde{\lambda}_{\text{M0}} = 4.2784$ and for the Model 2 PDEs, $\tilde{\lambda} = 3.9829$). Further, the diffusion coefficient for the Model 0 PDEs when $a_e = 1$ is $\tilde{D}_{\text{M0}} = 7 \times 10^{-4}$, which is closer to the calculated value of $D = 10^{-3}$ in the Model 2 PDEs. The case with $a_e = 0.1$ illustrates the benefits of calculating some of the model parameters via the discrete-continuum framework, especially with regards to predictions.

In general, we conclude that the Model 2 PDEs is the better predictive model at $t = 1.2$, though all models agree reasonably well with the averaged CA simulations results. At times $t = 1.4 - 1.8$, all models deviate from the averaged CA simulation results (though the Model 2 PDEs perform best), with the worst predictions occurring for $a_e = 0.1$. Certainly, when we allow loops to form via tip-to-tip anastomosis and tip-to-sprout anastomosis all PDE models yield better predictions than when we exclude loop formation by tip-to-tip anastomosis. This can, in part, be explained by the fact that active tip-to-tip anastomosis annihilates more TCs, leading to less pronounced EC VE effects. Estimated parameter values can be found in Tables E.10-E.12 in Appendix E.

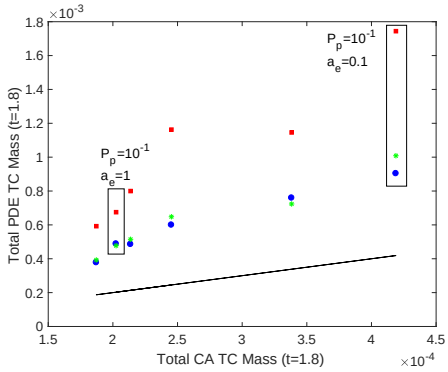

(a) TC Mass ($t = 1.8$)

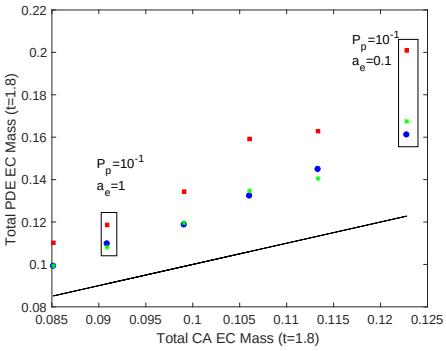

(b) EC Mass ($t = 1.8$)

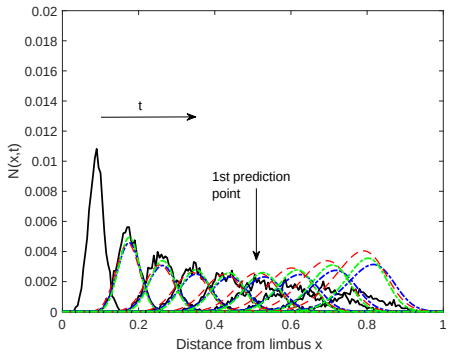

(c) TC density ($a_e = 1, P_p = 10^{-1}$)

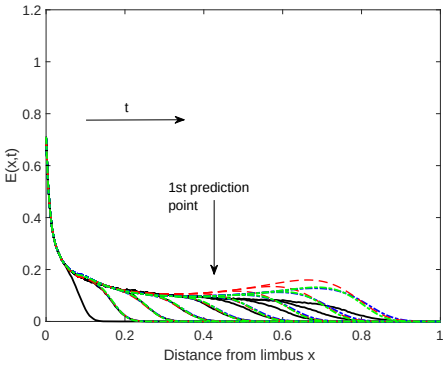

(d) EC density ($a_e = 1, P_p = 10^{-1}$)

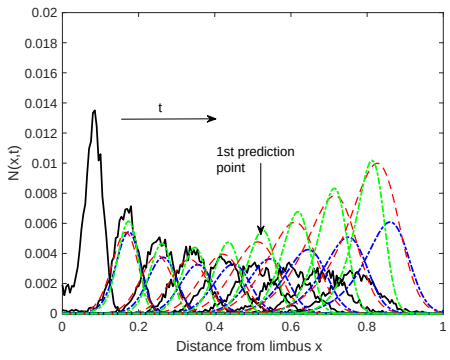

(e) TC density ($a_e = 0.1, P_p = 10^{-1}$)

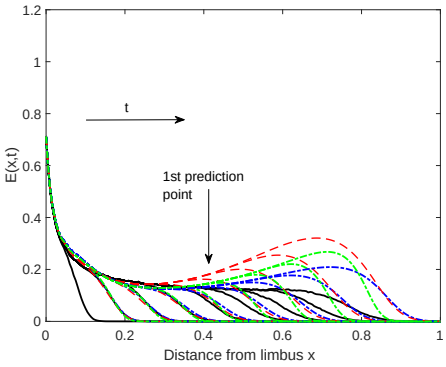

(f) EC density ($a_e = 0.1, P_p = 10^{-1}$)

Figure 5.6: Model 2 ($a_n = 1$): PDE Predictions. Key: Black = CA, Blue = Model 2 PDEs, Red = BC Model, Green = Model 0 PDEs. (a), (b) All models overestimate the CA mass (black line), though Model 0 and 2 approximate the mass more closely than the BC model. Each CA mass point corresponds to a distinct set of parameter values used in the CA model (see Table 5.4). Boxed data points correspond to CA parameters used in (c)-(f). (c)-(f) TC and EC density predictions ($t = 1.2, 1.4, \cdots, 2.0$). (c), (d) The PDE models predict the behaviour of averaged CA results at $t = 1.2$ well, but deviate from averaged CA simulations at subsequent time points. (e), (f) As a_e decreases, and EC VE effects become more important (long tails in the TC density), PDE predictions deviate more significantly from averaged CA simulations. Generally, Model 2 is the better predictive model.

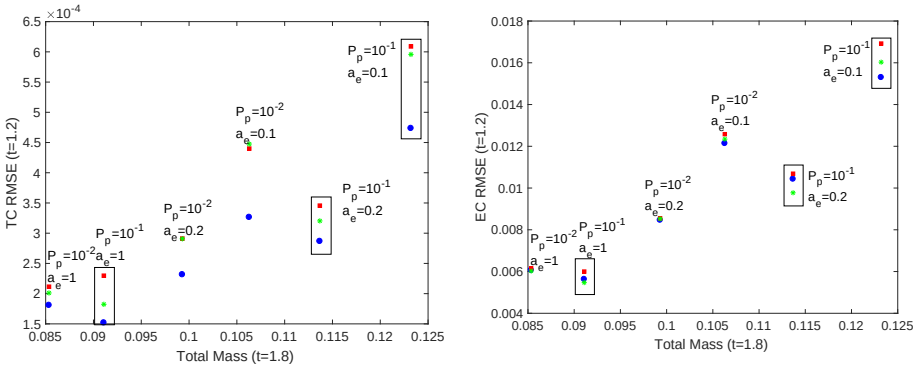

(a) TC RMSE ($t = 1.2$)

(b) EC RMSE ($t = 1.2$)

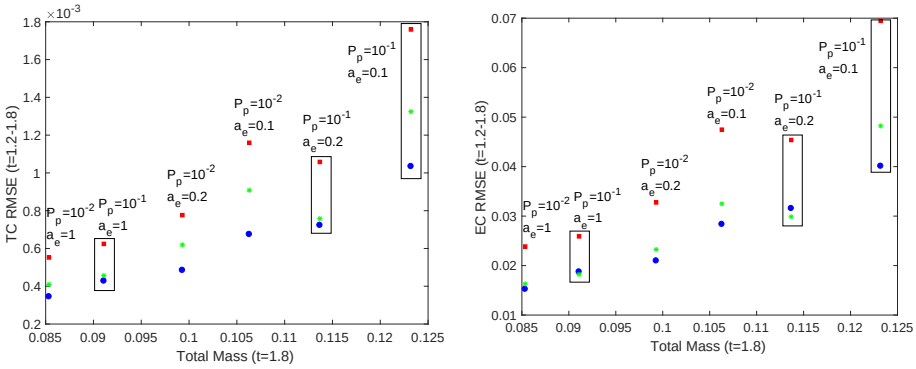

(c) TC RMSE ($t = 1.2 - 1.8$)

(d) EC RMSE ($t = 1.2 - 1.8$)

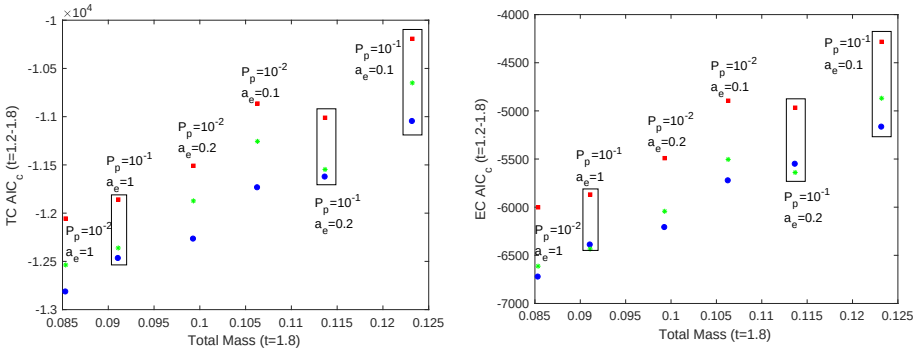

(e) TC $\mathrm{AIC_c}$ ($t = 1.2 - 1.8$)

(f) EC $\mathrm{AIC_c}$ ($t = 1.2 - 1.8$)

Figure 5.7: Model 2 ($a_n = 1$) Predictions: RMSE and $\mathrm{AIC_c}$ values for each PDE model visualised against mass determined from CA model (each mass point corresponds to a particular set of CA model parameters). Key: Blue = Model 2 PDEs, Red = BC Model, Green = Model 0 PDEs. (a), (b) At $t = 1.2$, all models predict the averaged CA simulation results well (similar RMSEs). (c), (d) The relative difference between the RMSEs for the BC model and the Model 0/2 PDEs is largest when $a_e = 0.1$. The Model 2 PDEs have the lowest RMSE (best predictive model). (e), (f) $\mathrm{AIC_c}$ values corroborate the RMSE findings. The BC model $\mathrm{AIC_c}$ values are larger than the corresponding values for the Model 0 and 2 PDEs, indicating poorer predictions from the BC model. CA branching parameters: $P_p = 10^{-1}$ (boxed data), $P_p = 10^{-2}$ (unboxed data).

5.6 Predictive and Descriptive Power

In this chapter, we have assessed the predictive power of PDE models. We have also performed the same analysis to assess the descriptive power of the PDE models. These results can be found in Appendix E. We note that for descriptive power, we fit the continuum models to averaged CA simulation results at all time points. Here, we highlight key differences between descriptive and predictive power.

The parameters estimated in the descriptive case (see Appendix E) are more tightly constrained (i.e. tighter confidence intervals) than in the predictive power case. This is reasonable, as many of the distinctive features of the averaged CA simulation results occur at later time points (e.g. the branching probability increases as the TC front approaches the TAF source and, thus, is higher for $t > 1$). We expect, therefore, more variability (larger confidence intervals) in the parameter values in the predictive case.

The RMSEs and AIC_c values are lower in the descriptive than predictive case. This is reasonable, as the fit is being performed over all time points when assessing descriptive power, thereby resulting in better goodness of fit metrics. The estimated parameters are quite different in the predictive and descriptive cases. As an example, we consider the BC model and Model 2 PDEs fit to averaged CA simulations generated by CA Model 2. The estimated parameters values for a branching probability of $P_p = 10^{-2}$, a tip-to-sprout anastomosis probability of $a_e = 0.1$ and a tip-to-tip anastomosis probability of $a_n = 1$ are given in Tables 5.5 and 5.6.

In general, the branching rates and anastomosis parameters are higher in the predictive case than in the descriptive case. The effective branching rates decrease at later time points as anastomosis increases (due to higher branching). In the BC model, the estimated diffusion coefficient is higher in the descriptive case, as the PDE model attempts to account for the longer tails in TC density that persist at later times (due to EC VE). Further, the confidence intervals for the estimated branching rates

Table 5.5: Model 2 ($a_n = 1, P_p = 10^{-2}, \lambda = 1.6, a_e = 0.1$): Model 2 PDEs fitted parameter values.

Descriptive				
P_p	λ	a_e	$\tilde{\lambda}$	$\tilde{a}_e$
10^{-2}	1.6	0.1	1.8305 ± 0.0578	0.1168 ± 0.0017
Predictive				
P_p	λ	a_e	$\tilde{\lambda}$	$\tilde{a}_e$
10^{-2}	1.6	0.1	5.1484 ± 0.2512	0.1636 ± 0.0036

Table 5.6: Model 2 ($a_n = 1, P_p = 10^{-2}, \lambda = 1.6, a_e = 0.1$): BC Model fitted parameter values.

Descriptive			
$\tilde{D}_{\mathrm{BC}}$	$\tilde{\chi}_{\mathrm{BC}}$	$\tilde{\lambda}_{\mathrm{BC}}$	$\tilde{\beta}_e$
0.0032 ± 0.0002	0.3539 ± 0.0022	1.9091 ± 0.0474	15.0410 ± 0.2189
Predictive			
$\tilde{D}_{\mathrm{BC}}$	$\tilde{\chi}_{\mathrm{BC}}$	$\tilde{\lambda}_{\mathrm{BC}}$	$\tilde{\beta}_e$
0.0016 ± 0.0001	0.3553 ± 0.0026	6.6074 ± 0.2052	22.7990 ± 0.4169

and anastomosis parameters are larger in the predictive than in the descriptive case.

We also note that the BC model predicts symmetric TC density distributions (see Sections 5.4 and 5.5), i.e. the TC distribution at each time point is symmetric in x. However, in the descriptive case, the BC model may produce asymmetric TC density distributions (see Section E.2 in Appendix E). The estimated parameter values in the descriptive case allow this asymmetric behaviour.

5.7 Discussion

In this chapter, we evaluated the predictive power of 4 PDE models of angiogenesis: the Model 0 PDEs and the BC model incorporate no explicit VE, Model 1 PDEs incorporate TC VE and Model 2 PDEs incorporate TC VE and EC VE. The BC model is linear in the diffusive, chemotactic and branching terms (assuming a linear TAF gradient), while the other PDE models are non-linear.

We assessed the predictive power of the different continuum models by fitting them to averaged simulation results generated using CA Models 1 and 2. Given that the Model 1 and 2 PDEs were derived from CA Models 1 and 2, respectively, we estimate only the branching rate and parameters controlling anastomosis. In the Model 0 PDEs and the BC model, we estimate the diffusion and chemotactic coefficients as well. In so doing, we evaluated whether simpler PDE models (including linear models) can account for macroscale non-linearities by suitable choice of parameter values.

To assess the predictive power, we fit the continuum models to the averaged CA simulation results at times $t = 0.4, 0.6, 0.8, 1.0$. We then used the estimated parameter values estimated to predict the averaged CA simulation results generated using CA Model 1 at times $t = 1.2, 1.4, \cdots 2.0$ and CA Model 2 at times $t = 1.2, 1.4, \cdots 1.8$. We quantified the predictive power of the continuum models using the following goodness of fit metrics: RMSEs and AIC_c values. We also compared the mass calculated from the continuum models to the true mass from the CA at the final time point.

In Appendix E, we quantified the descriptive power of the continuum models, by fitting them to averaged CA simulation results at all times (excluding the initial conditions), $t = 0.4, 0.6 \cdots 2.0$. In the discussion that follows, we will refer to both descriptive and predictive power.

For CA Model 1, all continuum models were comparable in terms of descriptive and predictive power, according to the AIC_c, RMSEs and mass approximations except when TC VE effects were significant at the macroscale, in which case the Model 1 PDEs performed better. The Model 1 PDEs include non-linear terms that account for TC VE effects in the diffusive and chemotactic terms, while the Model 0 PDEs and the BC model do not. We found that all continuum models predicted the averaged CA simulations at $t = 1.2$ (first prediction) well, and that the predictions from the Model 0 PDEs and the BC model deviated from the averaged CA simulation results at later times.

In CA Model 2, we have TC-TC and TC-EC interactions, and thus chose to examine the extremes, total TC VE, $a_n = 0$ and no TC VE, ($a_n = 1$, tip-to-tip anastomosis only). With these choices of a_n and $a_e \in [0.1, 1]$, we examined parameter ranges where there are likely to be differences in the predictive and descriptive powers of the continuum models. When tip-to-tip anastomosis is inactive, we found that the descriptive power of the Model 2 PDEs and BC model are similar. Both PDE models perform well, unless EC VE effects are significant. Both models predict averaged CA simulation results at $t = 1.2$ well, and thereafter, both models deviate from the averaged CA simulation results. According to goodness of fit metrics, the Model 2 PDEs are the better predictive model, though both models are poor predictors.

For active tip-to-tip anastomosis, the Model 0 and 2 PDEs, and the BC Model have similar descriptive power. In terms of predictive power, all models predict averaged CA simulations at $t = 1.2$ well. At later time points, the Model 2 PDEs outperform the Model 0 PDEs and the BC model. In general, when tip-to-tip anastomosis is active, the predictions from all PDE models are better than when it is inactive. Tip-to-tip anastomosis annihilates many TCs, and thereby dampens EC VE effects relative to cases for which tip-to-tip anastomosis is inactive.

In future, we will conduct a thorough sensitivity analysis and comparison of estimated parameters in the descriptive and predictive cases. We also remark that the goodness of fit metrics depend on the noise (accuracy) within the numerical solutions for each continuum model. Thus, where the goodness of fit metrics show no clear differences between the models, we have concluded that they have similar descriptive and predictive power. In cases where we have concluded that Model 1 or 2 PDEs are the better descriptive or predictive models, there are clear reasons for these choices, relating to non-negligible VE effects, which can be captured by the non-linearities in the Model 1 or 2 PDEs. Thus, simpler and/or linear continuum models will not always capture non-linear macroscale behaviour.

We were limited in terms of computational power (run time) in this study, but we have explored CA parameter spaces that give rise to regimes in which the continuum models differ in terms of descriptive and predictive powers. In future, we will explore a larger parameter space in the CA model, to produce a more comprehensive picture of the descriptive and predictive powers of the continuum models.

We have used non-linear least squares to estimate parameters, thereby implicitly assuming a Gaussian scatter (error) in our synthetic data (averaged CA simulation results). This assumption results in the AIC_c and RMSEs reducing to similar formulas (based on the residuals, squared differences between averaged CA simulations and PDE model solutions). In future work, we could quantify the error in the averaged CA simulation results and then use, for example, Bayesian methods to infer parameters in the continuum models, and utilise other model selection metrics/techniques based on a Bayesian approach (see Turner and Van Zandt (2012); Toni et al. (2009); Toni and Stumpf (2010); Oden and Prudencio (2013)).

Chapter 6

Relating Predictive and Descriptive Power to Network Structure

In this chapter, we use the framework developed in Chapters 2-5 to investigate whether it is possible to identify the best predictive and descriptive continuum model of population behaviour in terms of underlying network morphology generated by the CA models. This work is a proof of concept.

6.1 Introduction

In this thesis, we have developed a discrete to continuum framework that relates microscale and macroscale behaviours in different snail-trail models of corneal angiogenesis. In Chapters 2-4, we discussed the descriptive power of our continuum models; their ability to describe population behaviour. In Chapter 5, we detailed their predictive power. In this chapter, we explain how it may be possible to determine (choose) which continuum models have the best descriptive and/or predictive power based on the underlying network morphology generated by the CA models.

Experimental data of corneal angiogenesis may be in the form of images (see, for example, Connor et al. (2015)). Such images can be used to extract information about cell densities and/or morphology metrics (e.g. average length of sprouts, number of branch points, loops and mass/number of cells), provided the resolution of the data is sufficient (e.g. Connor et al. (2015); Smith et al. (2014, 2015); Smith (2013)). Thus, in the future, it may be possible to determine which continuum PDE models best predict and describe population behaviour by analysing the underlying network structure. In this chapter, we use our discrete-continuum framework to determine whether this is possible (see schematic in Fig. 6.1). We already know that the choice of CA model parameters affects the network structure (see Figs. 2.4 in Chapter 2, and Figs. 3.2a, 3.3a, 3.2b, 3.4a in Chapter 3). The network structure, in turn, produces distinct population behaviour (see Figs. 2.5 in Chapter 2, and Figs. 3.3 and 3.4 in Chapter 3). As we discussed in Chapter 4, distinct population behaviours (such as steepening of TC front caused by TC VE, and long tails in TC density caused by EC VE) allow us to distinguish continuum models. For example, the linear BC model cannot account for TC VE effects, while the Model 1 PDEs can. Thus, we can use this framework and insights gained to distinguish continuum models based on underlying network structure.

Our approach is motivated by ideas in other fields, for example, homogenization (Chapman et al., 2008; Shipley and Chapman, 2010; Penta and Ambrosi, 2015; Penta et al., 2015). In the aforementioned papers, a periodic network structure is assumed at the microscale, and upscaling is performed via asymptotic homogenization, to formulate PDEs for effective fluid transport at the tissue-scale. It has been an ongoing challenge to relax the assumption of network periodicity (see, for example, Bear (1988); Papanicolaou (1995); Papnicolaou and Varadhan (1982); Kozlov (1985); Davit et al. (2013); Cushman et al. (2002); Bruna and Chapman (2015)). The methodology we outline in this chapter allows for linking of network structures (which need not be

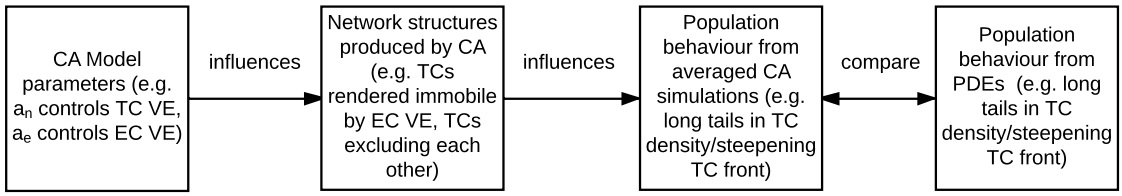

Figure 6.1: Schematic: Relating continuum models to network structure. From earlier chapters, we know that PDE solutions can capture certain features of population behaviour. Those features (e.g. tails in TC density/steepening TC front) arise through the choice of parameters in the CA model, which in turn influence individual network structures, and eventually macroscale behaviour (i.e. structure influences population behaviour and thereby influences which PDE we choose to capture it). As a proof of concept, we determine whether it is possible to relate the ability of the PDE models to predict and describe population behaviour to network structure i.e. we want to be able to choose the best descriptive and/or predictive model of population behaviour based on network structure.

periodic) with macroscale behaviours exhibited by PDE models.

6.2 Network Statistics, Predictive and Descriptive Power

In the previous chapter we assessed the predictive power of the PDE models in comparison to averaged CA simulation results using goodness of fit metrics. In this section, we relate the predictive power to underlying network structure (which ultimately influences population behaviour) extracted from the averaged CA simulations. We introduce the methodology for extracting network statistics from averaged CA simulations, and define a relative error for descriptive and predictive power. We note that all numerical methods are the same as outlined in Chapter 5.

6.2.1 Methodology for Extracting Network Statistics

As in previous chapters, we generate TC and EC density data from the CA simulations by averaging cell occupancy over the columns and multiple realizations (200) of the CA model. Each realization generates a network structure according to the CA rules

(see Chapters 2, 3 and 4). For each realization we collected the following statistics: number of branchings, number of loops formed by anastomosis and average sprout length (length of connections between branch points[1]) and loops, averaged over the number of sprouts). Over many realizations we extract information about the average number of branch points, loops formed by anastomosis, and averaged sprout length (averaged over many realizations). Further, as in Chapter 5, mass (equivalent measure of the number of cells) is calculated at the final time point (by integrating column-averaged cell densities over the spatial variable).

In what follows, we visualise these network statistics as functions of the branching and anastomosis probabilities used in the CA models. For CA Model 1, the branching and tip-to-tip anastomosis probabilities (25 combinations) are given in Table 5.3 in Section 5.4 in Chapter 5. For CA Model 2, the branching and anastomosis probabilities (6 combinations) are given in Table 5.4 in Section 5.5 in Chapter 5. As we considered fewer branching and tip-to-sprout anastomosis probabilities in CA Model 2, we add two additional tip-to-sprout anastomosis probabilities, $a_e = 0.01, 0.05$, which enables us to more clearly determine trends in network statistics (though we do not use these values of a_e when assessing predictive and descriptive power, as below $a_e = 0.1$, the PDE models are unable to account for non-negligible EC VE effects).

6.2.2 Relative Error

To more easily relate predictive power to network statistics, we need to compare goodness of fit across different averaged CA simulation results. For this purpose, we introduce the relative error, which measures the deviation of the continuum models from averaged CA simulation results, normalized by the true value of the EC and TC

[1]If a TC branched, the daughter TC produces a new sprout, whilst the parent remains.

densities (from the averaged CA simulation results), given by

$$\text{TC RE} = \frac{\mid N^i_{\text{PDE}} - N^i_{\text{CA}} \mid}{N^i_{\text{CA}}}, \text{ where } N^i_{\text{CA}} > 10^{-4},\ 0 \leq i \leq R \tag{6.1}$$

$$\text{EC RE} = \frac{\mid E^i_{\text{PDE}} - E^i_{\text{CA}} \mid}{E^i_{\text{CA}}}, \text{ where } E^i_{\text{CA}} > 10^{-2},\ 0 \leq i \leq R. \tag{6.2}$$

Here, we calculate the relative error when the TC and EC densities from the averaged CA simulation results exceed a threshold value, 10^{-4} and 10^{-2}, respectively. The thresholds are chosen based on the range of the TC and EC densities (the EC densities are always larger than the TC densities). Imposing threshold values ensures that we do not overestimate the error in the PDE solutions (i.e. if the TC density from the CA model is 10^{-5}, while the PDE solutions produce a TC density of 2×10^{-5}, the relative error is 100%). We calculate the relative errors for each time point of interest, and then we average the relative errors to determine a single relative error value for a particular time point or time interval. For example, we calculate equations (6.1) and (6.2) at $t = 1.2, 1.4, 1.6, 1.8$, and then average the resulting relative errors to determine a single relative error value, expressed as a percentage, for the time interval $t = 1.2 - 1.8$.

We now plot the network summary statistics, and relate these to descriptive and predictive power of the PDE models. In what follows, we present the predictive power statistics of Model 1 only, the predictive power statistics of Model 2 and descriptive power statistics of all models are included in Appendix E, Figs. E.2, E.4-E.6, and E.8-E.10.

6.2.3 Model 1: Network Features and Relative Errors

In Fig. 6.2 we show how varying the probabilities of tip-to-tip anastomosis (a_n) and branching (P_p) affects the morphology of the networks generated by the averaged CA simulations (e.g. the average length of sprouts, average number of branchings, average

number of anastomoses, and mass of cells).

Fewer TCs are annihilated as a_n decreases, and more TCs are introduced as P_p increases (number of branchings increase, see Fig. 6.2b), and thus the total cell mass increases (see Fig. 6.2a). The average number of tip-to-tip anastomoses generally increases as a_n decreases and P_p increases. Further, for fixed values of P_p, the maximum number of anastomoses occurs for $a_n = 0.05$. This is counterintuitive, as one would expect the number of anastomoses to increase as a_n increases. However, the higher a_n, the larger the number of TCs annihilated initially (at early times), and therefore there are fewer branchings, ultimately leading to fewer anastomoses than for a lower value of a_n. The average length of sprouts increases as the number of branchings and anastomoses decrease (as P_p and a_n decrease). This is expected, as new branchings introduce shorter sprouts, and anastomosis terminates sprout growth through TC annihilation.

The relative errors for $t = 1.2 - 2$ (prediction time points) for each PDE model are shown in Fig. 6.3. The Model 1 PDEs have lower relative errors than the BC model and Model 0 PDEs (compare Figs. 6.3a-6.3b to Figs. 6.3c-6.3f). The relative errors for the BC Model and Model 0 PDEs generally increase as a_n decreases and P_p increases (as mass increases). The range in the relative errors for the Model 1 PDEs is smaller than that for the Model 0 PDEs and the BC Model. The relative errors qualitatively agree with the findings determined using RMSEs and AIC_c values (see Figs. 5.3) in terms of which model best predicts the averaged CA simulation results. Comparison of Figs. 6.2 and 6.3 enables us to relate the relative errors to trends in the network morphology. We find that the Model 1 PDEs generate more accurate predictions as the mass and average number of branchings increase, and the average number of tip-to-tip anastomoses and sprout length decrease.

The reader is directed to Appendix E for a discussion of descriptive and predictive power in terms of network structure for Model 2 (see Figs. E.4-E.6, and E.8-E.10).

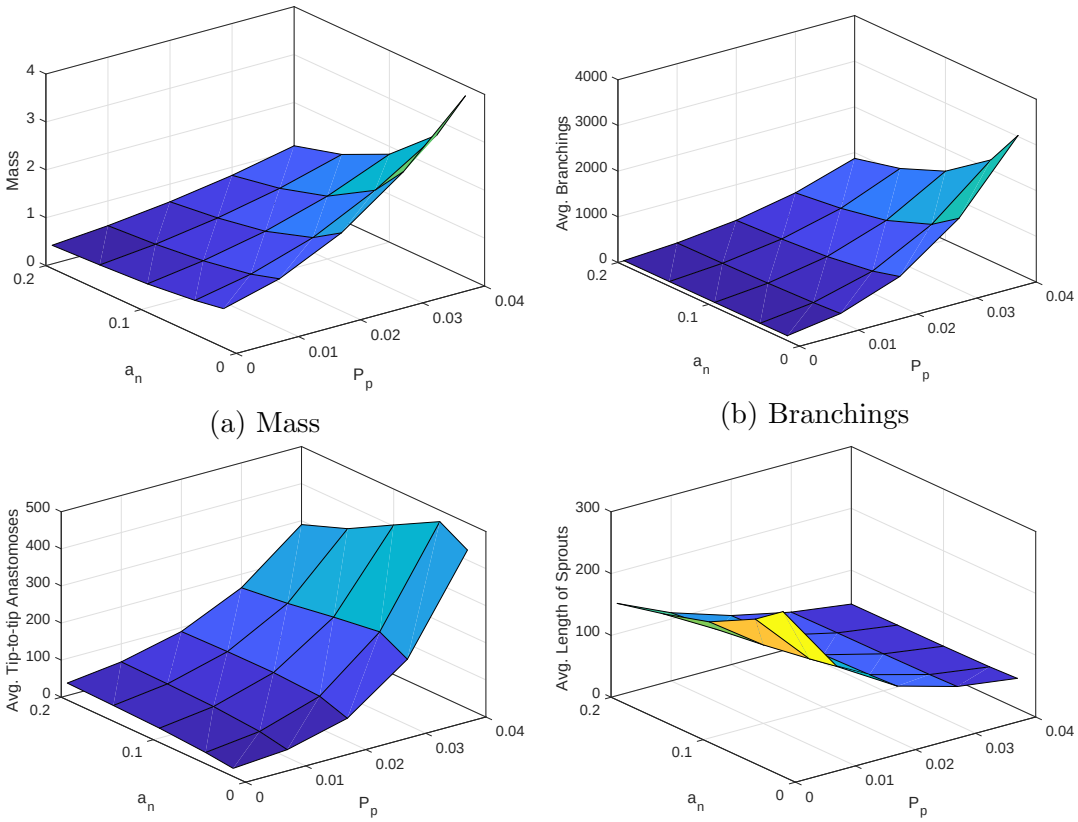

(a) Mass

(b) Branchings

(c) Tip-to-tip Anastomoses

(d) Sprout Length

Figure 6.2: Model 1 Network statistics. (a), (b) As the branching probability, P_p, increases and the anastomosis probability, a_n, decreases, the mass and average number of branchings increase. (c) The average number of anastomoses increases as a_n decreases and P_p increases, with the maximum occurring for $a_n = 0.05$ and $P_p = 4 \times 10^{-2}$. (d) The average length of sprouts, calculated as the number of cells in a sprout, increases as P_p and a_n decrease. Plots produced using MATLAB's *surf* function.

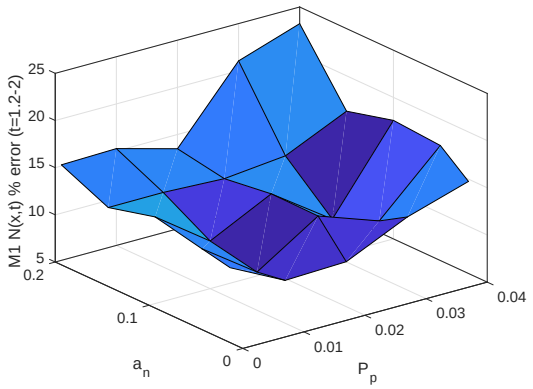

(a) M1 N(x,t) % error ($t = 1.2 - 2$)

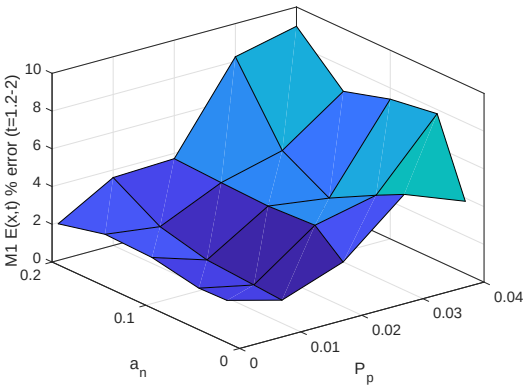

(b) M1: E(x,t) % error ($t = 1.2 - 2$)

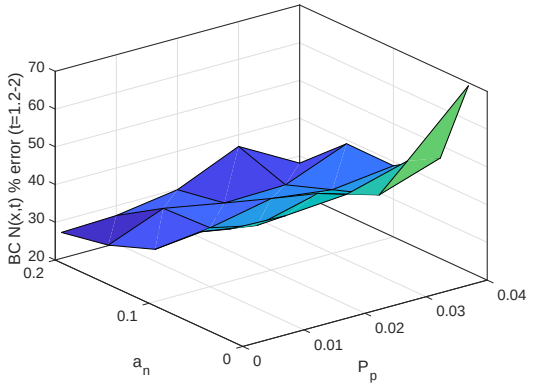

(c) BC : N(x,t) % error ($t = 1.2 - 2$)

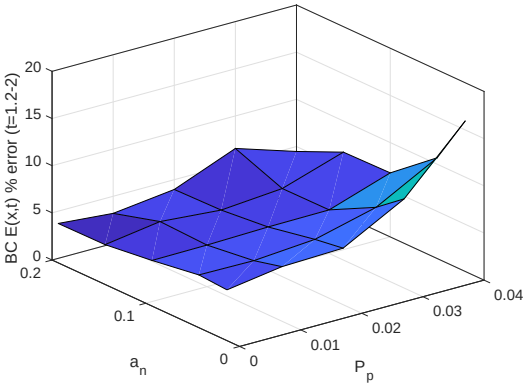

(d) BC: E(x,t) % error ($t = 1.2 - 2$)

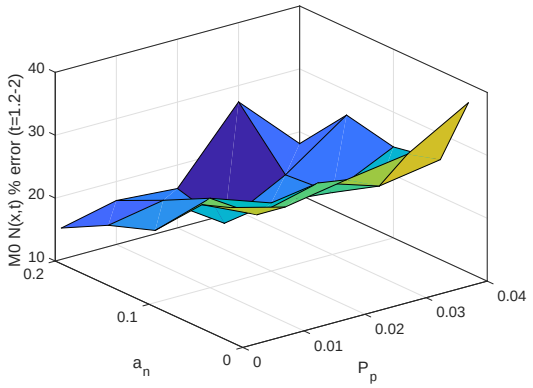

(e) M0: N(x,t) % error ($t = 1.2 - 2$)

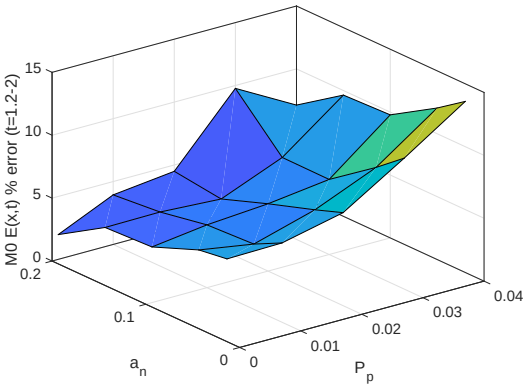

(f) M0: E(x,t) % error ($t = 1.2 - 2$)

Figure 6.3: Model 1: PDE Predictions: Relative errors for each PDE model as a function of CA model probabilities (a_n, tip-to-tip anastomosis probability, P_p, branching probability). Left panel: TC density, Right panel: EC density. (a), (b) The relative errors are much lower than those for Model 0 PDEs and the BC model (see (c)-(f)). (c)-(f) The relative errors generally increase as mass increases (as a_n decreases and P_p increases). According to the relative error, the Model 1 PDEs are the best predictive model, whilst the BC model and Model 0 PDEs are similar. We note that the relative error heavily penalises the BC model due to the thresholding of 10^{-4} we have chosen for the TC density (see equation (6.1)). If we increase the thresholding to 10^{-3}, the BC model and Model 0 are much closer in terms of the relative error for the TC density (results not shown). M1 = Model 1 PDEs, BC = BC Model, M0 = Model 0 PDEs.

6.3 Discussion

Our intent was to relate predictive and descriptive power to underlying network structure statistics extracted from the averaged CA simulations. Relating microscale structure to population behaviour (described by continuum models) is powerful, as it provides a framework to classify continuum models. That is, based on network structure statistics, we can choose which continuum model best describes and predicts the population behaviour. Given that experimental data may take the form of images of network morphology, the ideas discussed in this chapter are particularly useful for determining which continuum models to use to predict and describe population behaviour based on images of network structure.

For CA Model 1, we used branching probabilities P_p and tip-to-tip anastomosis probabilities a_n that illustrate network features and differences in the ability of the continuum models to capture those features. We considered anastomosis probabilities between 0.02 and 0.2, as this highlights how average sprout length, mass and average number of branchings change with the number of loops formed by tip-to-tip anastomosis. Above $a_n = 0.2$, the behaviour is similar: many anastomoses annihilate many TCs, a phenomenon that increases as the branching probability increases, resulting in lower overall mass in the system, and thus, a regime where TC VE effects are non-negligible and all continuum models perform well. Below $a_n = 0.02$, there is little change in the network features, other than increasing TC VE effects. We find that as a_n decreases and P_p increases, the mass, average number of branchings, and tip-to-tip anastomoses increase, while the average sprout length decreases.

For CA Model 1, we found that all continuum models were comparable in terms of descriptive and predictive power according to relative errors, except when TC VE was non-negligible at the macroscale, in which case the Model 1 PDEs perform better. This corresponds to a higher number of branchings, fewer loops/network connections formed through tip-to-tip anastomosis, higher mass and shorter average

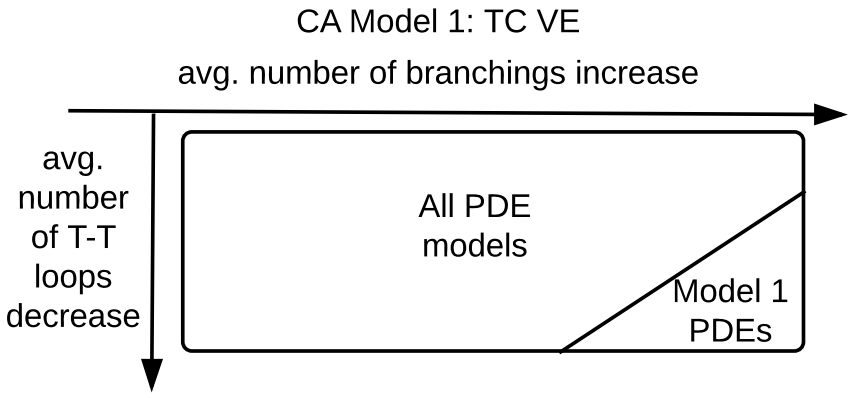

(a) Descriptive and Predictive Power

Figure 6.4: Schematic of descriptive and predictive power of PDE models in networks generated using CA Model 1 rules. When TC VE effects become non-negligible, corresponding to a higher number of branch points and fewer network connections formed through tip-to-tip (T-T) anastomosis, the Model 1 PDEs are the best descriptive and predictive model. Otherwise, the Model 0 and 1 PDEs, and BC Model have similar descriptive and predictive power.

sprout length. In Fig. 6.4, we illustrate the best descriptive and predictive models in networks generated through CA Model 1 rules.

For CA Model 2 (see Appendix E), we use probabilities of tip-to-sprout anastomosis and branching that emphasize interesting features in the networks produced by the CA, regimes where EC VE effects are non-negligible and regimes that highlight the differences between the continuum models in terms of their ability to capture averaged CA simulation results. We use $a_e = 1$ to illustrate the case for which the Model 2 PDEs were derived, and in which EC VE effects are negligible. As we lower a_e below 1, the behaviour of the averaged CA simulation results are similar until $a_e = 0.2$. At $a_e = 0.2$ and below, the effects of EC VE are evident, and non-negligible for $a_e < 0.1$. It is in this regime that differences (if any) between the continuum models in their ability to capture the averaged CA simulation results are evident. Below $a_e = 0.1$, we found in Chapter 4 that none of the continuum models capture the averaged CA simulation results, and thus we do not evaluate the descriptive and

predictive power of the continuum models below $a_e = 0.1$. We note that for each branching probability, it is the anastomosis probability that determines the features of the network, and thus we consider two values of P_p for comparison. For each value of P_p, the average number of tip-to-sprout anastomoses are similar for $a_e = 1$ to $a_e = 0.1$, with a sharp decrease for $a_e = 0.01$.

In CA Model 2, with inactive tip-to-tip anastomosis, generally, fewer loops are formed via tip-to-sprout anastomosis as a_e decreases, and more branchings occur as P_p increases. This corresponds to shorter average sprout length and high mass. We found that the descriptive power of the Model 2 PDEs and BC model are similar based on relative errors. Both PDE models perform well, unless EC VE effects are non-negligible. This corresponds (for each value of P_p) to fewer network connections formed through tip-to-sprout anastomosis, higher mass, higher number of branchings and longer average sprout length. According to our goodness of fit metrics, the Model 2 PDEs are the better predictive model, though both models are poor predictors. The best predictions from both models occur, for each value P_p, when many network connections form through tip-to-sprout anastomosis, and the mass is lowest.

For active tip-to-tip anastomosis in CA Model 2, far fewer network connections form through tip-to-sprout anastomosis, as many TCs form connections with other TCs (and are annihilated). Further, as a_e and P_p decrease, generally, the average number of branchings, tip-to-tip anastomoses and mass at $t = 2.0$ decreases while the average sprout length increases. The Model 0 and 2 PDEs, and the BC Model have similar descriptive power. The descriptive power decreases, for each value of P_p, as the average number of network connections formed by tip-to-sprout anastomosis decreases, the average sprout length increases, and the number of branchings (and mass) increase. In terms of predictive power, the Model 2 PDEs produce the best predictions, while the Model 0 PDEs and the BC model produce predictions that deviate substantially from the averaged CA simulation results. In general, the model

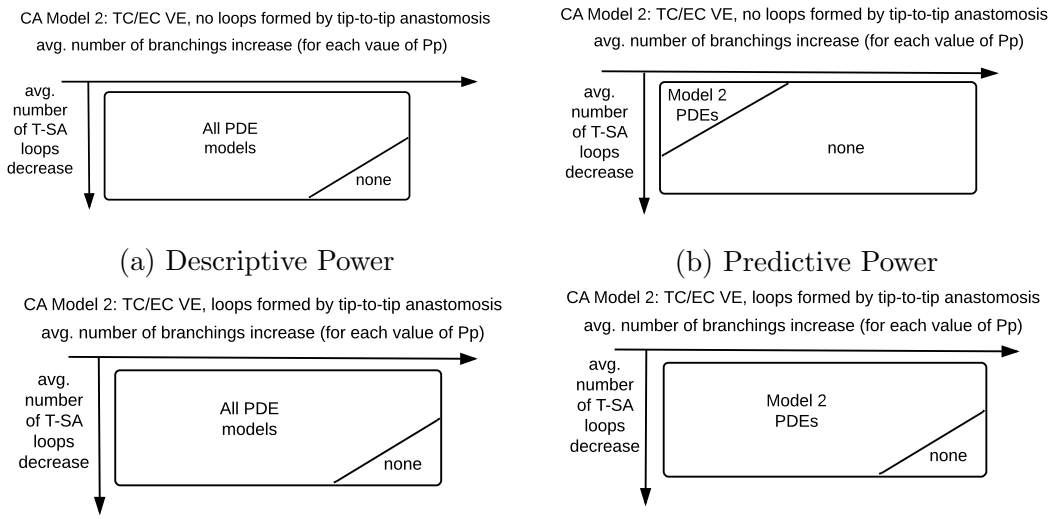

(a) Descriptive Power

(b) Predictive Power

(c) Descriptive Power

(d) Predictive Power

Figure 6.5: Model 2: Schematic of descriptive and predictive power in networks generated using Model 2 CA rules. When EC VE effects become non-negligible, corresponding to fewer network connections formed through tip-to-sprout anastomosis and a higher number of branch points, all models are poor descriptive and predictive models. (a), (b) TC VE, inactive tip-to-tip anastomosis. (c), (d) Active tip-to-tip anastomosis. (a) Model 2 PDEs and the BC model have similar descriptive power. (b) Model 2 PDEs produce better predictions than the BC model when EC VE effects are negligible. (c) Model 0 and 2 PDEs and the BC model have similar descriptive power. (d) Model 2 PDEs are the better predictive model.

predictions from all models when tip-to-tip anastomosis is active are better than when it is not. Tip-to-tip anastomosis annihilates many TCs, and this corresponds to more negligible EC VE effects than in the case of inactive tip-to-tip anastomosis, where there are many more TCs interacting with ECs through EC VE. We summarize the descriptive and predictive power schematically in Fig. 6.5.

We also remark that the relative errors depend on the noise (accuracy) within the numerical solutions for each continuum model, and thus where we have concluded that Model 1 or 2 PDEs are the better descriptive or predictive models, there are clear reasons for these choices, owing to non-negligible VE effects, and the non-linearity in the structure of the Model 1 and 2 PDEs that are able to account for them.

We note that our assessments of descriptive and predictive power in terms of network morphology outlined in Figs. 6.4 and 6.5 require further investigation. For CA

Model 2, we require more data points (more values of a_e and P_p) to determine network structure trends, and to assess the descriptive and predictive power of the continuum models. Further, we have related the relative errors for predictions to network statistics gathered at the final time point. In future work, we will collect network statistics over the time interval on which we perform the fitting in the predictive case, so as to relate predictive power to network statistics gathered during this time interval (and not during the prediction time intervals).

In future work, we intend to quantify network morphology in terms of more sophisticated metrics (using, for example, pair-wise correlation functions to distinguish dense/sparse areas of the networks). We also intend to determine whether it is possible to develop a functional relationship between, for example, relative error or other goodness of fit measures of a particular continuum model, and metrics that quantify morphology. In this manner, we could predict the descriptive and predictive power of the continuum models based on network morphology. We were limited in terms of computational power (run time) in this study. In future, we will explore a larger parameter space in the CA model, to produce a more comprehensive picture of network morphology and features (i.e. determining the sensitivity of network structure to changes in CA parameters and compared with Perfahl et al. (2017) for example).

As mentioned in the previous chapter, we could use other approaches, such as Bayesian methods, to infer parameters in the continuum models and select models (Turner and Van Zandt, 2012; Toni et al., 2009; Toni and Stumpf, 2010; Oden and Prudencio, 2013)). Ultimately, we would like to train our CA model on real networks, i.e. infer CA model network parameters from real data (using Bayesian methods), and then use our discrete to continuum framework to classify continuum models in terms of descriptive and predictive power based on real network morphology.

Chapter 7

Conclusions and Future Work

In this thesis, we systematically determined the macroscale behaviour of TCs and ECs in the form of PDE models from two-dimensional lattice-based CA implementations of the snail-model of corneal angiogenesis. The resulting PDEs incorporate novel terms (e.g. anastomosis terms) for describing processes at the microscale. Our framework, which relates microscale cell behaviour with population behaviour, enabled us to elucidate, at a more fundamental level, the assumptions underpinning the well-known phenomenological BC model. Crowding effects and VE are important in angiogenesis (and biological systems in general), as cells have finite size. Thus, we thoroughly investigated the effects of cell volume on microscale and population behaviour, as well as on the structure of PDEs. Finally, we evaluated the descriptive and predictive power of the continuum models and, as a proof of concept, linked descriptive and predictive power with underlying network morphology. In this thesis, we have linked the microscale and macroscale in snail-trail models of corneal angiogenesis, and developed a framework that can be extended and applied to experimental data sets of both network structure and population behaviour. In what follows, we summarise the key findings in each chapter before discussing directions for further investigation.

In Chapter 2, we developed a two-dimensional CA model of angiogenesis in the corneal assay, based on the snail-trail process. Using a mean-field approximation and DCEs, we derived a PDE model that describes the spatio-temporal evolution of the TC and EC densities. In contrast to the phenomenological continuum models (the BC model (Byrne and Chaplain, 1995a) and the model of Balding and McElwain (1985)), EC creation due to TC movement (vessel formation via the snail-trail) manifests as a source of TCs on the macroscale. Further, the BC model, in which EC creation is proportional to the flux of TCs in the direction of increasing chemoattractant concentration, qualitatively captures vessel formation in two dimensions, but must be modified by a scaling factor to accurately represent vessel formation. We found that this scaling factor depends on the precise microscale movement of the TCs in directions other than towards the chemoattractant. Additionally, we found that anastomosis imposes restrictions on cell density, which, if violated, leads to ill-posedness in our continuum model. These are not apparent in existing continuum models (Byrne and Chaplain, 1995a; Balding and McElwain, 1985; Spill et al., 2015), where anastomosis is incorporated via phenomenological sink terms, without any restrictions on cell density. We concluded that self-loops should be excluded when tip-to-sprout anastomosis is active in the discrete model to ensure propagation of the vascular front. To account for this in our continuum model, we estimated the parameter that controls the rate of tip-to-sprout anastomosis by fitting the PDE model to the averaged CA simulation results with self-loops excluded.

In Chapter 3, we extended the models in Chapter 2 to account for cell volume. We developed two CA models: for Model 1, TCs interact with TCs via tip-to-tip anastomosis and TC VE; for Model 2, in addition to TC-TC interactions, TCs interact with ECs via tip-to-sprout anastomosis and EC VE. We note that VE and anastomosis are mutually exclusive in our framework and we assume that anastomosis occurs whenever a TC encounters another cell (in line with other discrete models of angiogenesis

e.g. Tong and Yuan (2001); Anderson and Chaplain (1998)). We used a mean-field approximation to derive one-dimensional PDE models based on these CA models. Explicitly accounting for cell volume diminishes (and eliminates in some cases) the potential for ill-posedness in our continuum models, as the motility and branching mechanisms now impose the same density restrictions as anastomosis. Our PDEs for the TC density agree with existing results for simple and multi-species exclusion processes (e.g. Simpson et al. (2010a, 2009a); Penington et al. (2011)). However, the mean-field approximation leads directly to a backwards heat equation for the EC density when EC VE is active. We were unable to regularise these equations due to the complexity of the higher-order terms. From averaged CA simulations, we found that EC VE renders TCs immobile, especially at early times, as neighbouring sites are occupied by ECs, which creates long tails in the TC density. In keeping with restrictions imposed on the CA by the mean-field approximation, we kept the branching rate low and, as a result, the effects of TC VE at the macroscale were absent.

In Chapter 4 we relaxed some of the assumptions in Chapter 3 and accounted for EC VE. Firstly, we increased the branching rate in order to reproduce the brush-border effect and we introduced probabilities for anastomosis to occur (i.e. anastomosis does not occur every time a TC encounters another cell). To account for potential correlations, we fitted the PDE models to averaged CA simulation results and estimated parameters that arise from processes that lead to correlations. In particular, we estimated the branching rate, and the parameters that control tip-to-tip anastomosis and tip-to-sprout anastomosis. We used the same approach to capture EC VE effects instead of deriving more complicated non-linear mean-field PDE models, which, as we found in the previous chapter, leads to backward heat equations. We compared our continuum models and the linear modified BC model (modified in Chapter 2) with averaged CA simulation results to distinguish macroscale VE effects and establish the extent to which our non-linear models and the linear BC model can capture them.

We found good agreement between our Model 1 PDEs, the BC model and averaged CA simulation results when TC density is low, and TC VE effects negligible. When the TC density is high, averaged CA simulations indicate that TC VE produces a front that steepens at the back as TCs are prevented from moving towards the TAF (chemoattractant) source by other TCs. As the TC density increases, the BC model is unable to capture the increasing effects of TC VE, while the non-linear chemotactic terms in the Model 1 PDEs have been derived for this purpose. Both the BC Model and the Model 2 PDEs capture the averaged CA simulation results when EC VE effects are negligible. Neither PDE model captures the increasingly long tails in the TC density where EC VE is significant. In the context of angiogenesis, however, network connections are prevalent in experimental data and, thus, strong EC VE effects, which prevent connections via tip-to-sprout anastomosis, may not be relevant.

In all of the chapters discussed above, TC-EC interactions in the CA and PDE models produced less dense networks than when TCs interact with TCs only, as tip-to-sprout anastomosis annihilates TCs, and EC VE further prohibits TC movement. Further, for vessel networks that are less dense, the pronounced effects of TC VE do not arise (as the TC density is low). This should be considered when developing angiogenesis models, as including or excluding TC-EC interactions has a marked effect on the vessel densities.

In Chapter 5, we assessed the predictive power of our continuum models (the Model 0, 1 and 2 PDEs) and the BC model. We fit the continuum models to averaged CA simulations, and used the estimated parameters to simulate the PDE models at later times, thereby predicting the behaviour of the averaged CA simulations. We quantified predictive power of the continuum models in terms of the following goodness of fit metrics: RMSEs and AIC_c values. We found that the Model 1 PDEs had the greatest predictive power when TC VE was important at the macroscale, and that the Model 2 PDEs were the better predictive model when EC VE was active. In

all cases, however, all PDE models were similar in terms of predictive power at the first prediction time point.

The work in Chapter 6 is proof of concept (that exploits the discrete-to-continuum framework developed in this thesis). We determined that it is possible to relate the descriptive and predictive powers of PDE models to underlying network structure produced by the CA. We note that this chapter requires further work, including a comprehensive exploration of CA parameter space before general conclusions can be drawn. However, this work has the potential to be important (especially in drug development) if applied to experimental data sets of networks (images of networks produced via corneal angiogenesis), as it allows one to choose which continuum model best describes and predicts population behaviour based on the network morphology (similar to the idea of network structure influencing function studied in asymptotic homogenization e.g. Chapman et al. (2008); Shipley and Chapman (2010)).

In this thesis, we have gone beyond the typical complexity involved in formulating discrete to continuum frameworks using a mean-field approximation. In some cases, this has led us to problems (e.g. backward heat equations). We have overcome many of the difficulties by making further approximations or accounting for interactions through parameter estimation in the continuum models. In what follows, we outline the extensions that can be made to our modelling framework.

7.1 Future Work

We have identified a number of open questions and avenues for further investigation, as well as broader areas for future research.

- Correlations and their effects on mean-field PDE models have been discussed in this thesis. In future, we would like to conduct a correlation analysis (e.g. Simpson and Baker (2011); Baker et al. (2010); Markham (2014)) which determines

how CA model parameters enhance correlations between lattice sites (both short- and long-range correlations). This will enable us to identify more clearly why our mean-field PDE models break down, and may provide insight on how to correct them. Further, the mean-field approximation led to backwards heat equations when EC VE was active. We would like to expand on our attempts to regularise this equation (e.g. accounting for some of the higher-order terms, but not all), or find other ways to eliminate it (recasting the equations). Based on the correlation analysis, we could determine whether a moment dynamics approach (Simpson and Baker, 2011; Baker et al., 2010; Markham, 2014) is another reasonable methodology with which to derive an equation for the EC density when EC VE is active.

- In Chapters 4 and 5, we estimated parameters in the PDE models in the descriptive and predictive cases. In the descriptive cases, we would like to quantify the ability of our systematically-derived PDE models and the BC model to capture averaged CA simulation results in terms of the upscaled parameter $\tilde{\lambda}$. That is, for example, in CA Model 1, by varying a_n (on a more refined mesh) and considering how $\tilde{\lambda}$ ($\tilde{\lambda}_{BC}$) varies in relation to the calculated upscaled parameter, λ, for a variety of $\lambda \in [1.6, 6.4]$ (see Fig. 4.7a), it would be possible to determine the parameter regimes in which the Model 1 PDEs (BC model) deviate from averaged CA simulation results. Further, this analysis would also provide insight into the parameter regimes in which the Model 1 PDEs and BC model agree and disagree with each other. A similar analysis can be performed for CA Model 2 (see Fig. 4.10). This is a systematic methodology with which to determine the robustness of our PDE models to capture averaged CA simulation results as the anastomosis probabilities vary in the CA model.

  In future, we will also compare the estimated parameters in the descriptive and predictive cases, and compare them to calculated parameter values from the

discrete-continuum framework. We will also compare the confidence intervals in the descriptive and predictive cases, and the sensitivity of the parameters to changes in the CA model parameters. With this insight, we could link discrete and continuum models more closely (i.e. determine how CA model parameters affect estimated parameter values in the PDE models).

- We have derived one-dimensional PDE models and compared them to column-averaged CA simulation results. In future, we will compare two-dimensional PDE solutions and CA simulations, and determine if this provides further insight into how microscale dynamics influences macroscale properties.

- We have used a linear, quasi-steady-state TAF profile in this thesis. We could extend our framework to incorporate a two-dimensional time-dependent TAF field (e.g. Anderson and Chaplain (1998)). This requires us to utilise the two-dimensional PDE models derived, and compare these to two-dimensional averaged CA simulations. Coupling of the TAF field to TC/EC dynamics would be more challenging, as it requires us to develop a methodology to define uptake/production of TAFs by TCs/ECs in the CA. Instead, we could use the PDE models derived (for the TC and EC densities), and incorporate a third PDE for the TAF field which is coupled to the PDEs for the TC and EC densities. In this manner, we could determine how coupling between the TAF/cells affects population behaviour.

- We derived PDE models from two-dimensional CA models. The geometry introduces artifacts (e.g. anastomosis more likely in two dimensions than in three). We could investigate how adding a third dimension of small height affects CA model statistics. This could be tested in the new microvessel Chaste (Cancer, Heart and Soft Tissue Environment) framework (Grogan et al., 2017). Chaste is a computational package that allows for multi-scale simulations at the cell

level. Off-lattice CA models allow cells to move more freely (see Plank and Sleeman (2004); Plank and Simpson (2012); Dyson et al. (2012); Dyson and Baker (2015)). It would interesting to determine whether an off-lattice framework (which can also be tested in the Chaste framework) produces different population behaviour.

- Several findings in this thesis indicate that a signalling mechanism (Delta-Notch) mediates certain processes. For example, we found that self-loops creating stunted sprouts occurred frequently (in Chapter 2) unless explicitly prohibited and EC VE renders TCs immobile (in Chapter 3). Both of these issues could be resolved by a signalling mechanism that dynamically selects TCs and ECs. We could incorporate this signalling pathway (see Bentley et al. (2009, 2008); Jakobsson et al. (2010); Jain and Jackson (2013)). This may resolve the long tails in the TC density caused by EC VE, and therefore it may not be necessary to derive PDEs when EC VE effects are important.

- In future, we aim to quantify the error in our averaged CA simulations and network statistics. Usually, if these errors are given, the standard error of the mean (standard deviation of the mean divided by the square root of the number of realizations over which the CA simulations are averaged) is used (for example, as in Ross et al. (2015)). However, as the number of realizations over which the simulation results are averaged increases, the standard error, tends to zero. For $M = 200$, used in much of this thesis, the errors are negligible. We also found that the standard deviation produces very large error estimates. The question then is, how do we quantify the scatter in the averaged CA simulation results? This is a non-trivial question, and depends on a variety of factors including the method used to update agents at the beginning of each time step (see Rajewsky et al. (1998), Wolfram (1983)). In future, we would like to

conduct a thorough investigation of the errors within averaged CA simulations and network statistics.

- We could extend the two-dimensional discrete model developed in this thesis to include perfusion, the flow of blood in the network, following the methodology in Stéphanou et al. (2005); McDougall et al. (2002); Alarcón et al. (2005); Owen et al. (2009); Macklin et al. (2009); Alarcón et al. (2003). We would like to keep track of perfused and unperfused vessels computationally, and use this information to develop phenomenological terms in the continuum model to describe perfusion. This is an important extension to the snail-trail model as it allows for a more accurate description of angiogenesis, which must necessarily include blood circulation.

  In summary, in this thesis, we developed a discrete-continuum (microscale-macroscale) framework of corneal angiogenesis based on the snail-trail process that can be extended to include more detailed or realistic interactions, and can be used to predict and/or describe population dynamics.

Appendix A

Numerical Methods

In this section, we review the numerical methods employed in solving the PDEs in this thesis. We start with the BC model, and then continue on to our Model 0, 1 and 2 PDEs.

A.1 BC Model

We start by solving the original BC model (Byrne and Chaplain, 1995a), given by

$$\frac{\partial N}{\partial t} = D_{\mathrm{BC}}\frac{\partial^2 N}{\partial x^2} - \chi_{\mathrm{BC}}\frac{\partial}{\partial x}\left(N\frac{\partial c}{\partial x}\right) + \lambda_{\mathrm{BC}}Ec - \beta_e NE, \tag{A.1}$$

$$\frac{\partial E}{\partial t} = D_{\mathrm{BC}}\frac{\partial N}{\partial x} - \chi_{\mathrm{BC}}N\frac{\partial c}{\partial x} - \gamma E, \tag{A.2}$$

subject to

$$E(x,0) = 0 \text{ for } 0 \leq x < 1, \quad E(1,t) = E_{\min} + (1 - E_{\min})\exp(-vt),$$
$$N(x,0) = 0 \text{ for } 0 \leq x < 1, \quad N(0,t) = 0, \quad N(1,t) = \exp(-vt),$$
$$c(0,t) = 1, \quad c(1,t) = 0, \quad c(x,0) = 0 \text{ for } 0 \leq x < 1, \tag{A.3}$$

with $c = 1 - x$ (approximation, see Byrne and Chaplain (1995a)). We use the following parameters, taken from Byrne and Chaplain (1995a)

$$D_{\text{BC}} = 10^{-3}, \quad \chi = 0.4, \quad \gamma = 0.25, \quad \alpha = 50, \quad \beta_e = 50, \quad v = 5, \tag{A.4}$$

with $E_{\min} = 0.2$.

The PDE for N, equation (A.1), is an advection-diffusion equation. If we were to use an upwind scheme to approximate the first derivative of N that appears in the chemotactic term, and a central difference scheme to approximate the second derivatives of N that appear in the diffusive term, we would introduce numerical diffusion into the solution (Durran, 2010). This upwind scheme introduces non-negligible numerical diffusion if the numerical Péclet number $Pe = \chi_{\text{BC}}\delta x/D_{\text{BC}}$ is large, where δx is the grid spacing in the numerical scheme (Durran, 2010). The Péclet number quantifies the strength of advection to diffusion on the numerical grid. For a Péclet number which does not satisfy $Pe \ll 1$, numerical diffusion dominates the total diffusion, unless the grid resolution is decreased accordingly (Durran, 2010). To circumvent refining the mesh size for a large Péclet number, a less diffusive scheme, such as a central difference approximation to the first derivative, can be used to reduce numerical diffusion (Durran, 2010), and this is how we will proceed. The equation for the EC density is an advective equation in N, and we discretize it using an upwind scheme, which

introduces a small numerical diffusion term $O(\delta x^2)D \ll 1$, which smooths out high frequencies (if any).

We discretize equations (A.1) and (A.2) using $M+1$ spatial points, such that $x_j = j\delta x, j = 0, \cdots, M$ and $\delta x = 1/(M+1)$, as follows:

$$\frac{dN_j}{dt} = D_{\mathrm{BC}}\frac{(N_{j+1} - 2N_j + N_{j-1})}{\delta x^2} + \chi_{\mathrm{BC}}\frac{(N_{j+1} - N_{j-1})}{2\delta x} + \lambda_{\mathrm{BC}}E_j(1 - x_j)$$
$$-\beta_e N_j E_j, \tag{A.5}$$
$$\frac{dE_j}{dt} = D_{\mathrm{BC}}\frac{(N_j - N_{j-1})}{\delta x} + \chi_{\mathrm{BC}}N_j - \gamma E_j, \tag{A.6}$$

where we have used the definition of $c = 1 - x$ to simplify the chemotactic terms (and set the boundary terms using the boundary conditions described earlier). To solve these ODEs in time, we use MATLAB's *ode15s*, which implements adaptive time-stepping (Shampine and Reichelt, 1997) and is a variable-step, variable-order method based on numerical differentiation formulae of first to fifth order, and *ode45*, which implements an explicit single-step Runge-Kutta 4-5 method (Shampine and Reichelt, 1997). Both methods are implemented with an absolute and relative tolerance of 10^{-6}. The solutions are then linearly interpolated in time, using MATLAB's *interp1*, into the 0.2 time intervals we require. We also compare the solutions found using these time-stepping methods with solutions found using MATLAB's *pdepe*, which solves initial-value problems for parabolic and elliptic PDE systems in one spatial dimension. The *pdepe* algorithm discretizes the PDEs, and then uses *ode15s* to perform the time integration. The solutions to equations (A.1) and (A.2) subject to the boundary and initial conditions in (A.3) are shown in Fig. A.1, calculated with $\delta x = 1/400$. We see good agreement between all three methods. Further, this corroborates the results found in Byrne and Chaplain (1995a).

We now consider the modified BC model (see Chapter 2), reiterated for refer-

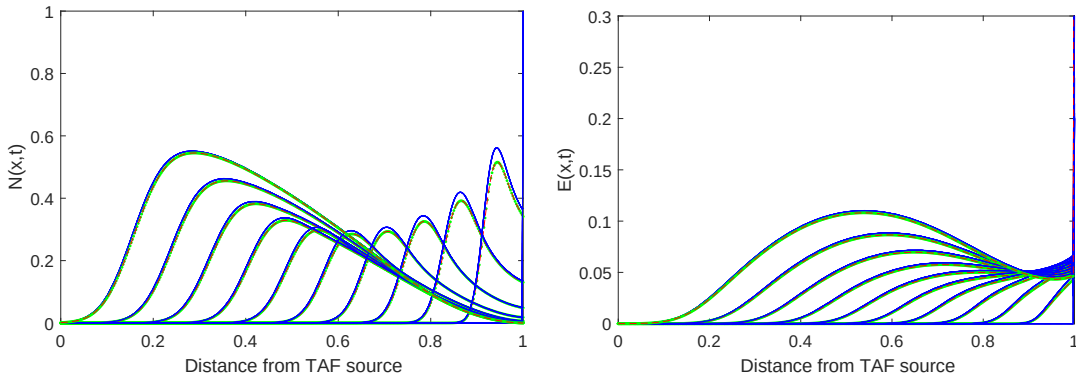

(a) (b)

Figure A.1: Numerical solutions to equations (A.1) and (A.2) with $\delta x = 1/400$. Solutions are shown from $t = 0 - 2$ in 0.2 intervals (fronts move from right to left). We used a finite difference scheme in space and time-stepping performed with MATLAB's *ode15s* (green dots) and MATLAB's *ode45* (red dashed line). Additionally, we used MATLAB's *pdepe* solver (blue solid line). All three methods agree, and agree with results in Byrne and Chaplain (1995a) (results not shown).

ence:

$$\frac{\partial N}{\partial t} = D_{\mathrm{BC}} \frac{\partial^2 N}{\partial x^2} - \chi_{\mathrm{BC}} \frac{\partial}{\partial x}\left(N \frac{\partial c}{\partial x}\right) + \alpha N c - \beta_e N E - \beta_n N^2, \quad \text{(A.7)}$$

$$\frac{\partial E}{\partial t} = \frac{2}{h}\left| D_{\mathrm{BC}} \frac{\partial N}{\partial x} - \chi_{\mathrm{BC}} N \frac{\partial c}{\partial x} \right|, \quad \text{(A.8)}$$

$$D_{\mathrm{BC}} \frac{\partial N}{\partial x} - \chi_{\mathrm{BC}} N = 0 \mid_{x=0,1}, \quad \text{(A.9)}$$

where we discretize the boundary conditions as $D_{\mathrm{BC}}(N_{j+1} - N_{j-1})/(2\delta x) - \chi_{\mathrm{BC}} N_j = 0$ at $j = 0$ and $j = M$. Following Byrne and Chaplain (1995a), we set $D_{\mathrm{BC}} = 10^{-3}$ and $\chi_{\mathrm{BC}} = 0.4$, with which the TC flux is always negative and thus the absolute value in equation (A.8) can be replaced by a negative sign. We now solve equations (A.7) and (A.8) (using the same discretization in equations (A.5) and (A.6)) subject to no flux boundary conditions, with parameters taken from Chapter 2 and initial conditions taken from averaged CA simulation results. We reproduce the results from Fig. 2.5 in Chapter 2, for Model 0 with active tip-to-tip and tip-to-sprout anastomosis. We see that solutions using all three

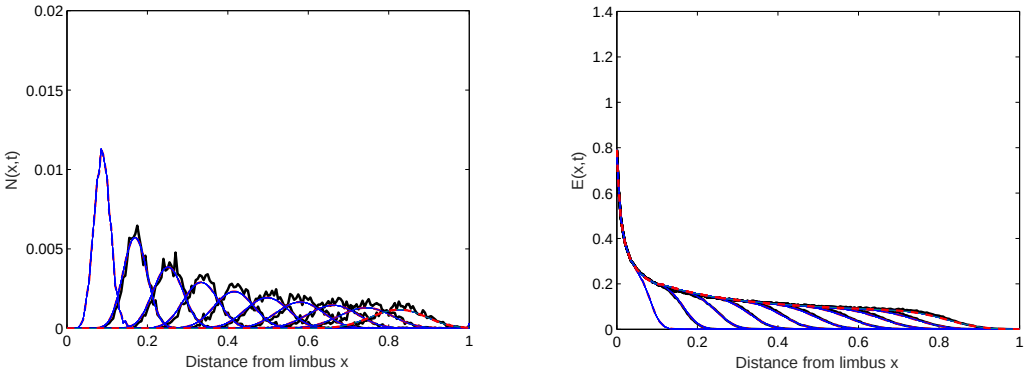

(a) (b)

Figure A.2: Numerical solutions to equations (A.7) and (A.8) with $\delta x = 1/400$ for TC motion, branching and active tip-to-tip and tip-to-sprout anastomosis. Solutions are shown from $t = 0 - 2$ in 0.2 intervals (fronts move from left to right). We used a finite difference scheme in space and time-stepping performed with MATLAB's *ode15s* (green dots) and MATLAB's *ode45* (red dashed line). Additionally, we used MATLAB's *pdepe* solver (blue solid line). All three methods agree, and agree with averaged CA simulation results (black). Parameters: $\alpha = 0.16, \beta_n = 160, \beta_e = 5.0648$.

methods agree in Fig. A.2, and these agree with averaged CA simulation results.

We consider another example, where only TC movement and branching are active (no anastomosis) in Model 0, as in Fig. 2.5, in Chapter 2. In Fig. A.3, we see that the PDE solutions using the three methods outlined above agree with averaged CA simulations results. We see that a dip (a local minimum) arises in the solutions to the EC density PDE at $x \approx 0.08$ (see Fig. A.3b).

To explain the local minimum that arises in the EC density in Fig. A.3b, we consider the purely advective problem with $D_{\text{BC}} = 0$ in equations (A.7) and (A.8) for the TCs and EC density, respectively

$$\frac{\partial N}{\partial t} = -\chi \frac{\partial N}{\partial x}, \tag{A.10}$$

$$\frac{\partial E}{\partial t} = \frac{2}{h}\chi N, \tag{A.11}$$

$$N(x, t = 0.2) = f(x), \quad E(x, t = 0.2) = g(x). \tag{A.12}$$

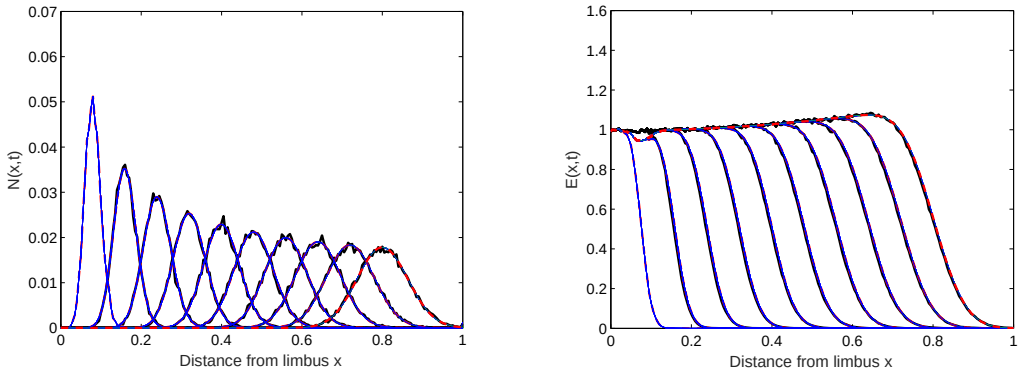

(a) (b)

Figure A.3: Numerical solutions to equations (A.7) and (A.8) with $\delta x = 1/400$ for TC motion and branching only. Solutions are shown from $t = 0 - 2$ in 0.2 intervals. We used a finite difference scheme in space and time-stepping performed with MATLAB's *ode15s* (green dots) and MATLAB's *ode45* (red dashed line). Additionally, we used MATLAB's *pdepe* solver (blue solid line). All three methods agree, and agree with averaged CA simulation results (black). Parameters: $\alpha = 0.16, \beta_n = 0, \beta_e = 0$.

To proceed analytically, we approximate the initial condition for N as a Gaussian of the form $f(x) = A \exp\left(-\frac{(x-x_0)^2}{2\sigma^2}\right)$ with $A = 0.098, x_0 = 0.08, \sigma = 0.02$. The analytical solutions for N and E are $N(x,t) = f(x - \chi t)$ and $E(x,t) = g(x) + \frac{2}{h}\chi \int_0^t f(x - \chi t)dt$. By differentiating the expression for $E(x,t)$ with respect to x, we find that

$$E_x(x,t) = g'(x) + \frac{2}{h}\left(f(x) - f(x - \chi t)\right). \tag{A.13}$$

By numerically differentiating the initial condition $g(x)$ for the EC density from the averaged CA simulations to find $g'(x)$, and plotting the results (see Fig. A.4), we see that $E_x(x,t)$ changes sign at $x \approx 0.08$ and therefore, $E(x,t)$ does have a local minimum at $x \approx 0.08$, precisely as seen in the numerical solutions to the full problem (see Fig. A.3b).

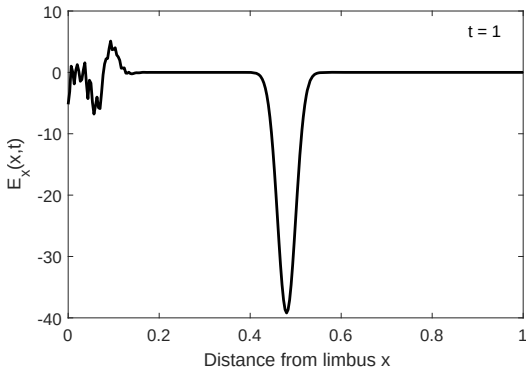

Figure A.4: Derivative of $E(x,t)$ (equation A.13) with respect to x at $t = 1$. A turning point occurs at $x \approx 0.08\ \forall t$, corresponding to a local minimum in $E(x,t)$.

A.2 DCE-Derived PDE Models

We reiterate the models derived and solved in this thesis. The Model 0 PDEs are

$$\begin{aligned}\frac{\partial N}{\partial t} &= (1 - a_n N - a_e E)\left(D\frac{\partial^2 N}{\partial x^2} - \chi\frac{\partial}{\partial x}\left(N\frac{\partial c}{\partial x}\right)\right) \\ &\quad -\mu(a_n N^2 + a_e N E) + \lambda c N, \qquad \text{(A.14)} \\ \frac{\partial E}{\partial t} &= \mu N + a_n N\left(\mu N + D\frac{\partial^2 N}{\partial x^2} - \chi\frac{\partial}{\partial x}\left(N\frac{\partial c}{\partial x}\right)\right), \qquad \text{(A.15)}\end{aligned}$$

subject to

$$D\frac{\partial N}{\partial x} - \chi N\frac{\partial c}{\partial x} = 0, \text{ at } x = 0, 1, \qquad \text{(A.16)}$$

and the Model 1 and 2 PDEs are given by

$$\begin{aligned}&\frac{\partial N}{\partial t} = D(1 - a_n N - B a_e E)\nabla^2 N \\ &-\chi\left(\nabla\cdot(N(1-N)\nabla c) + a_n N\nabla N\cdot\nabla c - B a_e E\nabla\cdot(N\nabla c)\right) \\ &-\mu\left(a_n N^2 + B a_e N E\right) + \lambda c N(1 - N - BE)^2, \qquad \text{(A.17)}\end{aligned}$$

and

$$\frac{\partial E}{\partial t} = \mu N\left(1 - N + 2a_n N\right) - ND\left((1-2a_n)\nabla^2 N\right)$$
$$-\chi N\left(\nabla c \cdot \nabla((1-a_n)N) + a_n \nabla \cdot (N\nabla c)\right), \tag{A.18}$$

subject to

$$D\nabla N - \chi N(1-(1-a_n)N)\nabla c\mid_{x=0,1} = 0, \tag{A.19}$$

with the initial conditions taken from the averaged CA simulation results

$$N(x, t_{IC}) = N_i(\bar{K}_{IC}),\ E(x, t_{IC}) = E_i(\bar{K}_{IC}),\ \forall x, i. \tag{A.20}$$

For each model, we use central difference approximations to the derivative terms in space, as motivated in the previous section detailing the solution of the BC model. We discretize equations (A.14)-(A.16) using $M+1$ points on $x_j = j\delta x, j = 0, \cdots, M$ and $\delta x = 1/(M+1)$ as follows:

$$\begin{aligned}
\frac{dN_j}{dt} &= (1 - a_n N_j - a_e E_j)\left(D\frac{(N_{j+1} - 2N_j + N_{j-1})}{\delta x^2} - \chi\frac{(N_{j+1} - N_{j-1})}{2\delta x}\right) \\
&\quad -\mu(a_n N_j^2 + a_e N_j E_j) + \lambda x_j N_j, \qquad \text{(A.21)} \\
\frac{\partial E}{\partial t} &= \mu N_j + a_n N_j\left(\mu N_j + D\frac{(N_{j+1} - 2N_j + N_{j-1})}{\delta x^2} - \chi\frac{(N_{j+1} - N_{j-1})}{2\delta x}\right), \qquad \text{(A.22)}
\end{aligned}$$

subject to

$$D\frac{N_{j+1} - N_{j-1}}{2\delta x} - \chi N_j = 0,\ \text{at } j = 0, M, \tag{A.23}$$

where we have used the definition of c, $c = x$. We discretize equations (A.17)-(A.19) as follows:

$$\frac{dN_j}{dt} = D(1 - a_n N_j - Ba_e E_j)\frac{(N_{j+1} - 2N_j + N_{j-1})}{\delta x^2}$$
$$-\chi\left((1 - 2N_j)\frac{(N_{j+1} - N_{j-1})}{2\delta x} + a_n N_j \frac{(N_{j+1} - N_{j-1})}{2\delta x}\right)$$
$$+\chi B a_e E \frac{(N_{j+1} - N_{j-1})}{2\delta x} - \mu\left(a_n N_j^2 + Ba_e N_j E_j\right)$$
$$+\lambda x_j N_j (1 - N_j - BE_j)^2, \tag{A.24}$$

and

$$\frac{dE_j}{dt} = \mu N_j\left(1 - N_j + 2a_n N_j\right) - N_j D(1 - 2a_n)\frac{(N_{j+1} - 2N_j + N_{j-1})}{\delta x^2}$$
$$-\chi N_j\left((1 - a_n)\frac{(N_{j+1} - N_{j-1})}{2\delta x} + a_n \frac{(N_{j+1} - N_{j-1})}{2\delta x}\right), \tag{A.25}$$

subject to

$$D\frac{(N_{j+1} - N_{j-1})}{2\delta x} - \chi N_j(1 - (1 - a_n)N_j) \mid_{j=0,M} = 0. \tag{A.26}$$

We solve these ODE systems using MATLAB's *ode15s* and *ode45* with absolute and relative tolerances of 10^{-6}. Note that we use the boundary conditions to solve for the ghost nodes at either boundary point. Further, the initial conditions are taken from the CA model (see equation (A.20)) and are linearly interpolated onto the mesh size used to solve the PDEs using Matlab's *interp1*. Since our PDEs are non-linear, they are not solvable by MATLAB's *pdepe* (with the exception of Model 0 with no anastomosis, which is similar to the BC model). We will therefore use additional MATLAB ODE solvers, namely *ode23t*, *ode23tb*, *ode113* with absolute and relative tolerances of 10^{-6} to confirm our results, though we will not show these results. Our additional validation for these

methods comes from the fact that the PDE solutions agree with the averaged CA simulation results when the mean-field assumption holds. We detail the MATLAB ODE solvers: *ode113* is a multi-step, variable-step, variable-order Adams-Bashforth-Moulton solver of orders 1 to 12 (Shampine and Reichelt, 1997), *ode23t* implements the trapezoidal rule (Crank-Nicolson) (Shampine and Reichelt, 1997), and *ode23tb* implements an implicit Runge-Kutta method along with a trapezoidal rule at its first stage, followed by an order two backward differentiation formula at its second stage (Shampine and Reichelt, 1997). The *ode23t*, *ode23tb* and *ode15s* can solve stiff problems while *ode113* and *ode45* solve non-stiff problems.

We will now solve the discretized equations and reproduce figures from the main text of the thesis. The model parameters are as indicated in the thesis (references will be given). To reiterate, the diffusion coefficient $D = 10^{-3}$ and $\chi = 0.4$, and the values of other parameters will be given in the captions.

A.2.1 Model 0

For Model 0, we reproduce the figures in Chapter 2, see Figs. 2.5f and 2.6, and we see that the PDE solutions found using the different time-stepping methods agree (see Fig. A.5).

A.2.2 Model 1

For Model 1, we reproduce Figs. 4.2a, 4.2b, 4.2e, 4.2f, 4.3e and 4.3f from Chapter 4, and we see that the PDE solutions found using the different time-stepping methods agree (see Fig. A.6).

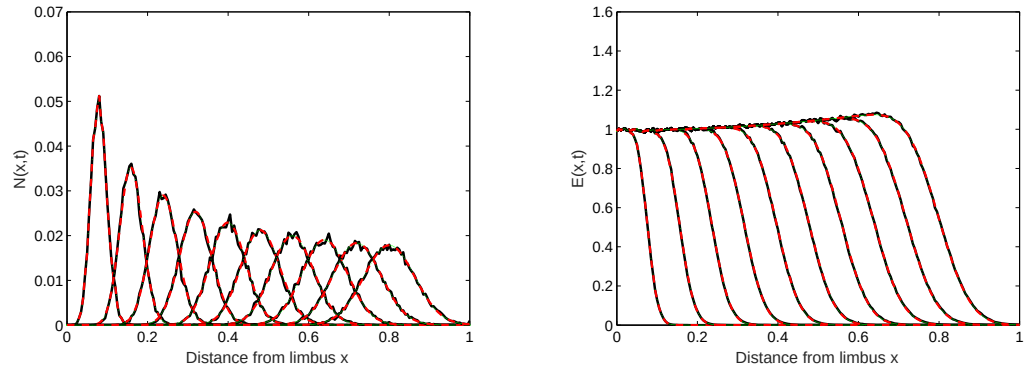

(a) $a_n = 0, a_e = 0$

(b) $a_n = 0, a_e = 0$

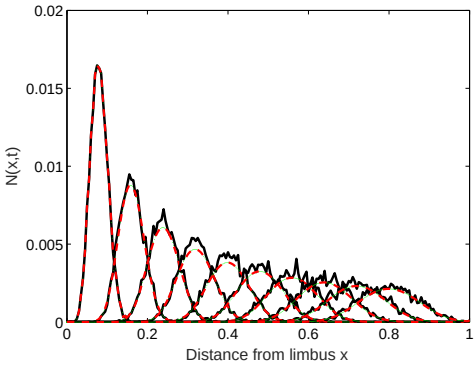

(c) $a_n = 1, a_e = 0$

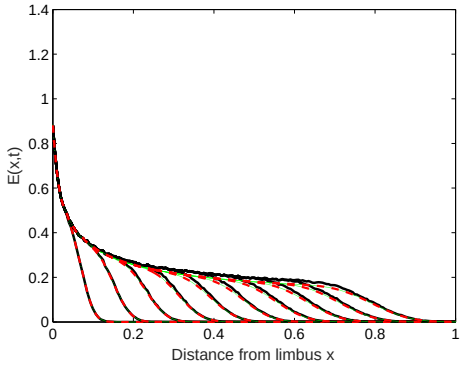

(d) $a_n = 1, a_e = 0$

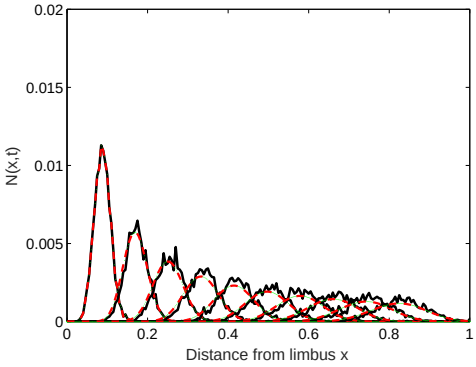

(e) $a_n = 1, a_e = 0.0343$

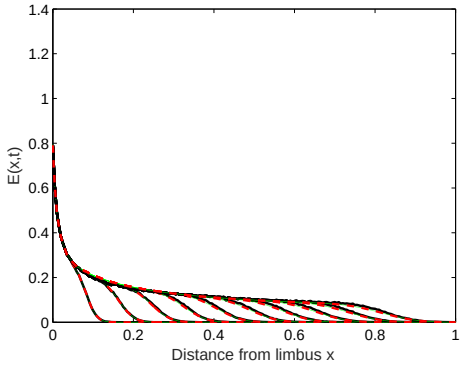

(f) $a_n = 1, a_e = 0.0343$

Figure A.5: Model 0: Numerical solutions to equations (A.14)-(A.16) with $\delta x = 1/400$. Solutions are shown from $t = 0 - 2$ in 0.2 intervals (fronts move from left to right). We used a finite difference scheme in space and time-stepping performed with MATLAB's *ode15s* (green dots) and MATLAB's *ode45* (red dashed line). We also used MATLAB's *ode113*, *ode23t* and *ode23tb* (results not shown). (a) Results also confirmed using MATLAB's *pdepe* (results not shown). All methods agree, and agree with averaged CA simulation results (black). Parameters: $D = 10^{-3}, \chi = 0.4, \lambda = 0.16$.

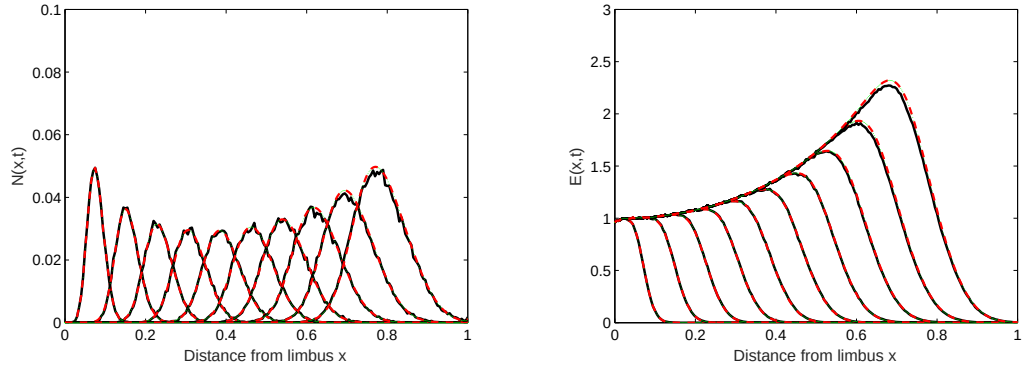

(a) $P_p = 10^{-2}, a_n = 0$

(b) $P_p = 10^{-2}, a_n = 0$

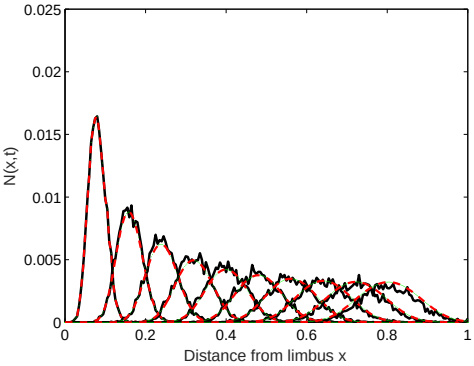

(c) $\tilde{\lambda} = 0.8582, a_n = 1$

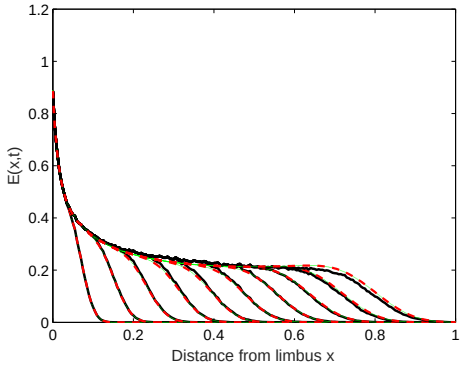

(d) $\tilde{\lambda} = 0.8582, a_n = 1$

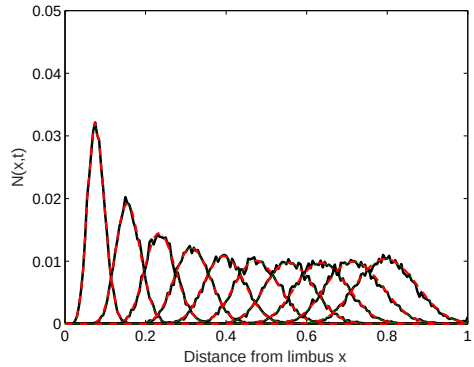

(e) $\tilde{\lambda} = 1.1821, \tilde{a}_n = 0.3001$

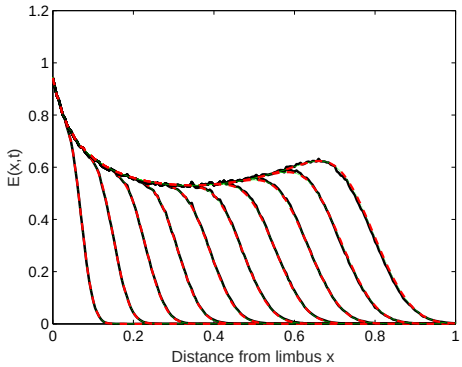

(f) $\tilde{\lambda} = 1.1821, \tilde{a}_n = 0.3001$

Figure A.6: Model 1, a_e N/A: Numerical solutions to equations (A.17)-(A.19) ($B = 0$) with $\delta x = 1/400$. Solutions are shown from $t = 0 - 2$ in 0.2 intervals (fronts move from left to right). We used a finite difference scheme in space and time-stepping performed with MATLAB's *ode15s* (green dots) and MATLAB's *ode45* (red dashed line). We also used MATLAB's *ode113*, *ode23t* and *ode23tb* (results not shown). All methods agree, and agree with averaged CA simulation results (black). Parameters: $D = 10^{-3}, \chi = 0.4$. (c)-(d) $P_p = 10^{-2}$, (e)-(f) $P_p = 10^{-2}, a_n = 0.2$.

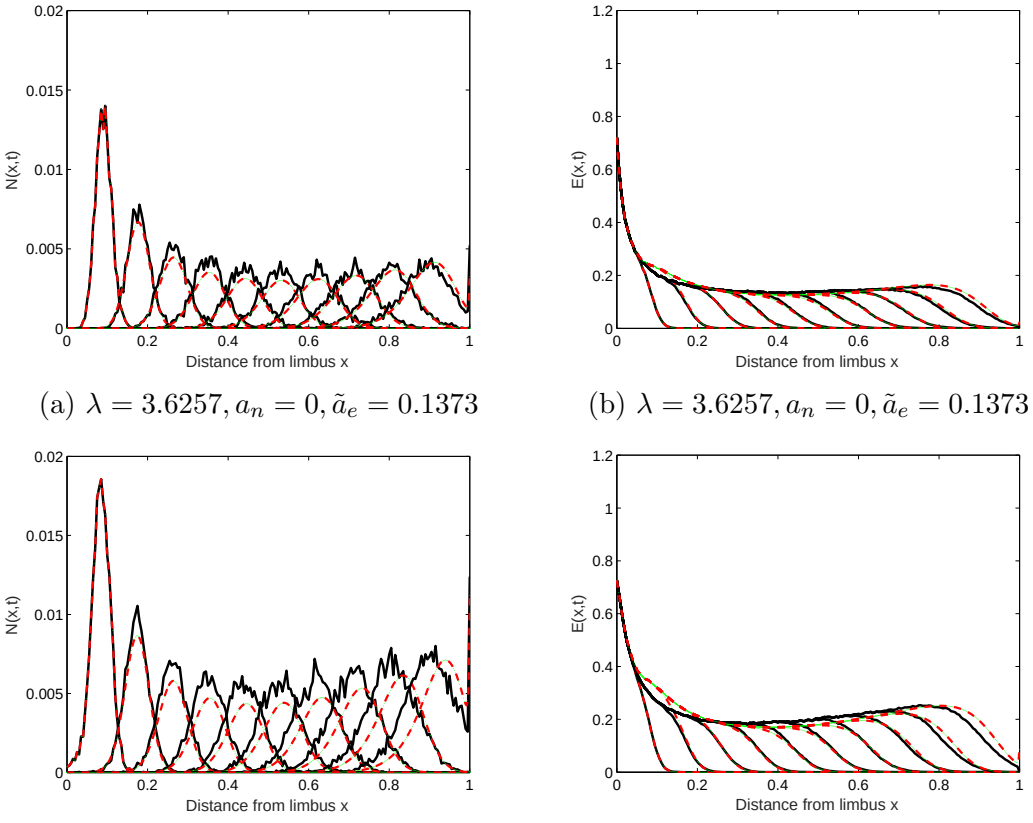

(a) $\lambda = 3.6257, a_n = 0, \tilde{a}_e = 0.1373$ (b) $\lambda = 3.6257, a_n = 0, \tilde{a}_e = 0.1373$

(c) $\lambda = 4.9136, a_n = 0, \tilde{a}_e = 0.1197$ (d) $\lambda = 4.9136, a_n = 0, \tilde{a}_e = 0.1197$

Figure A.7: Model 2: Numerical solutions to equations (A.17)-(A.19) ($B = 1$) with $\delta x = 1/400$. Solutions are shown from $t = 0 - 2$ in 0.2 intervals (fronts move from left to right). We used a finite difference scheme in space and time-stepping performed with MATLAB's *ode15s* (green dots) and MATLAB's *ode45* (red dashed line). We also used MATLAB's *ode113*, *ode23t* and *ode23tb* (results not shown). All methods agree, and agree with averaged CA simulation results (black). Parameters: $D = 10^{-3}, \chi = 0.4$, (a)-(b) $P_p = 10^{-1}, a_e = 1$, (c)-(d) $P_p = 10^{-1}, a_e = 0.2$.

A.2.3 Model 2

For Model 2, we reproduce Figs. 4.8a, 4.8b, 4.11a and 4.11b from Chapter 4 and we show figures for $a_e = 0.2$ (see captions in Figs. A.7 and A.8), and we see that the PDE solutions found using the different time-stepping methods agree (see Figs. A.7 and A.8). We note that MATLAB's *ode45* cannot be used to solve Model 2 with $a_n = 1$, as this system requires a stiff solver or multi-step solver. We use MATLAB's *ode113*, *ode23tb*, and *ode23t* in this case (see Fig. A.8).

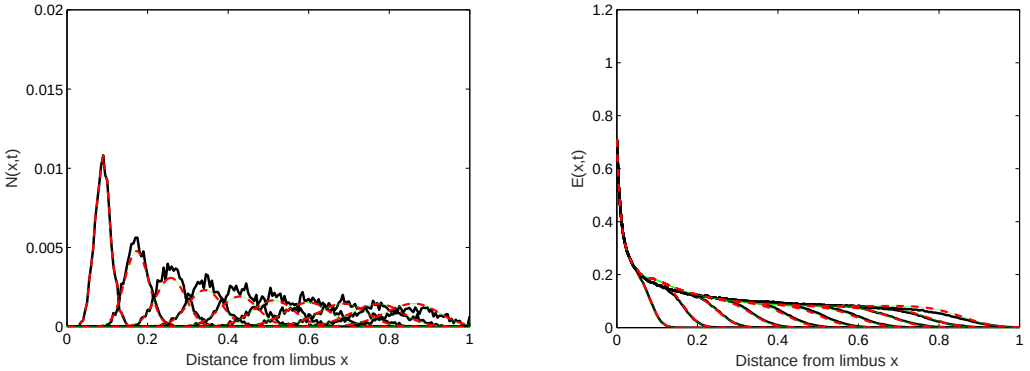

(a) $\tilde{\lambda} = 1.5406, a_n = 1, \tilde{a}_e = 0.1034$ (b) $\tilde{\lambda} = 1.5406, a_n = 1, \tilde{a}_e = 0.1034$

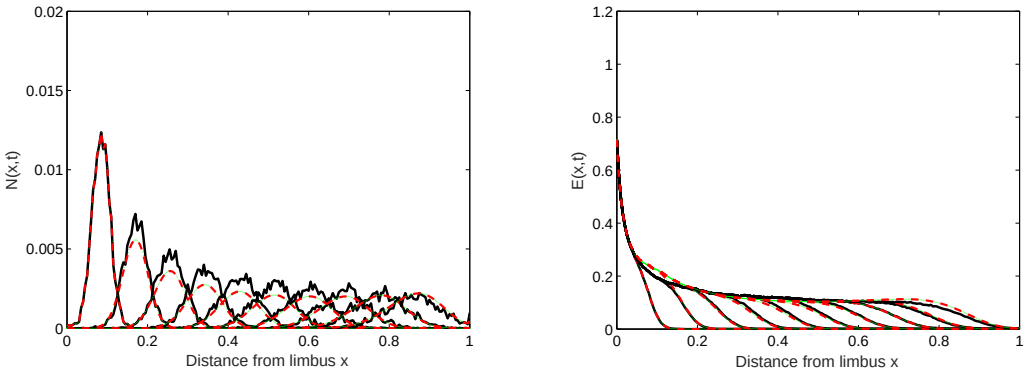

(c) $\tilde{\lambda} = 2.2644, a_n = 1, \tilde{a}_e = 0.0949$ (d) $\tilde{\lambda} = 2.2644, a_n = 1, \tilde{a}_e = 0.0949$

Figure A.8: Model 2: Numerical solutions to equations (A.17)-(A.19) ($B = 1$) with $\delta x = 1/400$. Solutions are shown from $t = 0-2$ in 0.2 intervals. We used a finite difference scheme in space and time-stepping performed with MATLAB's *ode15s* (green dots) and MATLAB's *ode23tb* (red dashed line). We also used MATLAB's *ode113* and *ode23t* (results not shown). All methods agree, and agree with averaged CA simulation results (black). Parameters: $D = 10^{-3}, \chi = 0.4$, (a)-(b) $P_p = 10^{-1}, a_e = 1$, (c)-(d) $P_p = 10^{-1}, a_e = 0.2$.

Appendix B

Robustness Tests

In this appendix, we compare the solutions to our systematically-derived PDE models to averaged CA simulation results for different values of the lattice spacing ($h = 1/100, h = 1/300$) to that used in the main text ($h = 1/200$). We show comparisons between CA Model 0 (no VE) and Model 0 PDEs, CA Model 1 (TC VE) and Model 1 PDEs and CA Model 2 (TC and EC VE) and Model 2 PDEs. We are confirming the validity of our continuum models for different CA lattice spacings.

B.1 Model 0: Robustness Tests

In this section, we reproduce Figs. 2.5 and 2.6 in Chapter 2 using a lattice spacing of $h = 1/100$ and $h = 1/300$ (solving equations (2.26)-(2.31)). We alter the values of h and k in the discrete model (see Table 2.1), and recalculate the corresponding values of τ and χ in the continuum model. In particular, for $h = 1/100$, we choose $k = 50$, so that $\chi = 0.2$ and $\tau = 1/40$. We run the discrete model for 160 discrete time steps in this case or 4 continuum time units. For $h = 1/300$, we choose $k = 100$, and therefore $\chi = 0.4$ and $\tau = 1/360$. We

run the discrete model for 720 discrete time steps for $h = 1/300$ or 2 continuum time units.

The lattice spacing used in Figs. 2.5 and 2.6 is $h = 1/200$, we have chosen larger and smaller values of the lattice spacing to show that our model can be used for other values of h, provided it is small, and that the qualitative behaviour of the discrete and continuum models are the same (see Figs. B.1 and B.2).

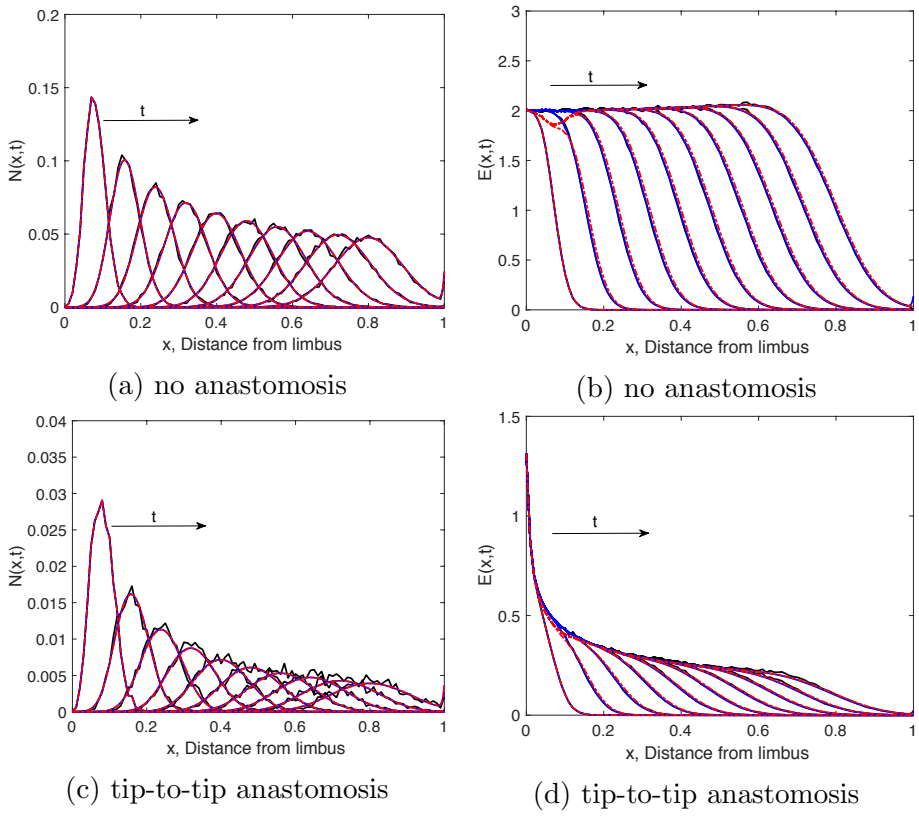

(a) no anastomosis (b) no anastomosis

(c) tip-to-tip anastomosis (d) tip-to-tip anastomosis

Figure B.1: Model 0 comparisons: $h = 1/100, k = 50, \tau = 1/40, \chi = 0.2$. (Left panel) Tip cell (TC) density, (Right panel) Endothelial cell (EC) density. TCs migrate via diffusion and chemotaxis towards the TAF source at $x = 1$, leaving behind a trail of ECs. (a), (b) A vessel network forms as TCs move and branch ($P_p = 10^{-3}$). (c), (d) Tip-to-tip anastomosis annihilates TCs producing a less dense vessel network than in (a). Column-averaged CA simulation results (black solid curve) are shown from $t = 0.4$ to $t = 4$ in 0.4 intervals (the arrow shows the direction of increasing time). The CA simulation results at $t_{IC} = 0.4$ are used as the initial conditions in the DCE-derived PDE models (blue curve, equations (2.26)-(2.31)) and BC model (red curves). Discrete and PDE model parameters are given in Table 2.1 and within caption text.

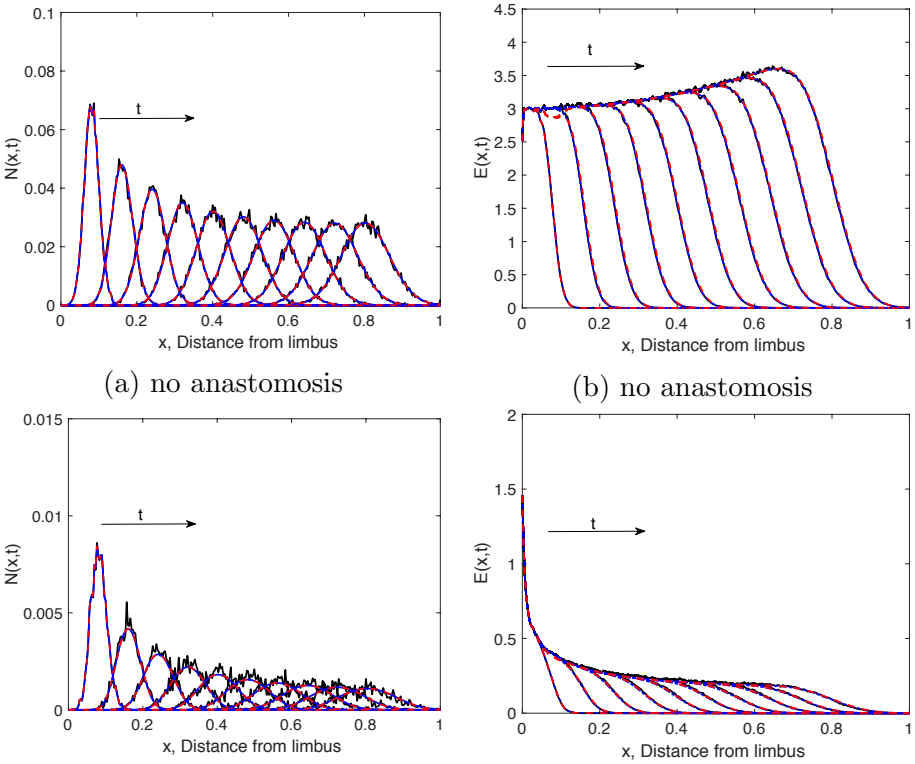

(a) no anastomosis

(b) no anastomosis

(c) tip-to-tip anastomosis

(d) tip-to-tip anastomosis

Figure B.2: Model 0 comparisons: $h = 1/300, k = 100, \tau = 1/360, \chi = 0.4$. (Left panel) Tip cell (TC) density, (Right panel) Endothelial cell (EC) density. TCs migrate via diffusion and chemotaxis towards the TAF source at $x = 1$, leaving behind a trail of ECs. (a), (b) A vessel network forms as TCs move and branch ($P_p = 10^{-3}$). (c), (d) Tip-to-tip anastomosis annihilates TCs producing a less dense vessel network than in (a). Column-averaged CA simulation results (black solid curve) are shown from $t = 0.2$ to $t = 2$ in 0.2 intervals (the arrow shows the direction of increasing time). The CA simulation results at $t_{IC} = 0.4$ are used as the initial conditions in the DCE-derived PDE models (blue curve, equations (2.26)-(2.31)) and BC model (red curves). In the BC model, we have rescaled the EC density with $\kappa \approx 3$. Discrete and PDE model parameters are given in Table 2.1 and within caption text, with the movement probabilities given as: $P^{x+} = \frac{5}{12}, P^{x-} = \frac{1}{12}, P^{y\pm} = \frac{1}{4}$.

B.2 Models 1 and 2: Robustness Tests

In this section, we reproduce Figs. 3.2 and 3.3 (lattice spacing $h = 1/200$) in Chapter 3 using a lattice spacing of $h = 1/100$ (see Figs. B.3-B.4) and $h = 1/300$ (see Figs. B.5 and B.6). In the discrete model, we alter the values of h and k (see Table 3.4), and in the continuum model this implies that the values of τ and χ will change (see Section B.1).

For $h = 1/300$, we do not show the comparisons between the PDEs and discrete model when TCs moves are aborted when prohibiting self-loops. In this case, the lattice is 300×300 and half of the 300 sites at $i = 1$ are initially seeded with TCs (see equation (2.10)). This implies that more ECs are created as there are more TCs in the domain, and thus, a larger EC VE effect during tip-to-sprout anastomosis leads to long tails in the EC density and a deviation from the continuum model. As we have mentioned, we need an alternate continuum model to quantify a non-negligible EC VE effect.

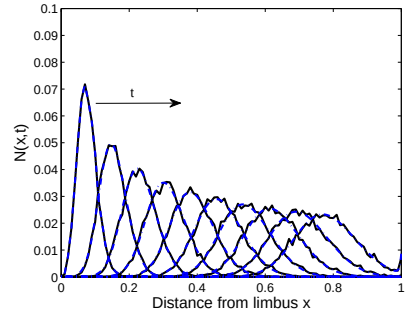

(a) a_e N/A

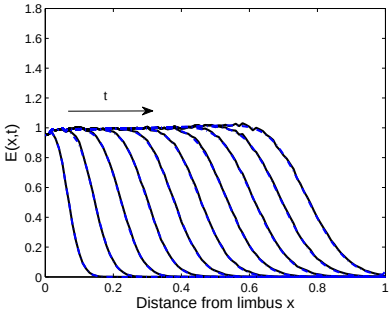

(b) a_e N/A

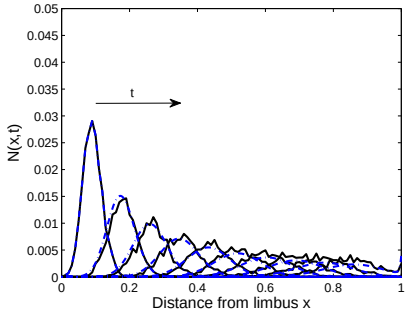

(c) $\tilde{a}_e = 0.1113 \pm 0.0011, a_e = 1$

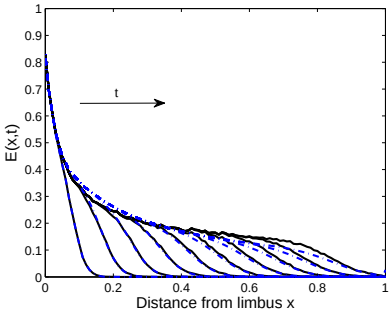

(d) $\tilde{a}_e = 0.1113 \pm 0.0011, a_e = 1$

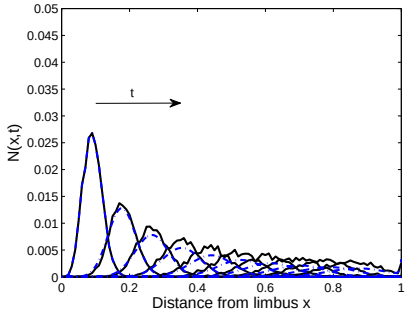

(e) $\tilde{a}_e = 0.1800 \pm 0.0024, a_e = 1$, EC VE

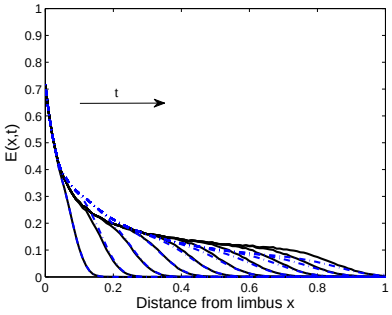

(f) $\tilde{a}_e = 0.1800 \pm 0.0024, a_e = 1$, EC VE

Figure B.3: Model 1 and 2 comparisons ($a_n = 0$): $h = 1/100, k = 50, \tau = 1/40, \chi = 0.2$. (Left panel) Tip cell (TC) density, (Right panel) Endothelial cell (EC) density. TCs migrate via diffusion and chemotaxis incorporating TC VE ($a_n = 0$) towards the TAF source at $x = 1$, leaving behind a trail of ECs. (a), (b) Model 1 (c), (d) Model 2: Tip-to-sprout anastomosis excluding self-loops, but TC move allowed (e), (f) Model 2: Tip-to-sprout anastomosis excluding self-loops with TC move aborted (EC VE). Column-averaged CA simulation results (black solid curve) are shown from $t = 0.4$ to $t = 4$ in 0.4 intervals. The CA simulation results at $t_{IC} = 0.4$ are used as the initial conditions in the DCE-derived PDE models (blue dashed-dot curve, equations (4.7)-(4.9)). Discrete and PDE model parameters are given in Table 3.4 and within caption and main text. The arrow shows the direction of increasing time.

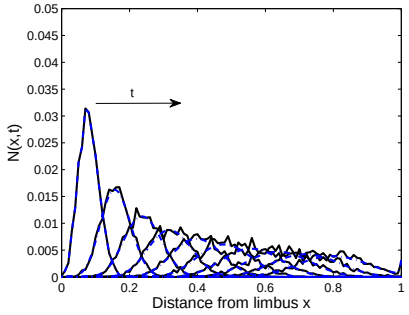

(a) a_e N/A

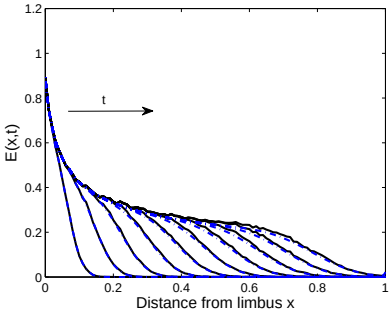

(b) a_e N/A

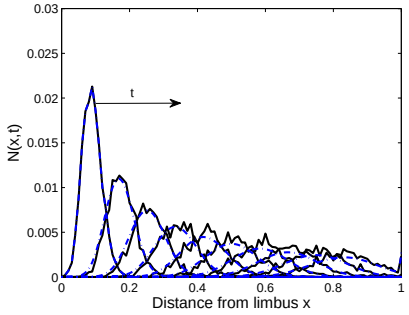

(c) $\tilde{a}_e = 0.0471 \pm 0.0007, a_e = 1$

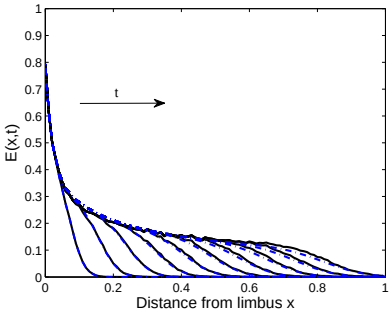

(d) $\tilde{a}_e = 0.0471 \pm 0.0007, a_e = 1$

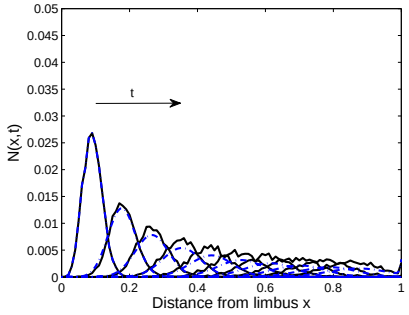

(e) $\tilde{a}_e = 0.1209 \pm 0.0023, a_e = 1$

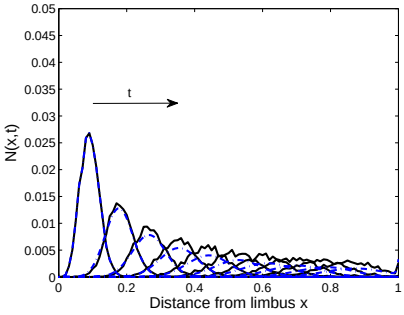

(f) $\tilde{a}_e = 0.1209 \pm 0.0023, a_e = 1$

Figure B.4: Model 1 and 2 comparisons ($a_n = 1$): $h = 1/100, k = 50, \tau = 1/40, \chi = 0.2$. (Left panel) Tip cell (TC) density, (Right panel) Endothelial cell (EC) density. Tip-to-tip anastomosis ($a_n = 1$) annihilates TCs, and thus the TC density is lower than in Fig. B.3 (left panel). As a result, the EC densities are also lower when tip-to-tip anastomosis is active. (a), (b) Model 1 (b), (c) Model 2: Tip-to-sprout anastomosis excluding self-loops, but TC move allowed (e), (f) Model 2: Tip-to-sprout anastomosis excluding self-loops with TC move aborted (EC VE). Column-averaged CA simulation results (black solid curve) are shown from $t = 0.4$ to $t = 4$ in 0.4 intervals. The CA simulation results at $t_{IC} = 0.4$ are used as the initial conditions in the DCE-derived PDE models (blue dashed-dot curve, equations (4.7)-(4.9)) with the PDE solutions. Discrete and PDE model parameters are given in Table 3.4 and within caption and main text The arrow shows the direction of increasing time.

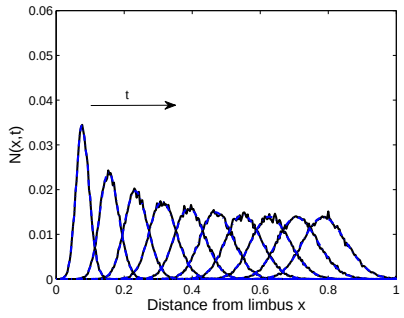

(a) a_e N/A

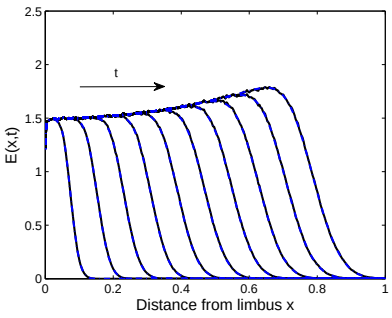

(b) a_e N/A

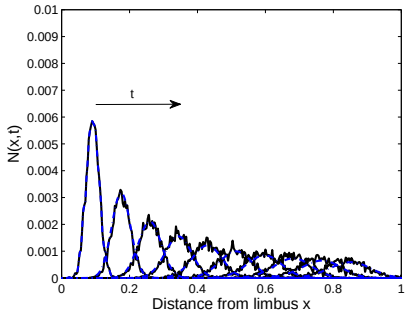

(c) $\tilde{a}_e = 0.0350 \pm 0.0001, a_e = 1$

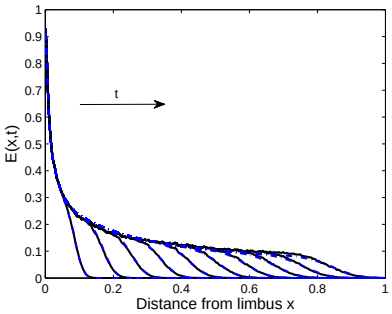

(d) $\tilde{a}_e = 0.0350 \pm 0.0001, a_e = 1$

Figure B.5: Model 1 and 2 comparisons ($a_n = 0$): $h = 1/300, k = 100, \tau = 1/360, \chi = 0.4$. (Left panel) Tip cell (TC) density, (Right panel) Endothelial cell (EC) density. TCs migrate via diffusion and chemotaxis incorporating TC VE ($a_n = 0$) towards the TAF source at $x = 1$, leaving behind a trail of ECs. (a), (b) Model 1 (c), (d) Model 2: Tip-to-sprout anastomosis excluding self-loops, but TC move allowed. Column-averaged CA simulation results (black solid curve) are shown from $t = 0.2$ to $t = 2$ in 0.2 intervals. The CA simulation results at $t_{IC} = 0.2$ are used as the initial conditions in the DCE-derived PDE models (blue dashed-dot curve, equations (4.7)-(4.9)). Discrete and PDE model parameters are given in Table 3.4 and within caption and main text. The arrow shows the direction of increasing time.

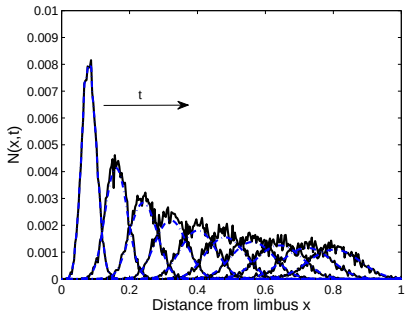

(a) a_e N/A

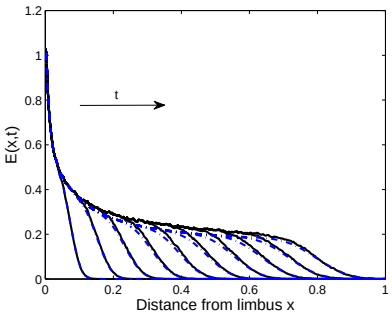

(b) a_e N/A

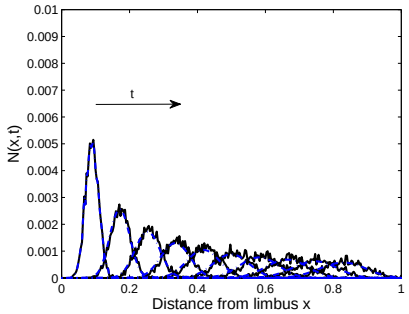

(c) $\tilde{a}_e = 0.0150 \pm 0.0001, a_e = 1$

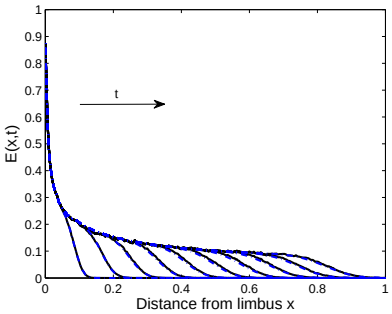

(d) $\tilde{a}_e = 0.0150 \pm 0.0001, a_e = 1$

Figure B.6: Model 1 and 2 comparisons ($a_n = 1$): $h = 1/300, k = 100, \tau = 1/360, \chi = 0.4$. (Left panel) Tip cell (TC) density, (Right panel) Endothelial cell (EC) density. Tip-to-tip anastomosis ($a_n = 1$) annihilates TCs, and thus the TC density is lower than in Fig. B.5 (left panel). As a result, the EC densities are also lower when tip-to-tip anastomosis is active. (a), (b) Model 1 (b), (c) Model 2: Tip-to-sprout anastomosis excluding self-loops, but TC move allowed. Column-averaged CA simulation results (black solid curve) are shown from $t = 0.2$ to $t = 2$ in 0.2 intervals. The CA simulation results at $t_{IC} = 0.2$ are used as the initial conditions in the DCE-derived PDE models (blue dashed-dot curve, equations (4.7)-(4.9)) with the PDE solutions shown from $t = 0.2$ to $t = 2$. Discrete and PDE model parameters are given in Table 3.4 and within caption and main text The arrow shows the direction of increasing time.

Appendix C

Appendix to Chapter 3

In this Appendix, we present calculations that augment the content of Chapter 3.

C.1 Column Averages and Continuum Model Derivation

We want to formulate the DCEs in terms of column averages, so that we can relate the resulting equation to a one-dimensional PDE. For the motility mechanism, we could either directly write down the terms that affect column averages, or multiply both sides of equations (3.4)-(3.7) by $1/R$ and sum over the column index j, and apply a mean-field approximation for column averages.

To elucidate the approximations being made, we will consider TC movement incorporating TC VE and separate the motility mechanism into terms that describe anastomosis and those that do not. To make the arguments easier to follow, we will explicitly write down transition probabilities in an idealised case (transition probability for random motion and bias ρ is $(1 \pm \rho)/4$).

Let us first consider diffusion only. If we formulate the DCEs for diffusion, and sum the expression over the columns, terms that describe movement within a column cancel (i.e. number of cells within that column remain unchanged) as follows:

$$\frac{1}{R}\sum_{j=1}^{R}\Bigg(\underbrace{\frac{1}{4}\left(n_{i+1,j}+n_{i-1,j}+n_{i,j+1}+n_{i,j-1}\right)\left(1-n_{i,j}\right)}_{\text{movement into }(i,j)}$$

$$\underbrace{-\frac{1}{4}n_{i,j}\left(\left(1-n_{i+1,j}\right)+\left(1-n_{i-1,j}\right)+\left(1-n_{i,j+1}\right)+\left(1-n_{i,j-1}\right)\right)}_{\text{movement out of }(i,j)}\Bigg)$$

$$=\frac{1}{R}\sum_{j=1}^{R}\frac{1}{4}\left(n_{i+1,j}-2n_{i,j}+n_{i-1,j}\right)=\frac{1}{4}\left(N_{i+1}-2N_i+N_{i-1}\right). \qquad \text{(C.1)}$$

Thus, we are left with the discretised version of linear diffusion in terms of the column averages, using the definitions in equations (2.12) and (2.13).

Next, we consider diffusion and chemotaxis with bias $\rho = O(h)$ in the x-direction (for simplicity) and TC VE. We sum the terms in the two-dimensional DCEs

over j to find

$$\begin{aligned}
&\frac{1}{R}\sum_{j=1}^{R}\underbrace{\frac{1}{4}\left((1+\rho)n_{i+1,j}+(1-\rho)n_{i-1,j}+n_{i,j+1}+n_{j-1}\right)(1-n_{i,j})}_{\text{movement into }(i,j)}\\
&-\frac{1}{R}\sum_{j=1}^{R}\underbrace{\frac{1}{4}n_{i,j}\left((1+\rho)(1-n_{i+1,j})+(1-\rho)(1-n_{i-1,j})\right)}_{\text{movement out of }(i,j)}\\
&-\frac{1}{R}\sum_{j=1}^{R}\underbrace{\frac{1}{4}n_{i,j}\left((1-n_{i,j+1})+(1-n_{i,j-1})\right)}_{\text{movement out of }(i,j)}\\
&=\frac{1}{R}\sum_{j=1}^{R}\frac{1}{4}\left(n_{i+1,j}-2n_{i,j}+n_{i-1,j}-\rho(1-2n_{i,j})\left(n_{i+1,j}-n_{i-1,j}\right)\right)\\
&=\frac{1}{4}\left(N_{i+1}-2N_i+N_{i-1}-\rho\frac{1}{R}\sum_{j=1}^{R}(1-2n_{i,j})\left(n_{i+1,j}-n_{i-1,j}\right)\right). \quad \text{(C.2)}
\end{aligned}$$

To further simplify the last term representing biased motion in i, we must use a mean-field approximation for column averages. The mean-field approximation assumes that the occupancy of lattice sites is independent, which implies that the occupancy of columns (and rows) is independent. Invoking this approximation, we find

$$\sum_j n_{i,j}n_{i+1,j} \approx \frac{\sum_j n_{i,j}\sum_j n_{i+1,j}}{R}, \quad \text{(C.3)}$$

$$\sum_j n_{i,j}n_{i-1,j} \approx \frac{\sum_j n_{i,j}\sum_j n_{i-1,j}}{R}, \quad \text{(C.4)}$$

where a $1/R$ term has been introduced. Using these approximations, the last term of equation (C.2) can be written as

$$\begin{aligned}
&-\frac{\rho}{4}\frac{\sum_j(1-2n_{i,j})}{R}\frac{\sum_j(n_{i+1,j}-n_{i-1,j})}{R}\\
&=-\frac{\rho}{4}(1-2N_i)(N_{i+1}-N_{i-1}), \quad \text{(C.5)}
\end{aligned}$$

and thus, we have reduced the column average over the motility mechanism (excluding anastomosis) to a one-dimensional discretised equation incorporating diffusion and chemotaxis. This result is expected as TC movement within a column does not alter the column average. The mean-field approximation for column averages was used in Simpson et al. (2009a) to derive a one-dimensional PDE for a biased random walk with single and multi-species exclusion.

When we include tip-to-tip anastomosis, movements within a column do alter the TC density. However, we can still apply a mean-field approximation to reduce the DCE as follows:

$$\begin{aligned}
&\underbrace{-\frac{1}{R}\sum_{j=1}^{R}\frac{1}{4}\left((1+\rho)n_{i+1,j}+(1-\rho)n_{i-1,j}+n_{i,j+1}+n_{j-1}\right)n_{i,j}}_{\text{tip-to-tip anastomosis}}\\
&\approx -\frac{1}{R}\sum_{j=1}^{R}\frac{1}{4}\left((1+\rho)n_{i+1,j}+(1-\rho)n_{i-1,j}+n_{i,j+1}+n_{j-1}\right)\frac{1}{R}\sum_{j}n_{i,j}\\
&= -\frac{1}{4}\left((1+\rho)N_{i+1}+(1-\rho)N_{i-1}+N_i+N_i\right)N_i \qquad \text{(C.6)}
\end{aligned}$$

where we have used the following mean-field approximations

$$\frac{1}{R}\sum_{j}n_{i,j}n_{i,j+1} \approx \frac{\sum_j n_{i,j}\sum_j n_{i,j+1}}{R^2} = N_iN_i, \qquad \text{(C.7)}$$

$$\frac{1}{R}\sum_{j}n_{i,j}n_{i,j-1} \approx \frac{\sum_j n_{i,j}\sum_j n_{i,j-1}}{R^2} = N_iN_i. \qquad \text{(C.8)}$$

The sum over j at the boundaries, $j = 1$ or $j = R$ is zero (as TCs cannot move off the lattice in our CA model).

For the EC density, TC movement within a column creates ECs, and thus movements out of a site to another site within a column must be retained by applying the approximations in equations (C.3)-(C.8) (see Chapter 3 for explicit expressions).

Lastly, we consider branching. To illustrate the approximations required to formulate DCEs in terms of column averages, we will consider TC VE only (see branching terms in equation (3.4)). If we multiply these branching terms in the DCE by $1/R$ and sum over j, we find

$$\begin{aligned}
&\frac{1}{R}\sum_j \underbrace{P_p c_i \left[n_{i,j-1}(1-n_{i,j})(1-n_{i,j-2}) + n_{i,j+1}(1-n_{i,j})(1-n_{i,j+2})\right.}_{\text{branching into (i,j)}} \\
&\underbrace{\left.-n_{i,j}(1-n_{i,j+1})(1-n_{i,j-1})\right]}_{\text{branching out of (i,j)}} \\
&= \frac{P_p c_i}{R}\sum_j n_{i,j}(1-n_{i,j-1})(1-n_{i,j+1}),
\end{aligned} \tag{C.9}$$

which is expected given that branching occurs within the columns only. If there were no TC VE, equation (C.9) would reduce to $P_p c_i N_i$ (this is what we found in Chapter 2 by integrating the two-dimensional PDEs over y). To proceed further in the TC VE case, which introduces the non-linear terms $(1-n_{i,j\pm1})$, we make the following mean-field approximations:

$$\begin{aligned}
&\frac{1}{R}\sum_j n_{i,j}(1-n_{i,j-1})(1-n_{i,j+1}) \approx \frac{\sum_j n_{i,j}(1-n_{i,j-1})}{R}\frac{\sum_j (1-n_{i,j+1})}{R} \\
&\approx \frac{\sum_j n_{i,j}}{R}\frac{\sum_j (1-n_{i,j-1})}{R}\frac{\sum_j (1-n_{i,j+1})}{R} \\
&\approx N_i(1-N_i)(1-N_i),
\end{aligned} \tag{C.10}$$

which, perhaps, is intuitive given that branching occurs within a column (only i dependence), provided there is sufficient space within the column (2 vacant sites within a column must be available in the CA model), quantified by the $(1-N_i)$ terms. In Chapter 2, we directly used the continuum analogue of the approximations outlined here.

We have considered simplified transition probabilities to illustrate the use of mean-field approximations for column averages, and we note that this approach

is appropriate for the transition probabilities in our model $P^{x\pm}, P^{y\pm}$, as these transition probabilities do not depend on j. We have considered only TC VE to illustrate the approximations made in formulating DCEs in terms of column averages, and we note that extending this framework to include EC VE is straightforward.

C.2 EC VE and the Backwards Heat Equation

In Chapter 3, we found that EC VE led to a backwards heat equation in the PDE for the EC density. To attempt to regularise the problem, we could include the $O(h^4)$ terms in the PDE derivation. We list the $O(h^4)$ terms in equation (3.29) below

$$-\frac{D}{12}h^2 N\left(\nabla^4(N+E)\right) - \frac{\chi}{6}h^2 N\left(\nabla c\cdot\nabla^3(N+E) + \nabla^3 c\cdot\nabla(N+E)\right), \tag{C.11}$$

and we note that the fourth (and third) order derivative of E is negative. To be consistent, if we were to include the $O(h^4)$ terms in the equation for the EC density, then we would have to add $O(h^4)$ terms to the TC density equation as well. We list those terms below

$$\begin{aligned}
&\frac{D}{12}h^2\left(N\nabla^4 E - E\nabla^4 N + \nabla^4 N\right) - \frac{\chi}{3}h^2\left(N(1-N-E)\nabla^4 c - N\nabla c\cdot\nabla^3 N\right)\\
&-\frac{\chi}{6}h^2\left(\nabla c\cdot\nabla^3 N - N\nabla c\cdot\nabla^3 E - E\nabla c\cdot\nabla^3 N - N\nabla^3 c\cdot\nabla E\right)\\
&-\frac{2\chi}{3}h^2(1-E)\nabla^3 c\cdot\nabla N - \frac{\chi}{2}h^2(1-N-E)\nabla^2 c\cdot\nabla^2 N\\
&+\frac{5\chi}{6}h^2 N\nabla^3 c\cdot\nabla N,
\end{aligned} \tag{C.12}$$

and we see that including the $O(h^4)$ terms renders the PDE model intractable. The $O(h^4)$ terms in equations (3.30) and (3.31) ($a_n = 1, a_e = 0$) are similar to

those in equations (C.11) and (C.12), though there are additional terms (results not shown). We therefore do not include $O(h^4)$ terms to attempt to regularise the backwards heat equations. Further, a moment dynamics framework utilising correlation functions is likely to be intractable (see Chapter 1), and will not enable us to derive a PDE model. In Chapter 4, we consider an alternative methodology to capture EC VE in the PDE models derived. We conclude that another methodology should be developed to systematically derive PDEs to capture EC VE.

C.2.1 Leading Order Behaviour

To elucidate the leading order behaviour of the EC density PDE when we have multi-species exclusion, we investigated two alternative versions of equation (3.29). Firstly, we dropped all $O(h^2)$ terms in equation (3.29), reasoned by the fact that the source term is the dominant contribution and that higher order terms are negligible. Additionally, we considered Byrne and Chaplain's (Byrne and Chaplain, 1995a) assumption that the rate of change of the EC density is proportional to the flux of TCs, $J = -\nabla \cdot D(1-N-E)\nabla N - DN\,(\nabla N + \nabla E) + \chi N(1-N-E)\nabla c$ (with the $2/h$ modification derived in Chapter 2). Thus, we consider the following two equations for EC density to elucidate the behaviour

of the system:

$$\frac{\partial E}{\partial t} = \mu(1 - N - E), \tag{C.13}$$

$$\frac{\partial E}{\partial t} = \frac{2}{h} \left| \nabla \cdot D(1 - N - E)\nabla N + DN\left(\nabla N + \nabla E\right) - \chi N(1 - N - E)\nabla c \right|, \tag{C.14}$$

$$\nabla \cdot D(1 - N - E)\nabla N + DN\left(\nabla N + \nabla E\right) + \chi N(1 - N - E)\nabla c \mid_{x=0,1} = 0, \tag{C.15}$$

$$E(x = 0, t) = E_{i=1}(\bar{K}_{IC}), \quad E(x = 1, t) = 0. \tag{C.16}$$

We solve equation (3.28) with no branching (i.e. $\lambda = 0$), reiterated below

$$\frac{\partial N}{\partial t} = D(1 - N - E)\nabla^2 N + DN\nabla^2(N + E) - \chi \nabla \cdot (N(1 - N - E)\nabla c)$$

along with each of the equations above, subject to no flux boundary conditions for N, and fixing E at $x = 0$ using the initial condition for E from the averaged CA simulation results, and fixing $E = 0$ at $x = 1$ (no ECs are created at $x = 1$, in keeping with the CA model). We solve the equations using central difference approximations in space, and MATLAB's *ode15s* to perform the time-stepping. We find that the solutions to equations (C.13) and (C.14) are similar (see Fig. C.1), though they do not capture the averaged CA results. However, the solutions for the TC and EC density do coincide with the leading edge of each front at each time step.

We also attempted to eliminate the backwards heat equation by adding equations (3.28) and (3.29), and replacing the equation for E with an equation for $N + E$, thereby eliminating the backwards heat equation. However, when solv-

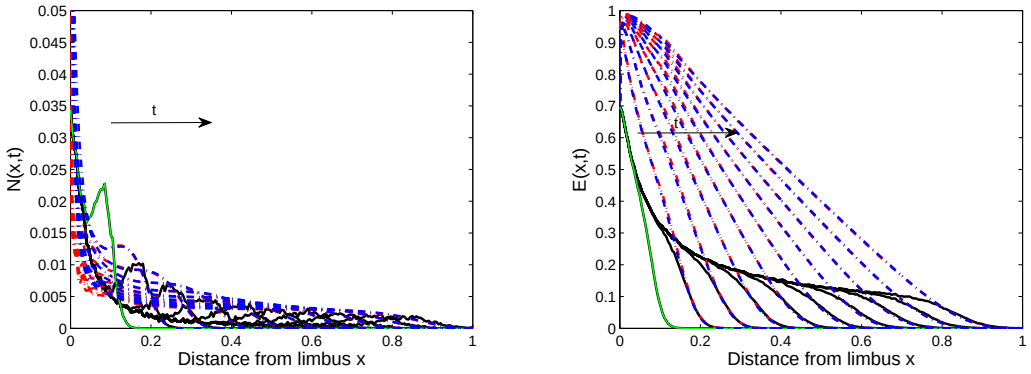

(a) TC density (b) EC density

Figure C.1: Comparison of discrete and continuum models, including only movement of TCs via chemotaxis and diffusion incorporating TC and EC VE. The results are shown for $t \in [0.2, 2]$ in $t = 0.2$ increments. The initial condition into the PDE models, taken from the averaged CA simulation results (black curves), are shown in green. The blue curves are the solutions to equations (3.28) and (C.13) (source term for EC density), and the red curves are the solutions to equations (3.28) and (C.14) (EC density proportional to TC flux). The PDE solutions agree with each other, but fail to capture the averaged CA simulation results. Note $N + E < 1 \, \forall t$.

ing this system of equations, we found that the solutions were very similar to those shown in Fig. C.1. We conclude, therefore, that the mean-field approximation does not generate equations that are able to account for EC VE processes occurring within our model of the snail-trail.

C.3 Prohibited Self-Loops without Aborted TC Moves

We note that the PDE model derived when tip-to-sprout anastomosis is active enables a TC to move to a site occupied by an EC. Thus, in fact, our equations model the situation where the TC move is allowed, even if we prohibit self-loops. By including aborted TC moves in the CA model, we are investigating an EC VE effect not explicitly accounted for in our PDE derivation, and as

we have shown, our PDE model, equations (3.22)-(3.27), is able to capture this behaviour (see Figs. 3.2 and 3.3 in Chapter 3, Section 3.5.1).

Here in Fig. C.2, we also compare PDE model solutions to the averaged CA simulation results with self-loops excluded, but where the TC move is allowed without tip-to-sprout anastomosis occurring (as in the non-volume excluding model in Chapter 2). We do this so that we can more easily determine the effect of the additional EC VE, which occurs when self-loops are prohibited.

By comparing Figs. C.2b and 3.2f (in Chapter 3, Section 3.5.1), it is clear that when we incorporate EC VE when aborting self-loops, the EC density declines more rapidly at $x \approx 0.1$. Aborted TC moves due to EC VE imply that no ECs are created, while if we allow the TC to move without tip-to-sprout anastomosis occurring, an EC is left behind. This is one reason why the PDE model solution for the EC density sits slightly above the averaged CA simulation results around $x \approx 0.1$. The decline in EC density exhibited in the averaged CA simulation results occurs early in space, as TCs interact with the ECs created immediately after initialization until most TCs are annihilated via tip-to-sprout anastomosis, beyond which the number of TCs no longer changes rapidly. A similar effect (a more rapid decline in EC density at $x \approx 0.1$) can be seen by comparing Figs. 3.4d-3.4f and C.2c-C.2d, we see that exclusion from ECs when prohibiting self-loops reduces the TC and EC density further as aborted TC moves imply that fewer ECs are created.

C.4 Branching Mechanisms

Firstly, we state the two-dimensional branching terms in the Model 1 and 2 PDEs that were omitted in Chapter 3 as we directly formulated the PDEs in one dimension. In what follows, $n(x, y, t)$ and $e(x, y, t)$ are respectively, the

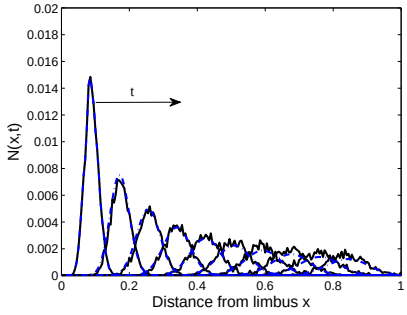

(a) Model 2, $a_n = 0$, $\tilde{a}_e = 0.0762 \pm 0.0004$, $a_e = 1$

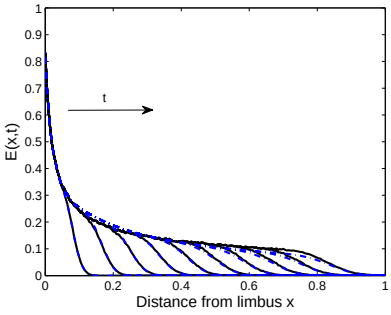

(b) Model 2, $a_n = 0$, $\tilde{a}_e = 0.0762 \pm 0.0004$, $a_e = 1$

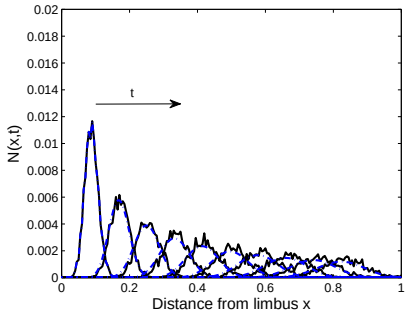

(c) Model 2, $a_n = 1$, $\tilde{a}_e = 0.0310 \pm 0.0003$, $a_e = 1$

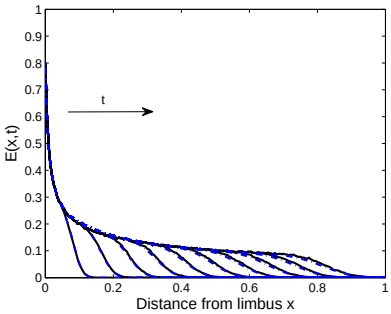

(d) Model 2, $a_n = 1$, $\tilde{a}_e = 0.0310 \pm 0.0003$, $a_e = 1$

Figure C.2: CA Model 2: Tip-to-sprout anastomosis with prohibited self-loops with TC movement (i.e. TC moves are not aborted). When we allow TC movement when we prohibit a self-loop, i.e. a TC movement occurs without tip-to-sprout anastomosis occurring, the TC and EC densities are higher than when the TC move is aborted (see Figs. 3.2 and 3.3 in Chapter 3), Section 3.5.1. Further, the PDE solutions (blue-dashed curves) agree better with the averaged CA simulation results (black curves, shown from $t = 0.2, 0.4, \cdots, 2.0$) than when TC moves are aborted, as the PDEs (equations (3.22)-(3.27)) do not explicitly incorporate EC VE. The CA simulation results at $t_{IC} = 0.2$ are used as the initial conditions in the DCE-derived PDE models (blue dashed-dot curve) with the PDE solutions shown from $t = 0.4 - 2$.

TC and EC densities in two dimensions. Further, we use the notation n_y to indicate the derivative of n with respect to y etc. In the Model 1 PDEs, the two-dimensional branching terms are

$$\lambda cn(1-n)^2 + \lambda h^2 \left(n_y^2(5n-4) + (1-5n+4n^2)n_{yy}\right) + O(h^4), \qquad \text{(C.17)}$$

and in the Model 2 PDEs, the two-dimensional branching terms are

$$\begin{aligned}
&\lambda cn(1-n-e)^2 \\
&+\lambda h^2 \left(e_y^2 n - 3e_{yy}n(1-n-e) - 2e_y(2-2e-3n)n_y + 4en_y^2\right) \\
&+\lambda h^2 \left(5nn_y^2 - 4n_y^2 + n_{yy} - 2en_{yy} + e^2 n_{yy} - 5nn_{yy} + 5enn_{yy} + 4n^2 n_{yy}\right) \\
&+O(h^4). \qquad \text{(C.18)}
\end{aligned}$$

We have considered branching from a TC into neighbouring sites. Now we briefly outline alternative branching mechanisms from an EC behind a TC (see Fig. C.3a), or a lattice site behind a TC (see Fig. C.3b), which can easily be extended to any number of lattice sites behind a TC. An EC is part of a sprout and therefore will have another EC at one of its remaining neighbouring sites. Therefore, an EC can only place a TC into one of the two remaining neighbouring sites (not necessarily in j only), provided those sites are unoccupied. For example, an EC at (i, j) in Fig. C.3a, located behind the TC at $(i+1, j)$, has one of the remaining neighbouring sites $(i-1, j)$ occupied by another EC. Thus, an EC at (i, j) can branch into $(i, j \pm 1)$ provided that site is unoccupied.

The two-dimensional DCEs for branching from an EC immediately behind a

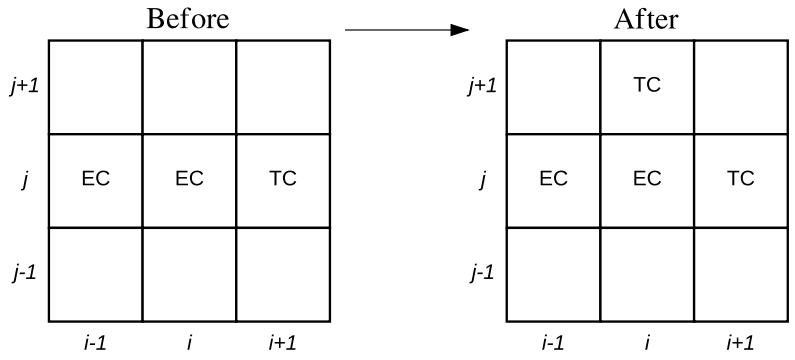

(a) Branching immediately behind a TC

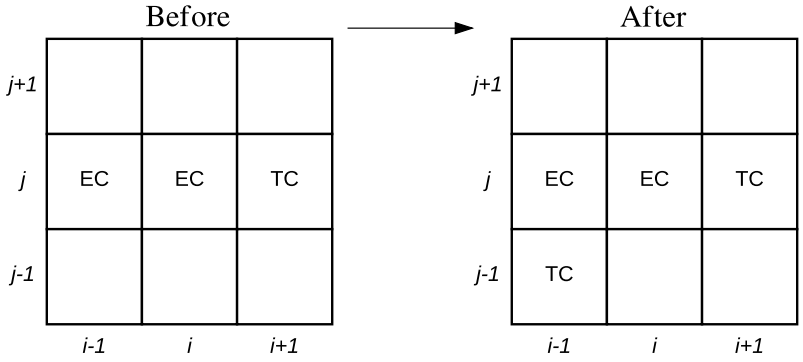

(b) Branching a lattice site behind a TC

Figure C.3: Schematic of branching from ECs. An EC can place daughter TCs at (a) $(i, j \pm 1)$ and (b) $(i - 1, j \pm 1)$.

TC, formulated using a mean-field approximation, is given by:

$$\begin{aligned}
&\delta n_{i,j} = \\
&\frac{P_b}{2}\left(n_{i+2,j}e_{i+1,j} + n_{i,j+2}e_{i,j+1} + n_{i-2,j}e_{i-1,j} + n_{i,j-2}e_{i,j-1} + n_{i+1,j-1}e_{i+1,j}\right. \\
&+n_{i+1,j-1}e_{i,j-1} + n_{i+1,j+1}\rho_{i+1,j} + n_{i+1,j+1}e_{i,j+1} + n_{i-1,j+1}e_{i,j+1} \\
&\left.+n_{i-1,j+1}e_{i-1,j} + n_{i-1,j-1}e_{i-1,j} + n_{i-1,j-1}e_{i,j-1}\right)(1 - n_{i,j} - e_{i,j}). \qquad \text{(C.19)}
\end{aligned}$$

The case for branching a lattice site behind a TC follows directly from the previous case (i.e. write down all possibilities enabling that branching configuration to arise) and is omitted here.

We remark that branching immediately behind a TC produces products of the

form ne, and branching a lattice site behind produces products of nee, and thus, if branching occurs m sites behind a TC, each product would consist of m e terms and one n term. If we take the continuum limit of the DCEs (in time and space in this case, i.e. $h \to 0$), we find that n satisfies

$$\frac{\partial n}{\partial t} = \lambda ne(1 - n - e), \tag{C.20}$$

$$\frac{\partial n}{\partial t} = \lambda ne^2(1 - n - e), \tag{C.21}$$

for branching immediately behind and a lattice site behind a TC, respectively, where $\lambda = \lim_{\tau \to 0} \frac{P_b}{2\tau}$.

We have described branching from a sprout of length one or two for simplicity. In reality, it is probable that branching only occurs provided the length of a sprout is greater than one or two cells. This is justified by the fact that experimentally observed networks exhibit an average vessel length larger than two cells (e.g. Zawicki et al. (1981)). We can extend our current framework to account for a larger minimum branching length. However, this would entail writing down all the possible configurations for branching from a sprout of a specified length. For example, if we want to impose a minimum length of 10, the transition probabilities would be products of 10 terms, specifying the occupancy of the TC and the 9 ECs behind it. In Chapter 4, we consider an alternative methodology (though parameter estimation) to account for branching from TCs at the head of a sprout of a set length.

Note

We note that if we had used a forward or backward difference approximation to the TAF gradient at the site of an agent (see equations (3.1)), and kept the

value of k (relates time and space scales in the chemotactic term, see equation (2.24)) the same, then the chemotactic coefficient would be halved. To ensure the same chemotactic coefficient, we would have to double the value of k. Thus, on the macroscale (up to $O(h^2)$), it is irrelevant whether a central, forward or backward difference is used in the CA model. On the microscale, however, using a central, forward or backward difference implies that filopodia interact with the environment differently.

Appendix D

Appendix to Chapter 4

Here we give the fitted parameter values for the results discussed in Chapter 4.

Table D.1: Model 1: Fitted Parameter Values. The CA model parameters a_n and the continuum analogue, λ, of the branching probability P_p, are also given. A branching rate of 1.6 corresponds to $P_p = 10^{-2}$ and 6.4 corresponds to $P_p = 4 \times 10^{-2}$.

λ	a_n	$\tilde{\lambda}$	$\tilde{a}_n$
1.6	0.02	1.4719 ± 0.0029	0.0333 ± 0.0003
1.6	0.05	1.3920 ± 0.0025	0.0811 ± 0.0003
1.6	0.1	1.3310 ± 0.0033	0.1606 ± 0.0005
1.6	0.15	1.2080 ± 0.0028	0.2297 ± 0.0005
1.6	0.2	1.1821 ± 0.0041	0.3001 ± 0.0008
6.4	0.02	5.4722 ± 0.0219	0.0216 ± 0.0010
6.4	0.05	4.9973 ± 0.0200	0.0574 ± 0.0013
6.4	0.1	4.4291 ± 0.0150	0.1039 ± 0.0014
6.4	0.15	4.0862 ± 0.0127	0.1590 ± 0.0016
6.4	0.2	3.8473 ± 0.0111	0.2164 ± 0.0017

Table D.2: Model 1: BC Model Fitted Parameter Values. The CA model parameters a_n and the continuum analogue, λ, of the branching probability P_p, are also given. A branching rate of 1.6 corresponds to $P_p = 10^{-2}$ and 6.4 corresponds to $P_p = 4 \times 10^{-2}$. The continuum analogues of the diffusion and chemotactic coefficients are $D = 10^{-3}$ and $\chi = 0.4$, respectively.

λ	a_n	$\tilde{D}_{\mathrm{BC}}$	$\tilde{\chi}_{\mathrm{BC}}$	$\tilde{\alpha}_{\mathrm{BC}}$	$\tilde{\beta}_n$
1.6	0.02	0.0011 ± 0.0000	0.3885 ± 0.0001	1.4698 ± 0.0085	5.7575 ± 0.1306
1.6	0.05	0.0011 ± 0.0000	0.3911 ± 0.0001	1.3744 ± 0.0084	13.1802 ± 0.1498
1.6	0.1	0.0010 ± 0.0000	0.3926 ± 0.0002	1.3265 ± 0.0094	25.9502 ± 0.2108
1.6	0.15	0.0010 ± 0.0000	0.3940 ± 0.0002	1.2025 ± 0.0089	36.5733 ± 0.2291
1.6	0.2	0.0010 ± 0.0000	0.3936 ± 0.0002	1.2000 ± 0.0088	48.0085 ± 0.2634
6.4	0.02	0.0006 ± 0.0000	0.3729 ± 0.0003	8.7030 ± 0.1141	31.1261 ± 0.7475
6.4	0.05	0.0009 ± 0.0000	0.3775 ± 0.0003	6.4969 ± 0.0969	28.4414 ± 0.9530
6.4	0.1	0.0012 ± 0.0000	0.3833 ± 0.0002	4.4815 ± 0.0508	20.6232 ± 0.7463
6.4	0.15	0.0012 ± 0.0000	0.3877 ± 0.0002	3.8890 ± 0.0268	24.6209 ± 0.4986
6.4	0.2	0.0011 ± 0.0000	0.3905 ± 0.0002	3.7604 ± 0.0202	34.9179 ± 0.4415

Table D.3: Model 2: Fitted Parameter Values. The CA model parameters a_e and the continuum analogue, λ, of the branching probability P_p, are also given. A branching rate of 16 corresponds to $P_p = 10^{-1}$.

$a_n = 0, \tilde{a} = 0$			
λ	a_e	$\tilde{\lambda}$	$\tilde{a}_e$
16	0.1	5.5277 ± 0.0705	0.1178 ± 0.0016
16	0.2	4.9136 ± 0.0528	0.1197 ± 0.0013
16	1	3.6257 ± 0.0346	0.1373 ± 0.0012
$a_n = 1, \tilde{a} = 1$			
λ	a_e	$\tilde{\lambda}$	$\tilde{a}_e$
16	0.1	2.7588 ± 0.0581	0.1001 ± 0.0017
16	0.2	2.2644 ± 0.0434	0.0949 ± 0.0014
16	1	1.5406 ± 0.0344	0.1034 ± 0.0013

Table D.4: Model 2: BC Model Fitted Parameter Values. The CA model parameters a_e are given. A branching probability of $P_p = 10^{-1}$ corresponds to a branching rate of $\lambda = 16$. The continuum analogues of the diffusion and chemotactic coefficients are $D = 10^{-3}$ and $\chi = 0.4$, respectively.

$a_n = 0, \beta_n = 0$				
a_e	$\tilde{D}_{\mathrm{BC}}$	$\tilde{\chi}_{\mathrm{BC}}$	$\tilde{\lambda}_{\mathrm{BC}}$	$\tilde{\beta}_e$
0.1	0.0017 ± 0.0001	0.3610 ± 0.0022	5.4489 ± 0.0680	18.4322 ± 0.2562
0.2	0.0016 ± 0.0001	0.3721 ± 0.0017	4.6978 ± 0.0511	18.4056 ± 0.2089
1	0.0014 ± 0.0001	0.3856 ± 0.0012	3.3656 ± 0.0348	20.2419 ± 0.1794
$a_n = 1, \beta_n = 160$				
a_e	$\tilde{D}_{\mathrm{BC}}$	$\tilde{\chi}_{\mathrm{BC}}$	$\tilde{\lambda}_{\mathrm{BC}}$	$\tilde{\beta}_e$
0.1	0.0024 ± 0.0001	0.3655 ± 0.0023	2.7258 ± 0.0537	14.0966 ± 0.2207
0.2	0.0019 ± 0.0001	0.3844 ± 0.0016	2.0614 ± 0.0397	13.6286 ± 0.1651
1	0.0016 ± 0.0001	0.3907 ± 0.0011	1.3811 ± 0.0313	14.8300 ± 0.1516

Appendix E

Appendix to Chapter 5

E.1 Parameter Estimation Bounds

When fitting the PDE models to averaged CA simulation results generated using Model 1 CA rules, we use the following bounds for the branching rate and anastomosis parameter in the Model 1 PDEs: $\tilde{\lambda} \in [0, 30]$, $\tilde{a}_n \in [0, 1]$. For the BC Model, the bounds are: $\tilde{D}_{\text{BC}} \in [10^{-4}, 10^{-3}]$, $\tilde{\chi}_{\text{BC}} \in [0.2, 0.5]$, $\tilde{\alpha} \in [0, 30]$ and $\tilde{\beta}_n \in [0, 80]$. For the Model 0 PDEs, the bounds are: $\tilde{D}_{\text{M0}} \in [10^{-4}, 10^{-3}]$, $\tilde{\chi}_{\text{M0}} \in [0.2, 0.5]$, $\tilde{\lambda}_{\text{M0}} \in [0, 30]$ and $\tilde{a}_n^{\text{M0}} \in [0, 1]$. The bounds for the branching parameters are used when $P_p = O(10^{-2})$. For $P_p = 10^{-3}$, we reduce the branching rate upper bound for all PDE models to 10.

When we fit PDE models to averaged CA simulation results generated using Model 2 CA rules, we use the following bounds: $\tilde{\lambda} \in [0, 30]$, $\tilde{a}_e \in [0, 1]$ for the Model 2 PDEs. For the BC Model, the bounds are: $\tilde{D}_{\text{BC}} \in [10^{-4}, 10^{-3}]$, $\tilde{\chi}_{\text{BC}} \in [0.2, 0.5]$, $\tilde{\alpha} \in [0, 30]$ and $\tilde{\beta}_e \in [0, 80]$. For Model 0, the bounds are: $\tilde{D}_{\text{M0}} \in [10^{-4}, 10^{-3}]$, $\tilde{\chi}_{\text{M0}} \in [0.2, 0.5]$, $\tilde{\lambda}_{\text{M0}} \in [0, 30]$ and $\tilde{a}_e^{\text{M0}} \in [0, 1]$.

E.2 Descriptive and Predictive Power Statistics

Methodology: Descriptive Power

We assess descriptive power as follows: we fit the PDE models to averaged CA simulation results at all time points ($t = 0.4 - 2.0$), and estimate the relevant parameters (discussed in Section 5.3.1 in Chapter 5). We then assess the goodness of fit in terms of a variety of metrics, including RMSEs, and AIC_c (discussed in Section 5.3.2), and rank models according to these metrics, termed the descriptive power of the models.

We run *lsqnonlin* for all time points ($t = 0.4, 0.6, \cdots 2.0$) with a tolerance of 10^{-7} from 30 randomly chosen initial guesses (in parallel using 2 to 4 MATLAB workers). The optimization problem when fitting to all time points is constrained (given that the features of the averaged CA simulation results over the entire time interval and spatial domain constrain the values that the parameters can take). Thus, 30 initial guesses within specified parameter bounds (given in the respective sections below) enable us to obtain parameter estimates with tight confidence intervals. In fact, given that the problem is constrained, *lsqnonlin* with a tolerance of 10^{-6} actually provides very similar (the same to four decimal places) parameter estimates as a tolerance of 10^{-7}. In general, running *lsqnonlin* and estimating parameters for each of the continuum PDEs models, for each set of averaged simulation results generated by the CA, takes approximately 1 hour.

We note that when considering predictive power (see Chapter 5), we lowered the tolerance (to *lsqnonlin's* default tolerance) and increased the number of initial guesses as the optimization problem, when fitting to the first four time points

$(t = 0.4 - 1)$, is not as constrained as in the descriptive power case, when we fit the models to all time points. The reasoning behind this is as follows: many of the distinctive features of the averaged CA simulation results occur at later time points, e.g. the branching probability increases as the TC front approaches the TAF source and, thus, is higher for $t > 1$. We expect, therefore, a little more variability (larger confidence intervals) in the parameter values than in the descriptive case. To account for this, we increase the number of randomly chosen initial guesses, and we lower the tolerance of *lsqnonlin* (as it may take much longer, or may not be able to satisfy a tolerance of 10^{-7}).

E.2.1 Model 1

In Fig. E.1, we consider the descriptive power, and we see that the TC and EC RMSEs for all three models are clustered together at low mass. As the mass increases (for different sets of CA parameter values), the differences between the TC RMSEs for each PDE model increases. The relative difference in the EC RMSEs however, do not increase as much as the TC RMSEs. Further, all models capture the EC mass well. For the TC mass, the models perform similarly with the exception of high cell mass (TC VE effects non-negligible), where Model 1 PDEs capture the TC mass better than the BC Model and Model 0. Generally, the AIC_c for the Model 1 PDEs is the lowest for both the TC and EC densities, while the AIC_c values for Model 0 PDEs and the BC Model are similar. The AIC_c values corroborate the results found using the RMSEs as a goodness of fit measure.

The relative errors (descriptive case) for the TC and EC densities for each model are shown in Fig. E.2. The Model 1 PDEs have lower relative errors than the BC model and Model 0 PDEs (compare Figs. E.2a and E.2b to Figs. E.2c-E.2f).

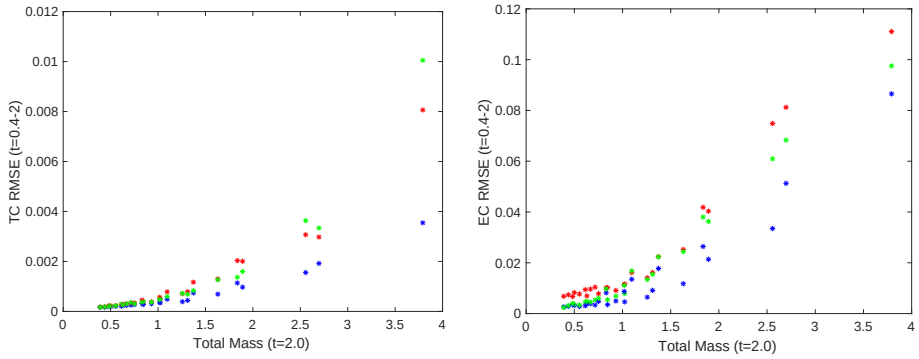

(a) TC RMSE

(b) EC RMSE

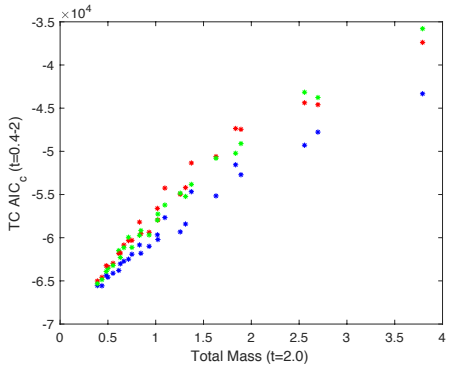

(c) TC AIC_c

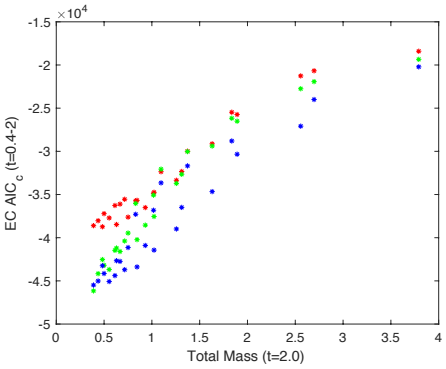

(d) EC AIC_c

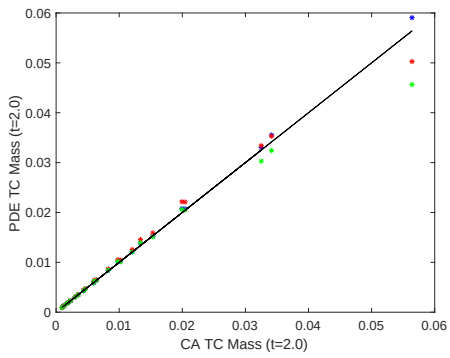

(e) TC Mass ($t = 2.0$)

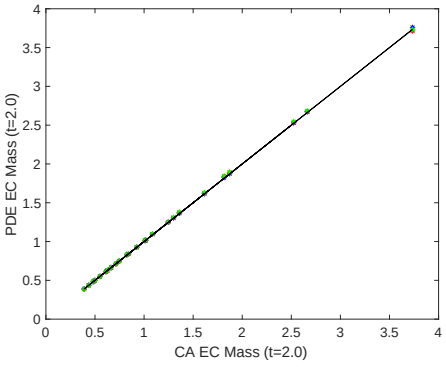

(f) EC Mass ($t = 2.0$)

Figure E.1: Model 1 Descriptions: RMSE and AIC_c values for each PDE model visualised against mass determined from CA model (each mass point corresponds to a particular set of CA model parameters). Key: Blue = Model 1, Red = BC Model, Green = Model 0. (a), (c) The TC RMSEs and AIC_c values are clustered together for all PDE models, except when the mass increases introducing non-linear TC VE effects. (b), (d) The EC RMSEs and AIC_c values for all PDE models are relatively close. (e) All PDE models approximate the TC mass from the CA model (black line, visualised as a continuum) well, except at high mass, where the Model 1 PDEs approximate the mass better than the other PDE models. (f) All PDE models capture the EC mass from the CA model (black line) well. Overall, the Model 1 PDEs are a better descriptive model of the TC density for high cell density, and otherwise, all PDE models have similar descriptive power.

The relative errors for the BC Model and the Model 0 PDEs generally increase as a_n decreases and P_p increases (as mass increases). The range in the relative errors for the Model 1 PDEs do not show the variation found in the Model 0 PDEs and the BC Model. We note that the relative error for the TC density (see equation (6.1)) penalises the BC model heavily, based on the thresholding we have chosen. The relative errors corroborate the results found using the RMSE and AIC_c. Overall, all models have comparable descriptive power, except at high cell density, where the Model 1 PDEs are able to capture non-linear TC behaviour due to TC VE. The parameter values found through fitting are given in Tables E.1, E.2 and E.3.

E.2.2 Model 2, $a_n = 0$

In Figs. E.3, we illustrate the descriptive power of the BC model and the Model 2 PDEs. The RMSEs and AIC_c values follow the same trend (see Figs. E.3a-E.3d): for the TC density, the Model 2 PDEs have smaller RMSEs and AIC_c values than the BC model except for $P_p = 10^{-1}$ and $a_e = 0.2, 0.1$. Recall from Chapter 4 that it was for these combinations of a_e and P_p that the Model 2 PDEs were out of phase with the averaged CA simulation results at $t = 2.0$. For the EC density, the BC model RMSEs and AIC_c are lower than the Model 2 PDEs. Generally, the differences in the RMSEs and the AIC_c values for the PDE models are not large and, thus, both models have similar descriptive power. In terms of mass (see Figs. E.3e and E.3f), both models approximate the mass from the averaged CA simulation results at $t = 2.0$ well, except that the Model 2 PDEs underestimate the mass for $P_p = 10^{-2}$ and $a_e = 0.1, 0.2$. Further, the AIC_c and RMSE values are much smaller than in the predictive case (see Fig. 5.5), indicating a better fit. Estimated parameter values can be found in Tables E.7, E.8 and E.9.

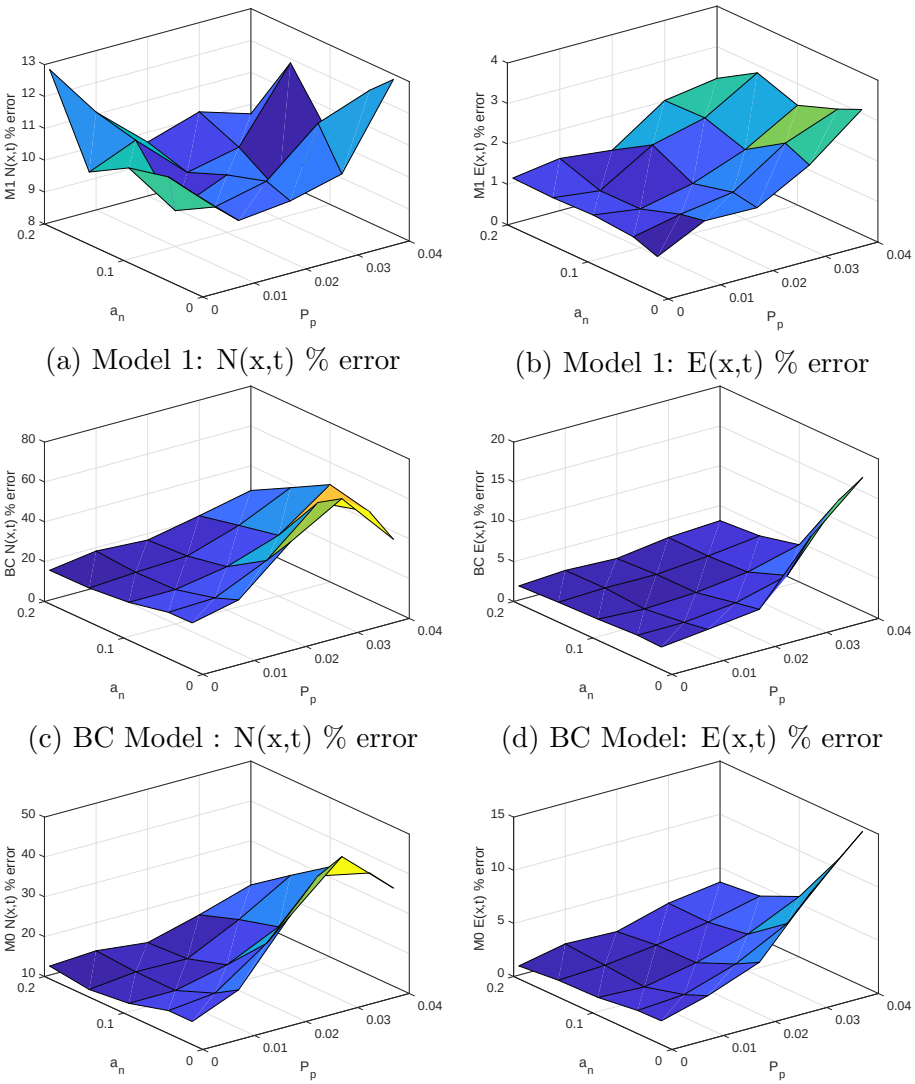

(a) Model 1: N(x,t) % error

(b) Model 1: E(x,t) % error

(c) BC Model : N(x,t) % error

(d) BC Model: E(x,t) % error

(e) Model 0: N(x,t) % error

(f) Model 0: E(x,t) % error

Figure E.2: Model 1: Relative errors for each PDE model as a function of CA model probabilities (a_n, tip-to-sprout anastomosis probability, P_p, branching probability). Left panel: TC density, Right panel: EC density. (a), (b) The relative error is much lower than those for Model 0 PDEs and the BC model (see (c)-(f)). (c)-(f) The relative errors generally increase as mass increases (as a_n decreases and P_p increases). According to the relative error, the Model 1 PDEs are the best descriptive model, whilst the BC model and Model 0 PDEs are similar.

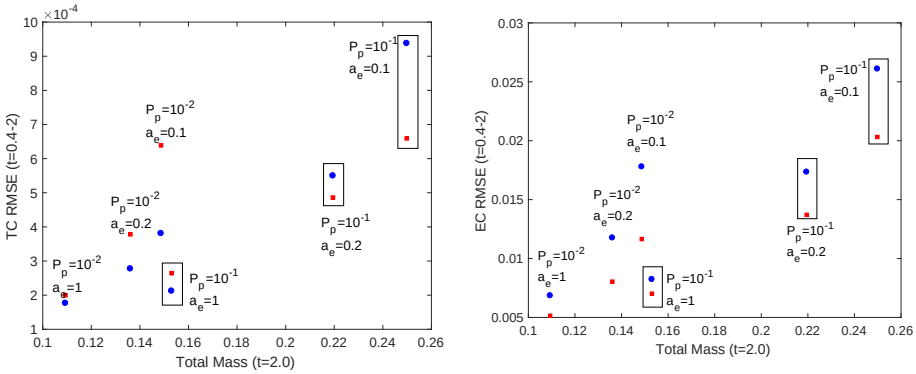

(a) TC RMSE (b) EC RMSE

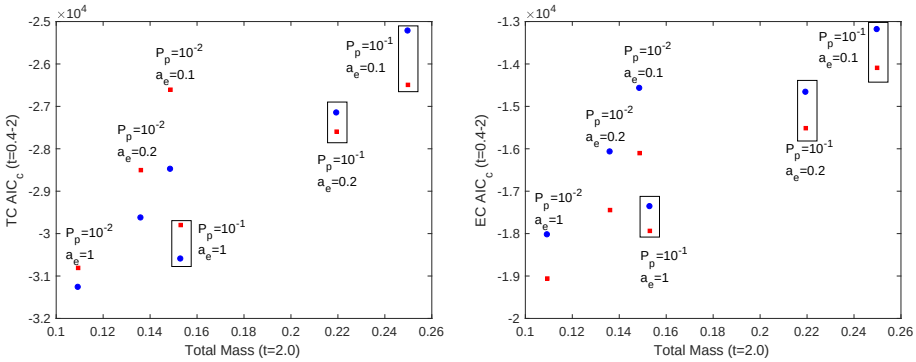

(c) TC AIC$_c$ (d) EC AIC$_c$

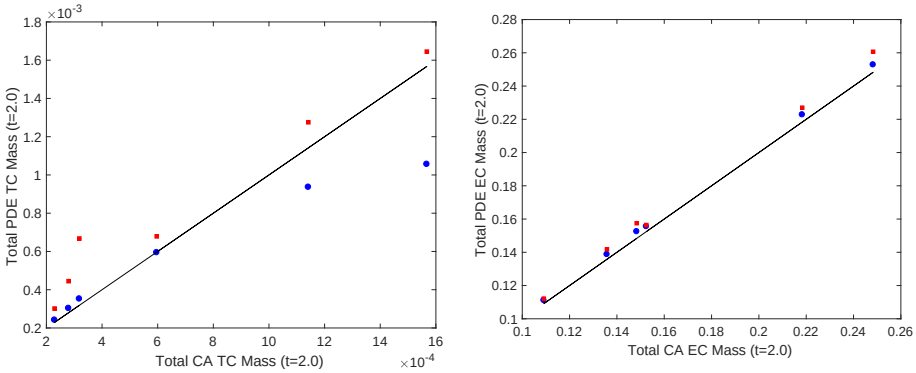

(e) TC Mass ($t = 2.0$) (f) EC Mass ($t = 2.0$)

Figure E.3: Model 2 ($a_n = 0$) Descriptions: RMSE and AIC$_c$ values for each PDE model visualised against mass determined from CA model (each mass point corresponds to a particular set of CA model parameters (annotated in (a)-(d)). Key: Blue = Model 2, Red = BC Model. (a), (b) For each value of P_p, the relative difference between the RMSEs for each model increases as a_e decreases. (c), (d) The AIC$_c$ values follow the same trend as the RMSEs in (a) and (b). (e), (f) The PDE models approximate the mass calculated from the CA model (black line) well, except for $P_p = 10^{-1}$ and $a_e = 0.2$ and $a_e = 0.1$. For these values, the BC model approximates the TC mass better than the Model 2 PDEs. In general, both models have similar descriptive power. Boxed data: $P_p = 10^{-1}$, Unboxed data: $P_p = 10^{-2}$.

Model 2 ($a_n = 0$): Network Features and Relative Errors

We plot features of the networks in Fig. E.4. More TCs are introduced as P_p increases (number of branchings increase, see Fig. E.4b), and thus the mass increases (see Fig. E.4a). The average number of tip-to-sprout anastomoses for each value of a_e generally increases as P_p increases. The maximum anastomoses occurs for $a_e = 0.1$ (and not $a_e = 1$) i.e higher anastomosis probabilities annihilate too many TCs, resulting in fewer anastomoses overall. Generally, the average sprout length increases as a_e and P_p decrease, implying fewer anastomoses and branchings.

In terms of relative error for descriptive power, the models are similar (see Fig. E.5). The relative errors increase as a_e decreases, due to increased EC VE effects. This corroborates the findings for the RMSE and AIC_c values, which increased as a_e decreased. The relative errors are highest for the lowest values of a_e ($a_e = 0.1$) and P_p ($P_p = 10^{-2}$), corresponding to a higher average sprout length, and therefore fewer branch points and loops formed via tip-to-sprout anastomosis. In contrast, the RMSEs and AIC_c were highest for $P_p = 10^{-1}$. However, the difference in the relative errors, RMSEs and AIC_c values for $P_p = 10^{-1}$ and $P_p = 10^{-2}$, for $a_e = 0.1$ are not significant. Thus, we conclude that the goodness of fit deteriorates as a_e decreases (fewer tip-to-sprout anastomoses), and the effects of EC VE become more pronounced (EC VE occurs with probability $1 - a_e$). For the same value of P_p, this corresponds to, in addition to fewer network connections formed through anastomosis, higher mass, higher number of branchings and longer average sprout length.

The relative errors at predicted times $t = 1.2 - 1.8$ (see Fig. E.6) for the Model 2 PDEs are lower than those for the BC model, though, for both models the relative errors are large ($> 200\%$ for the TC density and $> 60\%$ for the EC

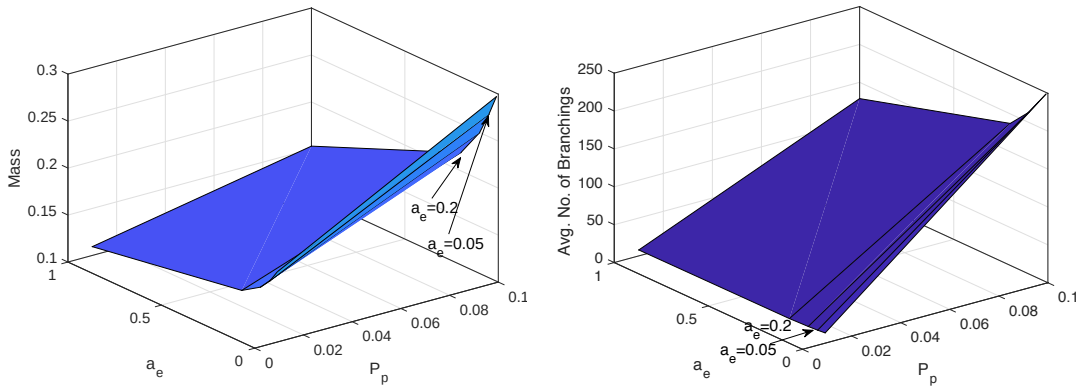

(a) Mass ($t = 2.0$)

(b) Branchings

(c) Tip-to-sprout Anastomoses

(d) Sprout Length

Figure E.4: Model 2 ($a_n = 0$) Network statistics. (a), (b) As the branching probability, P_p, increases and the anastomosis probability, a_e, decreases, the mass and average number of branchings increase. (c) The average number of anastomoses increase as a_e decreases and P_p increases, with the maximum occurring for $a_e = 0.1$ and $P_p = 10^{-1}$. (d) The average length of sprouts, calculated as the number of cells in a sprout, increases as P_p and a_e decrease. Plots produced using MATLAB's *surf* function.

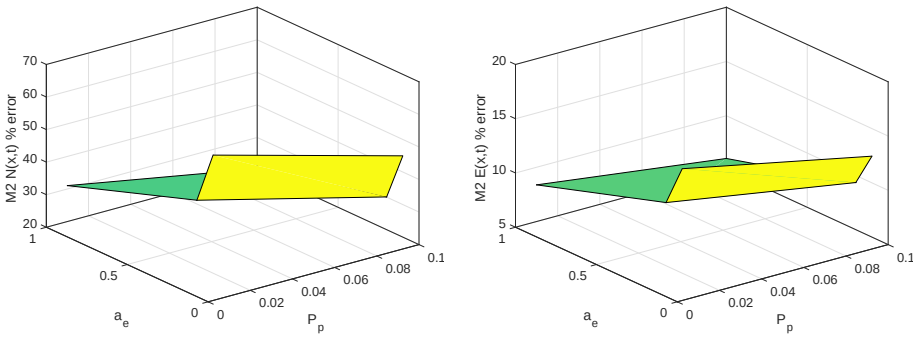

(a) M2: N(x,t) % error

(b) M2: E(x,t) % error

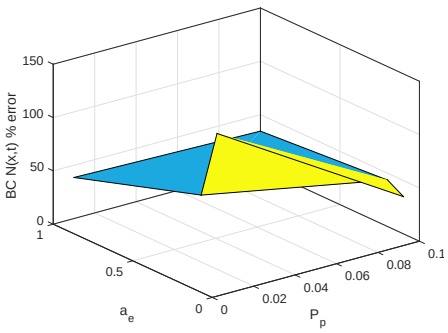

(c) BC : N(x,t) % error

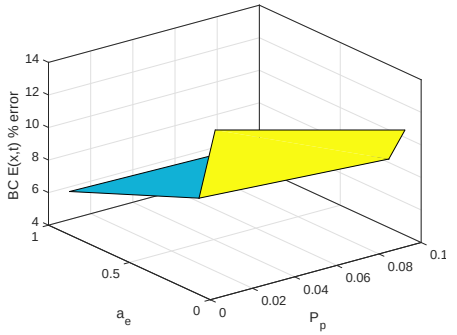

(d) BC: E(x,t) % error

Figure E.5: Model 2 ($a_n = 0$): PDE Descriptions: Relative errors for each PDE model as a function of CA model probabilities (a_e, tip-to-sprout anastomosis probability, P_p, branching probability). (a), (c) The relative errors for the TC density are higher for the BC model than the Model 2 PDEs. (b), (d) The relative errors for the EC density are similar for both models. The relative errors tend to be highest for the smallest value of a_e for each value of P_p, or as the average sprout length increases (see Fig. E.4d). M2 = Model 2 PDEs. BC = BC Model.

density). The relative errors increase as a_e decreases, due to increased EC VE effects. This corroborates the findings for the RMSE and AIC_c values, which increased as a_e decreased (see Fig. 5.5 in Chapter 5). The relative errors are highest for the lowest values of a_e ($a_e = 0.1$) and P_p ($P_p = 10^{-2}$), corresponding to a higher average sprout length, and therefore fewer branch points and loops formed via tip-to-sprout anastomosis. Thus, we conclude that the goodness of fit deteriorates as a_e decreases (fewer tip-to-sprout anastomoses), and the effects of EC VE become more pronounced (EC VE occurs with probability $1 - a_e$). For the same value of P_p, this corresponds to, in addition to fewer network connections formed through anastomosis, higher mass, higher number of branchings and longer average sprout length.

E.2.3 Model 2, $a_n = 1$

The Model 0 and 2 PDEs differ, in this case, by the branching term, $\lambda cN(1 - N - E)^2$ in Model 2 and λcN in Model 0. Thus, we expect these models to have similar descriptive power, except if there is sufficient mass in the system such that multi-species VE becomes important in the branching mechanism.

The descriptive power statistics in terms of RMSE, AIC_c and mass at $t = 2.0$ are given in Fig. E.7. The RMSEs and AIC_c values for the Model 0 and 2 PDEs are very similar, while the RMSEs and AIC_c values for the BC model are larger than for the other PDE models (see Figs. E.7a-E.7b). Generally, the relative differences between the RMSEs and AIC_c values for the BC model and Model 0/2 PDEs is largest for smaller values of a_e. All models capture the TC and EC mass (see Figs. E.7e-E.7f), though all models overestimate the mass. The Model 0 and 2 PDEs capture the TC mass better than the BC model. Estimated parameter values can be found in Tables E.7, E.8 and E.9.

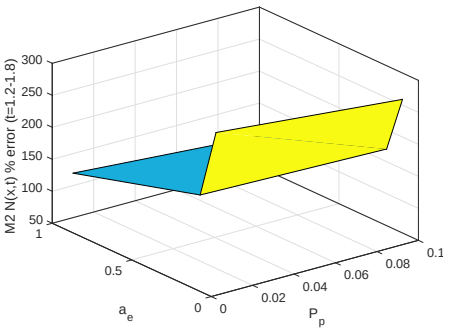

(a) M2 N(x,t) % error ($t = 1.2 - 1.8$)

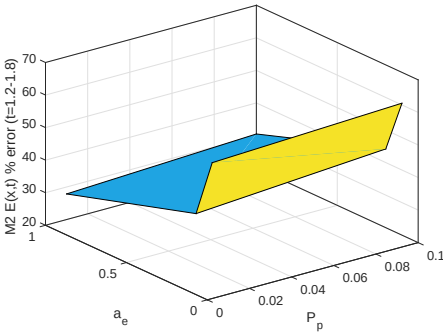

(b) M2: E(x,t) % error ($t = 1.2 - 1.8$)

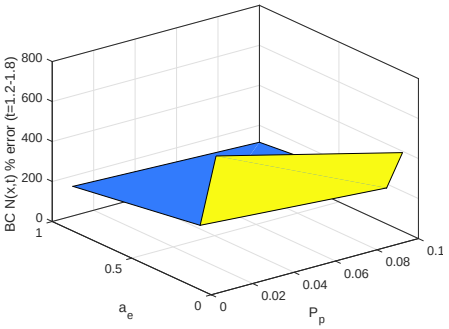

(c) BC : N(x,t) % error ($t = 1.2 - 1.8$)

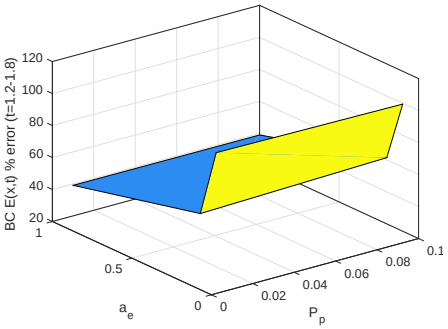

(d) BC: E(x,t) % error ($t = 1.2 - 1.8$)

Figure E.6: Model 2 ($a_n = 0$): PDE Predictions: Relative errors for each PDE model as a function of CA model probabilities (a_e, tip-to-sprout anastomosis probability, P_p, branching probability). (a)-(d) The relative errors for the TC and EC densities are higher for the predictions based on the BC model than the Model 2 PDEs. The relative errors are highest for the lowest value of a_e ($a_e = 0.1$) for each value of P_p, corresponding to more pronounced EC VE effects (fewer tip-to-sprout anastomoses and longer average sprout length). M2 = Model 2 PDEs. BC = BC Model.

Model 2 ($a_n = 1$): Network Features and Relative Errors

The average number of branchings, tip-to-tip anastomoses, and mass ($t = 2.0$) increases as a_e decreases and P_p increases (see Fig. E.8). The average sprout length is longer when there are fewer branchings and tip-to-sprout anastomoses (as a_e and P_p decrease). There are fewer tip-to-sprout anastomoses when tip-to-tip anastomosis is active (compare Figs. E.4c and E.8c), as tip-to-tip anastomosis annihilates many TCs, and thus fewer tip-to-sprout anastomoses occur. The maximum average number of tip-to-sprout anastomoses occurs for $a_e = 0.2$

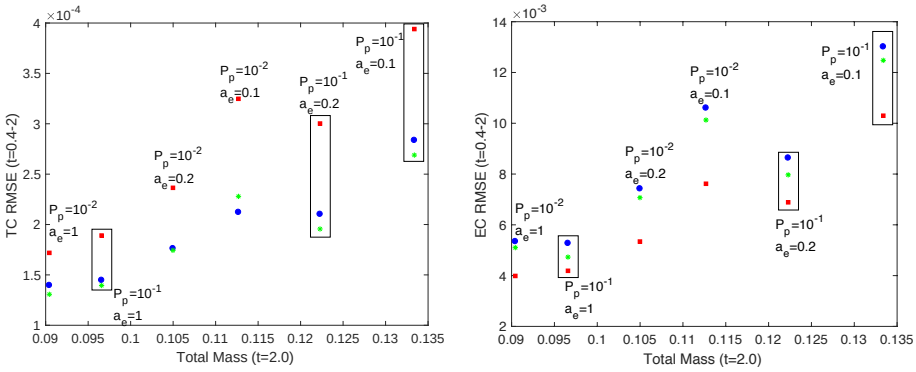

(a) TC RMSE (b) EC RMSE

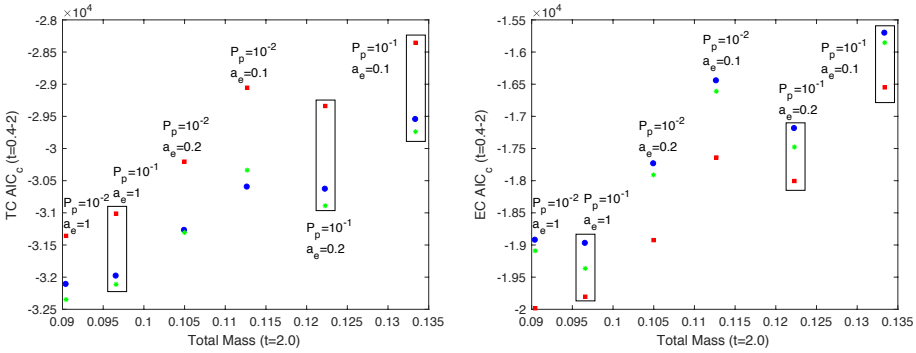

(c) TC AIC_c (d) EC AIC_c

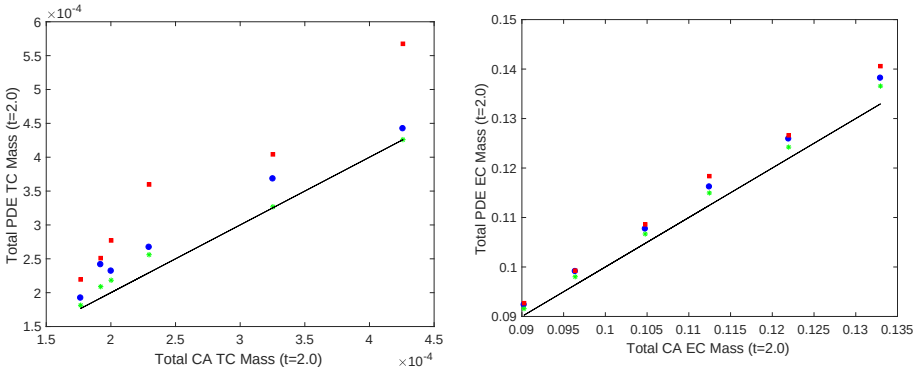

(e) TC Mass ($t = 2.0$) (f) EC Mass ($t = 2.0$)

Figure E.7: Model 2 ($a_n = 1$) Descriptions: RMSE and AIC_c values for each PDE model visualised against mass determined from CA model (each mass point corresponds to a particular set of CA model parameters (annotated in (a)-(d)). Key: Blue = Model 2, Red = BC Model, Green = Model 0. (a)-(d) The TC RMSE and AIC_c show similar trends. Generally, the RMSEs and AIC_c for the Model 2 and Model 0 PDEs are clustered together with the BC model metrics sitting higher ((a), (d)) or lower ((b), (c)). (e), (f) All models overestimate the true CA mass (black line), though all models approximate the mass well. There is little difference in the descriptive power of these PDE models, and all approximate the averaged CA simulation results well. Boxed data: $P_p = 10^{-1}$, Unboxed data: $P_p = 10^{-2}$.

($\forall P_p$), as larger values would annihilate too many TCs via tip-to-sprout anastomosis (and thus fewer branchings would occur, thereby resulting in a lower overall number of tip-to-sprout anastomoses).

From the relative errors for descriptive power (see Fig. E.9), it is can be deduced that all models have similar descriptive power as they have similar relative errors for the TC and EC densities (recall that the relative error heavily penalises the BC model for the TC density due to the thresholding we chose, see equation (6.1)). Once again, we see that the relative errors are highest for $a_e = 0.1$, corresponding to increased EC VE effects. In general, the descriptive power of the models decreases when the number of loops formed by tip-to-sprout anastomosis decreases, the number of loops formed by tip-to-tip anastomosis increases, and the average sprout length increases, though all models capture the averaged CA simulation results well.

The relative errors for predictions (see Fig. E.10) are largest for $a_e = 0.1$, when EC VE effects are non-negligible, corroborating the RMSE and $\mathrm{AIC_c}$ findings (see Fig. 5.7). Further, the predictions from all models are best when more loops form via tip-to-sprout anastomosis, fewer loops form via tip-to-tip anastomosis and the average sprout length is shorter. We also note that the relative errors are smaller when tip-to-tip anastomosis is active, compared to when it is not (see Fig. E.6), which can, in part, be explained by the fact that active tip-to-tip anastomosis annihilates more TCs, leading to less pronounced EC VE effects.

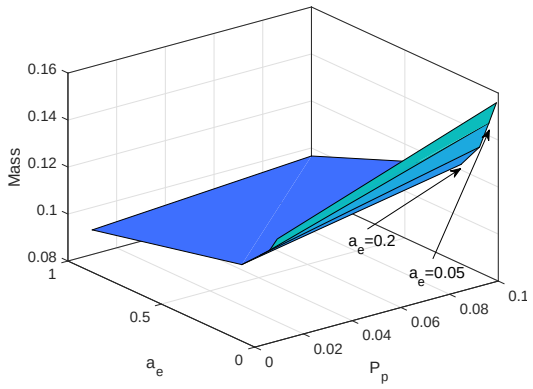

(a) Mass ($t = 2.0$)

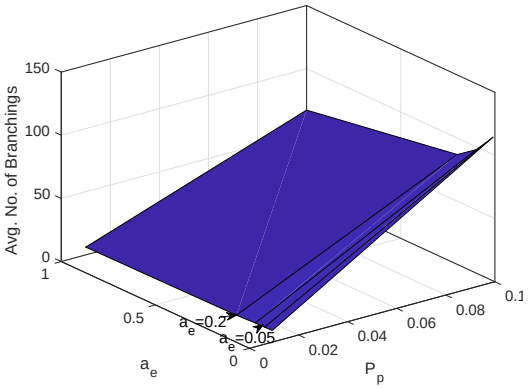

(b) Branchings

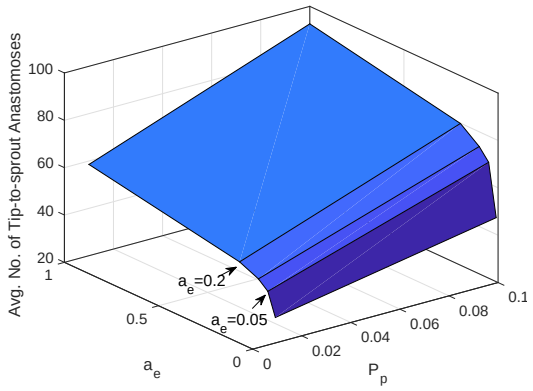

(c) Tip-to-sprout Anastomoses

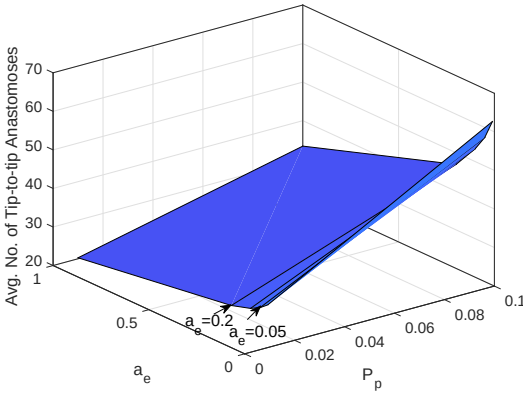

(d) Tip-to-tip Anastomoses

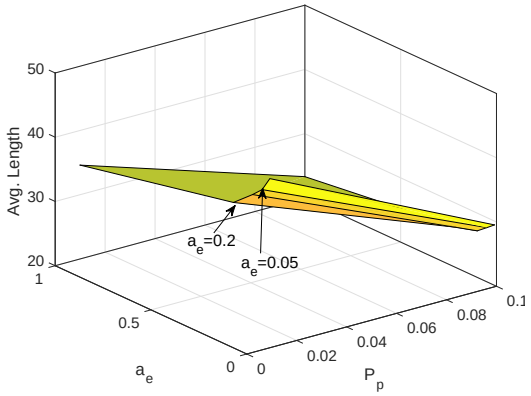

(e) Sprout Length

Figure E.8: Model 2 ($a_n = 1$) Network statistics. (a), (b), (d), (e) As the probability of tip-to-sprout anastomosis, a_e, and branching, P_p decrease, the average number of branchings, tip-to-tip anastomoses and mass at $t = 2.0$ increases while the average sprout length decreases. (c) Generally, the number of tip-to-sprout anastomoses increases as P_p increases with the maximum occurring for $a_e = 0.2$. Plots produced using MATLAB's *surf* function.

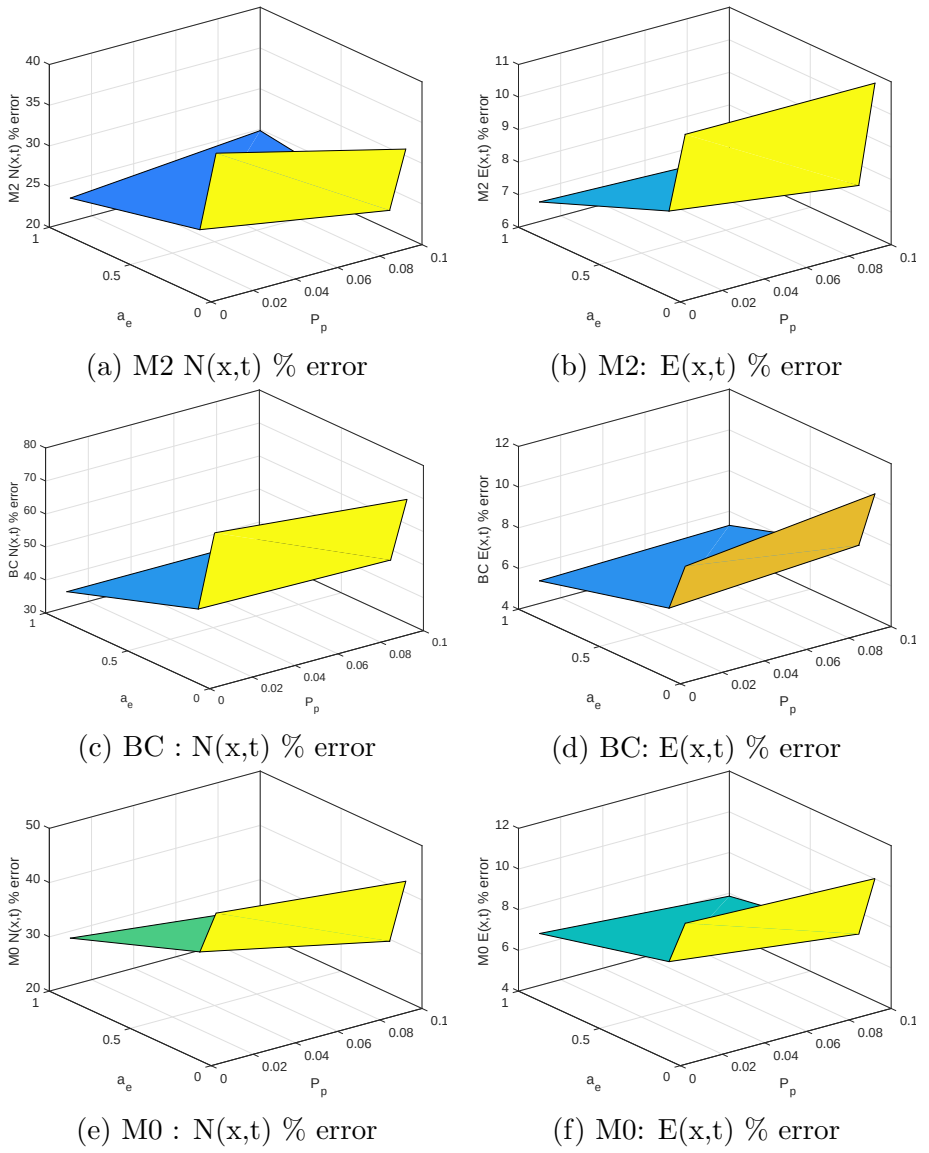

(a) M2 N(x,t) % error

(b) M2: E(x,t) % error

(c) BC : N(x,t) % error

(d) BC: E(x,t) % error

(e) M0 : N(x,t) % error

(f) M0: E(x,t) % error

Figure E.9: Model 2 ($a_n = 1$): PDE Descriptions: Relative errors for each PDE model as a function of CA model probabilities (a_e, tip-to-sprout anastomosis probability, P_p, branching probability). The relative errors for the TC and EC densities are similar across the models, though the BC model relative error for the TC density is slightly higher than the other models. Generally, the relative errors are highest when EC VE effects are non-negligible (smallest value of a_e, $a_e = 0.1$) and for fewer loops formed through tip-to-sprout anastomoses. M2 = Model 2 PDEs, BC = BC Model, M0 = Model 0 PDEs.

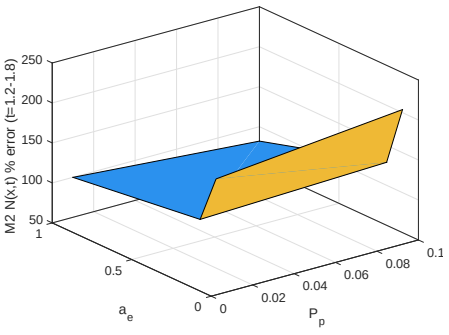

(a) M2 N(x,t) % error ($t = 1.2 - 1.8$)

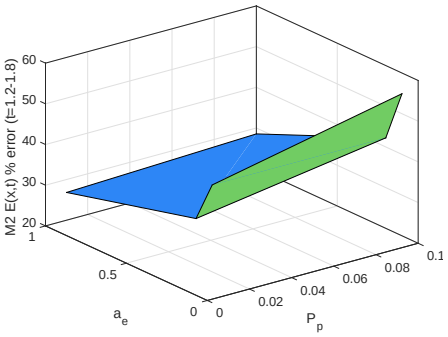

(b) M2: E(x,t) % error ($t = 1.2 - 1.8$)

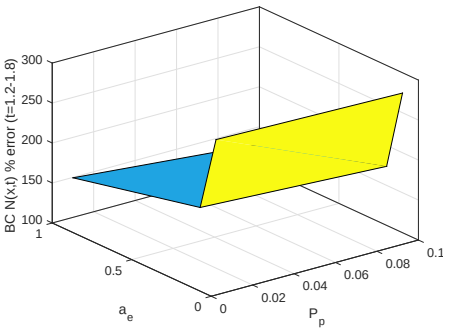

(c) BC : N(x,t) % error ($t = 1.2 - 1.8$)

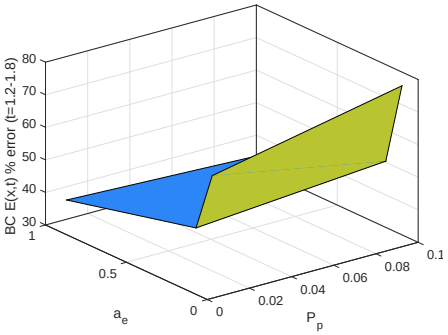

(d) BC: E(x,t) % error ($t = 1.2 - 1.8$)

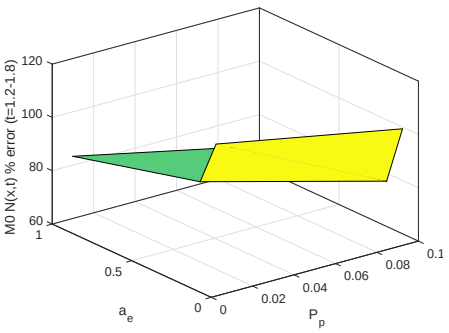

(e) M0 : N(x,t) % error ($t = 1.2 - 1.8$)

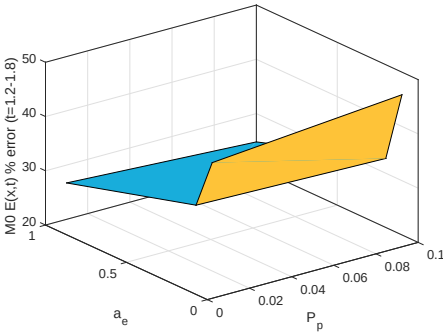

(f) M0: E(x,t) % error ($t = 1.2 - 1.8$)

Figure E.10: Model 2 ($a_n = 1$): PDE Predictions: Relative errors for each PDE model as a function of CA model probabilities (a_e, tip-to-sprout anastomosis probability, P_p, branching probability). (a), (c), (e) The relative errors for the TC density are similar ($\approx 300\%$) for the BC Model and the Model 2 PDEs, whilst the relative errors for the Model 1 PDEs are much lower ($\approx 100\%$). (b), (d), (f) The relative errors for the EC density are similar for all models, approximately $50 - 80\%$. The relative errors are highest for the lowest value of a_e as EC VE effects increase. This corresponds to fewer loops formed by tip-to-sprout anastomoses, more loops formed by tip-to-tip anastomoses and longer average sprout length. M2 = Model 2 PDEs, BC = BC Model, M0 = Model 0 PDEs.

E.3 CA Model 1: Tables of Fitted Parameter Values

Table E.1: CA Model 1 (Descriptive Power): Model 1 PDEs fitted parameter values. We also give the CA model parameters a_n and the continuum analogue, λ, of the branching probability P_p, for comparison with the estimated parameter values.

P_p	λ	a_n	$\tilde{\lambda}$	$\tilde{a}_n$
10^{-3}	0.16	0.02	0.1586 ± 0.0026	0.0362 ± 0.0003
10^{-3}	0.16	0.05	0.1687 ± 0.0027	0.0891 ± 0.0003
10^{-3}	0.16	0.1	0.2074 ± 0.0035	0.1807 ± 0.0005
10^{-3}	0.16	0.15	0.1692 ± 0.0035	0.2394 ± 0.0005
10^{-3}	0.16	0.2	0.1192 ± 0.0037	0.2959 ± 0.0007
10^{-2}	1.6	0.02	1.4719 ± 0.0029	0.0333 ± 0.0003
10^{-2}	1.6	0.05	1.3920 ± 0.0025	0.0811 ± 0.0003
10^{-2}	1.6	0.1	1.3310 ± 0.0033	0.1606 ± 0.0005
10^{-2}	1.6	0.15	1.2080 ± 0.0028	0.2297 ± 0.0005
10^{-2}	1.6	0.2	1.1821 ± 0.0041	0.3001 ± 0.0008
2×10^{-2}	3.2	0.02	2.7480 ± 0.0066	0.0167 ± 0.0005
2×10^{-2}	3.2	0.05	2.7385 ± 0.0040	0.0787 ± 0.0004
2×10^{-2}	3.2	0.1	2.4847 ± 0.0037	0.1500 ± 0.0005
2×10^{-2}	3.2	0.15	2.3077 ± 0.0041	0.2153 ± 0.0007
2×10^{-2}	3.2	0.2	2.0834 ± 0.0038	0.2705 ± 0.0007
3×10^{-2}	4.8	0.02	4.1451 ± 0.0132	0.0205 ± 0.0008
3×10^{-2}	4.8	0.05	3.8115 ± 0.0113	0.0563 ± 0.0009
3×10^{-2}	4.8	0.1	3.4990 ± 0.0062	0.1252 ± 0.0007
3×10^{-2}	4.8	0.15	3.2857 ± 0.0069	0.1931 ± 0.0010
3×10^{-2}	4.8	0.2	3.0097 ± 0.0073	0.2391 ± 0.0013
4×10^{-2}	6.4	0.02	5.4722 ± 0.0219	0.0216 ± 0.0010
4×10^{-2}	6.4	0.05	4.9973 ± 0.0200	0.0574 ± 0.0013
4×10^{-2}	6.4	0.1	4.4291 ± 0.0150	0.1039 ± 0.0014
4×10^{-2}	6.4	0.15	4.0862 ± 0.0127	0.1590 ± 0.0016
4×10^{-2}	6.4	0.2	3.8473 ± 0.0111	0.2164 ± 0.0017

Table E.2: CA Model 1 (Descriptive Power): BC Model fitted parameters values. We also give the CA model parameters a_n and the continuum analogue, λ, of the branching probability P_p, for comparison with the estimated parameter values. Branching probabilities of $P_p = 10^{-3}, 10^{-2}, 2 \times 10^{-2}, 3 \times 10^{-2}, 4 \times 10^{-2}$ correspond, respectively, to $\lambda = 0.16, 1.6, 3.2, 4.8, 6.4$. The continuum analogues of the diffusion and chemotactic coefficients in the CA model are $D = 10^{-3}$ and $\chi = 0.4$, respectively.

P_p	a_n	$\tilde{D}_{\mathrm{BC}}$	$\tilde{\chi}_{\mathrm{BC}}$	$\tilde{\lambda}_{\mathrm{BC}}$	$\tilde{\beta}_n$
0.16	0.02	0.0010 ± 0.0000	0.3907 ± 0.0002	0.1911 ± 0.0089	6.1911 ± 0.1350
0.16	0.05	0.0010 ± 0.0000	0.3916 ± 0.0002	0.2024 ± 0.0092	14.6240 ± 0.1632
0.16	0.1	0.0010 ± 0.0000	0.3936 ± 0.0002	0.2193 ± 0.0100	28.9080 ± 0.2198
0.16	0.15	0.0010 ± 0.0000	0.3939 ± 0.0003	0.1842 ± 0.0103	38.2010 ± 0.2630
0.16	0.2	0.0010 ± 0.0000	0.3958 ± 0.0003	0.1079 ± 0.0107	46.6590 ± 0.3048
1.6	0.02	0.0011 ± 0.0000	0.3885 ± 0.0001	1.4698 ± 0.0085	5.7575 ± 0.1306
1.6	0.05	0.0011 ± 0.0000	0.3911 ± 0.0001	1.3744 ± 0.0084	13.1802 ± 0.1498
1.6	0.1	0.0010 ± 0.0000	0.3926 ± 0.0002	1.3265 ± 0.0094	25.9502 ± 0.2108
1.6	0.15	0.0010 ± 0.0000	0.3940 ± 0.0002	1.2025 ± 0.0089	36.5733 ± 0.2291
1.6	0.2	0.0010 ± 0.0000	0.3936 ± 0.0002	1.2000 ± 0.0088	48.0085 ± 0.2634
3.2	0.02	0.0012 ± 0.0000	0.3838 ± 0.0002	2.6113 ± 0.0202	2.3035 ± 0.2667
3.2	0.05	0.0011 ± 0.0000	0.3884 ± 0.0001	2.6289 ± 0.0116	12.3240 ± 0.1865
3.2	0.1	0.0011 ± 0.0000	0.3918 ± 0.0001	2.4042 ± 0.0083	23.5980 ± 0.1698
3.2	0.15	0.0011 ± 0.0000	0.3931 ± 0.0001	2.2553 ± 0.0081	34.2140 ± 0.1976
3.2	0.2	0.0010 ± 0.0000	0.3935 ± 0.0001	2.0686 ± 0.0080	43.3900 ± 0.2228
4.8	0.02	0.0010 ± 0.0000	0.3765 ± 0.0003	5.1630 ± 0.0777	16.7220 ± 0.7771
4.8	0.05	0.0013 ± 0.0000	0.3820 ± 0.0002	3.7554 ± 0.0411	10.8120 ± 0.5543
4.8	0.1	0.0012 ± 0.0000	0.3886 ± 0.0001	3.3426 ± 0.0163	19.4580 ± 0.2883
4.8	0.15	0.0011 ± 0.0000	0.3906 ± 0.0001	3.1991 ± 0.0122	30.8630 ± 0.2645
4.8	0.2	0.0011 ± 0.0000	0.3919 ± 0.0001	2.9792 ± 0.0116	38.7730 ± 0.2934
6.4	0.02	0.0006 ± 0.0000	0.3729 ± 0.0003	8.7030 ± 0.1141	31.1260 ± 0.7475
6.4	0.05	0.0009 ± 0.0000	0.3775 ± 0.0003	6.4969 ± 0.0969	28.4414 ± 0.9530
6.4	0.1	0.0012 ± 0.0000	0.3833 ± 0.0002	4.4815 ± 0.0508	20.6232 ± 0.7463
6.4	0.15	0.0012 ± 0.0000	0.3877 ± 0.0002	3.8890 ± 0.0268	24.6209 ± 0.4986
6.4	0.2	0.0011 ± 0.0000	0.3905 ± 0.0002	3.7604 ± 0.0202	34.9179 ± 0.4415

Table E.3: CA Model 1 (Descriptive Power): Model 0 PDEs fitted parameter values. We also give the CA model parameters a_n and the continuum analogue, λ, of the branching probability P_p, for comparison with the estimated parameter values. Branching probabilities of $P_p = 10^{-3}, 10^{-2}, 2 \times 10^{-2}, 3 \times 10^{-2}, 4 \times 10^{-2}$ correspond, respectively, to $\lambda = 0.16, 1.6, 3.2, 4.8, 6.4$. The continuum analogues of the diffusion and chemotactic coefficients in the CA model are $D = 10^{-3}$ and $\chi = 0.4$, respectively.

λ	a_n	$\tilde{D}_{\mathrm{M0}}$	$\tilde{\chi}_{\mathrm{M0}}$	$\tilde{\lambda}_{\mathrm{M0}}$	$\tilde{a}_n^{\mathrm{M0}}$
0.16	0.02	0.0010 ± 0.0000	0.3935 ± 0.0001	0.2413 ± 0.0051	0.0521 ± 0.0005
0.16	0.05	0.0010 ± 0.0000	0.3947 ± 0.0001	0.2407 ± 0.0050	0.1052 ± 0.0006
0.16	0.1	0.0010 ± 0.0000	0.3969 ± 0.0001	0.2415 ± 0.0049	0.1934 ± 0.0007
0.16	0.15	0.0010 ± 0.0000	0.3972 ± 0.0001	0.2053 ± 0.0049	0.2531 ± 0.0009
0.16	0.2	0.0010 ± 0.0000	0.3989 ± 0.0001	0.1194 ± 0.0042	0.3024 ± 0.0008
1.6	0.02	0.0010 ± 0.0000	0.3908 ± 0.0001	1.5728 ± 0.0064	0.0557 ± 0.0007
1.6	0.05	0.0010 ± 0.0000	0.3936 ± 0.0001	1.4351 ± 0.0050	0.0985 ± 0.0006
1.6	0.1	0.0010 ± 0.0000	0.3953 ± 0.0001	1.3668 ± 0.0049	0.1783 ± 0.0007
1.6	0.15	0.0010 ± 0.0000	0.3968 ± 0.0001	1.2293 ± 0.0043	0.2435 ± 0.0008
1.6	0.2	0.0010 ± 0.0000	0.3967 ± 0.0001	1.2250 ± 0.0058	0.3179 ± 0.0012
3.2	0.02	0.0011 ± 0.0000	0.3859 ± 0.0001	2.9263 ± 0.0211	0.0512 ± 0.0018
3.2	0.05	0.0011 ± 0.0000	0.3907 ± 0.0001	2.7764 ± 0.0120	0.1026 ± 0.0013
3.2	0.1	0.0010 ± 0.0000	0.3944 ± 0.0001	2.4673 ± 0.0069	0.1660 ± 0.0010
3.2	0.15	0.0010 ± 0.0000	0.3959 ± 0.0001	2.2923 ± 0.0069	0.2305 ± 0.0011
3.2	0.2	0.0010 ± 0.0000	0.3963 ± 0.0001	2.0994 ± 0.0060	0.2890 ± 0.0011
4.8	0.02	0.0009 ± 0.0000	0.3795 ± 0.0002	5.2876 ± 0.0644	0.1277 ± 0.0042
4.8	0.05	0.0011 ± 0.0000	0.3848 ± 0.0002	4.1307 ± 0.0386	0.1126 ± 0.0034
4.8	0.1	0.0011 ± 0.0000	0.3910 ± 0.0001	3.5198 ± 0.0168	0.1538 ± 0.0020
4.8	0.15	0.0011 ± 0.0000	0.3933 ± 0.0001	3.2962 ± 0.0128	0.2199 ± 0.0019
4.8	0.2	0.0010 ± 0.0000	0.3946 ± 0.0001	3.0418 ± 0.0121	0.2663 ± 0.0021
6.4	0.02	0.0006 ± 0.0000	0.3752 ± 0.0002	8.4674 ± 0.1059	0.2081 ± 0.0048
6.4	0.05	0.0008 ± 0.0000	0.3803 ± 0.0002	6.4442 ± 0.0820	0.1943 ± 0.0054
6.4	0.1	0.0011 ± 0.0000	0.3862 ± 0.0002	4.7928 ± 0.0480	0.1734 ± 0.0046
6.4	0.15	0.0011 ± 0.0000	0.3904 ± 0.0002	4.1077 ± 0.0283	0.1946 ± 0.0035
6.4	0.2	0.0011 ± 0.0000	0.3932 ± 0.0002	3.8914 ± 0.0225	0.2511 ± 0.0033

Table E.4: CA Model 1 (Predictive Power): Model 1 PDEs fitted parameter values ($t = 0.4 - 1$). We also give the CA model parameters a_n and the continuum analogue, λ, of the branching probability P_p, for comparison with the estimated parameter values.

P_p	λ	a_n	$\tilde{\lambda}$	$\tilde{a}_n$
10^{-3}	0.16	0.02	0.2791 ± 0.0193	0.0407 ± 0.0009
10^{-3}	0.16	0.05	0.3098 ± 0.0174	0.0959 ± 0.0010
10^{-3}	0.16	0.1	0.3814 ± 0.0226	0.1900 ± 0.0015
10^{-3}	0.16	0.15	0.3468 ± 0.0235	0.2519 ± 0.0018
10^{-3}	0.16	0.2	0.2358 ± 0.0229	0.2998 ± 0.0019
10^{-3}	0.16	0.02	1.5015 ± 0.0189	0.0361 ± 0.0009
10^{-3}	0.16	0.05	1.4846 ± 0.0203	0.0857 ± 0.0011
10^{-3}	0.16	0.1	1.4390 ± 0.0216	0.1693 ± 0.0014
10^{-3}	0.16	0.15	1.3508 ± 0.0199	0.2376 ± 0.0015
10^{-3}	0.16	0.2	1.4234 ± 0.0210	0.3226 ± 0.0018
2×10^{-2}	3.2	0.02	2.9982 ± 0.0185	0.0312 ± 0.0008
2×10^{-2}	3.2	0.05	3.0803 ± 0.0161	0.0985 ± 0.0009
2×10^{-2}	3.2	0.1	2.7753 ± 0.0184	0.1687 ± 0.0012
2×10^{-2}	3.2	0.15	2.6447 ± 0.0244	0.2404 ± 0.0018
2×10^{-2}	3.2	0.2	2.3836 ± 0.0244	0.2975 ± 0.0020
3×10^{-2}	4.8	0.02	4.5740 ± 0.0162	0.0362 ± 0.0007
3×10^{-2}	4.8	0.05	4.3332 ± 0.0157	0.0856 ± 0.0008
3×10^{-2}	4.8	0.1	3.8348 ± 0.0190	0.1509 ± 0.0012
3×10^{-2}	4.8	0.15	3.7554 ± 0.0172	0.2344 ± 0.0012
3×10^{-2}	4.8	0.2	3.7265 ± 0.0232	0.3055 ± 0.0019
4×10^{-2}	4.8	0.02	5.6093 ± 0.0208	0.0193 ± 0.0009
4×10^{-2}	4.8	0.05	5.5621 ± 0.0188	0.0719 ± 0.0009
4×10^{-2}	4.8	0.1	5.1826 ± 0.0180	0.1507 ± 0.0011
4×10^{-2}	4.8	0.15	4.8646 ± 0.0216	0.2215 ± 0.0015
4×10^{-2}	4.8	0.2	4.6716 ± 0.0214	0.2925 ± 0.0017

Table E.5: CA Model 1 (Predictive Power): BC Model fitted parameter values ($t = 0.4 - 1$). We also give the CA model parameters a_n and the continuum analogue, λ, of the branching probability P_p, for comparison with the estimated parameter values. Branching probabilities of $P_p = 10^{-3}, 10^{-2}, 2\times10^{-2}, 3\times10^{-2}, 4\times10^{-2}$ correspond, respectively, to $\lambda = 0.16, 1.6, 3.2, 4.8, 6.4$. The continuum analogues of the diffusion and chemotactic coefficients in the CA model are $D = 10^{-3}$ and $\chi = 0.4$, respectively.

P_p	a_n	$\tilde{D}_{\mathrm{BC}}$	$\tilde{\chi}_{\mathrm{BC}}$	$\tilde{\lambda}_{\mathrm{BC}}$	$\tilde{\beta}_n$
0.16	0.02	0.0010 ± 0.0000	0.3854 ± 0.0006	0.4442 ± 0.0932	6.8561 ± 0.6426
0.16	0.05	0.0010 ± 0.0000	0.3868 ± 0.0006	0.4399 ± 0.0936	15.3650 ± 0.7203
0.16	0.1	0.0010 ± 0.0000	0.3895 ± 0.0007	0.3708 ± 0.0956	29.1430 ± 0.8798
0.16	0.15	0.0010 ± 0.0000	0.3901 ± 0.0007	0.3232 ± 0.0975	38.4520 ± 0.9985
0.16	0.2	0.0010 ± 0.0000	0.3917 ± 0.0007	0.1193 ± 0.0966	45.1860 ± 1.0869
1.6	0.02	0.0011 ± 0.0000	0.3846 ± 0.0006	1.6558 ± 0.0936	6.1727 ± 0.6467
1.6	0.05	0.0011 ± 0.0000	0.3867 ± 0.0006	1.5388 ± 0.0939	13.4430 ± 0.7285
1.6	0.1	0.0010 ± 0.0000	0.3881 ± 0.0007	1.5017 ± 0.1057	26.5480 ± 0.9388
1.6	0.15	0.0010 ± 0.0000	0.3896 ± 0.0006	1.3714 ± 0.0933	36.8130 ± 0.9475
0.16	0.2	0.0010 ± 0.0000	0.3913 ± 0.0006	1.3286 ± 0.0905	48.9300 ± 1.0355
3.2	0.02	0.0011 ± 0.0000	0.3841 ± 0.0005	3.0110 ± 0.0959	4.8756 ± 0.6403
3.2	0.05	0.0011 ± 0.0000	0.3868 ± 0.0005	3.0228 ± 0.0882	15.1500 ± 0.6711
3.2	0.1	0.0010 ± 0.0000	0.3883 ± 0.0006	2.7432 ± 0.0889	26.0690 ± 0.7822
3.2	0.15	0.0011 ± 0.0000	0.3901 ± 0.0006	2.5238 ± 0.0843	36.3970 ± 0.8432
3.2	0.2	0.0010 ± 0.0000	0.3902 ± 0.0006	2.3458 ± 0.0860	45.6580 ± 0.9491
4.8	0.02	0.0011 ± 0.0000	0.3838 ± 0.0004	4.4653 ± 0.0898	5.5317 ± 0.5872
4.8	0.05	0.0011 ± 0.0000	0.3858 ± 0.0005	4.2496 ± 0.0887	13.2590 ± 0.6550
4.8	0.1	0.0011 ± 0.0000	0.3874 ± 0.0006	3.7628 ± 0.0945	23.0690 ± 0.8195
4.8	0.15	0.0010 ± 0.0000	0.3895 ± 0.0005	3.6559 ± 0.0870	35.8390 ± 0.8646
4.8	0.2	0.0010 ± 0.0000	0.3897 ± 0.0006	3.7413 ± 0.0918	47.6180 ± 1.0112
6.4	0.02	0.0012 ± 0.0000	0.3812 ± 0.0004	5.4408 ± 0.0966	2.4888 ± 0.6024
6.4	0.05	0.0011 ± 0.0000	0.3851 ± 0.0004	5.2852 ± 0.0927	10.1560 ± 0.6612
6.4	0.1	0.0011 ± 0.0000	0.3874 ± 0.0005	5.0226 ± 0.0872	22.8660 ± 0.7432
6.4	0.15	0.0010 ± 0.0000	0.3882 ± 0.0005	4.8567 ± 0.0956	34.7890 ± 0.9223
6.4	0.2	0.0010 ± 0.0000	0.3915 ± 0.0005	4.4154 ± 0.0808	43.6850 ± 0.8773

Table E.6: CA Model 1 (Predictive Power): Model 0 PDEs fitted parameter values ($t = 0.4 - 1$). We also give the CA model parameters a_n and the continuum analogue, λ, of the branching probability P_p, for comparison with estimated parameter values. Branching probabilities of $P_p = 10^{-3}, 10^{-2}, 2\times10^{-2}, 3\times10^{-2}, 4\times10^{-2}$ correspond, respectively, to $\lambda = 0.16, 1.6, 3.2, 4.8, 6.4$. The continuum analogues of the diffusion and chemotactic coefficients in the CA model are $D = 10^{-3}$ and $\chi = 0.4$, respectively.

λ	a_n	$\tilde{D}_{\mathrm{M0}}$	$\tilde{\chi}_{\mathrm{M0}}$	$\tilde{\lambda}_{\mathrm{M0}}$	$\tilde{a}_n^{\mathrm{M0}}$
0.16	0.02	0.0010 ± 0.0000	0.3913 ± 0.0002	0.8413 ± 0.0466	0.0849 ± 0.0024
0.16	0.05	0.0010 ± 0.0000	0.3926 ± 0.0002	0.8102 ± 0.0399	0.1399 ± 0.0023
0.16	0.1	0.0010 ± 0.0000	0.3953 ± 0.0002	0.6559 ± 0.0384	0.2234 ± 0.0026
0.16	0.15	0.0010 ± 0.0000	0.3960 ± 0.0002	0.5965 ± 0.0371	0.2849 ± 0.0028
0.16	0.2	0.0010 ± 0.0000	0.3978 ± 0.0002	0.2975 ± 0.0340	0.3180 ± 0.0028
1.6	0.02	0.0010 ± 0.0000	0.3900 ± 0.0002	2.1676 ± 0.0476	0.0869 ± 0.0024
1.6	0.05	0.0010 ± 0.0000	0.3922 ± 0.0002	1.9553 ± 0.0420	0.1295 ± 0.0024
1.6	0.1	0.0010 ± 0.0000	0.3932 ± 0.0002	1.9236 ± 0.0331	0.2181 ± 0.0022
1.6	0.15	0.0010 ± 0.0000	0.3954 ± 0.0002	1.6454 ± 0.0355	0.2755 ± 0.0026
1.6	0.2	0.0010 ± 0.0000	0.3973 ± 0.0002	1.5340 ± 0.0357	0.3470 ± 0.0030
3.2	0.02	0.0010 ± 0.0000	0.3891 ± 0.0002	3.6295 ± 0.0511	0.0820 ± 0.0025
3.2	0.05	0.0010 ± 0.0000	0.3921 ± 0.0002	3.4636 ± 0.0419	0.1405 ± 0.0023
3.2	0.1	0.0010 ± 0.0000	0.3942 ± 0.0002	3.0404 ± 0.0422	0.2058 ± 0.0027
3.2	0.15	0.0010 ± 0.0000	0.3966 ± 0.0002	2.6940 ± 0.0460	0.2631 ± 0.0034
3.2	0.2	0.0010 ± 0.0000	0.3964 ± 0.0002	2.5603 ± 0.0451	0.3291 ± 0.0036
4.8	0.02	0.0010 ± 0.0000	0.3885 ± 0.0002	5.2174 ± 0.0663	0.0912 ± 0.0031
4.8	0.05	0.0010 ± 0.0000	0.3908 ± 0.0002	4.8181 ± 0.0486	0.1354 ± 0.0026
4.8	0.1	0.0010 ± 0.0000	0.3930 ± 0.0002	4.1630 ± 0.0433	0.1939 ± 0.0027
4.8	0.15	0.0010 ± 0.0000	0.3951 ± 0.0002	3.9617 ± 0.0375	0.2707 ± 0.0027
4.8	0.2	0.0010 ± 0.0000	0.3952 ± 0.0002	4.0582 ± 0.0422	0.3519 ± 0.0034
6.4	0.02	0.0010 ± 0.0000	0.3860 ± 0.0003	6.5014 ± 0.0835	0.0854 ± 0.0037
6.4	0.05	0.0010 ± 0.0000	0.3900 ± 0.0002	5.9809 ± 0.0644	0.1205 ± 0.0032
6.4	0.1	0.0010 ± 0.0000	0.3927 ± 0.0002	5.4830 ± 0.0486	0.1949 ± 0.0029
6.4	0.15	0.0010 ± 0.0000	0.3934 ± 0.0002	5.2893 ± 0.0430	0.2752 ± 0.0030
6.4	0.2	0.0010 ± 0.0000	0.3972 ± 0.0002	4.6120 ± 0.0362	0.3107 ± 0.0028

E.4 CA Model 2: Tables of Fitted Parameter Values

Table E.7: CA Model 2: Model 2 PDEs Fitted Parameter Values (descriptive power). We also give the CA model parameters a_e and the continuum analogue, λ, of the branching probability P_p, using equation (5.5), for comparison with the estimated parameter values.

P_p	λ	a_e	$\tilde{\lambda}$	$\tilde{a}_e$
			$a_n = 0, \tilde{a}_n = 0$	
10^{-2}	1.6	0.1	2.4145 ± 0.0756	0.1520 ± 0.0019
10^{-2}	1.6	0.2	2.0548 ± 0.0560	0.1499 ± 0.0015
10^{-2}	1.6	1	1.7080 ± 0.0408	0.1572 ± 0.0014
10^{-1}	16	0.1	5.5277 ± 0.0705	0.1178 ± 0.0016
10^{-1}	16	0.2	4.9136 ± 0.0528	0.1197 ± 0.0013
10^{-1}	16	1	3.6257 ± 0.0346	0.1373 ± 0.0012
			$a_n = 1, \tilde{a}_n = 1$	
10^{-2}	1.6	0.1	1.8305 ± 0.0578	0.1168 ± 0.0017
10^{-2}	1.6	0.2	1.4894 ± 0.0449	0.1104 ± 0.0014
10^{-2}	1.6	1	1.1739 ± 0.0384	0.1093 ± 0.0014
10^{-1}	16	0.1	2.7588 ± 0.0581	0.1001 ± 0.0017
10^{-1}	16	0.2	2.2644 ± 0.0434	0.0949 ± 0.0014
10^{-1}	16	1	1.5406 ± 0.0344	0.1034 ± 0.0013

Table E.8: CA Model 2: BC Model Fitted Parameters Values (descriptive power). We also give the CA model parameters a_e and the continuum analogue, λ, of the branching probability P_p, using equation (5.5), for comparison with the PDE fit parameters. Branching probabilities of $P_p = 10^{-1}, 10^{-2}$, correspond, respectively to $\lambda = 16, 1.6$. The continuum analogues of the diffusion and chemotactic coefficients in the CA model are $D = 10^{-3}$ and $\chi = 0.4$, respectively.

λ	a_e	$\tilde{D}_{\mathrm{BC}}$	$\tilde{\chi}_{\mathrm{BC}}$	$\tilde{\lambda}_{\mathrm{BC}}$	$\tilde{\beta}_e$
			$a_n = 0, \beta_n = 0$		
1.6	0.1	0.0068 ± 0.0002	0.2921 ± 0.0027	2.4866 ± 0.0535	14.1590 ± 0.2273
1.6	0.2	0.0029 ± 0.0001	0.3443 ± 0.0020	2.2874 ± 0.0416	18.6800 ± 0.2261
1.6	1	0.0016 ± 0.0001	0.3713 ± 0.0012	1.9170 ± 0.0341	22.1620 ± 0.1872
16	0.1	0.0017 ± 0.0001	0.3610 ± 0.0022	5.4489 ± 0.0680	18.4322 ± 0.2562
16	0.2	0.0016 ± 0.0001	0.3721 ± 0.0017	4.6978 ± 0.0511	18.4056 ± 0.2089
16	1	0.0014 ± 0.0001	0.3856 ± 0.0012	3.3656 ± 0.0348	20.2419 ± 0.1794
			$a_n = 1, \beta_n = 1$		
1.6	0.1	0.0032 ± 0.0002	0.3539 ± 0.0022	1.9091 ± 0.0474	15.0410 ± 0.2189
1.6	0.2	0.0019 ± 0.0001	0.3738 ± 0.0015	1.5556 ± 0.0365	15.4740 ± 0.1615
1.6	1	0.0014 ± 0.0001	0.3819 ± 0.0011	1.2633 ± 0.0324	15.8270 ± 0.1599
16	0.1	0.0024 ± 0.0001	0.3655 ± 0.0023	2.7258 ± 0.0537	14.0966 ± 0.2207
16	0.2	0.0019 ± 0.0001	0.3844 ± 0.0016	2.0614 ± 0.0397	13.6286 ± 0.1651
16	1	0.0016 ± 0.0001	0.3907 ± 0.0011	1.3811 ± 0.0313	14.8300 ± 0.1516

Table E.9: CA Model 2 ($a_n = 1$): Model 0 PDEs Fitted Parameters Values (descriptive power). We also give the CA model parameters a_e and the continuum analogue, λ, of the branching probability P_p, using equation (5.5), for comparison with the PDE fit parameters. A branching rate of 16 corresponds to $P_p = 10^{-1}$. The continuum analogues of the diffusion and chemotactic coefficients are $D = 10^{-3}$ and $\chi = 0.4$, respectively.

λ	a_e	D_{M0}	χ_{M0}	λ_{M0}	$\tilde{a}_e^{\mathrm{M0}}$
			$a_n = 1, a_n^{\mathrm{M0}} = 1$		
1.6	0.1	0.0004 ± 0.0001	0.4106 ± 0.0021	1.6674 ± 0.0710	0.1154 ± 0.0021
1.6	0.2	0.0006 ± 0.0001	0.4106 ± 0.0016	1.2535 ± 0.0558	0.1065 ± 0.0018
1.6	1	0.0006 ± 0.0000	0.4086 ± 0.0013	0.9612 ± 0.0484	0.1039 ± 0.0018
16	0.1	0.0005 ± 0.0001	0.4117 ± 0.0021	2.4319 ± 0.0746	0.0982 ± 0.0022
16	0.2	0.0007 ± 0.0001	0.4190 ± 0.0015	1.6478 ± 0.0538	0.0839 ± 0.0017
16	1	0.0008 ± 0.0000	0.4177 ± 0.0012	0.9798 ± 0.0420	0.0894 ± 0.0016

Table E.10: CA Model 2: Model 2 PDEs Fitted Parameter Values (predictive power). We also give the CA model parameters a_e and the continuum analogue, λ, of the branching probability P_p, using equation (5.5), for comparison to the PDE fit parameters. A branching rate of 16 corresponds to $P_p = 10^{-1}$.

P_p	λ	a_e	$\tilde{\lambda}$	$\tilde{a}_e$
			$a_n = 0, \tilde{a}_n = 0$	
10^{-2}	1.6	0.1	6.0881 ± 0.3238	0.1936 ± 0.0036
10^{-2}	1.6	0.2	4.8635 ± 0.2265	0.1883 ± 0.0028
10^{-2}	1.6	1	3.9921 ± 0.1622	0.2003 ± 0.0027
10^{-1}	16	0.1	9.9987 ± 0.3145	0.1746 ± 0.0035
10^{-1}	16	0.2	8.6753 ± 0.2216	0.1719 ± 0.0027
10^{-1}	16	1	6.4751 ± 0.1511	0.1853 ± 0.0024
			$a_n = 1, \tilde{a}_n = 1$	
10^{-2}	1.6	0.1	5.1484 ± 0.2512	0.1636 ± 0.0036
10^{-2}	1.6	0.2	4.2575 ± 0.1867	0.1537 ± 0.0029
10^{-2}	1.6	1	3.5567 ± 0.1626	0.1568 ± 0.0031
10^{-1}	16	0.1	6.8856 ± 0.2555	0.1575 ± 0.0037
10^{-1}	16	0.2	5.8056 ± 0.1790	0.1449 ± 0.0028
10^{-1}	16	1	4.2784 ± 0.1301	0.1522 ± 0.0025

Table E.11: CA Model 2: BC Model Fitted Parameter Values (predictive power). We also give the CA model parameters a_e and the continuum analogue, λ of the branching probability P_p, using equation (5.5), for comparison to the PDE fit parameters. A branching rate of 16 corresponds to $P_p = 10^{-1}$. The continuum analogues of the diffusion and chemotactic coefficients are $D = 10^{-3}$ and $\chi = 0.4$, respectively.

λ	a_e	$\tilde{D}_{\mathrm{BC}}$	$\tilde{\chi}_{\mathrm{BC}}$	$\tilde{\lambda}_{\mathrm{BC}}$	$\tilde{\beta}_e$
$a_n = 0, \beta_n = 0$					
1.6	0.1	0.0028 ± 0.0002	0.3131 ± 0.0038	8.2229 ± 0.2435	23.0110 ± 0.5722
1.6	0.2	0.0015 ± 0.0001	0.3498 ± 0.0018	6.6326 ± 0.1382	26.4140 ± 0.3015
1.6	1	0.0011 ± 0.0000	0.3665 ± 0.0013	5.4176 ± 0.1157	29.8910 ± 0.2885
16	0.1	0.0020 ± 0.0001	0.3284 ± 0.0036	12.0730 ± 0.2458	24.6180 ± 0.5107
16	0.2	0.0015 ± 0.0001	0.3529 ± 0.0020	10.0680 ± 0.1565	25.6910 ± 0.3086
16	1	0.0012 ± 0.0000	0.3703 ± 0.0014	7.4242 ± 0.1178	28.1520 ± 0.2829
$a_n = 1, \beta_n = 160$					
1.6	0.1	0.0016 ± 0.0001	0.3553 ± 0.0026	6.6074 ± 0.2052	22.7990 ± 0.4169
1.6	0.2	0.0012 ± 0.0001	0.3686 ± 0.0015	5.3530 ± 0.1309	22.3250 ± 0.2745
1.6	1	0.0011 ± 0.0000	0.3743 ± 0.0013	4.5861 ± 0.1207	23.3500 ± 0.2912
16	0.1	0.0014 ± 0.0001	0.3561 ± 0.0027	8.5791 ± 0.2167	23.3230 ± 0.4243
16	0.2	0.0012 ± 0.0001	0.3743 ± 0.0016	6.4725 ± 0.1434	21.5460 ± 0.2901
16	1	0.0012 ± 0.0000	0.3794 ± 0.0011	4.7928 ± 0.1008	22.3920 ± 0.2373

Table E.12: CA Model 2 ($a_n = 1$): Model 0 PDEs Fitted Parameter Values (predictive power). We also give the CA model parameters a_e and the continuum analogue, λ, of the branching probability P_p, using equation (5.5), for comparison to the PDE fit parameters. A branching rate of 16 corresponds to $P_p = 10^{-1}$. The continuum analogues of the diffusion and chemotactic coefficients are $D = 10^{-3}$ and $\chi = 0.4$, respectively.

λ	a_e	D_{M0}	χ_{M0}	λ_{M0}	$\tilde{a}_e^{\mathrm{M0}}$
$a_n = 1, \tilde{a}_n^{\mathrm{M0}} = 1$					
1.6	0.1	0.0003 ± 0.0001	0.3990 ± 0.0037	5.8441 ± 0.3831	0.1818 ± 0.0052
1.6	0.2	0.0004 ± 0.0001	0.4014 ± 0.0026	4.5788 ± 0.2898	0.1669 ± 0.0044
1.6	1	0.0005 ± 0.0001	0.4019 ± 0.0021	3.6929 ± 0.2611	0.1672 ± 0.0049
16	0.1	0.0003 ± 0.0001	0.3953 ± 0.0037	7.9667 ± 0.3973	0.1835 ± 0.0055
16	0.2	0.0004 ± 0.0001	0.4085 ± 0.0026	5.3167 ± 0.2858	0.1499 ± 0.0043
16	1	0.0007 ± 0.0000	0.4043 ± 0.0019	3.9829 ± 0.2218	0.1565 ± 0.0041

Appendix F

Analysis of PDE Models

This appendix is largely an analytical study of the one-dimensional TC dynamics in the Model 1 PDEs, with some investigations of Model 0 and 2 PDEs. We use a variety of analytic techniques, including asymptotic analysis and the method of characteristics, to uncover underlying behaviour, such as boundary layers, steep fronts, steady-state behaviour etc. We carry out all calculations with a diffusion coefficient that is much smaller than the chemotactic coefficient, which is what enables the use of asymptotic methods. Numerical methods (used to solve the PDEs in previous chapters) confirm the behaviours uncovered by analytical techniques, such as corroborating breaking times or steady-state behaviour. We have chosen to pursue an analytical study as it gives us insight into the behaviour of the PDEs we have derived. Recently, numerous papers dedicated to analysing the travelling wave or pattern forming behaviour that arise in tumour angiogenesis and volume-filling PDE models governed by diffusive and chemotactic dynamics have been published (see Mei et al. (2015); Ai et al. (2015); Lin and Wang (2014); Kavanagh (2014)). Thus, there has been much interest in understanding the behaviour of PDE systems similar to those we have derived and therefore, we believe this work is topical.

We introduced these non-dimensional Model 1 PDEs in Chapter 3, and we reiterate them here. For $a_n = 0$ (total TC VE in motility mechanism, no tip-to-tip anastomosis), the TC density, $N(x,t)$ satisfies

$$\frac{\partial N}{\partial t} = D\nabla^2 N - \chi\nabla\cdot(N(1-N)\nabla c) + \lambda c N(1-N)^2, \tag{F.1}$$

$$D\nabla N - \chi N(1-N)\nabla c\,|_{x=0,1} = 0, \tag{F.2}$$

while for $a_n = 1$ (tip-to-tip anastomosis), we have

$$\frac{\partial N}{\partial t} = (1-N)\left(D\nabla^2 N - \chi\nabla\cdot(N\nabla c)\right) - \mu N^2 + \lambda c N(1-N)^2, \tag{F.3}$$

$$D\nabla N - \chi N\nabla c\,|_{x=0,1} = 0, \tag{F.4}$$

with the initial condition given by

$$N(x,0) = f(x) = \exp\left(\frac{(x-x_0)^2}{2\sigma^2}\right). \tag{F.5}$$

The parameters are as follows: $D = 10^{-3}, \chi = 0.4$, $\mu = 160$ and $\lambda = 0.16$ or 1.6. The chemoattractant field, c, is assumed linear for simplicity, so that $c = x$, and thus $\nabla c = 1$ and $\nabla^2 c = 0$. We close each system with no flux boundary conditions, depending on whether TC VE is active or inactive.

F.1 Case 1: Movement and TC VE ($a_n = 0, \lambda = 0$)

The non-linear chemotactic term in equation (F.1) can be rewritten as $(1-2N)\frac{\partial N}{\partial x}$. Thus, we expect equation (F.1) to behave similarly to Burgers' equation

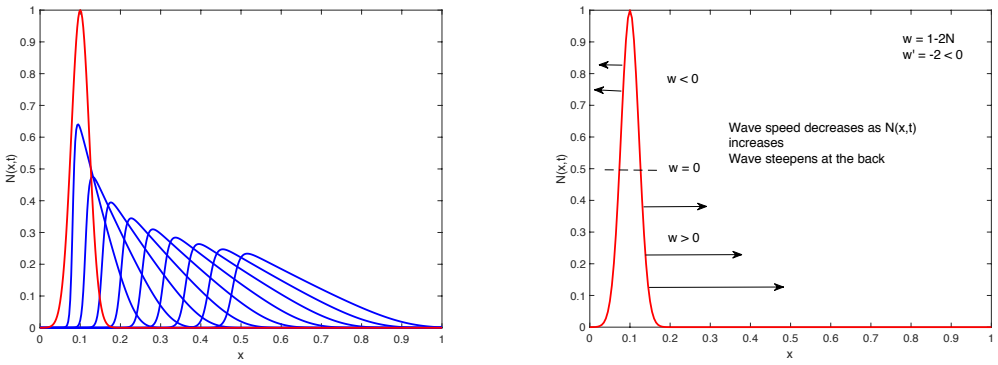

(a) (b)

Figure F.1: (a) Solution to equation (4.11), using a Gaussian initial condition (red curve) centred on $x = 0.1$ with a variance of $\sigma^2 = 0.0005$. The solutions are shown from $t = 0$ to $t = 1.8$. We see that the TC front steepens on the left, and develops a triangular travelling wave type shape. This steepening of the front at the back is caused by the non-linearity of the chemotactic term $(1 - 2N)\nabla N$, which implies that the wave speed decreases as N increases, as seen in (b).

(advective term of the form $-N\frac{\partial N}{\partial x}$), especially with regards to the formation of steep fronts (see Whitham (1974)). To illustrate the formation of steep fronts, we solve equation (F.1) numerically using a Gaussian initial condition (see Fig. 4.1 in Chapter 4), which is presented again here in Fig. F.1).

The steepening behaviour can be explained by neglecting the diffusion term in equation (F.1) and (F.2) as $D \ll \chi$ (we could also divide the equations by χ, and set $\varepsilon = D/\chi$), thereby arriving at a purely advective equation. To a first approximation, therefore, the wave speed, w, is $1 - 2N$, which decreases as N increases. Furthermore, $w < 0$ for $N > 0.5$, $w = 0$ for $N = 0.5$ and $w > 0$ for $N < 0.5$, indicating that initially the top half of the wave moves in the negative x-direction, while the bottom half moves in the positive x-direction, creating the steepening front at the back.

To find an approximate time at which the solution to equation (F.1) first steepens, we calculate the breaking time for equation (F.1) with $D = 0$ by using the method of characteristics. We rewrite the PDE as a system of ODEs, so that

we can solve for N along the characteristics, as follows:

$$\frac{dx}{dt} = (1-2N)\chi, \quad x=\xi \text{ when } t=0,\ 0<\xi<1, \tag{F.6}$$

$$\frac{dN}{dt} = 0,\ N=f(\xi) \text{ when } t=0 \text{ parametrizes } x-\text{axis}. \tag{F.7}$$

Solving for x we find

$$x = t(1-2f(\xi))\chi + \xi, \tag{F.8}$$

and therefore we can write N as

$$N = f(x-(1-2N)\chi t). \tag{F.9}$$

As the initial condition is bell-shaped, the characteristics will first cross at some point t_B at which the solution first becomes multi-valued. To find this breaking time, we differentiate equation (F.8) with respect to t and x, and we find that $\xi = \xi(x,t)$ satisfies

$$\xi_\tau = -\frac{(1-2f(\xi))}{1-2f'(\xi)t}, \tag{F.10}$$

$$\xi_\xi = \frac{1}{1-2f'(\xi)t}. \tag{F.11}$$

From these equations, it is clear that we cannot solve for ξ_t and ξ_x when $1-2f'(\xi)t=0$. By differentiating N with respect to x we obtain

$$N_x = \frac{f'(\xi)}{1-2f'(\xi)t}, \tag{F.12}$$

which confirms that the solution for N becomes becomes multi-valued when $1-2f'(\xi)t=0$. The breaking time, t_B, where N_x first becomes multi-valued,

is thus given by

$$t_B = \frac{1}{2\,|f'(\xi_B)|}, \tag{F.13}$$

where $\xi_B = \min\left[\xi \mid f'(\xi) > 0\right]$

Using equation (F.5) as the initial condition, we find that $\xi_B = x_0 - \sigma$, ($x_0 = 0.1, \sigma^2 = 0.0005$) and thus we calculate that the breaking time is $t_B \approx 0.046$. The solution at t_B is shown in Fig. F.2. The breaking time calculation approximates the time at which the TC front begins to steepen. In calculating t_B, we have made a further approximation by ignoring the boundary conditions (assuming that the initial condition does not interact with the boundary).

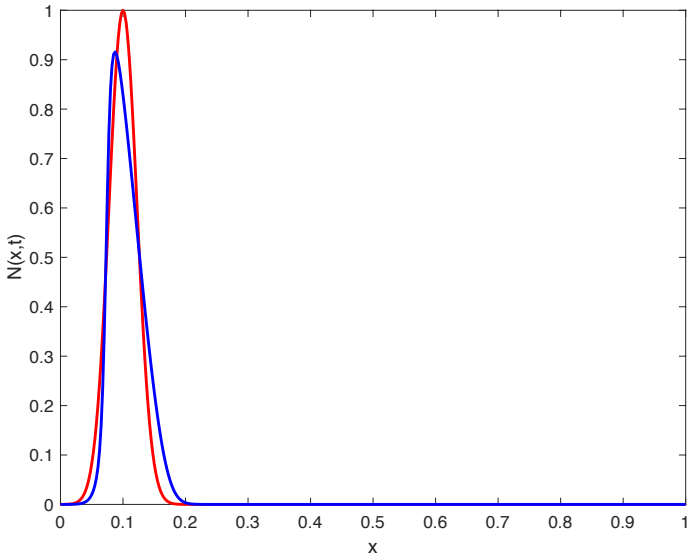

Figure F.2: The solution for $N(x,t)$ (blue curve) to the purely advective problem ($D = 0$ in equation (F.1)) breaks at approximately $t_B = 0.046$. Red = Gaussian initial condition.

F.1.1 Steady-State Behaviour

To find the steady-state solution, we set the time derivative to zero in equation (F.1) (with $\lambda = a_n = 0$). We then integrate this equation with respect to x and

use the boundary conditions, given in equation (F.2) to eliminate the constant of integration, to obtain

$$D\frac{\partial N}{\partial x} - \chi N = -\chi N^2, \tag{F.14}$$

which is Bernoulli's equation. If we divide through by χ, and define ε as

$$\varepsilon = D/\chi = 0.0025, \tag{F.15}$$

we find that the steady-state $N(x)$ solution is (found by solving Bernoulli's equation analytically)

$$N(x) = \frac{1}{1 + \alpha_0 \exp((1-x)/\varepsilon)}. \tag{F.16}$$

As there are no source and sink terms in equation (F.14) (equation (F.1) with $\lambda = a_n = 0$), we can determine the constant α_0 in equation (F.16) by using $\int_0^1 N(x,0)dx = \int_0^1 N(x,t)dx \,\forall\, t > 0$ (integrating the initial condition (equation (F.5)) over x). By using the steady-state profile, we obtain

$$\int_0^1 N(x,0)dx = \gamma = \int_0^1 \frac{1}{1 + \alpha_0 \exp((1-x)/\varepsilon)}dx. \tag{F.17}$$

After performing the integration on the right-hand side (using Mathematica) we obtain

$$\alpha_0 = \frac{(1 - \exp(\gamma - 1)/\varepsilon)}{\exp(\gamma/\varepsilon) - 1}. \tag{F.18}$$

We plot the steady-state solutions in Fig. F.3 for various initial conditions. We have used the Gaussian initial condition from equation (F.5), along with

$$\int_a^b \exp\left(\frac{(x-x_0)^2}{2\sigma^2}\right) = \frac{\sqrt{2\pi}\sigma}{2}\left(\text{erf}\left(\frac{b-x_0}{\sqrt{(}2)\sigma}\right) - \text{erf}\left(\frac{a-x_0}{\sqrt{(}2)\sigma}\right)\right), \tag{F.19}$$

as well as δ-function initial conditions, $N(x,0) = \delta(x - x_a)$ and $N(x,0) = 0.5\delta(x-x_a)$ centred on x_a within $(0,1)$. For $N(x,0) = \delta(x-x_a)$, the steady-state

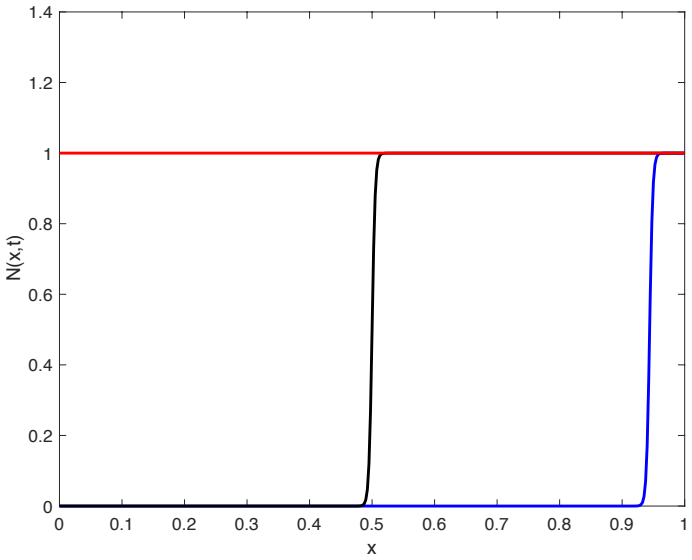

Figure F.3: Steady-state solutions for equation (F.1) with $\lambda = a_n = 0$ (no source or sink terms) for the following initial conditions: Gaussian initial condition (equation (F.5)) with $x_0 = 0.1$ and $\sigma^2 = 0.0005$ (blue), $N(x,0) = 0.5\delta(x - x_a), x_a \in (0,1)$ (black) and $N(x,0) = \delta(x - x_a)\, x_a \in (0,1)$ (red).

takes its maximum value of 1 for all values of x, whilst for $N(x,0) = 0.5\delta(x-x_a)$, $N = 1$ on half the domain. For the Gaussian initial condition, the width of the solution near $x = 1$ depends on the initial mass within the system, found by integrating the initial condition over the domain as in equation (F.17).

F.1.2 Analytical Solution on the Infinite Line

By dividing equation (F.1) by χ, and using the definition of ε in equation (F.15), we rescale t such that

$$\tau = \chi t. \tag{F.20}$$

In this way, we can write equation (F.1) as

$$\frac{\partial N}{\partial \tau} + (1-2N)\frac{\partial N}{\partial x} = \varepsilon \frac{\partial^2 N}{\partial x^2}. \tag{F.21}$$

We can transform this equation into Burgers' equation by letting $N = u + \frac{1}{2}$ and transforming the x axis as $\hat{x} = -x$ to find

$$\frac{\partial u}{\partial \tau} + 2u\frac{\partial u}{\partial \hat{x}} = \varepsilon \frac{\partial^2 u}{\partial \hat{x}^2}. \tag{F.22}$$

It well known that Burgers' equation, equation (F.22), can be transformed into the diffusion equation using the Cole-Hopf transformation (see Whitham (1974)). We transform equation (F.22) into a diffusion equation using the Cole-Hopf transformation given by

$$u = -\varepsilon \frac{\phi_{\hat{x}}}{\phi}. \tag{F.23}$$

With this transformation we obtain from equation (F.22) that ϕ satisfies the diffusion equation

$$\frac{\partial \phi}{\partial \tau} = \varepsilon \frac{\partial^2 \phi}{\partial \hat{x}^2}, \tag{F.24}$$

which can be solved analytically using Green's functions as follows

$$\phi(\hat{x}, t) = \frac{1}{\sqrt{4\pi\varepsilon t}} \int_{-\infty}^{\infty} \phi(\eta, 0) \exp\left(-\frac{(\hat{x}-\eta)^2}{4\varepsilon t}\right) d\eta, \tag{F.25}$$

where $\phi(\eta, 0)$ is given by

$$\phi(\eta, 0) = \exp\left(-\frac{1}{\varepsilon}\int^{\eta} u(\hat{x}, 0) d\hat{x}\right) = \exp\left(-\frac{1}{\varepsilon}\int^{\eta} g(\hat{x}) d\hat{x}\right), \tag{F.26}$$

where $u(x,0) = g(x)$. The solution for u, defined in equation (F.23), and satisfying equation (F.22), is given by

$$u = \frac{\int_{-\infty}^{\infty} \frac{(\hat{x}-\eta)}{2t} \exp(-\frac{G}{\varepsilon}) d\eta}{\int_{-\infty}^{\infty} \exp(-\frac{G}{\varepsilon}) d\eta}, \tag{F.27}$$

where

$$G = \int^{\eta} g(\hat{x}) d\hat{x} + \frac{(\hat{x}-\eta)^2}{4t}. \tag{F.28}$$

From this, we can find the solution for N, by using $N = u + \frac{1}{2}$ and setting $x = -\hat{x}$. As we have transformed our problem on the infinite line to one that resembles Burgers' equation, and further, given that our solutions for N exhibit a triangular wave type shape (see Fig. F.1), we direct the reader to the "single hump" analysis for Burgers' equation (see Whitham (1974)) for an analytical solution found by approximating the integrals in equations (F.27) and (F.28).

F.2 Case 2: Movement, TC VE and Branching $(a_n = 0, \lambda = 0.16)$

With a non-zero branching term, equation (F.1) gives rise to the steepening behaviour (see Fig. F.1b, discussed in Section F.1). To approximate a time at which the solution to equation (F.1) first steepens, we calculate the breaking time of the purely advective equation (found by neglecting the diffusion term, as in the previous section). Using the method of characteristics, we formulate the following ODEs (characteristic equations):

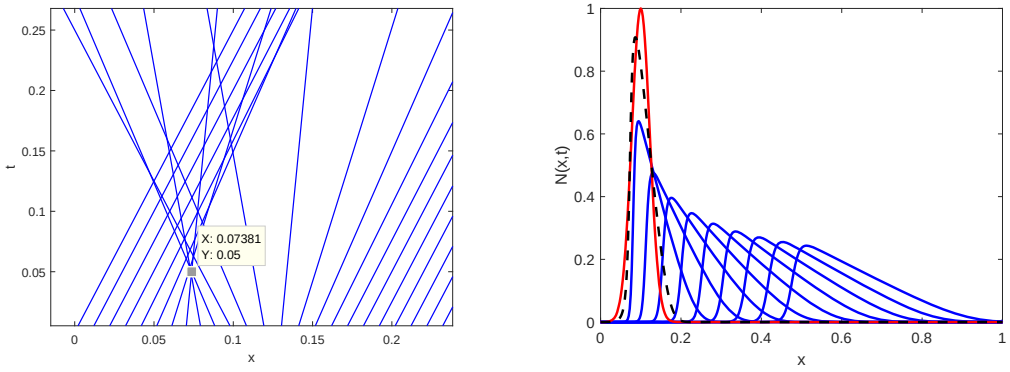

(a) (b)

Figure F.4: (a) Characteristic curves (solution to equations (F.29) and (F.30)) cross at $t_B \approx 0.05$ indicating the approximate breaking time (for the purely advective problem). (b) Using a Gaussian initial condition (red curve) centred on $x = 0.1$ with a variance of $\sigma^2 = 0.0005$, we plot the numerical solution for N from $t = 0.2 - 1.8$ (blue curves). The black curve indicates the time, t_B, at which the solution first steepens.

$$\frac{dx}{dt} = (1-2N)\chi, \quad x = \xi \text{ when } t = 0, 0 < \xi < 1, \tag{F.29}$$

$$\frac{dN}{dt} = \lambda x N(1-N)^2, \; N = f(\xi), \text{ when } t = 0 \text{ parametrizes x} - \text{axis}. \tag{F.30}$$

We solve this system of equations numerically (using MATLAB's *ode45*) to find the breaking time, using a Gaussian initial condition (see equation (F.5)). We plot the characteristics in the $t - x$ plane in Fig. F.4, and the point at which the characteristics cross gives the approximate breaking time, $t_B \approx 0.05$. We plot the solutions to equations (F.1) and (F.2) with $\lambda = 0.16$ in Fig. F.4 for a Gaussian initial condition (see equation (F.5)) and illustrate the steepening of the solution for N at t_B.

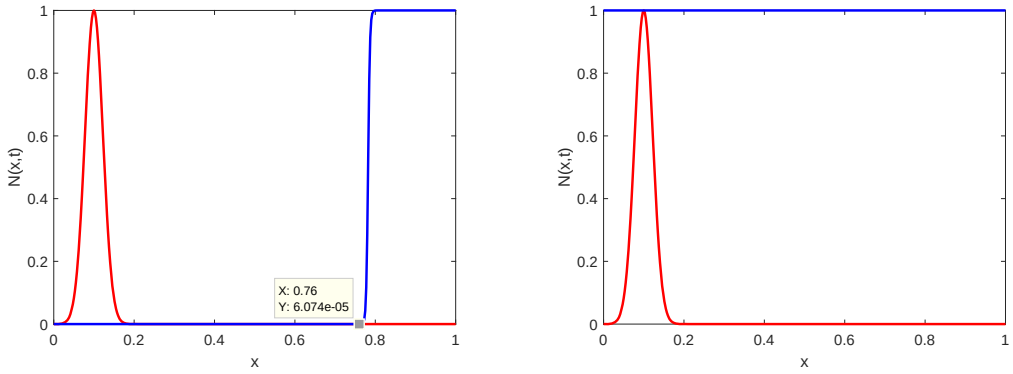

(a) $t = 1000$ (b) $t = 25000$

Figure F.5: Proliferation problem ($\lambda = 0.16$): approach to steady-state. (a) Solution at $t = 1000$ (blue curve) from Gaussian initial condition (red curve). (b) Solution at $t = 25000$. From the initial condition, the solution for N moves towards $x = 1$, is reflected at the boundary, and continues to move towards $x = 0$, until the domain is entirely filled, and $N = 1, \forall x$.

F.2.1 Steady-State Behaviour (Proliferation)

The steady-state behaviour for the proliferation problem is intuitive, given a long enough time, the system will reach equilibrium at $N = 1, \forall x$. If we begin with a Gaussian initial condition, then the TC front will move towards the boundary at $x = 1$, be reflected off that boundary (due to the no flux boundary conditions), and continue to proliferate and fill the domain until $N = 1, \forall x$. This behaviour can be seen in Fig. F.5, at time $t = 1000$ (approach steady-state) and $t = 25000$ (steady-state reached).

We now find an analytical expression for the leading edge of the solution for $N(x, t)$ as it approaches its steady-state. We divide equations (F.1) and (F.2) by χ, and define ε and τ as in equations (F.15) and (F.20). Furthermore, we introduce Λ as

$$\Lambda = \frac{\lambda}{\chi}, \tag{F.31}$$

to find

$$\frac{\partial N}{\partial \tau} = \varepsilon \frac{\partial^2 N}{\partial x^2} - \frac{\partial}{\partial x}(N(1-N)) + \Lambda x N(1-N)^2, \tag{F.32}$$

$$\varepsilon \frac{\partial N}{\partial x} - N(1-N) \mid_{x=0,1} = 0. \tag{F.33}$$

The leading edge of the front, $x(\tilde{\tau})$, moves from $x = 1$ to $x = 0$ slowly in time. A distinguished limit analysis gives $\tilde{\tau} = f(\tau) = \varepsilon\tau$ as the slow time behaviour. Further, we expand $x = x_0(\tilde{\tau}) + \varepsilon x_1(\tilde{\tau}) + \cdots$, and we aim to find the zeroth order location of the front edge of the layer.

In the transition layer, we let

$$y = \frac{x - x_0(\tilde{\tau})}{\varepsilon}, \quad N(x,\tau) = M(y). \tag{F.34}$$

Substituting these expressions into equations (F.32) and (F.33) we find

$$-M' x_0' \frac{\partial \tilde{\tau}}{\partial \tau} = M'' - (M(1-M))' + \varepsilon\Lambda(\varepsilon y + x_0) M(1-M)^2. \tag{F.35}$$

We expand M as $M = M_0(y) + \varepsilon M_1(y) + \ldots$. Upon substituting the expansion into equation (F.35), we obtain to leader order in ε that

$$M_0'' - (M_0(1-M_0))' = 0, \tag{F.36}$$

$$M_0 \to 1 \text{ as } y \to \infty,\ M_0 \to 0 \text{ as } y \to -\infty. \tag{F.37}$$

We solve for M_0 to obtain

$$M_0 = \frac{1}{1+\exp(-y)},, \tag{F.38}$$

and, without loss of generality, we have defined $M_0(0) = \frac{1}{2}$ as the "center" of

the transitions layer.

At the next order, we find

$$M_1'' - (M_1(1-2M_0))' = -M_0' x_0' - \Lambda x_0 M_0 (1-M_0)^2, \tag{F.39}$$

$$M_1' - M_1(1-2M_0) \to 0 \text{ as } y \to \pm\infty. \tag{F.40}$$

An ODE for $x_0(\hat{\tau})$ will arise from a solvability condition for equations (F.39) and (F.40). To determine this condition, we simply integrate equation (F.39) with respect to y to find

$$M_1' - (M_1(1-2M_0)) \,|_{-\infty}^{\infty} = \int_{-\infty}^{\infty} (-\Lambda x_0 M_0 (1-M_0)^2 - M_0' x_0')\, dy. \tag{F.41}$$

We then use the limiting conditions in equation (F.40) (arises from the boundary conditions, equation (F.33)) to obtain

$$-\Lambda x_0 \int_{-\infty}^{\infty} M_0 (1-M_0)^2\, dy - x_0' \int_{-\infty}^{\infty} M_0'\, dy = 0. \tag{F.42}$$

We can calculate these integrals given that M_0 is known analytically in equation (F.38). By evaluating the integrals, and then integrating the ODE for x_0, we find

$$x_0 = A_1 \exp\left(-\Lambda \varepsilon \tau / 2\right). \tag{F.43}$$

We can determine A_1 by matching equation (F.43) to the leading edge determined from the numerical solution for N at some point. We return to the original timescale t, and calculate A_1 for $\lambda = 0.16$ to find $A_1 = 0.9283$ (using $t = 500$). We then calculate the leading edge of the transition layer at $t = 1000$ using

$$x_0 = A_1 \exp\left(-\lambda \varepsilon t / 2\right), \text{ where } A_1 = 0.9283 \text{ for } \lambda = 0.16, \tag{F.44}$$

to find $x_0 = 0.76$, which coincides with the leading edge in Fig. F.5a and, for $t = 25000$, we find $x_0 \approx 0$, coinciding with the steady-state reached in Fig. F.5b.

F.3 Case 3: Movement, Tip-to-Tip Anastomosis and Branching ($a_n = 1, \lambda = 1.6$)

Here, the tip-to-tip anastomosis terms are active and the model is given in equations (F.3) and (F.4). To illustrate the solution behaviour, we numerically solve this PDE system using a Gaussian initial condition (see equation (F.5)). The numerical solutions are shown in Fig. F.6. We see that for $\mu > \lambda$ (including $\lambda = 0$), the solution for N decays to zero (F.6b and F.6f). If $\lambda = 1.6$ and $\mu = 1.6$, so $\lambda \approx \mu$, we obtain a non-zero steady-state solution for N at $x = 1$ (see Fig. F.6d). Further, for $\mu \gg \lambda$, we do not obtain the steepening behaviour as in other cases (see Fig. F.6e).

We find an approximate solution for N as it approaches zero when $\mu > \lambda$ by using the method of characteristics (neglecting the diffusion term as before). The characteristic equations are

$$\frac{dx}{dt} = (1-N)\chi, \quad x = \xi \quad \text{when} \quad t = 0, \quad 0 < \xi < 1, \tag{F.45}$$

$$\frac{dN}{dt} = -\mu N^2 + \lambda x N(1-N)^2, \; N = f(\xi), \; \text{when } t = 0 \text{ parametrizes x} - \text{axis.} \tag{F.46}$$

For the case $\lambda = 0$, we can solve for N explicitly as

$$N = \frac{1}{\mu t + c_1}, \tag{F.47}$$

where c_1 is a constant to be found. Therefore, we see that N decays to zero

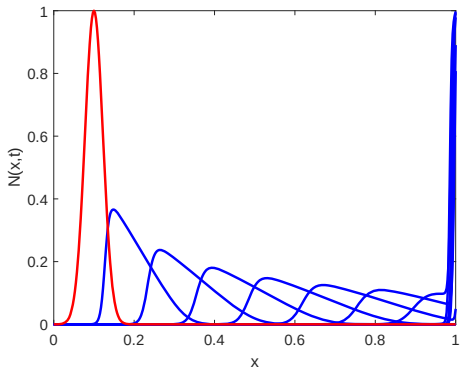

(a) $\lambda = 0, \mu = 1.6, t_f = 4$

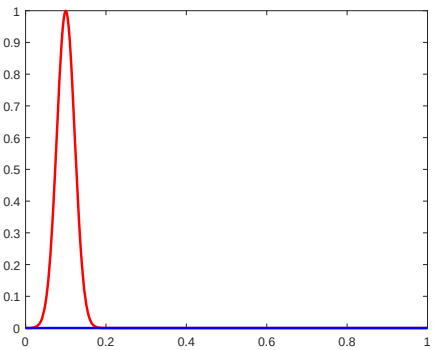

(b) $\lambda = 0, \mu = 1.6, t_f = 10$

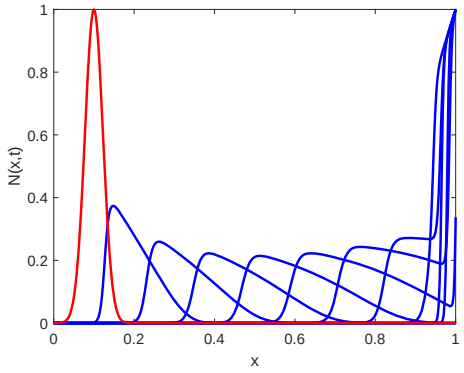

(c) $\lambda = 1.6, \mu = 1.6, t_f = 4$

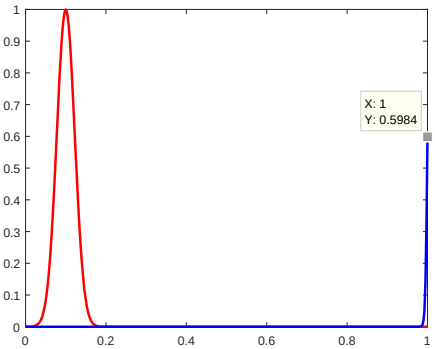

(d) $\lambda = 1.6, \mu = 1.6, t_f = 10$

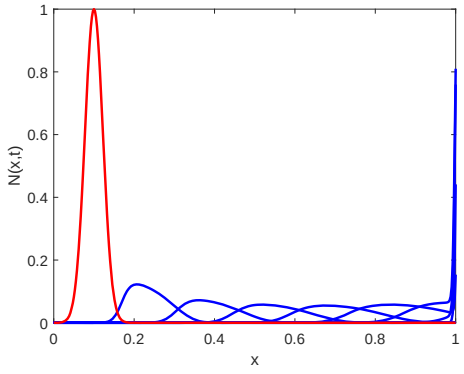

(e) $\lambda = 1.6, \mu = 16, t_f = 4$

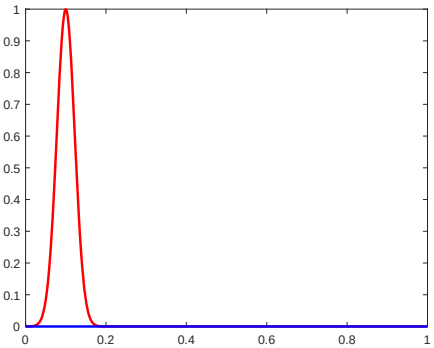

(f) $\lambda = 1, 6, \mu = 16, t_f = 10$

Figure F.6: Full problem: approach to steady-state (in $t = 0.4$ time increments). (a), (b), (e), (f) Solution (blue curve) reaches zero steady-state from Gaussian initial condition (red). (c), (d) Boundary layer at steady-state when $\mu \approx \lambda$. When $\mu > \lambda$, the steady-state is essentially zero. t_f = final time at which we show solutions.

algebraically for the purely advective problem and for $\lambda = 0$. We will not solve the system of ODEs numerically for N, as the numerical solution to the full problem with diffusion is shown in Fig. F.6.

We now construct the steady-state boundary layer solution at $x = 1$ that occurs for a Gaussian initial condition when $\mu = 1.6$ and $\lambda = 1.6$. We divide equations (F.3) and (F.4) by χ and define ε and τ as in equations (F.15) and (F.20), to find

$$(1-N)\left(\varepsilon\frac{\partial^2 N}{\partial x^2} - \frac{\partial N}{\partial x}\right) - \hat{\mu}N^2 + \Lambda x N(1-N)^2 = 0, \tag{F.48}$$

$$\varepsilon\frac{\partial N}{\partial x} - N\,|_{x=0,1} = 0, \tag{F.49}$$

where $\hat{\mu} = \mu/\chi$ and $\Lambda = \lambda/\chi$. In the boundary layer region, we let $y = \frac{1-x}{\varepsilon}$ and $M(y) = N[1-\varepsilon y]$. This leads to the boundary layer problem

$$\begin{aligned}&(1-M)\left(\frac{1}{\varepsilon}\frac{\partial^2 M}{\partial y^2} + \frac{1}{\varepsilon}\frac{\partial M}{\partial y}\right) - \hat{\mu}M^2 + \Lambda(1-\varepsilon y)M(1-M)^2 = 0,\\ &\frac{\partial M}{\partial y} - M = 0, \quad \text{at} \quad y = 0\end{aligned} \tag{F.50}$$

We expand M as

$$M = \frac{M_0}{\hat{\mu}} + \varepsilon\frac{M_1}{\hat{\mu}^2} + \ldots, \tag{F.51}$$

and, simplifying, we find at $O(\varepsilon^0)$, that the leading order boundary layer equations are

$$\left(1 - \frac{M_0}{\hat{\mu}}\right)\left(\frac{\partial^2 M_0}{\partial y^2} + \frac{\partial M_0}{\partial y}\right) = 0, \tag{F.52}$$

$$\frac{M_0}{\hat{\mu}} < 1, \tag{F.53}$$

$$\frac{\partial M_0}{\partial y} + M_0 = 0 \quad \text{at} \quad y = 0. \tag{F.54}$$

At $O(\varepsilon^1)$, we pick up other anastomosis and branching contributions. Solving for M_0 we find

$$M_0 = B\exp(-y), \tag{F.55}$$

which satisfies the boundary conditions at $y = 0$ with B undetermined. To find B, we must match or "glue" the inner and outer solutions together. We know that the outer solution is $N = 0$, and thus, we solve for B using a global conservation condition. We return to equations (F.48) and (F.49) (steady-state equations), and integrate these equations over x to find

$$\int_0^1 \hat{\tau}(N, x)dx = 0, \tag{F.56}$$

where we have used the boundary conditions at $x = 0, 1$ in equation (F.49). Here, we have defined

$$\hat{\tau}(N, x) = -\hat{\mu}\frac{N^2}{1-N} + \Lambda x N(1-N). \tag{F.57}$$

We know that for $\varepsilon \to 0$, the asymptotic solution vanishes away from the boundary layer near $x = 1$. Therefore, the main contribution to the integral in equation (F.56) arises from the boundary layer solution. We change to local/inner variables $y = \frac{1-x}{\varepsilon}$ to obtain that equation (F.56) becomes

$$\int_0^\infty \frac{1}{1-M}\left(-\hat{\mu}M^2 + \Lambda(1-\varepsilon y)M(1-M)^2\right)\, dy = 0. \tag{F.58}$$

To leading order with $M \approx M_0/\hat{\mu} + O(\varepsilon)$, equation (F.58) becomes

$$\int_0^\infty \frac{1}{1-M_0}\left(-\hat{\mu}M_0^2 + \Lambda M_0(1-M_0)^2\right)\, dy = 0. \tag{F.59}$$

Since M_0 is monotonic, we can change variables as follows: $dy = \frac{dy}{dM_0}dM_0$ with

$M_0 = B\exp(-y)$ (see equation (F.55)) and $M_0' = -M_0$. In this way, equation (F.59) becomes

$$\int_0^B \frac{1}{1-M_0}\left(-\hat{\mu}M_0 + \Lambda(1-M_0)^2\right) dM_0 = 0. \tag{F.60}$$

We note that we are considering the case where $\hat{\mu} = \Lambda$, and thus we can divide these out of the equation (F.60). We can integrate equation (F.60) exactly to find

$$F(B) = \frac{1}{2}\left(1-(1-B)^2\right) + B + \log(1-B) = 0, \tag{F.61}$$

for some $B = B_c$, which corresponds to the unknown value of B for the boundary layer solution. Further we know that $B \in [0,1]$ as N can take on a maximum value of 1 at $x = 1$ (from density restrictions on the equations and numerical solutions), and so we know that $F(0) = 0$ and $F(1) \to -\infty$. Further, for $0 < B \ll 1$, $F(B) > 0$. Thus in some region of $0 < B < 1$, $F(B) > 0$ and there must be a root in the interval.

In fact, given that equation (F.61) is quadratic in B (and M_0 before substitution of limits), we know there are only two roots, and one of those roots occurs at $B = 0$. Therefore, there is a unique root at some value of $B = B_c$ for each combination of $\frac{\Lambda}{\hat{\mu}}$ (we used a ratio of 1, but this solution method will work for any ratio of $\hat{\mu}$ and Λ, we would retain the terms in the solution methodology (i.e. not divide them out)). We find the other root by plotting $F(B)$ as a function of $B \in [0,1]$. We could also find B by matching the boundary layer solution M_0 (equation (F.55)) to the numerical solutions. For $\hat{\mu} = \Lambda = 1.6$, from plotting $F(B)$ we find that $B \approx 0.67$. From the numerics, we find that $B \approx 0.6$ and thus our zeroth boundary layer calculation slightly overestimates the value of B. We could make this approximation more accurate by considering terms at the next order in ε.

F.4 Ill-posedness of Models

In this section, we consider possible ill-posedness of all three models derived in this thesis, namely, the Model 0, 1 and 2 PDEs. These three models are re-iterated below:

Model 0 satisfies

$$\begin{aligned}\frac{\partial N}{\partial t} &= (1-a_nN-a_eE)\left(D\frac{\partial^2 N}{\partial x^2}-\chi\frac{\partial}{\partial x}\left(N\frac{\partial c}{\partial x}\right)\right)\\ &\quad -\mu(a_nN^2+a_eNE)+\lambda cN, \qquad \text{(F.62)}\\ \frac{\partial E}{\partial t} &= \mu N+a_nN\left(\mu N+D\frac{\partial^2 N}{\partial x^2}-\chi\frac{\partial}{\partial x}\left(N\frac{\partial c}{\partial x}\right)\right), \qquad \text{(F.63)}\end{aligned}$$

subject to

$$D\frac{\partial N}{\partial x}-\chi N\frac{\partial c}{\partial x}=0, \text{ at } x=0,1. \qquad \text{(F.64)}$$

In the equations below, we set $B=0$ for Model 1 and $B=1$ for Model 2 (a_e is non-zero in this case),

$$\begin{aligned}\frac{\partial N}{\partial t} &= D\left((1-a_nN-Ba_eE)\frac{\partial^2 N}{\partial x^2}\right)-\chi\left(\underbrace{(1-2N}_{\text{TC VE}}+a_nN-Ba_eE)\frac{\partial N}{\partial x}\frac{\partial c}{\partial x}\right.\\ &\left.+N(1-N-Ba_eE)\frac{\partial^2 c}{\partial x^2}\right)-\mu\left(a_nN^2+Ba_eNE\right)+\lambda cN\underbrace{(1-N-BE)^2}_{\text{VE}}, \qquad \text{(F.65)}\\ \frac{\partial E}{\partial t} &= \mu N\left(\underbrace{1-N}_{\text{TC VE}}+2a_nN\right)-N\left(D\underbrace{(1-2a_n)}_{\text{TC VE}}\frac{\partial^2 N}{\partial x^2}\right)\\ &-\chi N\left((1-a_n)\underbrace{\frac{\partial c}{\partial x}\frac{\partial N}{\partial x}}_{\text{TC VE}}+a_n\frac{\partial}{\partial x}\left(N\frac{\partial c}{\partial x}\right)\right), \qquad \text{(F.66)}\end{aligned}$$

subject to

$$D\frac{\partial N}{\partial x} - \chi N \underbrace{(1-(1-a_n)N)}_{\text{TC VE}} \frac{\partial c}{\partial x} \mid_{x=0,1} = 0, \tag{F.67}$$

where the diffusion and chemotactic coefficients, D and χ, are defined by

$$D = \frac{\mu h^2}{4} = \lim_{\tau \to 0} \frac{P_m h^2}{4\tau}, \quad \chi = \mu k h^2 = \lim_{\tau \to 0} \frac{P_m k h^2}{\tau}, \tag{F.68}$$

and μ and λ are defined as

$$\mu = \lim_{\tau \to 0} \frac{P_m}{\tau}, \quad \lambda = \lim_{\tau \to 0} \frac{P_p}{\tau}. \tag{F.69}$$

In all three models, we see that the diffusive and chemotactic terms are $O(h^2)$ terms ($h \ll 1$) due to the definitions of the diffusion and chemotactic coefficients (see equation (F.68)). Thus, if we let $\varepsilon = h^2$, and expand N and E as $N = N_0 + \varepsilon N_1 + \cdots$ and $E = E_0 + \varepsilon E_1 + \cdots$, to a zeroth order approximation in ε, the dynamics of these systems at a fixed point in $x \in [0,1]$ (pre-determined, where we have used $c = x$, linear TAF gradient) can be approximated by the following ODEs for Model 0

$$\frac{dN_0}{dt} = \lambda x N_0 - a_n \mu N_0^2 - a_e \mu N_0 E_0, \tag{F.70}$$

$$\frac{dE_0}{dt} = \mu N_0 + a_n \mu N_0^2, \tag{F.71}$$

Model 1,

$$\frac{dN_0}{dt} = \lambda x N_0 (1-N_0)^2 - a_n \mu N_0^2, \tag{F.72}$$

$$\frac{dE_0}{dt} = \mu N_0 (1 - N_0 + 2a_n N_0), \tag{F.73}$$

and Model 2,

$$\frac{dN_0}{dt} = \lambda x N_0(1 - N_0 - E_0)^2 - a_n \mu N_0^2 - a_e \mu N_0 E_0, \tag{F.74}$$

$$\frac{dE_0}{dt} = \mu N_0(1 - N_0 + 2a_n N_0), \tag{F.75}$$

respectively, where we have considered only binary choices of a_n and a_e.

We rewrite the left-hand side of equations (F.70), (F.71), (F.74) and (F.75) in vector notation as (N_0', E_0') and the right-hand of equations (F.70) and (F.71) (Model 0) as (f_1, f_2) and the right-hand of equations (F.74) and (F.75) (Model 2) as (g_1, g_2). Thus, $(N_0', E_0') = (f_1, f_2)$ for Model 0 and $(N_0', E_0') = (g_1, g_2)$ for Model 2, and we can use methods from dynamical systems to determine whether the solutions of these systems adhere to the restriction $N_0 + E_0 \leq 1$ (trapping region, see Fig. F.7) when $a_e = 1$ and $a_n = 1, 0$. These are the cases for which Models 0 and 2 may become ill-posed due to the multiplication of the diffusion term by $(1 - a_n N - a_e E)$ in equations (F.62), (F.63), (F.65), and (F.66).

If the trajectories stay within the trapping region, then for Model 0, we have for any trajectory that

$$(N_0', E_0') \cdot (1, 1) < 0, \tag{F.76}$$

$$\rightarrow (f_1, f_2) \cdot (1, 1) < 0, \tag{F.77}$$

$$\rightarrow f_1 + f_2 < 0 \tag{F.78}$$

$$\rightarrow \mu N_0^2 + \lambda c N_0 < 0, \tag{F.79}$$

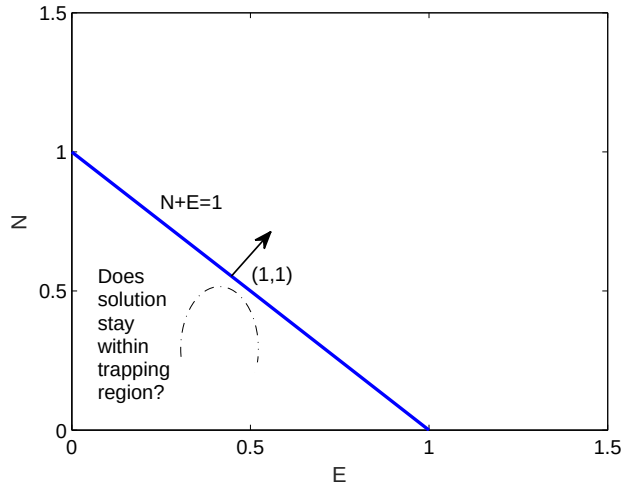

Figure F.7: We want to determine whether the trajectory of the solutions near $N_0 + E_0 = 1$ to equations (F.70), (F.71), (F.74) and (F.75) remain within the trapping region (defined by $N_0 + E_0 \leq 1$ with $N_0 \geq 0, E_0 \geq 0$). To this end, we want to determine whether $(N_0', E_0') \cdot (1, 1) < 0$ where $(1, 1)$ is the unit outward normal to $N_0 + E_0 = 1$.

and for Model 2

$$\rightarrow (g_1, g_2) \cdot (1, 1) < 0, \tag{F.80}$$

$$\rightarrow \mu a_n N_0^2 + \lambda c N_0 (1 - N_0 - E_0)^2 < 0, \tag{F.81}$$

where we have used the fact that $E_0 = 1 - N_0$ to simplify the equations above. A key observation is that for both Models 0 and 2 (with $a_n = 1$), the conditions determined for the trajectories to remain within the trapping region are impossible as all terms are positive, provided $N_0 \in [0, 1]$, and thus the equations for the full parabolic system for Models 0 and 2 can become ill-posed in the singular limit of small diffusion coefficient. In Model 2, for $a_n = 0$, if we set $\lambda = 0$ when $N_0 + E_0 = 1$, then the trajectory will remain on the boundary of $N_0 + E_0 = 1$, and thus the corresponding PDE model remains well-posed.

We illustrate the behaviour of equations (F.70), (F.71), (F.74) and (F.75) in Fig. F.8. Without loss of generality, we choose $x = 0.7450$ in the aforementioned

equations (note that x takes on a maximum value of 1 and scales the branching rate λ). We solve the equations for the following set of parameter values: $\lambda = 1.6$, $\mu = 160$, from $t = 0.2 - 2$, and we depict the values of $N_0 + E_0$ at time $t = 2.0$ as a function of the initial value of N_0 chosen. For the initial values, we let $N_0 \in [0, 1]$ in increments of 0.05 and $E_0 = 1 - N_0$. We also impose the condition in Model 0 and 2 that $\lambda = 0$ if $N_0 + E_0 > 1$ or N_0 and E_0 are negative.

We see that for $a_n = 1$, except for $N_0 = 0$ initially, $N_0 + E_0$ at $t = 2$ exceeds 1 (see Figs. F.8a and F.8b). For $a_n = 0$, Model 2 remains well-posed, while the density restrictions are exceeded in Model 0 (see Figs. F.8c and F.8d). Furthermore, for Model 0, the values of $N_0 + E_0$ at certain values of N_0 at $t = 0.2$ do not follow the trend of the curve and sit higher or lower. This occurs because the positivity of N is violated in these cases. It turns out that the VE term $(1 - N - E)^2$ in the branching term actually serves to keep the solutions for N_0 and E_0 positive. Further, we note that as $N_0 + E_0$ approaches 1, the effective branching rate $\lambda(1 - N - E)^2$ actually decreases in Model 2, while in Model 0 the branching rate λ remains the same. We also note that for $a_n = 0$ in Model 2, the $(1 - N)$ term in the source term for E (see equation (F.66)) ensures that $N_0 + E_0$ does not exceed one.

As we have mentioned in this thesis, provided we choose initial conditions that are not close to $N_0 + E_0 = 1$, the solutions to the equations do not become ill-posed, and density restrictions are adhered to. We illustrate this in Fig. F.9 where we have chosen initial values of $N_0 \in [0, 0.7]$ and $E_0 = 0.2$. For these choices of initial conditions, the models only become ill-posed if $N_0(0.2)$ exceeds a threshold value. Once again, for Model 2 with $a_n = 0$, the density restrictions are not violated for all initial values of N_0 (see Fig. F.9d). Further, Models 0 and 2 show similar behaviour, and thus, in this regime, positivity is preserved in Model 0.

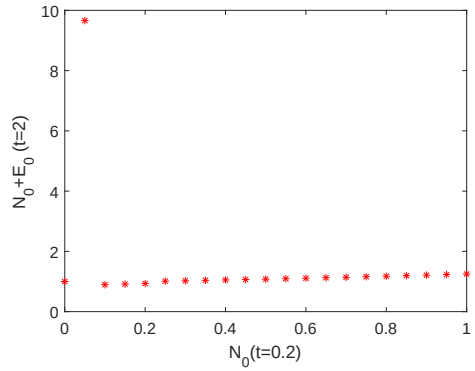

(a) Model 0, $a_e = 1, a_n = 1$

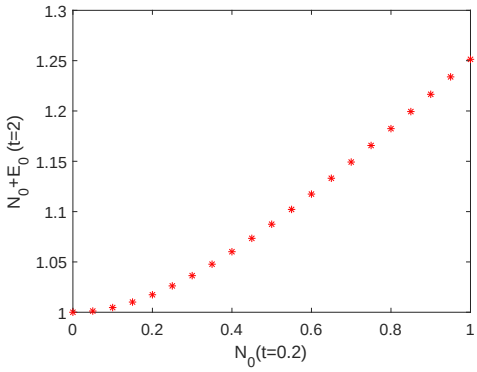

(b) Model 2, $a_e = 1, a_n = 1$

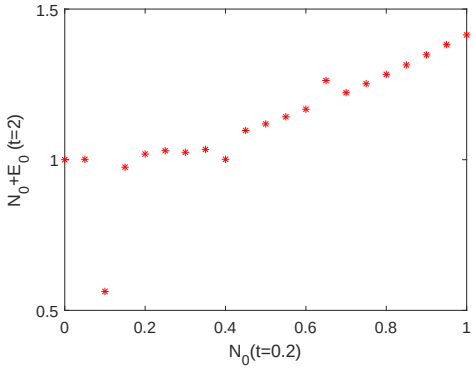

(c) Model 0, $a_e = 1, a_n = 0$

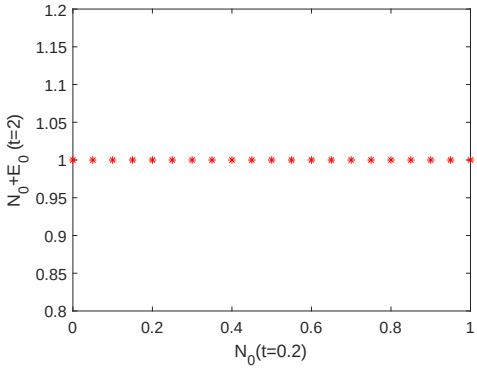

(d) Model 2, $a_e = 1, a_n = 0$

Figure F.8: Model 0 and 2 ill-posedness (non-zero a_e): Solutions to equations (F.70), (F.71), (F.74) and (F.75), where we depict $N_0 + E_0$ at time $t = 2.0$ as a function of initial values for N_0, ($E_0(0.2) = 1 - N_0(0.2)$). In (a)-(c), $N_0 + E_0$ exceeds 1 (except for $N_0 = 0$ initially). (d) $N_0 + E_0$ does not exceed 1, due to the VE term in the equation for E (equation (F.66)). We note that due to the linearity of the branching term in Model 0, positivity is not preserved, resulting in solutions that sit either above or below the trend of the curve e.g. $N_0 + E_0 \approx 10$ in (a).

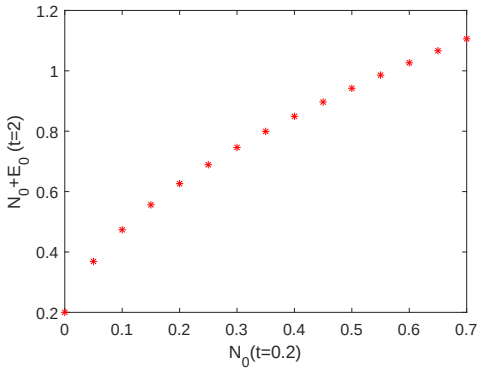

(a) Model 0, $a_e = 1, a_n = 1$

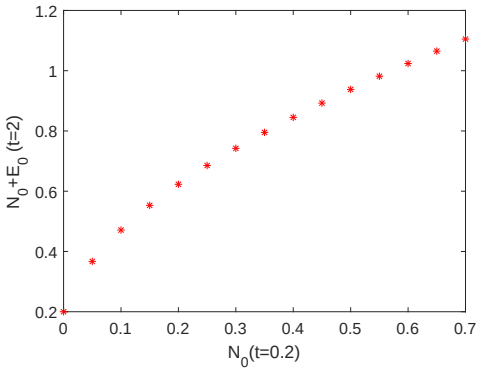

(b) Model 2, $a_e = 1, a_n = 1$

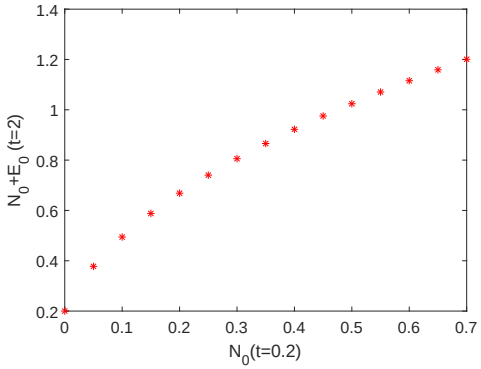

(c) Model 0, $a_e = 1, a_n = 0$

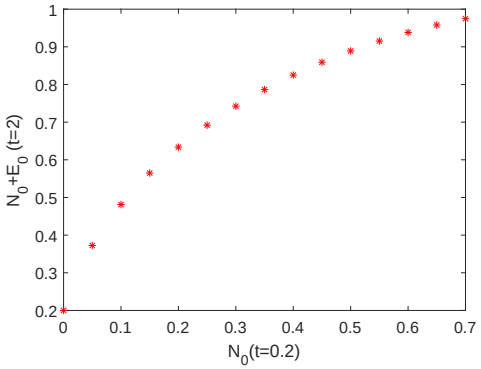

(d) Model 2, $a_e = 1, a_n = 0$

Figure F.9: Model 0 and 2 ill-posedness (non-zero a_e): Solutions to equations (F.70), (F.71), (F.74) and (F.75), where we depict $N_0 + E_0$ at time $t = 2.0$ as a function of initial values for N_0 and $E_0(0.2) = 0.2$. $N_0 + E_0$ exceeds 1 when $N_0(0.2) > 0.55$ in (a) and (b) and when $N_0(0.2) > 0.45$ in (c). In (d), the density restriction is not exceeded due to the VE term in the equation for E (equation (F.65)).

We also note that in Figs. F.8 and F.9, the value of N_0 at $t = 2$ is zero, or near zero, due to the large sink terms representing anastomosis in equations (F.70) and (F.74), and thus the value of $N_0 + E_0$ at $t = 2.0$ is approximately the value of E_0 at $t = 2.0$ (essentially at steady-state).

In Model 1 and Model 0 (with $a_e = 0$), we want to determine whether N can exceed 1 when $a_n = 1$, thereby leading to ill-posedness as the diffusion term is multiplied by a factor $(1 - a_n N)$ (see equations (F.62) and (F.65)). Further, we note that the equations for N are decoupled from the equations for E, and thus

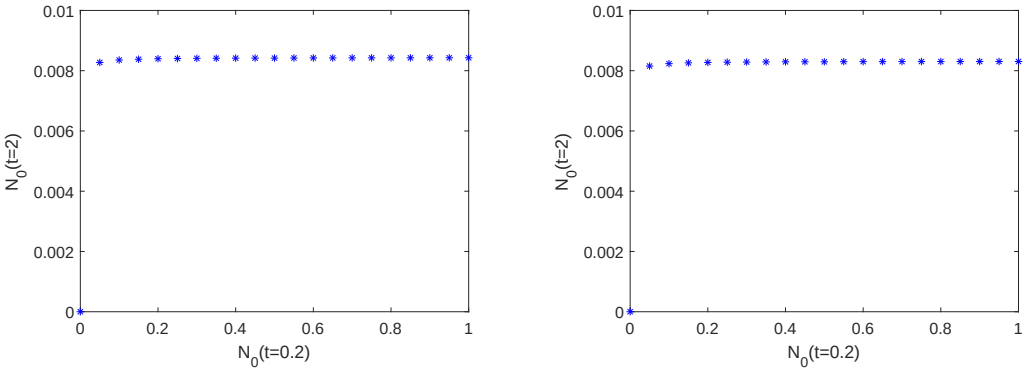

(a) Model 0, $a_e = 0, a_n = 1$ (b) Model 1, a_e N/A, $a_n = 1$

Figure F.10: Model 0 ($a_e = 0$) and Model 1 ill-posedness: Solutions to equations (F.70), (F.71), (F.72) and (F.73), where we depict N_0 at time $t = 2.0$ as a function of initial values for N_0 at $t = 0.2$ and $E_0(0.2) = 0$. The value of N_0 at $t = 2$ does not exceed 1. We also see that the solutions (apart from $N_0(0.2) = 0$), reach a steady-state for our choice of λ. The values for E_0 at $t = 2$, not shown, increase from 0 for $N_0(0.2) = 0$ to 8 for $N_0(0.2) = 1$.

the solutions for E do not affect the values of N. We solve the ODEs in equations (F.72), (F.73), (F.70) and (F.71) where we have chosen $x = 0.7450$ without loss of generality, and used the following set of parameter values: $\lambda = 1.6$, $\mu = 160$, from $t = 0.2 - 2$. We depict the values of N_0 at time $t = 2.0$ as a function of the initial value of N_0 in Fig. F.10. For the initial values, we let $N_0 \in [0, 1]$ in increments of 0.05, and $E_0 = 0$. We also impose the condition in Models 0 and 2 that $\lambda = 0$ if $N_0 > 1$ or N_0 and E_0 are negative. We see that for all initial values of N_0, N_0 at $t = 2$ does not exceed 1. We have investigated a wide range of values for λ (results not shown), and we have found that the solutions for N in Model 1 at $t = 2$ do not exceed 1, while in Model 0, they can exceed 1. This can be attributed to the VE term in the branching term in Model 1, $(1 - N)^2$, which implies that as N approaches 1, the effective branching rate $\lambda(1 - N)^2$ decreases. In Model 0, the branching rate is entirely determined by λ and thus as N approaches 1, the branching rate does not decrease.

In conclusion, Models 1 and 2 (for $a_n = 0$) remain well-posed. Model 2, with

$a_n > 0$, remains well-posed as long as appropriate initial conditions and branching rates are used. Model 0, as noted in Chapter 2, can become ill-posed, to a larger extent than in Model 2, if inappropriate initial conditions, branching and anastomosis rates are used. In Models 0 and 2 for non-zero a_e values, the equations for E are coupled to the equations for N, and this is the source of potential ill-posedness. As long as N is non-zero, E increases due to the source term μN in equations (F.63) and (F.66) in Models 0 and 2 ($a_n = 1$), respectively. This, in turn, eventually leads to ill-posedness via the $(1 - a_n N - a_e E)$ term pre-multiplying the diffusion term in the equations for N, equations (F.62) and (F.65), in Models 0 and 2, respectively. In this thesis, we have ensured that Models 0, 1 and 2 remain well-posed with positivity of solutions preserved by choosing appropriate initial conditions and parameter values.

Bibliography

S. Ai, W. Huang, and Z. Wang. Reaction, diffusion and chemotaxis in wave propagation. *Discrete and Continuous Dynamical Systems Series B*, 20:1–21, 2015.

H. Akaike. Information theory as an extension of the maximum likelihood principle. In B. N. Petrov and F. Csaki, editors, *Second International Symposium on Information Theory*, pages 267–281, 1973.

T. Alarcón, H. M. Byrne, and P. K. Maini. A cellular automaton model for tumour growth in inhomogeneous environment. *Journal of Theoretical Biology*, 225:257–274, 2003.

T. Alarcón, H. M. Byrne, and P. K. Maini. A multiple scale model for tumour growth. *SIAM Multiscale Modelling and Simulation*, 3:440–475, 2005.

T. Alarcón, H. M. Byrne, P. K. Maini, and J. Panovska. *Studies in Multidisciplinarity*, volume 3, chapter 20. Elsevier B.V., 2006.

M. Alber, W. Chen, P. M. Lushnikov, and S. A. Newman. Continuous macroscopic limit of a discrete stochastic model for interaction of living cells. *Physical Review Letters*, 99:168102, 2007.

A. R. A. Anderson and M. A. J. Chaplain. Continuous and discrete mathemati-

cal models of tumour-induced angiogenesis. *Bulletin of Mathematical Biology*, 60:857–900, 1998.

R. Auerbach, R. Lewis, B. Shinners, L. Kubai, and N. Akhtar. Angiogenesis assays: A critical overview. *Clinical Chemistry*, 49:32–40, 2003.

D. H. Ausprunk and J. Folkman. Migration and proliferation of endothelial cells in preformed and newly formed blood vessels during tumor angiogenesis. *Microvascular Research*, 14:53–65, 1977.

C. T. H. Baker, G. A. Bocharov, J. M. Ford, P. M. Lumb, and S. J. Norton et al. Computational approaches to parameter estimation and model selection in immunology. *Journal of Computational and Applied Mathematics*, 184:50–76, 2005a.

C. T. H. Baker, G. A. Bocharov, C. A. H. Paul, and F. A. Rihan. Computational modelling with functional differential equations: Identification, selection, and sensitivity. *Applied Numerical Mathematics*, pages 107–129, 2005b.

R. E. Baker and M. J. Simpson. Correcting mean-field approximations for birth-death-movement processes. *Physical Review E*, 82:041905, 2010.

R. E. Baker, C. A. Yates, and R. Erban. From microscopic to macroscopic descriptions of cell migration on growing domains. *Bulletin of Mathematical Biology*, 72:719–762, 2010.

D. Balding and D. L. S. McElwain. A mathematical model of tumour-induced capillary growth. *Journal of Theoretical Biology*, 114:53–73, 1985.

A. L. Bauer, T. L. Jackson, and Y. Jiang. A cell-based model exhibiting branching and anastomosis during tumour-induced angiogenesis. *Biophysical Journal*, 92:3105–3121, 2007.

A. L. Bauer, T. L. Jackson, Y. Jiang, and T. Rohlf. Receptor cross-talk in angiogenesis: mapping environmental cues to cell phenotype using a stochastic, boolean signaling network model. *Journal of Theoretical Biology*, 264: 838–846, 2010.

J. Bear. *Dynamics of Fluids in Porous Media*. Dover Publications Inc N.Y., 1988.

P. Benitez and S. Heilshorn. *Mechanical and Chemical Signaling in Angiogenesis*. Springer-Verlag, 2013.

K. Bentley, H. Gerhardt, and P. A. Bates. Agent-based simulation of notch-mediated tip cell selection in angiogenic sprout initialisation. *Journal of Theoretical Biology*, 250:25–36, 2008.

K. Bentley, G. Mariggi, H. Gerhardt, and P. A. Bates. Tipping the balance: Robustness of tip cell selection, migration and fusion in angiogenesis. *PLoS Computational Biology*, 5:e1000549, 2009.

S. Benzekry, C. Lamont, A. Beheshti, A. Tracz, and J. M. L. Ebos et al. Classical mathematical models for description and prediction of experimental tumor growth. *PLOS Computational Biology*, 10:e1003800, 2014.

R. Blanco and H. Gerhardt. VEGF and notch in tip and stalk cell selection. *Cold Spring Harbor Perspectives in Medicine*, 3:a006569, 2013.

L. L. Bonilla, V. Capasso, M. Alvaro, and M. Carretero. Hybrid modeling of tumor-induced angiogenesis. *Physical Review E*, 90:062716, 2014.

M. Bruna and S. J. Chapman. Diffusion in spatially varying porous media. *SIAM Journal on Applied Mathematics*, 75:1648–1674, 2015.

K. P. Burnham and D. R. Anderson. *Model selection and multimodal inference: a practical information-theoretic approach*. Springer, 2002.

K. P. Burnham, D. R. Anderson, and K. P. Huyvaert. AIC model selection and multimodel inference in behavioral ecology: some background, observations, and comparisons. *Behavioral Ecology and Sociobiology*, 65:23–25, 2011.

H. M. Byrne. Dissection cancer through mathematics: from the cell to the animal model. *Nature Reviews*, 10:221–230, 2010.

H. M. Byrne and M. A. J. Chaplain. Mathematical models for tumour angiogenesis: Numerical simulations and nonlinear wave solutions. *Bulletin of Mathematical Biology*, 57:461–486, 1995a.

H. M. Byrne and M. A. J. Chaplain. Explicit solutions of a simplified model of capillary sprout growth during tumour angiogenesis. *Applied Mathematics Letters*, 8:71–76, 1995b.

H. M. Byrne, T. Alarcón, M. R. Owen, S. D. Webb, and P. K. Maini. Modelling aspects of cancer dynamics: a review. *Philosophical Transactions of The Royal Society*, 364:1563–1578, 2006.

P. Carmeliet. Angiogenesis in life, disease and medicine. *Nature*, 438:932–936, 2005.

P. Carmeliet and R. K. Jain. Molecular mechanisms and clinical applications of angiogenesis. *Nature*, 473:298–307, 2011.

M. A. J. Chaplain. The mathematical modelling of tumour angiogenesis and invasion. *Acta Biotheoretica*, 43:387–402, 1995.

M. A. J. Chaplain. Avascular growth, angiogenesis and vascular growth in solid

tumours: The mathematical modelling of the stages of tumour development. *Mathematical and Computer Modelling*, 23:47–87, 1996.

M. A. J. Chaplain. Mathematical modelling of angiogenesis. *Journal of Neuro-Oncology*, 50:37–51, 2000.

M. A. J. Chaplain and M. Stuart. A model mechanism for the chemotactic response of endothelial cells to tumour angiogenesis factor. *IMA Journal of Mathematics Applied in Medicine & Biology*, 10:149–168, 1993.

S. J. Chapman, R. J. Shipley, and R. Jawad. Multiscale modeling of fluid transport in tumors. *Bulletin of Mathematical Biology*, 70:2334–2357, 2008.

E. A. Codling, M. J. Plank, and S. Benhamou. Random walk models in biology. *Journal of the Royal Society Interface*, 5:813–834, 2008.

T. F. Coleman and Y. Li. On the convergence of reflective newton methods for large-scale nonlinear minimization subject to bounds. *Mathematical Programming*, 67:189–224, 1994.

T. F. Coleman and Y. Li. An interior, trust region approach for nonlinear minimization subject to bounds. *SIAM Journal on Optimization*, 6:418–445, 1996.

A. J. Connor, R. P. Nowak, E. Lorenzon, M. Thomas, and F. Herting et al. An integrated approach to quantitative modelling in angiogenesis research. *Journal of the Royal Society Interface*, 12:20150546, 2015.

J. H. Cushman, L. S. Bennethum, and B. X. Hu. A primer on upscaling tools for porous media. *Advances in Water Resources*, 25:1043–1067, 2002.

K. J. Davies, J. E. F. Green, N. G. Bean, B. J. Binder, and J. V. Ross. On the

derivation of approximations to cellular automata models and the assumption of independence. *Mathematical Biosciences*, 253:63–71, 2014.

Y. Davit, C. G. Bell, H. M. Byrne, L. A. C. Chapman, L. S. Kimpton, and G. E. Lang et al. Homogenization via formal multiscale asymptotics and volume averaging: How do the two techniques compare? *Advances in Water Resources*, 62:178–206, 2013.

D. R. Durran. *Numerical Methods for Fluid Dynamics*. Springer, second edition, 2010.

L. Dyson and R. E. Baker. The importance of volume exclusion in modelling cellular migration. *Journal of Mathematical Biology*, 71:691–711, 2015.

L. Dyson, P. K. Maini, and R. E. Baker. Macroscopic limits of individual-based models for motile cell populations with volume exclusion. *Physical Review E*, 86:031903, 2012.

L. Edelstein. The propagation of fungal colonies: A model for tissue growth. *Journal of Theoretical Biology*, 98:679–701, 1982.

R. Erban, S. J. Chapman, and P. K. Maini. A practical guide to stochastic simulations of reaction-diffusion processes. *arxiv.org*, arXiv:0704.1908:1–35, 2007.

R. A. Fisher. The wave of advance of advantageous genes. *Annals of Eugenics*, 7:353–369, 1937.

J. Folkman. Tumor angiogenesis: Therapeutic implications. *The New England Journal of Medicine*, 285:1182–1186, 1971.

J. Folkman. The vascularization of tumors. *Scientific American*, 234:58–73, 1976.

J. Folkman and M. Hochberg. Self-regulation of growth in three dimensions. *The Journal of Experimental Medicine*, 138:745–753, 1973.

J. Folkman and M. Klagsbrun. Angiogenic factors. *Science*, 235:442–447, 1987.

D. T. Gillespie. Exact stochastic simulation of coupled chemical reactions. *Journal of Physical Chemistry*, 81:2340–2361, 1977.

M. A. Gimbrone, R. S. Cotran, S. B. Leapman, and J. Folkman. Tumor growth and neovascularization: An experimental model using the rabbit cornea. *Journal of the National Cancer Institute*, 52:413–427, 1974.

J. A. Glazier and F. Graner. Simulation of the differential adhesion driven rearrangment of biological cells. *Physical Review E*, 47:2128–2154, 1993.

F. Graner and J. A. Glazier. Simulation of biological cell sorting using a two-dimensional extended Potts model. *Physical Review Letters*, 69:2013–2016, 1992.

J. Grogan, A. J. Connor, B. Markelc, R. J. Muschel, P. K. Maini, H. M. Byrne, and J. M. Pitt-Francis. Microvessel chaste: An open library for spatial modelling of vascularized tissues. *Biophyscial Journal*, 112:1767–1772, 2017.

D. Hanahan and R. A. Weinberg. The hallmarks of cancer. *Cell*, 100:57–70, 2000.

D. Hanahan and R. A. Weinberg. Hallmarks of cancer: The next generation. *Cell*, 144:646–674, 2011.

H. A. Harrington, M. Maier, L. Naidoo, N. Whitaker, and P.G. Kevrekidis. A hybrid model for tumor-induced angiogenesis in the cornea in the presence of inhibitors. *Mathematical and Computer Modelling*, pages 513–524, 2007.

T. Hillen and K. J. Painter. A user's guide to PDE models for chemotaxis. *Journal of Mathematical Biology*, 58:183–217, 2009.

C. M. Hurvich and C-L Tsai. Regression and time series model selection in small samples. *Biometrika*, 76:297–307, 1989.

J. D. Hywood, E. J. Hackett-Jones, and K. A. Landman. Modeling biological tissue growth: Discrete to continuum representations. *Physcial Review E*, 88: 032704, 2013.

H.V. Jain and T. L. Jackson. A hybrid model of the role of vegf binding in endothelial cell migration and capillary formation. *Frontiers in Oncology*, 3: 1–15, 2013.

R. K. Jain. Normalizing tumor vasculature with anti-angiogenic therapy: A new paradigm for combination therapy. *Nature Medicine*, 7:987–989, 2001.

R. K. Jain. Antiangiogenesis strategies revisited: From starving tumors to alleviating hypoxia. *Cancer Cell*, 26:605–622, 2014.

L. Jakobsson, C. A. Franco, K. Bentley, R. T. Collins, B. Ponsioen, I. M. Aspalter, I. Rosewell, M. Busse, G. Thurston, A. Medvinsky, S. Schulte-Merker, and H. Gerhardt. Endothelial cells dynamically compete for the tip cell position during angiogenic sprouting. *Nature Cell Biology*, 12:943–953, 2010.

E. Kavanagh. Interface Motion in the Oswald Ripening and Chemotaxis Systems. Master's thesis, University of British Columbia, 2014.

E. F. Keller and L. A. Segel. Initiation of slime mold aggregation viewed as an instability. *Journal of Theoretical Biology*, 26:399–415, 1970.

E. F. Keller and L. A. Segel. Model for chemotaxis. *Journal of Theoretical Biology*, 30:225–234, 1971.

M. Klagsbrun and M. A. Moses. Molecular angiogenesis. *Chemistry & Biology*, 6:R217–R224, 1999.

S. Kozlov. The method of averaging and walks in inhomogeneous environments. *Russian Math Surveys*, 40:97–128, 1985.

T. M. Liggett. *Stochastic Interacting Systems: Contact, Voter and Exclusion Processes*. Springer-Verlag, 1999.

T. Lin and Z. Wang. Development of traveling waves in an interacting two-species chemotaxis model. *Discrete and Continuous Dynamical Systems*, 34: 2907–2927, 2014.

P. M. Lushnikov, N. Chen, and M. Alber. Macroscopic dynamics of biological cells interacting via chemotaxis and direct contact. *Physical Review E*, 78: 061904, 2008.

P. Macklin, S. McDougall, A. R. A. Anderson, M. A. J. Chaplain, V. Cristini, and J. Lowengrub. Multiscale modelling and nonlinear simulation of vascular tumour growth. *Journal of Mathematical Biology*, 58:765–798, 2009.

N. V. Mantzaris, S. Webb, and H. G. Othmer. Mathematical modeling of tumour-induced angiogenesis. *Journal of Mathematical Biology*, 49:111–187, 2004.

D. C. Markham. *Spatial Correlation Models for Cell Populations*. D.Phil thesis, University of Oxford, 2014.

S. R. McDougall, A. R. A. Anderson, M. A. J. Chaplain, and J. A. Sherratt. Mathematical modelling of flow through vascular networks: Implications for

tumour-induced angiogenesis and chemotherapy strategies. *Bulletin of Mathematical Biology*, 64:673–702, 2002.

M. Mei, H. Peng, and Z. Wang. Asymptotic profile of a parabolic-hyperbolic system with boundary effect arising from tumor angiogenesis. *Journal of Differential Equations*, 259:5168–5191, 2015.

H. Motulsky and A. Christopoulos. *Fitting models to biological data using linear and nonlinear regression.* Oxford University Press, 2004.

V. R. Muthukkaruppan, L. Kubai, and R. Auerbach. Tumor-induced neovascularization in the mouse eye. *Journal of the National Cancer Institute*, 69: 699–708, 1982.

J. T. Oden and E. E. Prudencio. Selection and assessment or phenomenological models of tumor growth. *Mathematical Models and Methods in Applied Sciences*, 23(7), 2013.

T. Oden, R. Moser, and O. Ghattas. Computer predictions with quantified uncertainty, part I. *SIAM News*, 43(9), 2010a.

T. Oden, R. Moser, and O. Ghattas. Computer predictions with quantified uncertainty, part II. *SIAM News*, 43(10), 2010b.

M. E. Orme and M. A. J. Chaplain. Two-dimensional models of tumour angiogenesis and anti-angiogenesis strategies. *IMA Journal of Mathematics Applied in Medicine & Biology*, 14:189–205, 1997.

H. G. Othmer and A. Stevens. Aggregation, blowup, and collapse: The ABC's of taxis in reinforced random walks. *SIAM Journal on Applied Mathematics*, 57:1044–1081, 1997.

M. R. Owen, T. Alarcón, P. K. Maini, and H. M. Byrne. Angiogenesis and vascular remodelling in normal and cancerous tissues. *Journal of Mathematical Biology*, 58:689–721, 2009.

K. J. Painter and T. Hillen. Volume-filling and quorum sensing in models for chemosensitive movement. *Canadian Applied Mathematics Quarterly*, 10: 501–543, 2002.

G. C. Papanicolaou. *Diffusion in Random Media*. Plenum Press, 1995.

G. C. Papnicolaou and S. R. S. Varadhan. *Boundary Value Problems with Rapidly Oscillating Random Coefficients*. North Holland, 1982.

C. J. Penington, B. D. Hughes, and K. A. Landman. Building macroscale models from microscale probabilistic models: A general probabilistic approach for nonlinear diffusion and multispecies phenomena. *Physical Review E*, 84: 041120, 2011.

R. Penta and D. Ambrosi. The role of microvascular tortuosity in tumor transport phenomena. *Journal of Theoretical Biology*, 364:80–97, 2015.

R. Penta, D. Ambrosi, and A. Quarteroni. Multiscale homogenization for fluid and drug transport in vascularized malignant tissues. *Mathematical Models and Methods in Applied Sciences*, 25:79–108, 2015.

H. Perfahl, H. M. Byrne, T. Chen, V. Estrella, and T. Alarcón et al. Multiscale modelling of vascular tumour growth in 3D: The roles of domain size and boundary conditions. *PLoS One*, 6:e14790, 2011.

H. Perfahl, B. D. Hughes, T. Alarcon, P. K. Maini, M. C. Lloyd, M. Reuss, and H. M. Byrne. 3D hybrid modelling of vascular network formation. *Journal of Theoretical Biology*, 414:254–268, 2017.

S. Pillay, H. M. Byrne, and P. K. Maini. Modeling angiogenesis: A discrete to continuum description. *Physical Review E*, 95:012410, 2017.

M. J. Plank and M. J. Simpson. Models of collective cell behaviour with crowding effects: comparing lattice-based and lattice-free approaches. *Journal of the Royal Society Interface*, 2012.

M. J. Plank and B. D. Sleeman. Lattice and non-lattice models of tumour angiogenesis. *Bulletin of Mathematical Biology*, 66:1785–1819, 2004.

M. Potente, H. Gerhardt, and P. Carmeliet. Basic and therapeutic aspects of angiogenesis. *Cell*, 146:873–887, 2011.

N. Rajewsky, L. Santen, A. Schadschneider, and M. Schreckenberg. The asymmetric exclusion process: Comparison of update procedures. *Journal of Statistical Physics*, 92:151–194, 1998.

R. J. H. Ross, C. A. Yates, and R. E. Baker. Inference of cell-cell interactions from population density characteristics and cell trajectories on static and growing domains. *Mathematical Biosciences*, 264:108–118, 2015.

R. S. Samant and L. A. Shevde. Recent advances in anti-angiogenic therapy of cancer. *Oncotarget*, 2:122–134, 2011.

D. Schulz, M. E. Iliev, B. E. Frueh, and D. Goldblum. In vivo pachymetry in normal eyes of rats, mice and rabbits with the optical low coherence reflectometer. *Vision Research*, 43:723–728, 2003.

M. Scianna, C. G. Bell, and L. Preziosi. A review of mathematical models for the formation of vascular networks. *Journal of Theoretical Biology*, 333: 174–209, 2013.

L. F. Shampine and M. W. Reichelt. The MATLAB ODE suite. *SIAM Journal on Scientific Computing*, 18:1–22, 1997.

R. J. Shipley and S. J. Chapman. Multiscale modelling of fluid and drug transport in vascular tumours. *Bulletin of Mathematical Biology*, 72:1464–1491, 2010.

A. Shirinifard, J. S. Gens, B. L. Zaitlen, N. J. Poplawski, M. Swat, and J. A. Glazier. 3D multi-cell simulation of tumor growth and angiogenesis. *PLoS One*, 4:e7190, 2009.

M. J. Simpson and R. E. Baker. Corrected mean-field models for spatially dependent advection-diffusion-reaction phenomena. *Physical Review E*, 83: 051922, 2011.

M. J. Simpson, A. Merrifield, K. A. Landman, and B. D. Hughes. Simulating invasion with cellular automata: Connecting cell-scale and population-scale properties. *Physical Review E*, 76:021918, 2007.

M. J. Simpson, K. A. Landman, and B. D. Hughes. Multi-species simple exclusion processes. *Physica A*, 388:399–406, 2009a.

M. J. Simpson, K. A. Landman, and B. D. Hughes. Pathlines in exclusion processes. *Physical Review E*, 79:031920, 2009b.

M. J. Simpson, K. A. Landman, and B. D. Hughes. Cell invasion with proliferation mechanisms motivated by time-lapse data. *Physica A*, 389:3779–3790, 2010a.

M. J. Simpson, K. A. Landman, B. D. Hughes, and A. E. Fernando. A model for mesoscale patterns in motile populations. *Physica A*, 389:1412–1424, 2010b.

M. J. Simpson, R. E. Baker, and S. W. McCue. Models of collective cell spreading with variable cell aspect ratio: A motivation for degenerate diffusion models. *Physcial Review E*, 83:021901, 2011.

A. F. Smith. *Multi-scale Modelling of Blood Flow in the Coronary Microcirculation*. D.Phil thesis, University of Oxford, 2013.

A. F. Smith, R. J. Shipley, J. Lee, G. B. Sands, I. J. LeGrice, and N. P. Smith. Transmural variation and anisotropy of microvascular flow conductivity in the rat myocardium. *Annals of Biomedical Engineering*, 42:1966–1977, 2014.

A. F. Smith, T. W. Secomb, A. R. Pries, N. P. Smith, and R. J. Shipley. Structure-based algorithms for microvessel classification. *Microcirculation*, 22:99–108, 2015.

F. Spill, P. Guerrero, T. Alarcón, P. K. Maini, and H. M. Byrne. Mesoscopic and continuum modelling of angiogenesis. *Journal of Mathematical Biology*, 70:485–532, 2015.

A. Stéphanou, S. R. McDougall, A. R. A. Anderson, and M. A. J. Chaplain. Mathematical modelling of flow in 2D and 3D vascular networks: Applications to anti-angiogenic and chemotherapeutic drug strategies. *Mathematical and Computer Modelling*, 41:1137–1156, 2005.

C. L. Stokes and D. A. Lauffenburger. Analysis of the roles of microvessel endothelial cell random motility and chemotaxis in angiogenesis. *Journal of Theoretical Biology*, 152:377–403, 1991.

N. Sugiura. Further analysis of the data by Akaike's information criterion and the finite corrections. *Communications in Statistics - Theory Methods*, 7: 13–26, 1978.

F. Terragni, M. Carretero, V. Capasso, and L. L. Bonilla. Stochastic model of tumor-induced angiogenesis: Ensemble averages and deterministic equations. *Physical Review E*, 93:022413, 2016.

S. Tong and F. Yuan. Numerical simulations of angiogenesis in the cornea. *Microvascular Research*, 61:14–27, 2001.

S. Tong and F. Yuan. Dose response of angiogenesis to basic fibroblast growth factor in rat corneal pocket assay: Ii. numerical simulations. *Microvascular Research*, 75:16–24, 2008.

T. Toni and M. P. H. Stumpf. Simulation-based model selection for dynamical systems in systems and population biology. *Bioinformatics*, 26:104–110, 2010.

T. Toni, D. Welch, N. Strelkowa, A. Ipsen, and M. P. H. Stumpf. Approximate bayesian computation scheme for parameter inference and model selection in dynamical systems. *Journal of The Royal Society Interface*, 6:187–202, 2009.

B. M. Turner and T. Van Zandt. A tutorial on approximate bayesian computation. *Journal of Mathematical Psychology*, 56:69–85, 2012.

Cancer Research UK. http://www.cancerresearchuk.org/health-professional/cancer-statistics/incidence, Accessed October 2017, 2017.

G. Vilanova, I. Colominas, and H. Gomez. Coupling of discrete random walks and continuous modeling for three-dimensional tumour-induced angiogenesis. *Computational Mechanics*, 53:449–464, 2014.

G. B. Whitham. *Linear and Nonlinear Waves*. John Wiley & Sons, Inc, 1974.

S. Wolfram. Statistical mechanics of cellular autumata. *Reviews of Modern Physics*, 55:601–644, 1983.

D. F. Zawicki, R. K. Jain, G. W. Schmid-Schoenbein, and S. Chien. Dynamics of neovascularization in normal tissue. *Microvascular Research*, 21:27–47, 1981.

H. Zhang, L. Wang, Y. Xie, S. Liu, and X. Deng et al. The measurement of corneal thickness from center to limbus in vivo in c57bl/6 and balb/c mice using two-photon imaging. *Experimental Eye Research*, 115:255–262, 2013.

X. Zheng, G. Y. Koh, and T. Jackson. A continuous model of angiogenesis: Initiation, a continuous model of angiogenesis: Initiation, modulated by vascular endothelial growth, factor, angiopoietins, platelet-derived growth factor-b, and pericytes. *Discrete and Continuous Dynamical Systems Series B*, 18: 1109–1154, 2013.